Synthesis and thermoelectric properties of Fe-Ti-Al based alloys

Sukhwinder Singh

A thesis submitted for the degree of Doctor of Philosophy

CARDIFF SCHOOL OF ENGINEERING

MAGNETICS AND MATERIALS RESEARCH GROUP

November 2022

SUMMARY

Thermoelectric materials usually refer to the materials that can use temperature difference to generate electricity, which has potential to contribute to clean energy and environment. The drawback associated with the current thermoelectric materials is that these materials usually contain highly toxic, expensive and less earth-abundant elements, which limit their economic viability of large-scale applications. This study explores the possibility of developing economically viable thermoelectric materials based on Fe-Ti-Al alloys, which are low-cost, abundant, and less-toxic. The first stage of this research focused on establishing suitable preparation conditions (such as ball milling period, cold pressing pressure, and annealing temperature) that enables fabrication of $Fe_{11}Ti_3Al_6$ alloys with satisfactory thermoelectric properties and offers a convenient route for substitution experiments. The samples prepared after 5 hours of ball milling, followed by cold pressing under 2200 MPa and annealing at 700 ^{0}C exhibit a power factor of $12x10^{-5}$ W/mk^2 with a Seebeck coefficient of 32.3μV/K and electrical resistivity of 8.6μΩm. The second stage of the research investigates the possibility of further improving thermoelectric properties of $Fe_{11}Ti_3Al_6$ alloy through elemental substitution. A systematic investigation was carried out by substituting Fe using an element from Group V-VII (V, Mn, Cr, W, Mo) or Group IX-X (Co and Ni). It is found that the substitution using Group V-VII element resulted in an increase in the Seebeck coefficient by 6 - 32% while the substitution using Group IX-X element led to a transition from p-type to n-type – a phenomenon normally associated with semiconductors only. The final stage of the research focused on preparation and characterisation of $Fe_{10}Cr_1Ti_3Al_6$ alloy (identified in the second stage of the research) using Spark Plasma Sintering (SPS), which facilitates preparation of high-density materials. The samples prepared using the SPS technique exhibit a significantly improved power factor of $64x10^{-5}$ W/mK^2, which is approximately 5 times higher than that prepared by cold pressing and annealing. The thermoelectric properties as a function temperature were also characterised. The results show that the peak ZT of 0.02 was achieved at 98 ^{0}C.

Dedication

This thesis is dedicated to my late paternal grandfather Sardar Pritam Singh Bajaj, and my late maternal grandmother Sardarni Prakash Kaur.

*Both passed away recently. I know you are no longer in this world, but your valuable teachings, experiences, and lovely memories will help to regulate my life. Thank you for your guidance, support and encouragement**s**.*

ACKNOWLEDGEMENTS

Firstly, I would like to express my sincere gratitude to my primary supervisor, Prof. Gao Min, for his support, motivation, and guidance throughout my PhD project. I would also like to thank my co-supervisor, Dr Victoria García Rocha, for her fruitful suggestions and assistance during my research.

I would especially like to thank Dr Matthew Burton for his helping hands in measuring the temperature-dependent thermoelectric properties at the Faculty of Science and Engineering, Swansea University. Many thanks to Dr Daniel Zabek for SEM measurements at the School of Engineering, Cardiff University. A special thanks to Mr Joseph Alemzadeh and Dr Guillermo Menendez Rodriguez for providing training on spark plasma sintering and tubular furnace equipment, respectively. I also appreciate Dr Quanquan Han for giving a training session on the planetary ball mill.

I would like to acknowledge the technical staff of the Mechanical and Electrical workshop, School of Engineering, Cardiff University. Thank you, particularly to Andrew Rankmore, Malcolm Seaborne, Stephen Roberts, Andrew Girdler, Stephen Mead, Paul Malpas, Alan Reynolds, Gareth Harvey and Denley Slade, for your endless technical support. I am incredibly grateful to Mr J Rowland and Dr Fei Jin for their assistance in XRD measurements.

My sincere thanks to our research group members- Godwin, Dr Matthew Phillips, Ali, Hamed, Martin, Alex and Mohammad for their support and encouragement. Additionally, I would like to thank Dr Gbadebo Yusuf, Dr Sachin Nanavti, Mr Prasad Rayamane, Dr Tanuj Singh, and Dr Pawan Mishra for their assistance in editing this thesis. Thanks to all of you for your time, suggestions, and patience.

I would also like to say thanks to Prof. R.K Puri, HOD, Department of Physics, Panjab University, and Dr Ravi Bhatia, Assistant Professor of Physics at GJU S&T, Hisar, India, who encouraged me to pursue a PhD abroad. A special thanks also go to my closest friend, Mr Rishabh Bansal (PCS), who has supported, motivated, and encouraged me to study abroad.

A special thanks to my family and friends. I can't express in words how grateful I am to my mother and father, maternal grandfather Sohan Singh and his cousin Bhupinder Singh, Mama Darshan Singh, Uncle Ram Singh and Ramandeep Singh (Goldy) and his family for all the support and sacrifices they made for me throughout my life. I am pleased to acknowledge the inestimable care and love received from Mr Jarnail Singh and his wife, Mrs Sudeshan Kaur, in Cardiff. My unalloyed appreciation also goes to Mr Angrez Singh and his wife for their support and usual hospitality.

Above all, I would like to thank my wife, Ekam, for her love and constant support over the past years. Thanks for being my editor, proof-reader, and sounding board. The most important thing to me is that you are my best friend. Thank you so much for everything.

Last but not least, I would like to thank the Ministry of Social Justice & Empowerment, Government of India, for the financial supporting this PhD programme.

ORAL PRESENTATIONS

- **Title: Preparation and Thermoelectric Properties of p-type $Fe_{10}Cr_1Ti_3Al_6$,** Virtual Conference on Thermoelectrics- (20-22nd July 2021)
- **Title: Improving the Seebeck coefficient of $Fe_{11}Ti_3Al_6$ by W substitution**, Gregynog Conference, UK (11th June 2021). (Secured Second Place)
- **Title: Preparation and Thermoelectric Properties of p-type $Fe_{11}Ti_3Al_6$,** Virtual Conference on Thermoelectrics- (21-23rd July 2020)

Publications

- **Thermoelectric properties of Fe-Cr-Ti-Al synthesised by mechanical alloying and Spark Plasma Sintering** Sukhwinder Singh, Joseph Alemzadeh, Guillermo Menendez Rodriguez, Matthew Phillips, Daniel Zabek, Matthew Burton, Victoria G. Rocha and Gao Min (Ready to submit)
- **Improving the room temperature thermoelectric performance of Fe-Ti-Al sample by Cr-substitution** Sukhwinder Singh, Godwin Ugwuanyi, Matthew Phillips, Victoria G. Rocha, and Gao Min (under preparation)

Contents

LIST OF SYMBOLS

Symbol	Definition
E_g	Energy band gap
α	Seebeck coefficient
ρ	Electrical resistivity
k	Total thermal conductivity
k_e	Electronic thermal conductivity
k_l	lattice thermal conductivity
T	Temperature
ΔT	Temperature difference
β	Thomson coefficient
Π	Peltier coefficient
Q	Heat Exchange
μ	Drift mobility
μ_w	Weighted mobility
σ	Electrical conductivity
L	Lorenz number
ρ_{app}	Apparent density
ρ_{Arch}	Archimedes density
d	Sample thickness
M	Mass of sample
E_F	Fermi level

LIST OF ABBREVIATIONS

TE	Thermoelectric
ZT	Dimensionless figure of merit
PF	Power factor
LMT	laser melting technique
VEC	Valence electron concentration
RTG	Radioisotope thermoelectric generators
US	United States
MRS	Material research society
HH	Half-Heusler
DOS	Density of States
DFT	Density functional theory
SPB	Single Parabolic Band
SPH	Small Polaron Hopping
NTF	Narrow transport function
DTF	Dispersive transport function
PGEC	Phonon glass electron crystal
HT	Hydrothermal technique
ST	Solvothermal technique
CVD	Chemical Vapour deposition
BM	Ball milling
MA	Mechanical alloying
PBM	Planetary ball mill
SEM	Scanning electron microscope
XRD	X-ray diffraction
EDX	Energy dispersive X-ray spectroscopy
FAST	Field-assisted sintering technique
PECS	Pulsed Electric Current Sintering
PAS	Plasma activated sintering
SPS	Spark Plasma sintering

CP	Cold press
ICDD	International Centre for Diffraction Data
COD	Crystallography Open Database
FWHM	Full width at half maximum
VSM	Vibrating Sample Magnetometer
TM	Transport mechanisms

LIST OF FIGURES

LIST OF TABLES

Chapter 1: Introduction

1.1 Background

United Nations Intergovernmental Panel on Climate change (IPCC) reported in 2018 that the average global temperature had increased by approximately 1^0C since the industrial era. This panel warned that due to the increase in human activities and industrialization, the temperature increase would reach 1.5 ^{0}C before 2030[1]. The temperature rise has begun melting the glaciers and raising the ocean levels, enhancing drought and floods, intense heat waves, and affecting agricultural productivity. Extreme climate change and natural disasters will render a large portion of the earth uninhabitable in the future. The world is facing climate change challenges primarily due to the rise of carbon dioxide (CO_2) emissions from the high consumption of fossil fuels such as coal, natural gas and crude oil. Over the last three decades, coal production worldwide has significantly increased from 750 million tons to 2500 million tons to meet the energy demand[2, 3]. A report by OPEC (Organization of Petroleum Exporting Countries) predicted that globally oil demand for the transportation sector in 2045 would rise from 90 to 109 million barrels per day[4]. To reduce the reliance on fossil fuels and tackle the climate change challenge, alternative green energy sources such as solar, wind, tidal, thermoelectric, and hydropower-based technologies are necessary to be widely developed. Among these technologies, thermoelectricity provides a potential eco-friendly route to harness the waste heat energy dissipated from transport, power and industrial sector and convert it to electricity[5, 6].

Thermoelectric devices are robust and have applications in the aerospace sector, power generation, refrigeration and biomedical devices[7, 8]. These devices have the noiseless operation. Thermoelectric materials are the core of thermoelectric devices. If a material shows a high figure-of-merit ZT, then it indicates that the material can convert heat into electricity more efficiently. The ZT is called the Dimensionless Figure of merit, and this parameter is useful to determine the conversion efficiency of thermoelectric materials. The reports suggest that thermoelectric materials having ZT close to 1, shows an energy conversion efficiency ability of 10% or less[9]. Theoretically, studies predict that if the experimentally ZT ≥ 4 is achieved, then the energy conversion efficiency between heat and electricity could reach 30%, which exhibits a highly attractive prospect for practical applications[10]. SnSe, Cu-Se, Pb-Te, and Bi-Te based alloys have been

discovered as the most efficient thermoelectric materials. According to recent reports, these efficient materials attained ZT values between 1.5 to 2.7[10]. Among these materials, SnSe alloy displays excellent ZT of 2.2 at 773 K[11] because of ultralow lattice thermal conductivity induced by Sn vacancies. Furthermore, Na-substituted based nanostructured PbTe alloy achieved ZT ~2.6 at 873K, due to the existence of lattice strain and band convergence effect[12]. Besides this, $Cu_{1.94}In_{0.01}Se$ attained ZT of 2.6 at 850K, this attributed to the localization of Cu^{+} ions occurred by the incorporation of In element into Cu_2Se lattice[13]. Moreover, $Bi_{0.45}Sb_{1.55}Te_3$ alloy demonstrates ZT of 1.75 at 270 K, which is approximately 60% higher than commercial state-of-art Bi_2Te_3 material near room temperature[14]. The low thermal conductivity was responsible for this improvement due to the increased phonon scattering. The major disadvantage of efficient materials is that they contain highly toxic, expensive elements, which limit their production and usage at a large scale[15]. Due to these problems, attention has been given to discovering thermoelectric materials based on elements that are inexpensive, highly abundant on earth and low-cost[15].

In the last two decades, intermetallic alloys based on low-cost transition metals and non-toxic aluminium or silicon elements such as Fe_2VAl and CoSi alloys have been identified as promising thermoelectric materials[16]. These alloys are believed to have a pseudo-gap with sharp density-of-states near the Fermi level (E_F), resulting in a high Seebeck coefficient of >100μV/K and metallic-like resistivity < 500μΩm[16-20]. However, these materials exhibit low ZT (~0.1), due to high thermal conductivity of 25-30 W/mK[16, 20]. The thermoelectric properties of ternary alloys such as Fe-Al-Si[19], Ti-Ni-Si[21] and Fe-Ti-Al[22] also have been studied. Jorge García-Cañadas[22] et al. identified n-type $Fe_3Ti_4Al_1$ and p-type $Fe_{11}Ti_3Al_6$ materials as promising thermoelectric materials to be further investigated. The n-type $Fe_3Ti_4Al_1$ sample displays a maximum power factor of $130x10^{-5}$ W/mK^2 with a Seebeck coefficient of -57 μV/K and electrical resistivity of 2.5μΩm. p-type $Fe_{11}Ti_3Al_6$ attained Seebeck coefficient of +27 μV/K and electrical resistivity of 1μΩm, resulting in a power factor of $70x10^{-5}$ W/mK^2. Further data analysis indicates that the electrical conductivity of these materials is too high and a reduction in the electrical conductivity can lead to a decrease in the electronic contribution to total thermal conductivity. In addition, the power factor of the materials may also be improved with the carrier concentration shifted towards their optimal values. This offers a promising route to improve the ZT of these materials, which may be achieved by controlling the “doping” level of the materials as being employed in semiconductors. Although the “doping” method has long been widely used in semiconductor industries, the validity of applying this approach to intermetallic alloys has not been demonstrated.

This research work was proposed to tackle this challenge by investigating the possibility of improving the thermoelectric properties of Fe-Ti-Al alloys by an elemental substitution approach.

The thesis describes the strategies and research efforts employed to achieve this goal, which involve developing the techniques and processes to facilitate convenient materials mixing, element substitution and sample fabrication, performing systematic experimental investigations to demonstrate the proposed approach, and focused effort in improving the thermoelectric performance of Fe-Ti-Al based alloys.

1.2 Aims and objectives

The project aims to develop low-cost and non-toxic thermoelectric materials based on Fe-Ti-Al alloys. The research activities involve the preparation of Fe-Ti-Al samples and the characterisation of their thermoelectric properties, with a focus on enhancing scientific understanding for further improvement. To achieve this aim, the specific objectives of this research programme are as:

- To Identify the optimum conditions for the preparation of n-type and p-type Fe-Ti-Al alloys by mechanical alloying, cold pressing, and annealing
- To investigate the effect of elemental substitution on phase structure and thermoelectric properties of Fe-Ti-Al alloys
- To examine the relation between elemental substitution and thermoelectric properties of Fe-Ti-Al alloys
- To explore the feasibility of improving the thermoelectric properties of Fe-Ti-Al alloys based on elemental substitution approach
- To employ the Spark Plasma Sintering (SPS) technique for the fabrication of high-density Fe-Ti-Al alloys with improved thermoelectric properties
- To characterise and evaluate the temperature dependence of the thermoelectric properties of the SPS fabricated Fe-Ti-Al based alloys

1.3 Thesis structure

The thesis gives a detailed account on a systematic investigation into the feasibility of improving the thermoelectric properties of Fe-Ti-Al alloys based on the elemental substitution method. It consists of seven chapters. The main focuses of each chapter are summarised below:

Chapter 1: This chapter provides a brief introduction to the background and reasons for this research work. A brief description of the aim and objectives of this research programme is also presented.

Chapter 2: This chapter begins with an overview of the history of thermoelectricity, its fundamentals, and the state-of-the-art thermoelectric materials. The most common strategies to improve

the performance of thermoelectric materials are reviewed, with a focus on nano-structuring routes to fabricate the thermoelectric bulk samples.

Chapter 3: The chapter describes experimental techniques employed in this study. These include materials and methods for the preparation of alloy powders; consolidation techniques based on cold-pressing and annealing, or spark plasma sintering; and characterisation techniques for phase structure analysis and thermoelectric properties measurement.

Chapter 4: The primary aim of this chapter was to determine the optimal conditions, including ball milling time, cold-pressing pressure, and annealing temperature, for the successful fabrication of the samples with satisfactory thermoelectric properties. The research efforts were focused on establishing a reliable material preparation procedure and producing high-quality benchmark materials. In addition, the issues associated with the preparation of n-type Fe-Ti-Al alloys were also discussed.

Chapter 5: This chapter describes a systematic experimental investigation of the effect of elemental substitution on the phase structure and thermoelectric properties of $Fe_{11}Ti_3Al_6$ based alloys. Efforts were made to identify if the Seebeck coefficient and power factor can be increased through elemental substitution. The feasibility of the elemental substitution approach and strategy to improve the thermoelectric properties of Fe-Ti-Al alloys are discussed. A new composition with the improved thermoelectric property was identified.

Chapter 6: The chapter focuses on the investigation of $Fe_{10}Cr_1Ti_3Al_6$ alloys, which was identified from the work described in chapter 5. Spark Plasma Sintering was employed to increase the sample density beyond the values that cannot be obtained using the cold-pressing/annealing method. The effect of sintering temperatures on the phase structure and density was investigated. The thermoelectric properties, including the Seebeck coefficient, electrical resistivity and thermal conductivity, were characterised over a temperature range of 50^{o}C to 800^{o}C. The results demonstrated an improvement in the thermoelectric performance of $Fe_{10}Cr_1Ti_3Al_6$ alloy compared to the benchmark materials (i.e., $Fe_{11}Ti_3Al_6$). The mechanisms responsible for improvement were discussed.

Chapter 7: The chapter summarises the main outcomes and conclusions of this research. The interesting observations and remaining challenges for further research were also proposed.

Chapter 2: Literature Review

2.1 Introduction

This chapter aims to provide an overview of the history of thermoelectricity, including its fundamentals and the various types of potential thermoelectric materials that have been discovered. Additionally, common strategies for improving the potential of thermoelectric materials are discussed briefly, as well as various developed theoretical models to predict charge transport mechanisms were reviewed. The last section describes the most common technologies used to fabricate thermoelectric materials.

2.2 Historical background

The beginning of the thermoelectricity field is considered with the discovery of the Seebeck effect by German physicist Thomas Johan Seebeck in 1821[23]. Fig 2.1 illustrates a drawing of the historical equipment used by Seebeck to demonstrate the thermoelectric effect. In the drawing, where op represents a base strip consisting of Bi, mn represents an arc made of Cu, a denotes a magnetic needle[24], and the arrow shows the current direction.

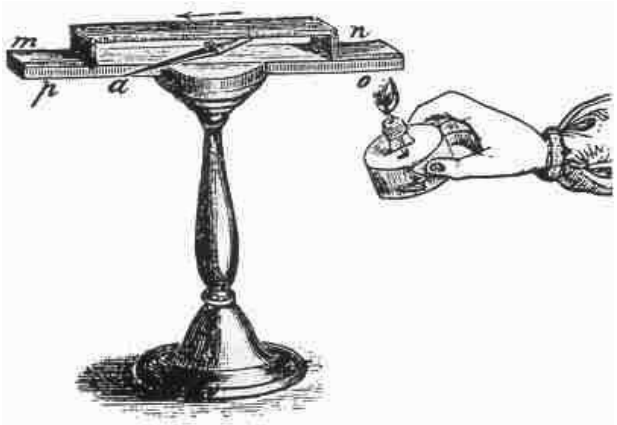

Figure 2. 1 Instrument used by Seebeck for the discovery of the Seebeck effect [Ref [23]]

Seebeck noted that when a circuit consists of two dissimilar metals with junctions held at different temperatures, a deflection in the compass needle can be noticed. Initially, Seebeck believed

this deflection occurred due to a magnetic effect resulting from a temperature difference and thought it might be related to the Earth's magnetic field. However, Danish physicist Hans Christian Orsted explained the physics behind this phenomenon and concluded that the movement of the needle occurred due to a magnetic field induced by an electric current flowing in the circuit[25]. This electrical current was produced due to the movement of electrical charges (holes or electrons) away from the hot junction.

Thirteen years later, a French watchmaker and part-time physicist, Jean Charles Athanase Peltier, discovered the Peltier effect[26]. He observed that when an electric current passed across a circuit made of two dissimilar metals, a change in temperature at the junction occurred. He attempted to explain the physics behind the observed phenomenon via the Joule theory of heat dissipation but failed to provide a satisfactory explanation. After four years, Russian physicist Heinrich Freidrich Emil Lenz[27] explained the Peltier effect using the experimental set-up consisting of Bismuth-Antimony. He demonstrated that water could be frozen at the junction by flowing an electrical current and noted that if the current was reversed, the ice could be melted again. It proved that changing the current direction could cause the heat at the junction to be absorbed or generated. In 1851, British physicist William Thomson[28] (later known as Lord Kelvin) provided the theoretical description of the Seebeck and Peltier effects. He combined the descriptions of both discovered thermoelectric effects into a single formulation using thermodynamic concepts. During the theoretical analysis of the relationship between both effects, he observed an additional effect called the Thomson effect nowadays. The Thomas effect describes the heat produced or absorbed along with a homogeneous material when current flows in a conductor with a temperature gradient.

In 1885, Lord John William Rayleigh[29] suggested that electrical power could be generated based on the Seebeck effect. German scientist Edmund Atlenkirch [30] was inspired by Rayleigh's research work and derived the efficiency of a thermopile (An electronic device which can convert thermal power into electrical energy which composed of thermocouples connected in series or in parallel) from the material properties relevant for practical applications. Scientist Atlenkirch demonstrated that a potential thermoelectric material should have a high Seebeck coefficient, a low electrical resistivity value to minimise the joule heat and a low thermal conductivity to maintain the temperature gradient.

Around 1920, the Russian physicist Abram Fedorovich Ioffe[31] conducted experimental studies on the electrical and thermal properties of the semiconductor. He observed that these types of materials are potential candidates for thermoelectrical applications. Ioffe predicted that a semiconductor thermoelectric generator (TEG) could deliver an efficiency of 2.5-4%. In 1947,

Hungarian American scientist Maria Tekles (later nicknamed the "Sun Queen") developed the first (solar) thermoelectric power generator based on Zn-Sb/BI-Sb alloys which can deliver conversion efficiency higher than 5%. She also designed the first thermoelectric refrigerator in 1953 using semiconductor materials[32]. In the meantime, loffe conducted research activities to search for new thermoelectric materials and find ways to optimise their performance. He successfully introduced the "Dimensionless figure of merit" (ZT), which is defined as $ZT = \frac{\alpha^2 T}{k\,\rho}$ where T represents the absolute temperature, α is the Seebeck coefficient, ρ is electrical resistivity and k is thermal conductivity. The term α^2/ρ is called the power factor (PF), which can be used to estimate the energy conversion performance of the thermoelectric material[32]. Based on the ZT value definition, he concluded that maximisation of ZT will lead to maximised conversion efficiencies for TEG and coolers.

In 1954, the physicist Hiroshi Julian Goldsmid designed a thermoelectric device using thermoelements based on Bi_2Te_3. At research laboratories of The General Electric company in the UK, using a thermoelectric device based on Bi_2Te_3 thermocouple, he demonstrates for the first time that it is possible to achieve cooling up to 0^0C [33]. Additionally, he was also the first scientist to identify the importance of high mobility and effective mass in combination with the low thermal conductivity of materials in determining thermoelectric performance. In the 1950s, A thermoelectric generator(TEG) based ZnSb/ Constantan thermocouples (based on Ni-Cu alloy) was invented and commercialised by the Soviet Union[34]. They used the developed TEG to convert heat produced by kerosene lamps into electricity to power the radio receivers in rural areas. In 1959, Chasmar and Stratton suggested a new way to express the ZT in terms of the thermoelectric material factor. The material factor depends only on the physical properties of the material, such as effective mass, carrier mobility and thermal conductivity, and its maximisation corresponds to obtaining the maximum possible ZT for a given material having a given charge carrier concentration[35].

Progress in thermoelectric slowed around the 1960s due to the very low conversion efficiency (about 5%) of thermoelectric devices. Many attempts to commercialise thermoelectric devices failed. Gradually, thermoelectrics became limited to niche applications. Because thermoelectric devices do not have moving parts, this technology provides reliable and maintenance-free operation. As a result, thermoelectric devices found widespread applications in areas where the availability of a source, reliability, and durability of the operation was more important than efficiency and cost. Consequently, thermoelectric devices are used as energy generators in a deep space mission, where photovoltaic energy converters become inoperative. In space probes, thermoelectric generators produce electricity by converting heat generated by the decay of radioactive

materials, which became known as radioisotope thermoelectric generators (RTG)[36]. The United States (US) launched the first RTG, SNAP-III-equipped spacecraft Transit-4A, into space in 1961. Then, several other space missions such as Voyager 1, Voyager 2, Pioneer 10, Pioneer 11, Galileo, Ulysses, Cassini and New Horizons had RTGs aboard them. During the 1970s, thermoelectric generators were used in the biomedical sector to power cardiac pacemakers. However, these generators were soon replaced by lithium batteries due to issues regarding nuclear waste disposal[37].

In 1968, Goldsmid and Penn theoretically proposed that the lattice thermal conductivity of the material can be reduced by the increase in the phonon scattering at the grain boundaries (i.e., by fabricating finer-grained material)[38]. In 1974, D M Rowe reported the theoretical optimisation of ZT of heavily doped hot-pressed Si-Ge alloys and proposed that a sample with a finite grain size of 10^{-4} m to 10^{-8} m can demonstrate a greater ZT value than the single crystal[39]. D.M. Rowe et al. experimentally investigated the feasibility of proposed ideas and confirmed that the lattice thermal conductivity of the Si-Ge sample could be decreased with a reduction in grain size[40]. They also reported that the Si-Ge sample with a grain size less than 5 µm showed a ~28 % reduction in thermal conductivity at room temperature compared to the single-crystal sample[40]. In 1979, Glen Slack proposed the phonon-glass-electron-crystal concept. This concept was used to study bulk thermoelectric materials, thin-film and superlattice structures, and electric and thermal transport across interfaces. Slack suggested that the potential thermoelectric material should possess thermal transport properties like glass and the electrical properties of crystalline material[41].

In 1993, L. D. Hicks and Mildred Dresselhaus published theoretical work and suggested that the ZT values of materials could be increased by preparing them in quantum-well superlattice structures[42]. In 1996, L.D.Hicks et al. implemented the suggestion of Dresselhaus for PbTe alloys and found that the theoretical prediction is consistent with experimental observations[43]. In 1998, the Fall Materials Research Society (MRS) meeting was held in Boston[44]. In this meeting, Glen Slack delivered an introductory talk titled "Holey and Unholy Semiconductors and Thermoelectric Refrigeration Materials". He characterised the materials as "holey" or cage-structure materials "unholey", depending on how low electrical resistivity and glass-like thermal conductivity can be achieved in the same material. This concept is related to slack's phonon-glass-electron-crystal model. Skutterudites and Clathrates are discovered as holey semiconductors and exhibit very low thermal conductivity (k< 1.5W/mK). In contrast, Half-Heusler alloys (for example, ZrTiSn) were found as unholy materials with favourable electrical properties for potential thermoelectric materials. Up to 2020, the materials based on Bi-Te, Sn-Se, Cu-Se, half-heusler, Oxides and GeTe/PbTe are identified as potential materials having ZT>1[10].

2.3 Thermoelectric effects and Dimensionless Figure of Merit

Thermoelectricity is the combination of thermal and electrical phenomena in the material, which offers a route through which thermal energy or waste heat can be converted into electricity. There are three thermoelectric effects: the Seebeck effect, the Peltier effect, and the Thomson effect. These three effects are interrelated by the Kelvin relationships and form the basis of thermoelectricity.

2.3.1 Seebeck effect

German physicist T. J Seebeck discovered the Seebeck effect in 1821[23]. The Seebeck effect describes that an open circuit voltage difference (V_{AB}) is produced when a temperature difference (ΔT) is applied across the junctions of two dissimilar metals, as shown in Fig 2.1.

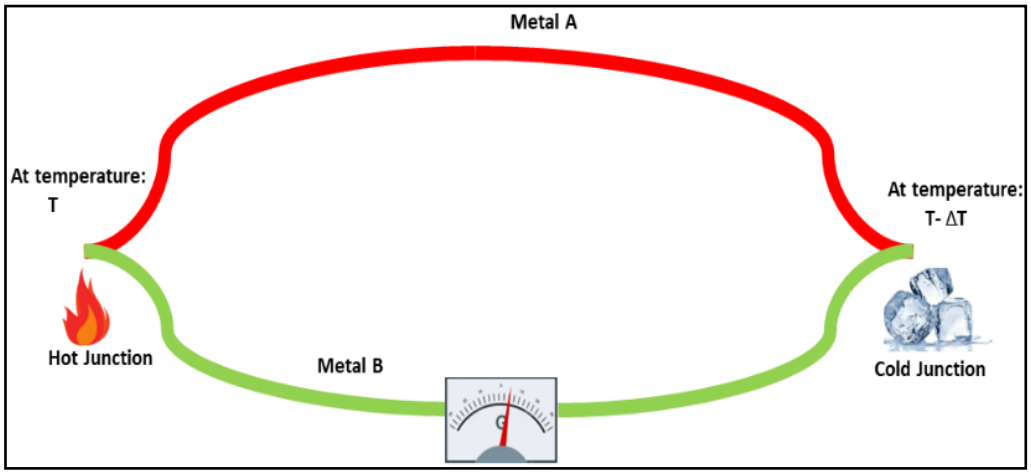

Figure 2. 2 Schematic experimental set-up for the Seebeck effect

The generated voltage difference (V_{AB}) between junctions is given as:

$$V_{AB} = \alpha_{AB}\Delta T \tag{2.1}$$

where ΔT is the temperature difference between the hot and cold junction, mathematically, it can be expressed as $\Delta T=T_h-T_c$. α_{AB} defines the relative Seebeck coefficient, which mathematically can be expressed as $\alpha_{AB}= \alpha_A-\alpha_B$. The α_A is the absolute Seebeck coefficient of metal A whereas α_B is the absolute Seebeck coefficient of metal B. The produced voltage difference is also called the Seebeck voltage. The ratio of the generated voltage difference and the applied temperature difference defines the Seebeck coefficient, which is expressed in units of μV/K. The

Seebeck coefficient usually varies as a function of temperature, and under a small temperature difference, it can be defined as:

$$\alpha_{AB} = \frac{V_{AB}}{\Delta T}, \Delta T \rightarrow 0 \quad (2.2)$$

The Seebeck voltage is conventionally measured versus the hot side, and it can be positive (for p-type materials) or negative (for n-type materials). When the one junction is subjected to a heat source, thermodynamically, the majority charge carriers (may be electrons or holes), depending upon the nature of the material, will move from the hot side to the cold side to achieve equilibrium. If the temperature difference is maintained, the flux of charge carriers creates a current flowing from the hot side to the cold side due to the potential difference between the two sides.

To scrutinise the sign of majority charge carriers, the Seebeck coefficient is a valuable tool. If the measured Seebeck coefficient is positive, then the material will p-type. On the other hand, if the measured Seebeck coefficient is negative, the material will n-type.

2.3.2 Peltier effect

French physicist Jean Peltier discovered the Peltier effect in 1834. He observed temperature changes at the junctions of two different conductors when an electrical current passed through these junctions. He noticed that heat is absorbed in one junction and evolves at the other, depending on the current direction. The heat absorption or evolution at two junctions can be reversed by changing the direction of the electric current. This effect is a reversible phenomenon and the basis of thermoelectric refrigeration or heating applications.

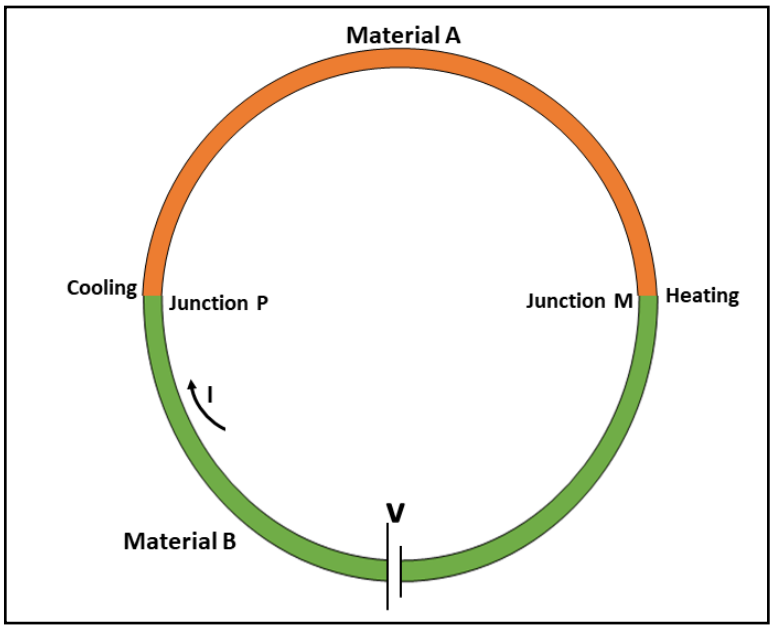

Figure 2. 3 Schematic for the Peltier effect

Fig 2.3 illustrates the Peltier effect for two dissimilar materials A and B. When two different metals are joined together, then contact potential is established at the junctions. Consider a case (Fig 2.3) where an electrical potential (V) is applied to the circuit, the current (I) flows clockwise and electrons flow anticlockwise through it. Heat is absorbed and produced cooling in junction P because of the movement of an electron from a lower potential to a higher potential. On the other hand, at junction M, heat evolves when an electron jumps from a higher to a lower potential and releases energy. The heating/cooling process at the junctions can be reversed if the direction of current changes.

According to J.Peltier, the amount of the heat exchange (Q) at the junction directly depends upon Peltier coefficients of both materials Π_A and Π_B and the applied current (I) in the circuit, as described in equation (2.3).

$$Q=(\Pi_{A-B})I \tag{2.3}$$

where Π_{A-B} is the relative Peltier coefficient, this effect establishes thermoelectric refrigeration or heating.

2.3.3 Thomson effect

In 1851, Physicist William Thomson (Lord Kelvin) discovered the third thermoelectric effect called the Thomson effect, a reversible effect. Thomson effect describes the evolution or absorption of heat when electricity passes through a circuit consisting of a homogeneous material with a temperature difference along its length. The rate of heat (Q) generation per unit volume can be given as[45]:

$$Q = \rho J^2 - \beta I \Delta T \tag{2.4}$$

where ρ is the resistivity, J is the current density, β is the Thomson coefficient, and I is the current in homogenous material, ΔT is a temperature gradient along the conductor. The first term in Eq. (1.7) is the Joule heating effect (irreversible effect), and the second term is the reversible Thomson heat. β is positive if heat is absorbed from the surroundings when current and ΔT are parallel. This effect helps to build a bridge between the Seebeck and Peltier effects.

2.3.4 Kelvin relationships

Lord Kelvin derived the relationship between Seebeck coefficient (α), Peltier coefficient (Π) and Thomson coefficient (β) based on the first and second thermodynamics laws,[46]. Furthermore, these relationships confirm that all three thermoelectric effects (Seebeck, Peltier and Thomson effect) occur together in any thermoelectric device under operation (temperature difference and electric current). He linked the Seebeck coefficient (α) and the Peltier coefficient (Π) based on the following equation:

$$\Pi_{AB} = \alpha_{AB} T_j \tag{2.5}$$

where T_j is the temperature at the junction. The above eq. (2.5) provides a straightforward method to determine the Peltier coefficient by measuring the Seebeck coefficient because it is easier to measure voltages and temperatures than to measure heat absorption or dissipation at the junction. In addition, the above equation also implies that materials that are suitable for power generation are also appropriate for refrigeration due to their direct relationship.

Similarly, Lord Kelvin linked the Seebeck and Thomson coefficient are related based on the following relation[45]:

$$\beta_a - \beta_b = T \frac{d\alpha_{AB}}{dT} \quad (2.6)$$

Equation (2.6) follows energy conservation.

2.3.5 Dimensionless figure of merit (ZT)

The dimensionless figure of merit (ZT) concept was introduced by A.F. loffe in 1949[35]. This concept helps to estimate the energy conversion efficiency of thermoelectric materials. It can also guide making strategies to improve the conversion efficiency of materials. ZT, in general, describes the temperature-dependent material properties derived from temperature-dependent parameters of materials such as Seebeck coefficient α (T), resistivity ρ (T) and thermal conductivity k (T). The energy conversion efficiency of thermoelectric can be determined based on the following equation:

$$ZT = \frac{\alpha^2 T}{\rho k} \quad (2.7)$$

where α is the Seebeck coefficient, ρ is the electrical resistivity, k is thermal conductivity, and T is the absolute temperature. The Seebeck coefficient is also called thermopower. The quantity α^2/ρ is known as the power factor (PF). The thermal conductivity (k) usually occurs due to electrons and lattice vibrations. Mathematically the thermal conductivity can be expressed as:

$$k=k_e+k_l \quad (2.8)$$

Here, k_e is electronic thermal conductivity, and k_l is lattice thermal conductivity. The electronic thermal conductivity of the sample can be calculated by using the Wiedemann-Franz law[47], based on the equation : $k_e = LT/\rho$, where L is the Lorenz number and ρ is electrical resistivity. According to the classical free-electron model, the Lorenz number is equal to $2.44 \times 10^{-8} W\Omega K^{-2}$. The high ZT value requires low electrical resistivity (ρ), high thermopower (α), and low thermal conductivity (k). Thermoelectric parameters such as α, ρ and k_e primarily depend on carrier concentration[48].

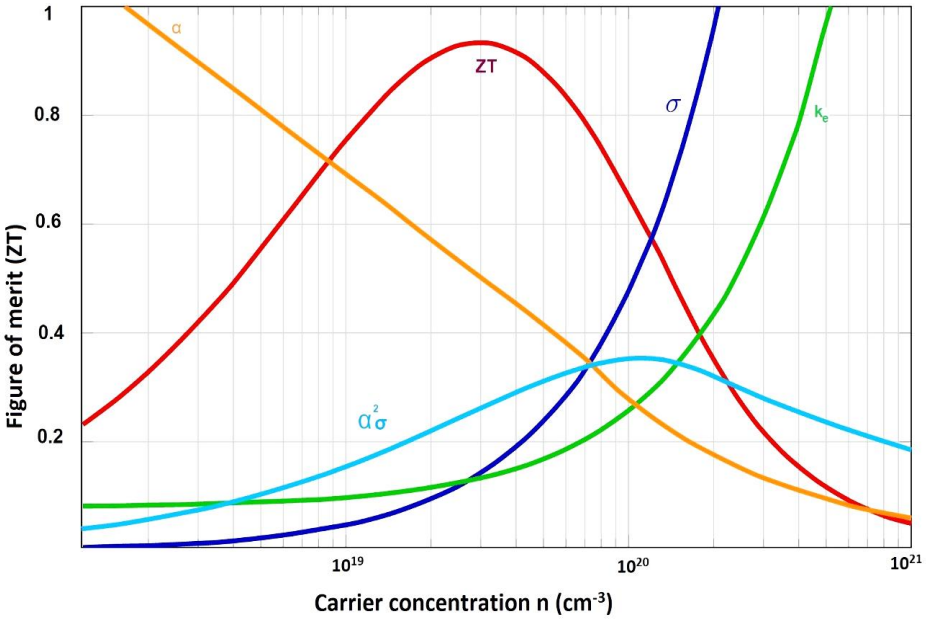

Figure 2. 4 Dependence of α, σ, and k_e on carrier concentration [Ref 48]

Fig 2.4 illustrates the relationship between thermoelectric properties and the magnitude of the carrier concentration[48]. Below 10^{19} cm^{-3} concentration, the material behaves like an insulator with a high resistivity (ρ=1/σ) and high Seebeck coefficient, and low electronic thermal conductivity. However, the material in heavily doped semiconductor limit (above 10^{20} cm^{-3}) demonstrates a low Seebeck coefficient and resistivity and thermal conductivity. It seems that it is challenging to increase the σ of the material by increasing the carrier concentration to optimise ZT without affecting the α and k_e. The plot suggests that between 10^{19} cm^{-3} to 10^{20} cm^{-3} carrier concentration, the materials display optimal ZT value due to the highest PF and low electronic thermal conductivity. In general, an efficient thermoelectric material should have ZT>1. It is only possible to achieve if the material attains a high-PF ($\alpha^2\sigma$) and low thermal conductivity (k).

2.4 Thermoelectric materials

This section presents various types of discovered thermoelectric materials and provides information about their thermoelectric efficiency and applications. Fig 2.5 represents the highest ZT values achieved for different thermoelectric materials classes up to 2021, and their details are described in the following sub-sections:

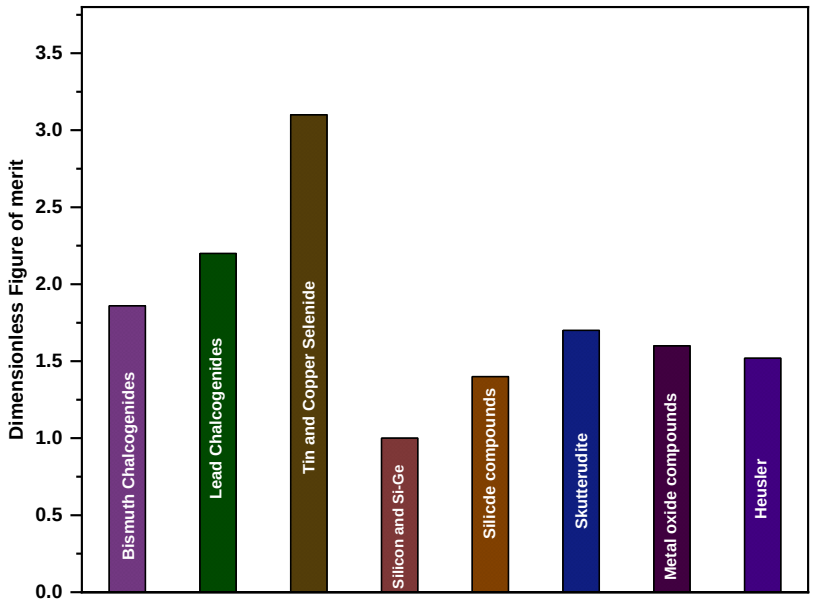

Figure 2. 5 Maximum ZT value for different class of thermoelectric materials

2.4.1 Bismuth chalcogenides

In 1815, Bi_2Te_3 material was discovered in Telemark, Norway[49]. Bi_2Te_3 is an indirect bandgap semiconductor with a band gap of approximately 0.15eV[50]. It attains a tetradymite structure with the $R\bar{3}m$ space group, as it is represented in Fig 2.6[32]. This material has the layered tetradymite structure that is held together via Van der Waals interactions. Due to layered motif material exhibits highly anisotropic properties, demonstrating the best thermoelectric performance along the direction perpendicular to the c-axis[51].

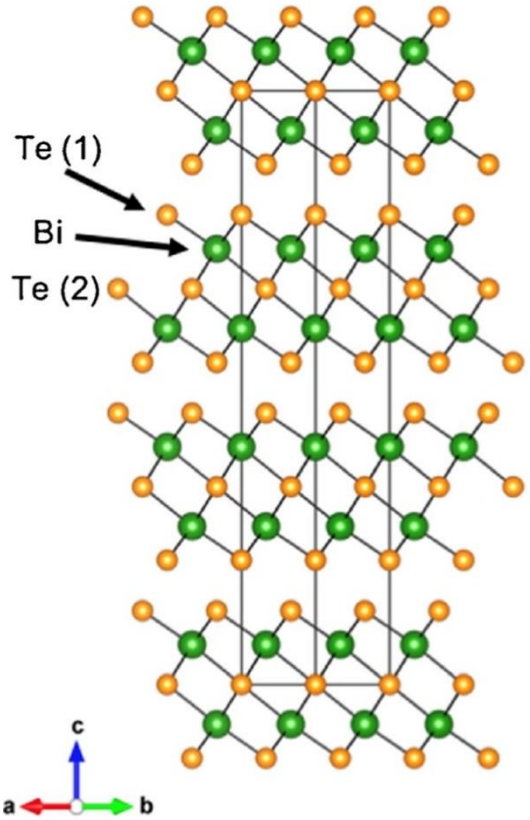

Figure 2. 6 Crystal structure of Bi_2Te_3 (the layered tetradymite structure) Ref no. [32]

Bi_2Te_3 and its alloys, such as p-type $Bi_{2-x}Sb_xTe_3$ and n-type $Bi_2Te_{3-x}Se_x$ found as potential thermoelectric materials for room temperature applications and have been used for applications commercially since the 1950's[52, 53].In 1954, H.J.Goldsmid[33] reported the thermoelectric properties of Bi_2Te_3 for the first time and claimed that this alloy could also be used for cooling applications. In addition, p-type $Bi_{2-x}Sb_xTe_3$ and n-type $Bi_2Te_{3-x}Se_x$ were discovered as potential materials for cooling and low-temperature applications with ZT~1.0 at 300K[32, 54]. In the following decades, limited progress occurred with these materials because many believed that the upper limit of ZT was reached. Nonetheless, the development of these alloys recommenced due to the advent of new strategies to achieve low thermal conductivity[55]. In 2008, Poudel and his coworkers[56] developed a technique to synthesise $Bi_{0.5}Sb_{1.5}Te_3$ with a higher grain boundary density by hot pressing prepared nano powders and reported that this alloy achieved ZT of 1.4 at 373K and low thermal conductivity (~1.0$Wm^{-1}K^{-1}$) due to additional phonon scattering at the nanoscale. C.Liu et al.[14] fabricated the Bi-Sb-Te alloys by hydrothermal methods followed by cold-pressing and sintering. They found that due to low thermal conductivity, $Bi_{0.45}Sb_{1.55}Te_3$ displays a ZT value of 1.75 at 270K. In 2015, Kim et al.[57] reported the impact of dense dislocation on the transport

properties of $Bi_{0.5}Sb_{1.5}Te_{3,}$ and it exhibited a ZT of 1.86 at 320 K due to the combined effect of grain boundary and point defect scattering.

2.4.2 Lead chalcogenides

In 1845, PbTe was first discovered as the rare mineral altaite. The lead chalcogenides possess a rock salt-type structure in a cubic crystal system with an Fm-3m space group, and the direct bandgaps range from 0.27 to 0.41 eV. These materials display a temperature-dependent increase in band gaps, from which band convergence is observed. The thermoelectric performance of these alloys is improved by modifying the density of states to create the resonance levels in the conduction band that enhance the Seebeck coefficient[58, 59]. The thermal conductivity of these materials is attempted to reduce in various studies by adopting different fabrication routes[59, 60].

The measured intrinsic ZT for p-type and n-type Pb-Te are 1.4[61, 62], and 1.2 for n-type and p-type Pb-Se[63, 64]. Pei et al. demonstrated that the energy offset between the valence band maximum (L-band) and the heavy band (Σ-band) in p-type PbTe could be modified by Se doping, which raised the valley degeneracy from 4 to 16 at high temperatures[65]. Furthermore, due to point defects, the thermal conductivity decreases and Consequently, Na-doped $PbTe_{0.85}Se_{0.15}$ achieved ZT of 1.8 at 850 K. Heremans et al.[58] investigated the thermoelectric properties of Tl-doped PbTe alloy and observed that due to resonant states at the Fermi level, $Tl_{0.01}Pb_{0.99}Te$ alloy attained high thermopower and achieved ZT of 1.5 at 773K. K.F. Hsu et al.[66] reported that n-type $AgPb_mSbTe_{2+m}$ (m = 10, 18) exhibits a high ZT of 2.2 at 800 K due to low lattice thermal conductivity. One major drawback is that these alloys contain highly toxic Pb and Te elements which is low abundant. This makes these alloys expensive and limit their scope.

2.4.3 Tin and copper selenide

Recent studies have identified SnSe as a potential thermoelectric candidate for mid-temperature range applications. Advantageously, these alloys are cheaper and less toxic than lead-based alloys[67]. This material exhibits the layered GeSe-type structure with a orthorhombic crystal system; this material shows a phase transition from the Pnma to the Cmcm space group between 750-800K[68]. SnSe has an indirect bandgap of 0.86 eV, and its electronic structure confirms the presence of multiple extrema in both the valence and conduction band[69].

This material has anisotropic transport properties. It attains a ZT of 2.6±0.3 at 923K along the b-axis of the crystal, while along the a-axis SnSe achieved a ZT value of 0.8±0.2, along the c-axis, its show ZT of 2.3±0.3[70]. Additionally, SnSe achieved an ultralow thermal conductivity of $0.23 Wm^{-1}K^{-1}$ at 973K[70]. In 2016, Duong et al.[71] reported that Bi-doped n-type SnSe achieves a

ZT of 2.2 at 733K along the b-axis of the single crystal. In 2018, L.Shan et al.[72] investigated the thermoelectric properties of Br-doped n-type SnSe polycrystalline and reported that $SnSe_{0.90}Br_{0.1}$ sample attained ZT of 1.3 at 773K along the hot pressing direction. Recently, C.Zhou et al. reported that $Na_{0.03}Sn_{0.965}Se$ polycrystalline sample showed a ZT value of 3.1 at 783K and claimed that the Polycrystalline p-type SnSe sample demonstrated high ZT values than the single-crystal SnSe sample[73].

Like SnSe, Cu-Se and Cu-S alloys consist of earth-abundant and non-toxic elements[74]. $Cu_{2-x}Se$ has a complex structure and exhibits α-phase at low temperature while β-phase at high-temperature[75]. In 2012, H.Liu et al. reported that the β-Cu_2Se sample achieved a ZT value of 1.6 and low thermal conductivity of 0.7 $Wm^{-1}K^{-1}$ at 1000K[75]. Olvera et al. achieved a remarkable ZT of 2.6 at 850K for Cu_2Se/ $CuInSe_2$ nanocomposites due to increasing carrier mobility and decreased thermal conductivity[13]. Recently, D. Yang et al.[76] investigated the thermoelectric properties of Cu_2Se_{1+x}/yBiCuSeO and attained the highest ZT value of 2.7 at 973K due to optimisation of carrier concentration and intensified phonon scattering. Both SnSe and Cu_2Se are potential thermoelectric candidates, but it is unclear whether these materials will serve in thermoelectric applications in the future.

2.4.4 Silicon and Silicon-germanium alloys

Silicon is low-cost and the second-most abundant element on Earth with high mechanical and thermal stability. Over the last five decades, Silicon (Si) has been used in the microelectronic and photovoltaics industry for various applications. The researchers also made an effort to investigate the thermoelectric performance of Si and Si-based alloys. Around 1950, Geballe et al. studied the thermoelectric properties of single-crystalline Si sample[77]. Silicon demonstrates ZT of approximately 0.01 at room temperature with high thermal conductivity of 120W/mK[32]. Germanium (Ge) and Silicon (Si) also possess high thermal conductivity. However, alloying of Si with Ge show a significant impact in impeding phonon transport[78]. In 1964, Dismukes et al. reported a ZT value of 1 for n-type and 0.7 for p-type $Si_{0.7}Ge_{0.3}$ sample at 1100K[79]. With the influx of nanotechnology, the Silicon nanowires with a diameter smaller than 100nm were obtained by electrochemical method[80] or lithography[81]. Due to dimensional constraints, the reduction in thermal conductivity is observed, which leads the ZT close to 1 at room temperature. A similar approach was adopted for SiGe alloy and found that for SiGe nanowires, the ZT improved by two times (ZT=0.18 at 300K) when compared to their bulk alloy sample[82].

2.4.5 Silicide compounds

Silicide-based materials have been identified as potential thermoelectric candidates for mid-temperature range applications. Magnesium silicides (Mg_2Si) materials are based on low-cost, highly abundant, and eco-friendly elements. Mg_2Si is a semiconductor material with an indirect bandgap of 0.61ev at 300K[83].

In 1958, the first investigation on silicides for thermoelectric applications was carried out by Nikitin et al. [84]. In 2011, Fedorov et al. reported the impact of Sn substitution on transport properties of Mg_2Si and achieved ZT of 1.2 at 750K[85]. In 2013, A.U.Khan and his co-workers attained ZT ~1.4 for Bi-doped and ZT~1.2 for Sb-doped Mg_2Si samples at 800K. Recently, Z. Li et al. fabricated the MnTe/HMS (Higher Manganese silicide) composites and demonstrated a successful increase the ZT value from 0.41 to 0.70 at 773K.

2.4.6 Skutterudites compounds

Skutterudite is a naturally occurring mineral and in 1845, it was discovered in Skotterud, Norway. These compounds have crystallised in a Cobalt arsenide ($CoAs_3$)-type cubic structure, which is a distorted version AB_3 type structure of perovskite.

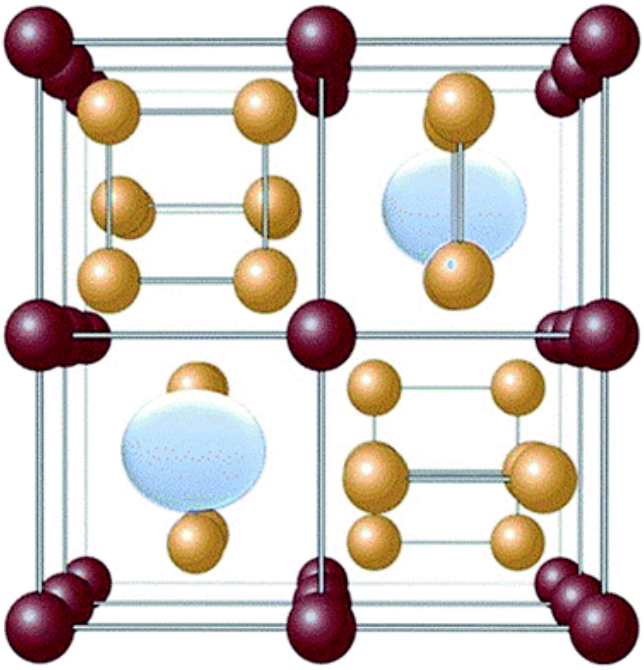

Figure 2. 7 Unit cell of skutterudite defined by Oftedal et al. In the figure, transition elements are represented by red spheres, pnictogen atoms by yellow spheres and voids in the structure or filled atoms by light blue spheres [Ref [86]]

In 1928, Oftedal reported that the Skutterudite have a cubic structure containing 32 atoms in space group $Im\bar{3}$ (as shown in Fig 2.7). The unit cell of these compounds consists of eight corner-shared transition metals (such as a Co, Ir, Rh) occupying the 8c sites (1/4,1/4,1/4). The six out of eight cubes filled with pnictogen (such as Sb, As and P) near square planar rectangles and occupy the 24g sites. There are two voids in the unit cell which can be filled by atoms with ionic radii smaller than the cage[86].

Firstly, $CoSb_3$-based Skutterudite was identified as a potential thermoelectric candidate, demonstrating a high power factor and high thermal conductivity (~10W/mK) at room temperature[87]. The main drawback of these Skutterudite is its high thermal conductivity. In the last 20 years, researchers attempted to improve thermoelectric performance of $CoSb_3$-based samples by filling the voids with low-coordination ions based on rare-earth elements[88, 89]. This approach successfully decreases the thermal conductivity significantly without decreasing the conductivity, leading to improved ZT value[88]. In the case of n-type Skutterudite, a ZT value of 0.9 at 750K for single crystal $CoSb_3$ co-doped with Pt and Pd[90]. Lu et al.[91] reported a significant thermal conductivity reduction for double-filled Co-Sb Skutterudite. Shi and his co-workers reported the highest ZT of 1.7 at 850K for multiple filled $Ba_{0.08}La_{0.05}Yb_{0.04}Co_4Sb_{14}$ Skutterudite[92]. Based on the void filling strategy, the ZT of p-type $FeSb_3$ Skutterudite was also improved from 0.5 to 1.3 [93].

2.4.7 Metal oxides compounds

Metal oxides are suitable for high-temperature applications due to their high thermal and chemical stability in air, large Seebeck coefficient and low thermal conductivity. In addition, most oxides materials are based on abundant and cheap metals. However, these thermoelectric materials demonstrate low ZT values. Nowadays, It is challenging to fabricate modules based on metal oxides due to high contact resistances at the oxide/metal electrode junction[94].

In 1997, Terasaki et al. discovered that $NaCo_2O_4$ single-crystal displays a high Seebeck value of +100μV/K and metal-like conductivity equal to 5000 Scm^{-1} at 300K[95]. p-type single crystals of $NaCo_2O_4$ achieved ZT >1 at 800K, whereas the polycrystalline samples attained ZT of 0.8 at 1000K[89]. Metal oxides such as $Ca_3Co_4O_{9[96]}$, $(BiPb)_2Sr_2Co_2O_{8[97]}$, $TlSr_2Co_2O_{y[98]}$ and (Hg, Pb)$Sr_2Co_2O_{y[99]}$ have also been identified as promising thermoelectric candidates. Recently, Y.Gu et al. investigated the thermoelectric properties of p-type polycrystalline $Bi_{0.94}Pb_{0.06}CuSe_{1.01}O_{0.99}$ and reported the highest ZT of 1.6 at 873K[100].

On the other hand, n-type metal oxides display lower ZT values due to high thermal conductivity. n-type $SrTiO_3$ exhibits a high Seebeck coefficient (α=-380μV/K at 300K) but high thermal

conductivity (9-12$Wm^{-1}K^{-1}$) at room temperature[101]. Heavily doped $SrTiO_3$ with Nb and La element attained ZT values of 0.37 and 0.26 at 1000K, respectively[102].

2.4.8 Heusler compounds

Fritz Heusler discovered Heusler compounds in 1903[103]. These compounds adopt the element formula A_2BC. Certain alloys of this class material are magnetic and have applications in spintronics[104]. Half-Heusler compounds are a variant of the Heusler compounds with the elemental formula ABC (i.e., vacancies at the A-site). Many Half-Heusler (HH) materials have narrow band gaps[104]. Due to this feature, HH materials are suitable for thermoelectric applications[105]. HH materials consist of elements with high melting temperatures, such as Hf, Zr, Ti or Co, and elements with relatively low melting temperatures, such as Sn or Sb.

HH materials are potential thermoelectric candidates for high-temperature applications (800-1000K). Because they have the potential to display a high Seebeck value, up to ~ 300 μV/K at room temperature, and their high conductivity (~ 10^3 to 10^4 S/cm)[106, 107]. The major drawback of HH materials is their high thermal conductivity (K~10W/mK). So, researchers are attempting to decrease the thermal conductivity by increasing the phonon scattering. Hohl et al.[108] successfully reduced thermal conductivity by three times for different temperatures by introducing disorder on the A-sites in $A_{0.5}A'_{0.5}NiSn$ (A, A' = Ti, Zr, Hf). In 2005, Y.Kimura et al. reported ZT= 0.9 for $Hf_{0.5}Zr_{0.5}NiSn$ at 960 K[109]. Moreover, S.Sakurada et al. reported the highest ZT of 1.5 for $Zr_{0.25}Hf_{0.25}Ti_{0.5}NiSn_{0.998}Sb_{0.002}$ at 700 K[110]. Recently, H.Zhu et al. discovered TaFeSb-based half-heuslers and reported a ZT of 1.52 at 973K[111].

2.4.9 Pseudo-gap-based materials

Over the last two decades, pseudo-gap-based materials have attracted the attention of the thermoelectric community due to the sharp DOS (density of states) feature near the Fermi level[112]. The materials which exhibit a narrow band gap in the range of 1-200 meV are called pseudo-gap materials. The significance of the sharp DOS feature near Fermi level for thermoelectric materials can be understood based on the Mott equation Eq (2.9). For metallic systems, the Seebeck coefficient at temperature (T) can be expressed as:

$$\alpha(T) = \frac{\Pi^2 K_B^2}{3e} T \left(\frac{\partial \ln\sigma\,(\mathrm{E})}{\partial E}\right)_{E=E_F} \tag{2.9}$$

where σ(E) is the electrical conductivity and K_B is the Boltzmann constant. In general, the electrical conductivity is directly proportional to the DOS. According to Eq (2.9), a large α value for thermoelectric material can be achieved if DOS combined with its steep slope $\frac{\partial \ln\sigma\,(E)}{\partial E}$ in the vicinity of the Fermi level will exist. Fig 2.8 illustrates the two hypothetical density of states. Through that it could be understand, how steep DOS is useful to achieve a large Seebeck coefficient. It can be seen in Fig 2.8 (b) that DOS varies rapidly near Fermi level (E_F) and demonstrates a large slope in comparison to Fig 2.8 (a). Based on Equation (2.9), it is expected that system (b) will exhibit a large Seebeck coefficient due to a steep slope $\frac{\partial \ln\sigma\,(E)}{\partial E}$ in the vicinity of the E_F [89].

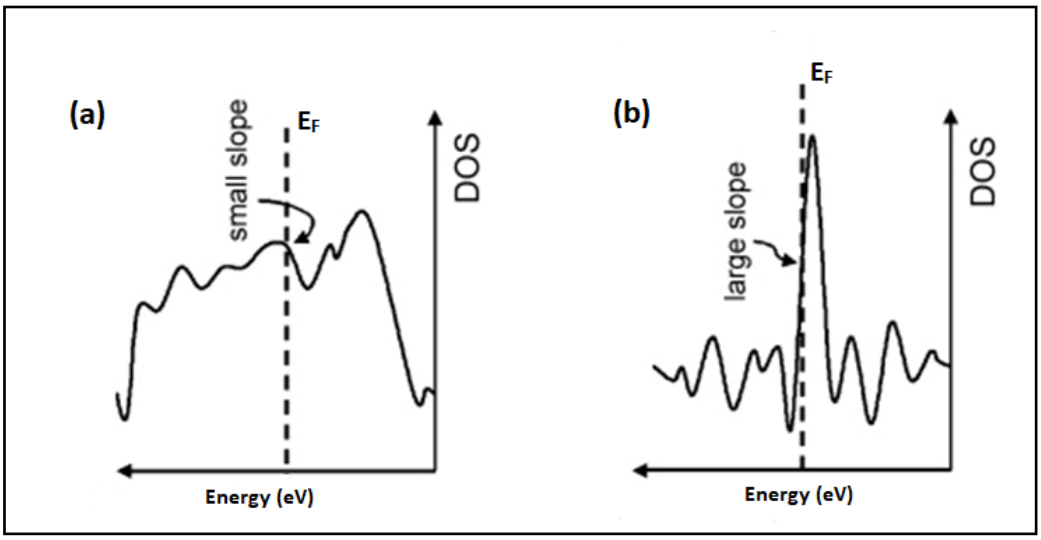

Figure 2. 8 Hypothetical DOS with (a) a small slope and (b) a large slope near Fermi level E_F [Ref 89]

Fe_2VAl material is a non-magnetic semimetal with a pseudo-gap near the Fermi level and exhibits bcc atom arrangements. The existence of a pseudo-gap for this material has been experimentally confirmed[113, 114]. An NMR investigation found an energy gap of 200meV and small DOS at the Fermi level for this material[115]. Hall measurements indicate that the Fe_2VAl material is p-type and has an approximate carrier concentration of $5x10^{20}$ cm^{-3} at 300K[116].

Fig 2.9 represents the DOS calculations for the Fe_2VAl sample based on the DFT theory [113, 117]. The band calculation suggests that pseudo-gap is formed due to a very strong hybridisation of the s and p bands with d bands for Fe_2VAl [113].

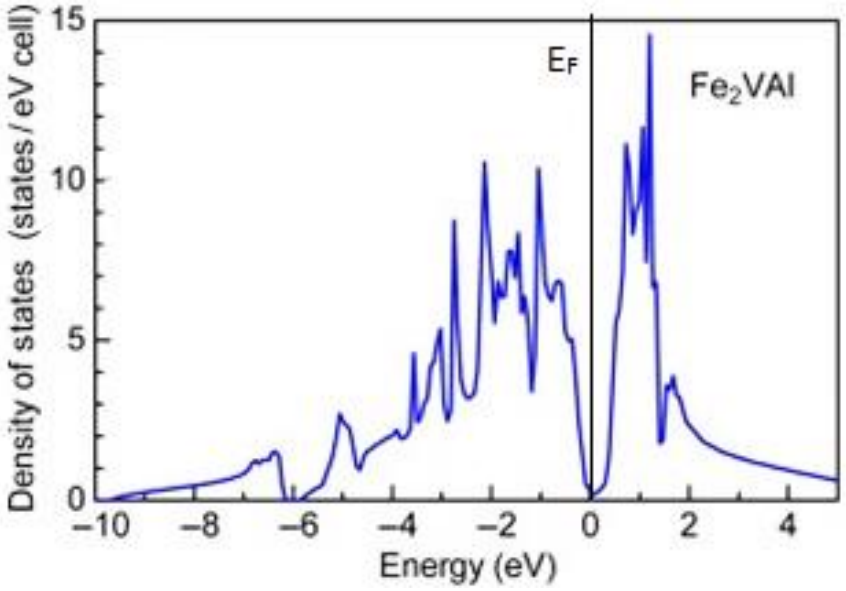

Figure 2. 9 Calculated electronic structure of Fe_2VAl [Ref. no. 113,117]

From Fig 2.9 it can be seen that near Fermi level the sharp DOS feature exists on both side of bands (i.e., on valence electron and conduction electron band side). In various reports, it was found that the Seebeck coefficient for Fe-V-Al samples can be enhanced by the shifting of the Fermi level towards sharp DOS [118, 119]. The variation in Valence electron concentration (VEC) with the substitution of elements is found to be a beneficial method to shift the Fermi level towards conduction or valence band. The VEC represents the number of electrons per atom, including the d-electrons involved in the valence band[113]. The electronic configuration of Fe is [Ar] $3d^6\ 4s^2$, V is [Ar] $3d^3\ 4s^2$and Al is [Ne] $3s^2\ 3p^1$ and Fe_2VAl has 24 valence electrons per formula unit, and it has VEC of 6.0.

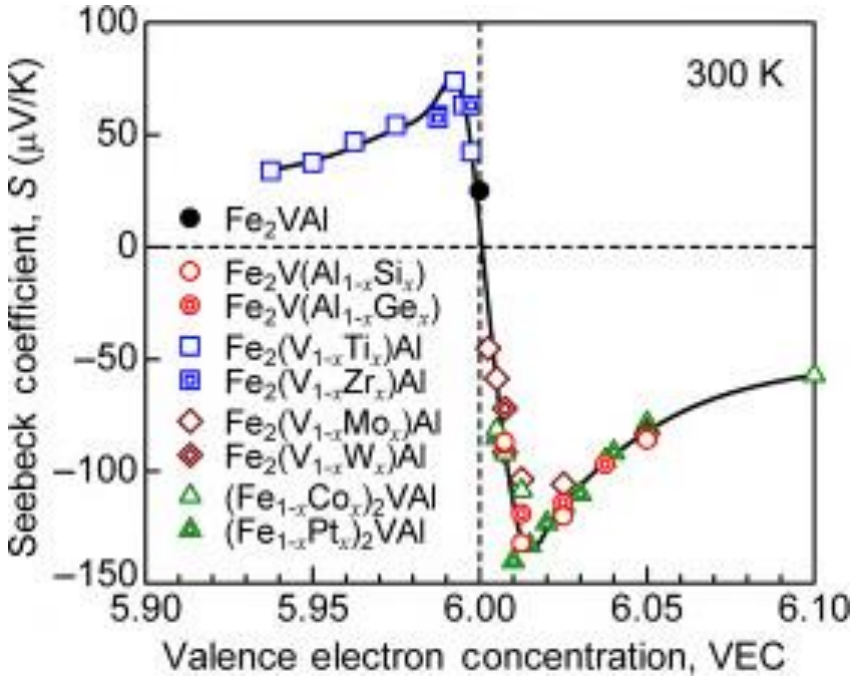

Figure 2. 10 Seebeck coefficient for various Fe_2VAl -based alloys as the function of VEC [Ref. (113)]

Fig 2.10 displays the Seebeck coefficient (α) at room temperature for Fe_2VAl -based alloys as a function of VEC. The Seebeck coefficient, including its sign, changes significantly around VEC=6. The sign of α is positive at VEC≤ 6 but becomes negative for VEC>6. The significant increase in the α value occurred with a decrease of VEC<6 (i.e., the substitution of Ti and Zr having a Valence electron lower than V) due to the shift of Fermi level from pseudo gap toward the steep slope of the valence electron band (Fig 2.9). Similarly, with the increase of VEC >6(i.e. substitution of elements having valence electron higher than Fe, V and Al) there is a large change in the Seebeck coefficient observed because the movement of Fermi level from pseudo gap toward conduction band in sharp DOS origin (Fig 2.9)[113].

In 2004, Y.Nishino et al. investigated thermoelectric properties of Fe_2VAl Heusler-type material[120] and observed that this material demonstrates PF ~5m W/mK^2 at 300K larger than $Bi_2Te_{3[17]}$. Y.Nishino et al. also investigated the effect of off-stoichiometry on the thermoelectric properties of $(Fe_{2/3}V_{1/3})_{100-y}Al_y$ sample and reported that a small change in Al concentration from y=25 results in an increase in the room temperature Seebeck value from +20-30μV/K to -130μV/K for the Al-poor concentration samples and +75μV/K for the Al-rich samples[121]. Recently, N.Reumann et al. investigated the effect of Cr substitution on the Fe-site of Fe_2VAl and achieved 1.8 times higher Seebeck value (~70μV/K) for the $Fe_{1.975}Cr_{0.025}VAl$ sample compared to Fe_2VAl(~40μV/K) at 300K[122]. However, due to high thermal conductivity (27 W/mK), Fe_2VAl cannot be considered an alternative to Bi_2Te_3[17]. Researchers adopted various strategies to

reduce the thermal conductivity, such as heavy element substitution and multi-substitution of elements. In 2006, Nishino and his co-workers successfully decreased the lattice thermal conductivity (K_L) from 27 W/mK to 11 W/mK at 300K via Ge substitution on the Al site of Fe_2VAl alloy[123]. A decade ago, T.Takesuchi et al. reported that K_L could decrease up to 6 W/mK at 300K via multi—substitution of Ti and W elements on the V-site of Fe_2VAl alloy[124]. K.Fukuta et al. improved the ZT of Fe-V-Al by using a grain refinement approach and achieved the highest ZT of 0.37 at 400K for $Fe_2V_{0.98}Ta_{0.10}Al_{0.92}$ [125].

Al-Fe-Si material also exhibits a narrow band gap near the Fermi level. In 2018, Y. Takagiwa et al. studied the transport properties of $Al_2Fe_3Si_3$ and observed that fine-tuning of Si/Al concentration allows for changes in the conduction type of material and also enhances PF[126]. They reported that $Al_2Fe_3Si_3$ demonstrates PF of $70x10^{-5}$ W/mK^2 for n-type and $40x10^{-5}$ W/mK^2 for p-type at 373K. A.K.Srinithi et al. improved the PF of p-type Fe-Al-Si from $25x10^{-5}$ W/mk^2 to $88x10^{-5}$ W/mk^2 by implementing microstructure engineering concepts[19]. The thermoelectric properties of Heusler type Fe_2TiAl pseudo gap-based material was also studied. Suzuki et al.[127] found that $(Fe_{0.3}Co_{0.7})_2TiAl$ and $(Fe_{0.2}Co_{0.8})_2TiAl$ alloy show good n-type thermoelectric behaviour with Seebeck coefficient of -34 μV/K while $Fe_2(Ti_{0.6}Cr_{0.4})Al$ demonstrate potential p-type thermoelectric material with Seebeck coefficient of +50 μV/K[127]. In 2016, Garcia-Canadas et al.[22] reported that p-type $Fe_{11}Ti_3Al_6$ sample exhibiting a PF of $70x10^{-5}$W /mK^2 at room temperature with an Seebeck coefficient of +27μV/K and resistivity of 1μΩm. While n-type $Fe_3Ti_4Al_1$ sample achieved PF of $133x10^{-5}$W /mK^2 (Seebeck coefficient = -57μV/K and resistivity =2.5μΩm) at room temperature. In 2017, Zou et al.[128] studied the thermoelectric properties of $Fe_{2-x}Mn_xTiSn$ (x=0-0.05) and found that Mn substitution improved PF and ZT approximately two times over a pristine sample. Furthermore, they reported the highest value of PF = $36x10^{-5}$ W/mK^2 at 320 K for the $TiFe_{1.9815}Mn_{0.0185}Sn$ sample. Using arc-melting and spark plasma sintering techniques, Y. Huang et al.[129] investigated thermoelectric properties of a pseudo-gap-based Ti-Ni-Si alloy and observed a peak P.F value of $46x10^{-5}$ W/mK^2 at 560K. Recently, Shamim et al.[130] studied thermoelectric properties of pseudo-gap Co-Si alloys and demonstrated a peak Seebeck value of -93μV/K at 560K. They also reported that Co-Si alloys exhibit ZT of 0.15 at 630K.

2.5 Overview of Fe-Al alloys

This section provides an overview of the phase diagram and structural properties of Fe-Al based intermetallic alloys. Intermetallic alloys are defined as ordered alloy phases formed between two or more metallic elements. These alloys have crystal structures that differ from those of their constituent metallic components and exhibit long-range ordered superlattices. In

comparison to conventional metallic materials, intermetallic alloys have advantages such as high melting point and high specific strength, making them promising high-temperature structural materials for applications in the automotive, aircraft, and aerospace industries. Among various intermetallic compounds, the Fe-Al, Ni-Al, and Ti-Al systems have received the most attention. Fe-Al alloys, which contains up 50 at % (atomic percentage) Al, have been extensively studied for their potential use as structural materials[131]. This is due to their excellent corrosion resistance at high temperatures and low density compared to steels[131, 132].

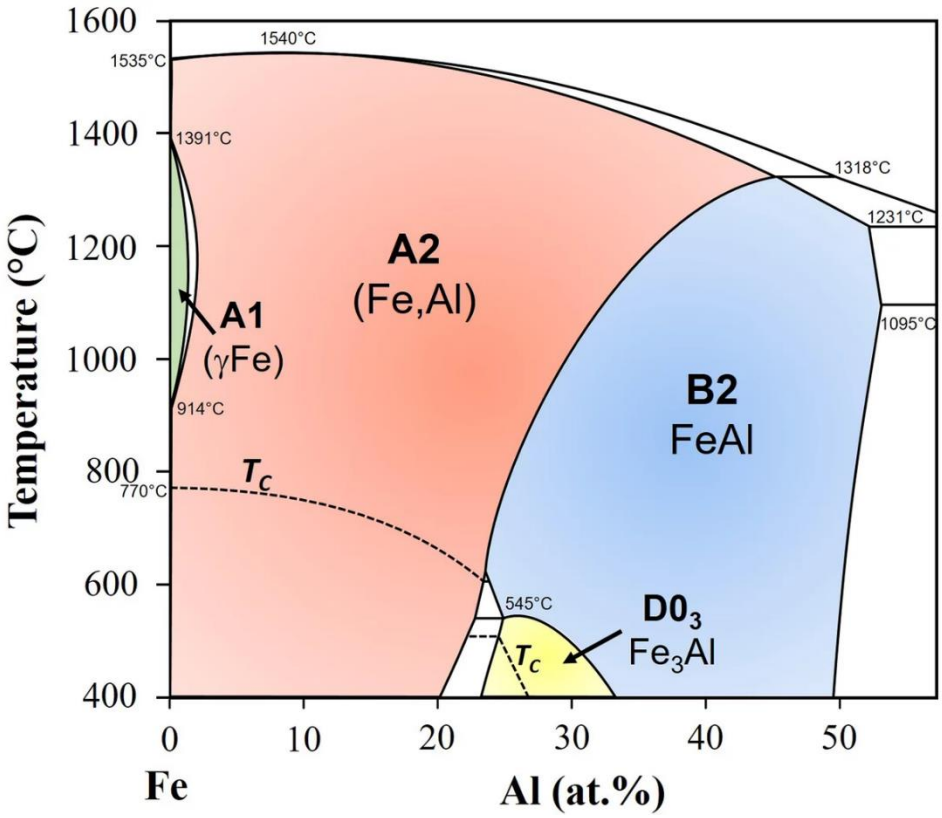

Figure 2. 11 Fe-Al phase diagram showing the extended phase fields of the A2-disordered solid solution (Fe,Al), B2-ordered solid solution (FeAl), and $D0_3$-ordered solid solution (Fe_3Al). T_c is the ferromagnetic Curie temperature [133]

Fig 2.11 represents the Fe-Al phase diagram for Al concentration ranging from 0 to 50 at%. Fe-Al system is a binary alloy that exhibits a complex equilibrium phase diagram, as well as variety of metastable non-equilibrium phases[134]. Due to the significant difference in atomic radii between Fe (0.124 nm) and Al (0.143 nm), there is a lattice mismatch between the two elements. Furthermore, Fe has a body-centred cubic (bcc) lattice, while Al has a face-centred cubic (fcc) lattice. These differences in crystal structure and atomic radius limit the solubility of Al in Fe, leading to the formation of various phase structures. The phase diagram can be divided into different regions based on the crystal structures as described below:

I. Disordered A2 structure: The A2 phase is a continuous disordered solid solution based on the bcc crystal structure of Fe where Al atoms can replace Fe atoms in a statistically random manner, as shown in Fig 2.12 (a). This phase can accommodate up to approximately 20 at% Al at low temperatures, but at high temperatures above 1300°C, up to 45 at% Al can be dissolved in the disordered Fe-Al solid solution.

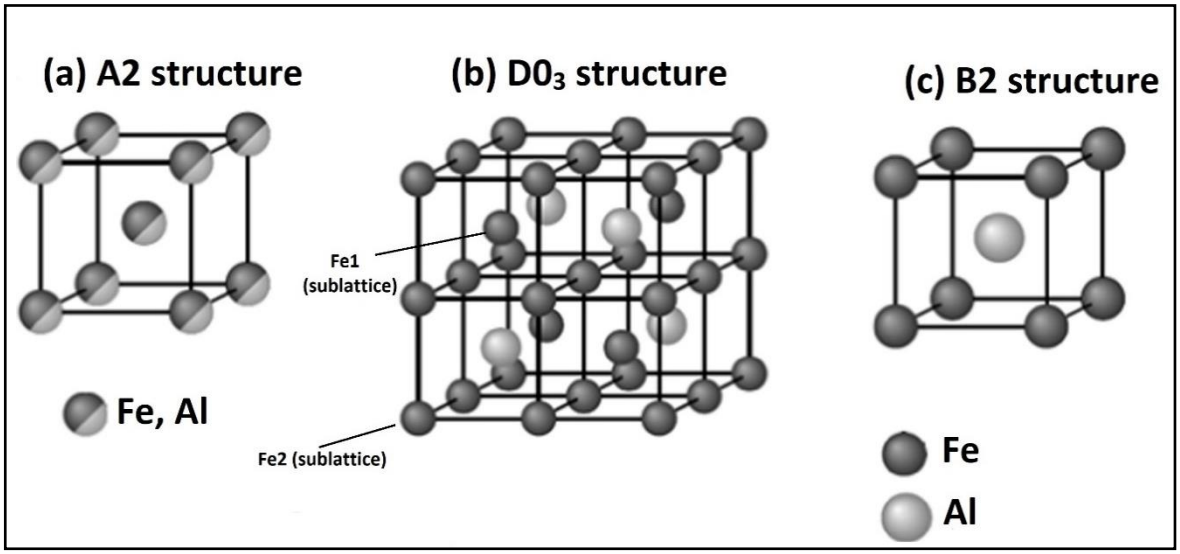

Figure 2. 12 Crystallographic structures a) disordered A2 structure, b) B2 structure and c) $D0_3$ structure [134].

II. $D0_3$ structure (Fe_3Al): This structure is observed around 25 at % of Al in Fe system and remain stable in interval 25-36 at % of Al below 600 °C. The lattice structure of Fe_3Al may be viewed as composed of two interpenetrating simple cubic lattices [134] as shown in Fig 2.12 (b). The $D0_3$ unit cell consists of three Fe and one Al site, whereby the Fe basis atoms are grouped in two symmetry shells[135]. One Fe site belongs to the Fe1 sublattice and two Fe sites to the Fe2 sublattice. As a bcc structure, each Fe site has 8 nearest-neighbor sites. Whereas the Fe2 atoms have mixed Fe/Al nearest neighbourhood in tetrahedral configuration, the Fe1 atom has only Fe nearest neighbours in an octahedral configuration [135, 136]. In another way, this structure can be views as composed of eight B2-type superlattices stacked with alternating Fe and Al atoms[137]. In a perfectly ordered $D0_3$ structure, the atomic distribution of Fe and Al is 75:25, respectively.

Fe_3Al-based alloys are well-known for their high strength, which is attributed to their unique $D0_3$ superlattice structure[138, 139]. However, binary Fe_3Al alloys show phase transformation around 550 ^{0}C and 820 ^{0}C as depicted in Fig 2.11, which can have detrimental effects on the material's structural applications[139]. It has been discovered that the addition of transition metals such as Ti, V, Cr, Zr, Nb, Mo and W is beneficial in increasing the $D0_3$

to B2 phase transition temperature, or vice versa[139]. In case of Ti, it has been found that its addition resulting in the increase the $D0_3$-B2 phase transition temperature from 550 ^{0}C to 1200 ^{0}C and stabilizes both phases, depending on the concentration of Ti [140].The experimental studies discovered that Ti element occupy the sublattice of Fe1 site rather than Fe2 site [141]. Thermoelectric properties of Fe_3Al composition have been studied. It attained power factor of $4x10^{-4}$ W/mK^2 with Seebeck coefficient of ≈ -20 μV/K and electrical resistivity of 1μΩm. It is noteworthy that systematic research has been conducted on the effect of adding a fourth element, such as V, Cr, Nb, or Mo, in Fe-Ti-Al-X alloys on their order-disorder transitions[139]. However, in this project, the focus is primarily on investigating the effect of fourth element substitution in Fe-Ti-Al based alloys to determine their thermoelectric potential.

III. Ordered B2 structure: The B2 phase exists in the Fe-Al alloy system in the composition range of approximately 36-50 at% of Al. Above 1100°C, there is a phase transformation existence from B2 to the A2 phase order. This phase has an ordered crystal structure, where the Fe atoms occupy the corners of the unit cell, and the Al atoms are located at the centre positions[134], as shown in Fig 2.12. Stoichiometrically, B2 phase can be represented by 50:50 atomic distributions of Fe and Al.

2.6 Theoretical Models

The measured thermoelectric properties can be analysed by adopting the developed models by other researchers. At the present time, there are various theoretical models available to analyse different types of charge transport mechanisms. Theoretical models provide the route to find a method to optimise the thermoelectric efficiency of materials. In this project, based on the following models, the attempt was made to analyse the transport properties where it will be required to understand the conduction mechanism of materials.

2.6.1 Single Parabolic band model

The Single Parabolic band (SPB) model is a powerful tool to guide the optimization of thermoelectric performance of the material. It can predict the presence of complex transport behaviour, which affects thermoelectric efficiency. It is based on the Boltzmann transport equations and the relaxation time approximation. In this model, the Seebeck coefficient (α) and carrier concentration (n) can be expressed as following[142]:

$$\alpha = \pm\frac{K_B}{e}\left[\frac{(2+r)F_{1+r}(\beta)}{(1+r)F_r} - \beta\right] \quad (2.10)$$

$$n = \frac{4\pi(2K_BTm^*)^{\frac{3}{2}}}{h^3}F_{\frac{1}{2}}(\beta) \quad (2.11)$$

$$F_i(\beta) = \int_0^\infty \frac{x^i dx}{1+\exp(x-\beta)} \quad (2.12)$$

where K_B is the Boltzmann constant, e is the elementary charge, r is the scattering factor, h is the Planck constant, m^* is an effective mass of the electron, β is the reduced Fermi energy, $F_i(\beta)$ is the Fermi integral, and x is the reduced energy.

Based on Equation (2.10-2.11), this model allows to the calculated effective mass by using the experimental α (Seebeck coefficient) and n (carrier concentration) data. It is usually used to analyse the transport mechanism of heavily doped semiconductors or where transport due to minority carrier is negligible[143]. However, this model is not helpful in analysing the transport properties for materials having multiple bands or non-parabolicity[143]. In the limit of a degenerate electron gas (large β, which is approximately equal to the Fermi energy E_F), the α in the SPB model can relate to carrier concentration (n) and an effective mass m^* as follow[143]:

$$\alpha = (1+r)\frac{\pi^2 {K_B}^2 T}{3eE_F} = (1+r)\frac{8\pi^2 {K_B}^2 Tm^*}{3eh^2}\left(\frac{\pi}{3n}\right)^{2/3} \quad (2.13)$$

It can be noted that the above equation will not show good data fitting for Seebeck data where the influence of minority charge carriers on transport properties exists. Because due to the influence of minority carriers, the Seebeck decreases.

2.6.2 Weighted mobility

Recently, G.J.Snyder et al. developed the Weighted mobility model[144]. He suggests that Weighted mobility is a better descriptor of inherent transport properties than Hall mobility measurements because it is independent of charge carrier concentration and magnetic impurities[144]. In addition, Weighted mobility is the quantitative parameter to assess the electronic transport properties of thermoelectric material and help to predict whether the material can deliver high energy conversion efficiency or not. This analysis also allows to understand scattering mechanisms in materials.

Generally, the carrier mobility (μ) of the sample is estimated using the Hall effect and electrical resistivity measurements. However, the weighted carrier mobility can be calculated based on the simple measurement of electrical resistivity and Seebeck coefficient, which can be more easily

measured than hall measurements[144]. The weighted mobility (μ_w) can relate to drift mobility (μ) based on the following equation:

$$\mu_w \sim \mu\left(\frac{m^*}{m}\right)^{3/2} \tag{2.14}$$

where m^* is the density of state effective mass and m is the electron mass. The model developer suggests the μ_w as the electron mobility weighted by the density of states[144]. The weighted mobility can provide the same information about electron mobility as the Hall mobility.
Snyder suggest that if the experimental data of Seebeck coefficient (α) and resistivity (ρ) for any sample is available, then based on the following equation, the weighted mobility can be estimated:

$$\mu_w = \frac{3h^3\sigma}{8\pi e(2mK_BT)^{3/2}}\left(\frac{\exp\left[\frac{|\alpha|}{\frac{k_B}{e}}-2\right]}{1+\exp\left[-5\left(\frac{|\alpha|}{\frac{k_B}{e}}-1\right)\right]}+\frac{\frac{3}{\pi^2}\frac{|\alpha|}{\frac{k_B}{e}}}{1+\exp\left[5\left(\frac{|\alpha|}{\frac{k_B}{e}}-1\right)\right]}\right) \tag{2.15}$$

where K_B is the Boltzmann constant, σ is the conductivity (reciprocal of resistivity), m is the mass of the electron, T is the absolute temperature and K_B/e = 86.3μV/K. The numerator on the left side of equation (2.13) $\exp\left[\frac{|\alpha|}{\frac{k_B}{e}}-2\right]$ for non-degenerate limit (semiconductor) while the numerator on the right side of equation (2.13) $\frac{3}{\pi^2}\frac{|\alpha|}{\frac{k_B}{e}}$ for the degenerate limit (metals).The drift mobility can also estimate from weighted mobility if the m^*/m can be predicted or assumed. The estimated drift can be used to calculate the carrier concentration using the resistivity data based on the following equation:

$$n = \frac{1}{\rho e \mu} \tag{2.16}$$

2.6.3 Small Polaron Hopping model

In semiconductors an electronic charge carrier moves between atomic sites too rapidly for surrounding atoms (relatively slow moving) to alter their positions in response. However, when electron motion is slowed sufficient, a charge carrier can collapse into a self-trapped state[51, 145]. Then the electron carrier is bound within the potential well that is produced as surrounding atoms assume altered equilibrium positions. The unit comprised of the self-trapped charge carrier

and the pattern of atoms with displaced equilibrium position is termed 'polaron'[51]. Conwell and Mott called this process Hopping conduction and suggested a model to understand this process of conduction in which charge carriers conduct electric current by thermally (phonon) activated tunnelling from an occupied site to an empty site[146, 147]. They consider that hopping conduction is equivalent to the conduction process of a random network of small conductance that link sites[148].

In the case of thermoelectric materials, Small Polaron hopping model can be used to predict the hopping conduction mechanism. The data fitting of temperature-dependent-transport properties with the model equations can assist in examining the existence of hopping conduction. In the high-temperature region where thermally activated polarons govern the transport, then the experimental Seebeck data can be fitted with Mott equation[149, 150]:

$$\alpha = \frac{K_B}{e}\left(\frac{E_a}{K_B T} + A\right) \tag{2.17}$$

where E_a is the activation energy associated with charge carrier generation, and A is a constant related to the kinetic energy of the polarons.

Similarly, in the high-temperature range, the electrical conductivity data can be fitted based on the following expression of SPH model[151]:

$$\sigma = \frac{\sigma_0}{T}\exp\left(-\frac{E_{HOP}}{K_B T}\right) \tag{2.18}$$

where σ is electrical conductivity, σ_0 is a constant, T is the temperature in K, K_B is the Boltzmann constant, and E_{HOP} is the energy required for the electron to hop from its original site to an empty localised site.

If the measured transport properties data fit well with the SPH model, then it can be considered that transport mechanisms occur due to the hopping mechanism.

2.7 Strategies to improve ZT

In the last three decades, researchers developed various methods to improve the ZT (Dimensionless Figure of merit). This section reviews the most common methods used to improve the thermoelectric performance of materials. There are two common strategies have been followed to enhance the dimensionless figure of merit (ZT):

a) Reduce the thermal conductivity:

Thermal conductivity (K) has a major contribution from lattice thermal conductivity (K_L) and electronic thermal conductivity (K_e). The electronic thermal conductivity can be determined by the Wiedemann-Franz law[47]. This law can be described as: $K_e = \frac{LT}{\rho}$,where L is the Lorenz number, ρ is electrical resistivity and based on the classical free-electron model, the calculated value of L is $2.44 \times 10^{-8} W\Omega K^{-2}$. The electrical thermal conductivity is primarily influenced by the carrier concentration/conductivity. However, the lattice thermal conductivity is influenced by various parameters such as the mass of the unit cell and the grain size.

Thermal conductivity could be reduced by creating the scattering centres (point defects /interfaces) by synthesising isostructural solid-solution alloys that can produce phonon scattering and blocks phonon propagation. The phonon scattering is primarily affected by interparticle spacing, matrix grain size and distribution of the secondary phase[51]. The structural constituent such as point defects, strain, dislocation, and displacement of layers and nanoparticles in the bulk sample can contribute to phonon scattering, all these effects can scatter phonons with different frequencies. The following methods can be adopted to reduce the thermal conductivity:

- Based on PGEC (Phonon glass electron crystal) concept: In the case of Skutterudites and clathrates materials, the synthesis was carried out based on the PGEC concept. Both materials contain cages/tunnels in their structure[51]. The heavy elements can fill the cages/tunnels in the structure to create rattling and increase the number of phonons scattering centres, which reduces the lattice thermal conductivity. Moreover, these materials possess thermal transport properties like glass and the electrical properties of crystalline material[41].
- Nano-structuring: By adopting this approach, the interfaces (grain boundaries) can be increased significantly. The literature suggests that phonons having high frequency are mainly scattered by point defects and atomic vacancies, whereas interfaces scatter low-frequency phonons[152]. Due to this feature, the efficient scattering of phonons at the grain boundaries at the interfaces can probably occur, reducing the thermal conductivity. The other advantage of this approach is that the Seebeck coefficient can also be increased due to the quantum confinement effect[153].

b) Optimisation of Power Factor (PF) by Band Engineering:

The PF of the material can be optimised using the band engineering method[154]. This strategy helps to improve the Seebeck coefficient without varying the electrical conductivity. This

method is usually adopted to enhance the ZT peak. The band structure modification can be carried out by:

- Depressing bipolar effect at high temperature: The bipolar effect is usually observed when both electrons and holes contribute to the transport process[155]. This effect is commonly observed for narrow bandgap thermoelectric materials. At high temperatures, the electrons in the valence band can be thermal excited to the conduction band or vice-versa, which reduces the Seebeck coefficient. There are three approaches to reducing the bipolar effect:
    - Increasing the bandgap can reduce the number of thermally activated minority carriers at high temperatures[52].
    - Synthesis of mesoscale microstructures with multiple grain boundaries: The grain boundaries can scatter the electrons and holes in various ways, degrading the bipolar effect[156].
    - By increasing the carrier concentration, the energy levels in the conduction band become occupied. Due to that, the electron in the valence band now requires higher energy to excited into the conduction band.
- Electronic resonance states: The dopants/ substitution elements can generate resonant levels, which can improve the DOS (density of states) near the Fermi level and enhance the Seebeck coefficient due to the increase of electron effective mass without affecting the carrier concentration[58, 157].

2.8 Fabrication routes of thermoelectric bulk sample

The thermoelectric properties primarily depend on crystal structure, composition, defects, and sample fabrication route. In this section, the key existing thermoelectric material fabrication routes are reviewed. Generally, there are two main approaches to fabricating nano-structured materials: (a) the top-down and (b) the bottom-up. In the case of the former approach, the bulk sample is broken down into micro or nanosized particles using ball milling (BM), spin melting or thermal cycling. In this approach, it is difficult to control the crystalline structure and grain size due to the thermodynamics and kinetics of the reactions[143].

On the other hand, Bottom-up is a conventional material synthesis approach. This approach relies on the conjugation of atoms/nanoparticles to build a nano-structured bulk sample. This approach allows a way to control the carrier concentration through doping and grain size, shape and size distribution[143]. The fabrication routes can be categorised as follows:

2.8.1 Physical routes of fabrication

- Solid-state synthesis reaction: In this method, stoichiometric or a mixture of elemental components, in powder or compacted form, are heat-treated for an extended time in a sealed tube or inert gas at a temperature below the melting temperature of elements to form thermoelectric material phase. This method is beneficial for tuning the doping level. Examples of thermoelectric materials prepared using this method are Zn_4Sb_3 [158], ZrNiSn[159] and Ni-substituted $CoSb_3$ [160]. It is found that the combination of solid-state synthesis with ball-milling allows for achieving nano-structured materials[143].
- Vacuum Arc-melting: This technique is widely used for the fabrication of intermetallic and metal-based composites at research laboratories and industrial scale for the production of commercial metallic products. The equipment used for this technique is generally called Arc melting furnace or Electric arc furnaces. A laboratory-scale furnace is known as DC arc melting furnace. This furnace allows for the rapid melting of the sample up to 3000°C by an electric arc generated between a cathode (usually composed of thoriated tungsten (W) alloy in the form of rod) and metallic anode (made of copper (Cu))[161]. Arc is generated by applying a low voltage (30-60 V) and high current (300-600 A) between the cathode and anode. It is beneficial for quickly producing materials. It is also useful for the preparation of samples having small quantities with negligible loss during melting, which could be an advantage for the fabrication of alloy based on rare earth-metals. The major limitation of this technique is that it is not suitable for the preparation of non-conducting ceramics. In the case of multi-component alloys, where the difference in melting temperature of added elements is large. Arc melting may cause deviation from desired stoichiometry due to vaporization or loss of low melting (or highly vaporizing) constituents[161]. This technique has been used to fabricate thermoelectric materials based on Co-Sb[162], Nb-Co-Sb[163] and Nb-Fe-Sb[164].
- Mechanical alloying (MA): MA is a powder processing method. This method allows the fabrication of homogeneous alloys starting from blended elemental powder mixtures without heating or melting the powder samples[165]. In this process, mixtures of powders of elements are milled together in a high-energy-ball-mill. Due to the mechanical impact during milling, the blended sample transforms into homogeneous material. The milled sample might have achieved solid solution, an intermetallic or amorphous phase[165], which can be identified using the XRD technique. Currently, high-energy ball millers such as SPEX shakers, planetary ball mills (PBM) and Attritor mills are available to fabricate the alloys[165]. In the case of thermoelectric materials fabrication, to achieve the desired

material phase/microstructure, the optimisation of ball miller parameters such as milling speed, milling time and ball-to-powder (B.P.R) weight ratio is achieved[165]. The thermoelectric materials such as Bi-Te[166], Co-Sb[167], Sn-S[168] and Mg-Si[169] have been fabricated by combining the MA with Spark plasma sintering (SPS) and others like Co-Sb[170], Bi-Te[171] and Cu-Sb-Se[172] combining MA with hot Press.

- Melt-alloying: In this technique, the stoichiometric or a mixture of elemental components is heated above the melting temperatures, and then the sample slowly cools down to grow the crystal structure of the desired phase[143]. The PbTe[173], SnTe[174] and PbSe[63] have been fabricated by implementing this method.

2.8.2 Chemical routes of fabrication

Chemical fabrication routes are based on bottom-up strategies, providing a controlled way to achieve small particle sizes and morphology of nano-structured materials.

- Sol-gel technique: In 1932, this method was first used to prepare aerogels[175]. Currently, this method is commonly used to fabricate Nano-structured oxide thermoelectric materials and inorganic oxide materials. This technique is allowed to preform chemical reactions at low temperatures and offers good composition control. This method starts with a colloidal solution (sol) preparation resulting from hydrolysis and condensation of the precursors. Metal compounds, such as metal alkoxides and acetylacetonates, are used as precursors. The condensation process is usually combined with solvent evaporation, which results in gel formation[176]. This process is generally followed by heat treatment (400-600^{0}C) to remove the organic products. This calcination process is useful for obtaining the final product[177]. Nanocrystalline Bi_2Te_3 powder sample was prepared by Ritter et al.[178] by a reaction mixture of Bi_2O_3, Te metal, nitric acid, ethylene glycol and DL-tartaric acid using the sol-gel technique[143]. Furthermore, $CoSb_3$-based skutterudites have also been fabricated using the sol-gel technique[143].
- Hydrothermal and solvothermal techniques: Both techniques are used to prepare chemical compounds. In these methods, the materials/ samples are placed in a stainless-steel autoclave (closed system) with a solvent at high temperatures (≈ 500^{0}C) and pressures (≈ 10-80MPa). The difference between the two techniques is the solvent used in each reaction; water is used in the hydrothermal (HT) case, while the non-aqueous solvent is used for solvothermal techniques (ST). These techniques are based on the ability of the solvent to dilute substances that are practically insoluble under normal conditions, such as oxides, silicates, sulphides and zeolites. During the process, A surface-active agent

(SAA) is also used to reduce the surface tension, and it helps to produce the oxide compounds in the hydrothermal solution. The main experimental parameters include the initial pH scale of the medium, temperature of the synthesis, pressure in the vessel and selection of solvents, precursors, and surfactants are affect the final sample[179]. Co-Sb TE samples have been prepared by combining the HT and ST techniques[176].

- Chemical vapour deposition (CVD): In this method, a volatile gaseous compound (precursor) reacts with the wafer/substrate, producing a non-volatile thin solid film onto the substrate. In conventional CVD, when gas compounds are unable to produce chemical reactions at room temperature. Then, in this case, gas passes over a substrate heated to a specific temperature, where the reactants can decompose or combine with other constituents to form a layer on the substrate. There are three components in the CVD system, namely, (1) a vapour precursor gas that is the desired material, (2) a reactor where the deposition takes place, and (3) an effluent gas handling system that removes the by-products and unreacted precursor. Through this technique, various Chemical reactions can be carried out using different reactants or precursors along with different ratios and conditions (temperature, pressure, and gas composition)[179, 180]. This technique is used in the solid-state microelectronic and semiconductor industries.

2.8.3 Consolidation methods of the powder sample

Various sintering techniques may be employed to produce a nano-structured bulk sample from loose-powders. In this section, the review of three widely used consolidation methods is described:

- Cold pressing and Annealing

  The consolidation of the powder sample in this method is carried out by applying pressure in a uniaxial direction at room temperature. The mechanical or hydraulic based-pressing technique is used to compact the loose powder. In most cases, the cold-pressed compact sample is annealed at high temperatures. In order to improve the grain-to-grain connectivity and also relax internal stress.[143]

- Hot pressing

  This consolidation technique allows for the fabrication of bulk samples by simultaneously applying heat and pressure in a uniaxial direction. It is a high-pressure (≈ 50-100MPa) sintering method. The pre-compacted samples by cold press method can also be sintered via this technique. In this method, the loose powder or pre-compacted is loaded into a

mould/die-set, and it heats up to high temperatures using induction or resistance heating methods. To heat the mould, the following methods can be used:

- **Inductive heating:** Through this method, heat is generated within the mould by applying a high-frequency electromagnetic field. The electromagnetic field is generated by connecting the induction coil to an electronic generator. The main advantage of this heating method is that the pressure and the power can be applied independently. However, the major drawback of this heating technique is that it is costly to generate a high frequency[181].
- **Indirect resistance heating:** In this method, the mould is placed in the heating chamber. The mould made of Graphite element is used as a heating element which is heated up by applying an electrical current. The graphite elements are firstly heated up and then heat is transferred into the mould via convection. This heating process is called indirect resistance heating. The advantage of this method is that high temperatures can be easily achieved. Despite this, the major disadvantage is that it takes a long time to heat the mould[182].

- Spark plasma sintering (SPS)

  SPS is a novel rapid powder consolidation technique that utilizes the electric current to produce a dense sample in a very short period by using relatively high sintering pressure. In the present days, this technique is used in a wide range of metallic, ceramic, and functional materials. It is also referred to as Pulsed Electric Current Sintering (PECS) or Field Assisted Sintering Technology (FAST)[183, 184].

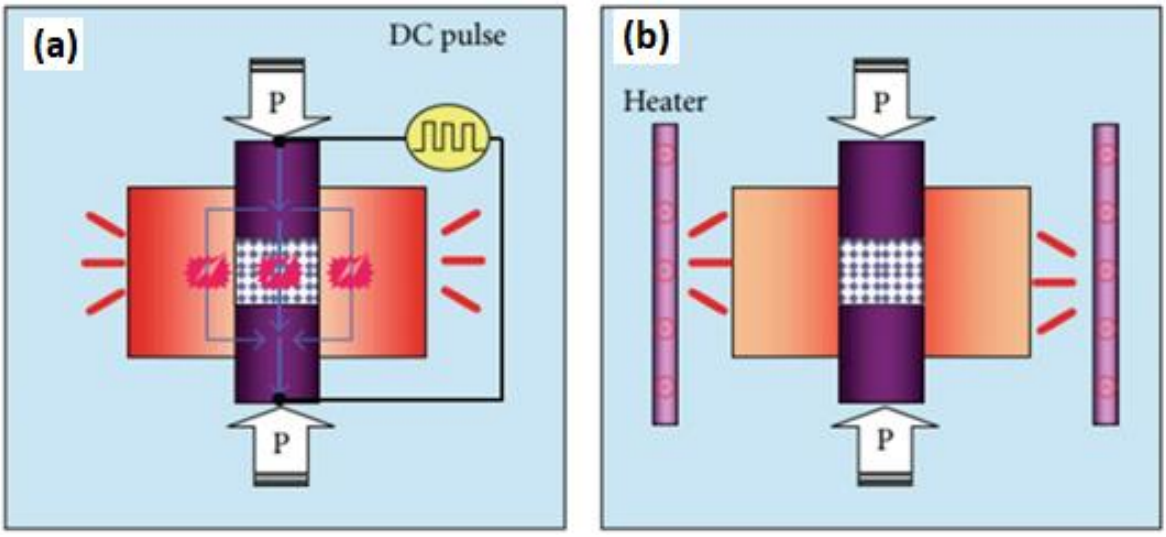

Figure 2.13 Comparison between (a) Spark plasma sintering and (b) Conventional sintering [Ref [173]]

It is necessary to understand the major difference between Spark plasma sintering and conventional sintering technique such as the Hot-pressing consolidation method. Fig 2.13 shows a comparison between both methods. In the case of SPS (Fig 2.13 a), a direct current, or a pulse of current in an on-off sequence, is passed through the graphite punch-and-die set and the powder sample[185]. Therefore, in this technique sample is heated from inside and outside the die. However, in the case of the conventional consolidation methods, the sample is heated using an external heating source such as Inductive and Indirect heating-based methods.

In this technique (Fig 2.13 (a)), when the electrical discharge of pulsed DC passes between spaces of powder, it generates a spark between them. This effect also generates the Joule heating effect (i.e., the transformation of electric energy into heat through an ohmic resistor) which assist to raise the internal localised temperature between the junction of particles. It leads to fast necking and diffusion process that reduces intergranular gaps[186]. This entire process allows for the densification of fine-grained powders and helps to produce dense bulk samples. There are key advantages of SPS compared to the conventional methods are listed below.

- SPS sintered the compact in a much shorter time than HP.
- High reproducibility, energy efficiency reliability, and sintering speed.
- Ease operation and accurate control of sintering conditions.
- Rapid consolidation of powder samples at high heating rates helps to inhibit grain growth.

The main disadvantage of using the SPS technique is that it only allows for the preparation of simple symmetrical shaped samples. Additionally, the pulse DC generator used in the SPS machine is quite expensive[185].

2.9 Review of Traditional thermoelectric material fabricated based on MA

This section presents a review of the processing of traditional thermoelectric materials over last few decades based on mechanical alloying (MA) combined with different consolidation techniques to investigate the thermoelectric properties.

• Si-Ge alloys

In 1988, Davis et al. reported that the MA technique could be utilised to fabricate Si-Ge alloys[187]. Cook et al. prepared the n-type SiGe samples with phosphorus and gallium phosphide by MA method using SPEX 8000 mixer miller and investigated their transport properties. They suggested that this technique provides a route to fabricate the homogeneous and fine-grained Si-Ge alloys

at room temperature[188]. P-type Si-Ge materials were also fabricated by the MA method using SPEX 8000 and a Fritsch P5/4 planetary mill. In 1998, H.Okamura et al. prepared the p-type $Si_{80}Ge_{20}$-xB_x (at % x=0.2-1) composition for thermoelectric properties investigation by MA-based Vibratory mill and hot-pressing consolidated technique[189]. A few years back, A.A.Usenko et al. fabricated the Si-Ge alloys using a Planetary ball mill- Spark plasma sintering (SPS) route. They reported the enhancement in ZT values due to a reduced thermal conductivity which is most correlated with the nanostructure feature[190].

- Pb-Te based alloys

In 1999, N.Bouad et al. reported that MA is a beneficial technique for producing smaller grain size powders of Pb-Te[191]. They also investigated the phase transformation study of Pb-Te powders during the MA process and suggested that 3 h is reasonable milling timing to obtain PbTe stoichiometric sample[192]. Papageorgiou et al. also prepared the PbTe alloys based on planetary ball mill using a tungsten carbide bowl and reported that samples having the average crystalline size of 10 nm order demonstrate higher Seebeck values[193]. In 2013, Zhang investigated the effect of Al on transport properties of PbTe alloys using MA (SPEX 8000D) -HP route and observed a 27-46 % higher Seebeck value than reported data, peak ZT of 1.2 at 770 K for $Al_{0.03}$PbTe samples[194].

- Bi-Sb-Te alloys

In 1997, P.Pierrat et al. prepared the Bi-Te-Sb samples in a planetary ball mill using tungsten carbide vessels along with n-pentane (control agent)[195]. Masafumi et al. fabricated the Bi-Sb composite by MA followed by Cold pressing and hot-pressing methods. They reported that with the increase in the milling period, the thermal conductivity decreases due to the increase in grain boundary area[196]. A few years later, L.Xue-Dong and his co-worker prepared the $(Bi_{1-x}Sb_3)_xTe_3$ alloys by MA-Pulse discharge sintering route and mentioned that this route is beneficial to achieve single-phase alloys[197]. Lee et al. prepared the p-type Bi_2Te_3-Sb_2Te_3 samples using MA and hot-pressing routes under different process conditions[198]. Moreover, they observed a reduction in the carrier concentration and increased mobility at higher hot-pressing temperatures. Recently, H.Mansouri et al. fabricated the p-type $(Bi,Sb)_2Te_3$ materials using MA- SPS route and reported that $Bi_{0.5}Sb_{1.5}Te_3$ material demonstrates the highest homogeneity and lowest grain size[199].

- Fe-Si based alloys

In 1994, M. Umemoto prepared the β-$FeSi_2$ doped with Al and Mn by mechanical alloying (MA) technique and reported that the bulk samples fabricated by hot pressing technique from milled powder showed smaller grain size and lowered thermal conductivity than traditional ingot metallurgy[200]. A few years later, H.Nagai et al. studied the thermoelectric properties of β-$FeSi_2$ mechanically alloyed with Si and C and observed an improvement in ZT values due to the reduction

in thermal conductivity because of dispersion of fine α-SiC particles[201]. In 2005, the transport properties of hot-pressed β-$FeSi_2$ with yttria dispersion by MA were reported and observed an enhancement in room temperature Seebeck coefficient of doped samples. They also noticed a significant reduction in thermal conductivity with an increasing concentration of Y_2O_3 due to an increase in phonon scattering due to the dispersion of fine Y_2O_3 particles[202].

- Skutterudites

The structural details of this class materials were described in Section 2.4.6. In 2003, J.Yang et al. synthesis the $CoSb_3$ skutterudites by MA technique utilizing a QM-4F planetary ball mill and reported that the milled powders can be transformed into single phase of $CoSb_3$ after heat treatment at 700^0C. They also concluded that MA-HT is an efficient route for synthesizing the $CoSb_3$ phase[203]. A year later, Itoh et al. studied the effect of milling time and rotation speed on the synthesis of $CoSb_3$ and concluded that Seebeck coefficient and electrical conductivity of the sample are influenced by the milling period and the rotation speed[204]. In 2006, the thermoelectric properties of Fe-doped $CoSb_3$ bulk samples fabricated by MA and hot pressing were investigated. They noticed a significant reduction in lattice thermal conductivity which led to an enhancement in ZT value compared to the pristine sample[205]. Trivedi et al. fabricated the Ni-doped Dy-filled $CoSb_3$ samples for thermoelectric studies by utilizing the MA-SPS route and reported an enhancement in PF due to an enhancement in electrical conductivity. They observed a drastic reduction in lattice thermal conductivity due to enhanced phonon scattering from point defects and grain boundaries[206].

- Other alloy systems

Mg-Si, Cu-Te and Fe-V-Al based alloys were also prepared by utilizing mechanical alloying[207-209]. Aizawa et al. successfully fabricated the single phase $Mg_2Si_{1-x}Ge_x$ (x=0-1) by MA-HP route and studied the temperature-dependent transport properties of prepared bulk samples[210]. Sridhar and his co-worker synthesis the hexagonal Cu_2Te by mechanical alloying and transport properties[209]. M.Mikami et al. investigated the thermoelectric properties of Fe-V-Al bulk samples prepared by MA-PCS technique and concluded that the PF of the sintered alloy made up from grains of 200-300 nm is comparable to the arc-melted samples. They also reported that sintered alloy attained much lower thermal conductivity than the arc-melted sample due to phonon scattering at grain boundaries[207].

Chapter 3: Materials and Experimental Methods

3.1 Introduction

This chapter describes the experimental techniques used throughout this thesis. The mechanical alloying of blended powders was performed by employing the planetary ball milling technique. To produce the bulk samples from milled powders, cold pressing followed by an annealing route and spark plasma sintering technique were adopted. The phase analysis of the powder and bulk samples was performed using the X-ray diffraction (XRD) technique. The thermoelectric properties of bulk samples were characterised using a homemade hot probe, 4-multifunctional probes, ULVAC ZEM-3 and a laser flash system (NETZSCH-LFA 457 Micro flash, Germany).

3.2 Raw materials

The raw powders of iron (Fe), titanium (Ti), vanadium (V), chromium (Cr) and aluminium (Al) with 99.99% purity and particle size ranging from (60-75 microns) were purchased from Goodfellow Cambridge Ltd, UK. However, the raw powders of manganese (Mn; particle size <50 > 325 mesh), molybdenum (Mo; particle size < 100 mesh), tungsten (W; particle size 12 microns), Nickel (Ni;99.99% Puratronic (metals basis) C<100ppm) and Copper (Cu; particle size <50 mesh) were pre-available in the lab and were purchased from Alfa Aesar, Johnson Matthey GmbH and Goodfellow respectively.

3.3 Sample preparation set-up

A glove box manufactured by Saffron Scientific Equipment Ltd shown in Fig 3.1 (a) was used to store the powders described in the above section. The nitrogen gas (Pureshield 11-W, 11 m^3) purchased from BOC was used to fill the glove box to create an inert gas environment. The pressure of 2 bar of Nitrogen gas was maintained during sample preparation. A balance (Precisa, series 40SM-200A) having readability up to five digits, was placed inside the glove box (in the product storage chamber) to weigh the powders. Throughout this research work, an inert gas environment was preferred to prepare samples to avoid the oxidation of powders. This set-up was used to mix the powders in stoichiometric ratio and load the blended powder in grinding bowl for mechanical alloying.

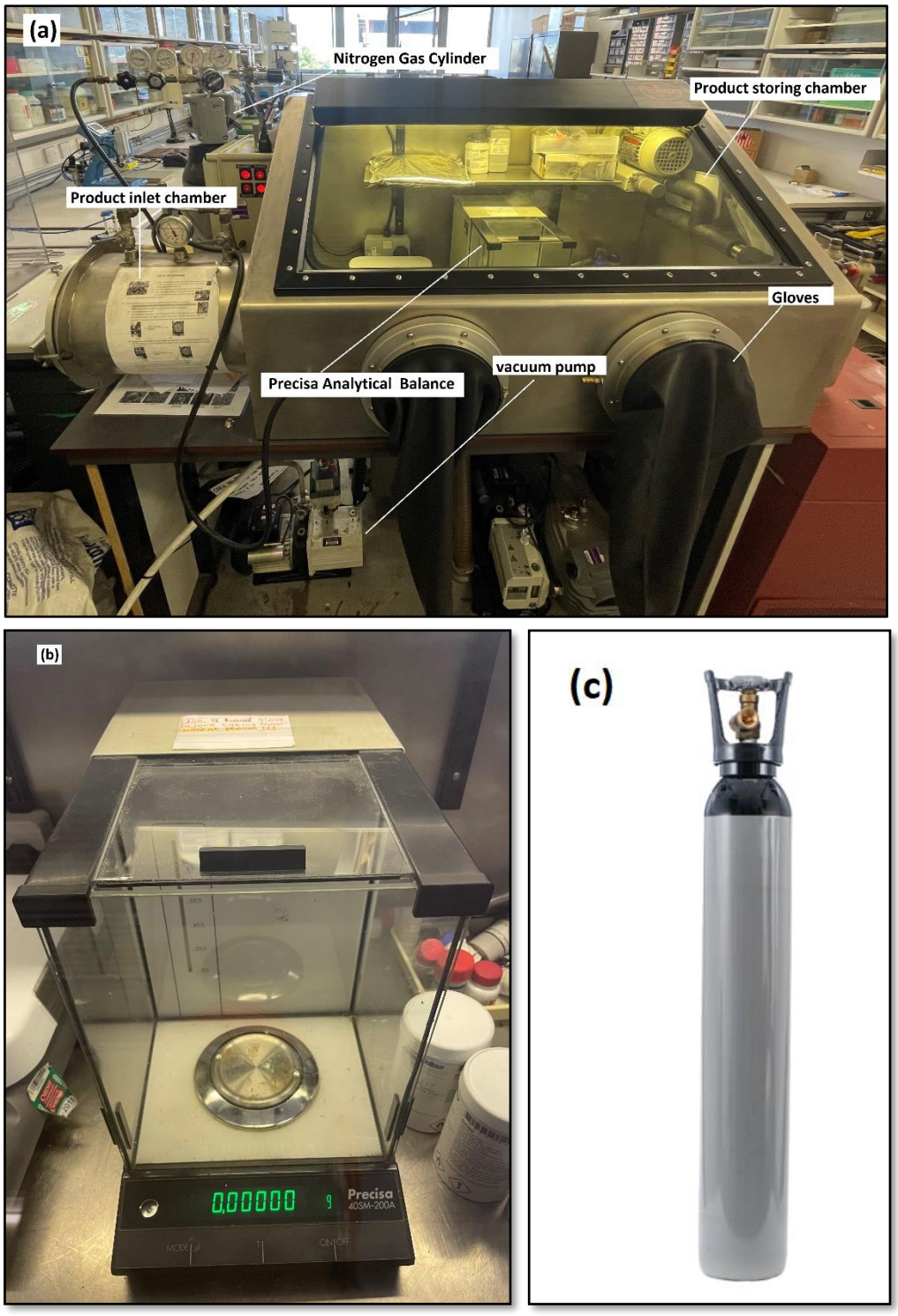

Figure 3. 1 Photograph of (a) Glove box (b) Precisa Balance and (c) Nitrogen gas cylinder

- Procedure adopted to place powder in storage chamber of Glove box

There are two chambers in the glove box: (a) Product inlet chamber and (b) Product storage chambers. The manufacturer separated both chambers by designing an internal lid (located inside the equipment) which can be opened by inserting the hands into the glove box through gloves. The following procedure was adopted to place the products in the storage chamber:

Firstly, the lid of the product inlet chamber was opened manually, and then the products were placed in it. After that, the lid of the chamber was tightly sealed. Subsequently, the existing gases inside the chamber were purged out by utilising a vacuum pump which resultant to reduce pressure from 0 bar to -1 bar. In the next step, this chamber was filled with nitrogen gas (by an opening valve) to achieve pressure of 0 bar. This procedure was repeated twice to expunge the gases into the atmosphere. Afterwards, the internal lid was opened, and products were shifted from the product inlet to the product storage chamber after which the internal lid was closed. A similar procedure was also adopted to load the grinding bowl with the sample.

3.4 Mechanical alloying

Mechanical alloying (MA) is a solid-state materials-processing technique. When blended powders are milled in a ball miller then continuous collision of balls with powder particles happens. The mechanical impact produced by balls resulted in the cold welding, fracturing, and re-welding of powder particles repeatedly at different milling stages. This process leads to the formation of alloys such as solid solution, and intermetallic and amorphous compound. The benefit of this technique is that it allows the preparation of alloys at or near room temperature [211]. Another advantage of the MA technique is that it provides a convenient route to investigate the effect of element substitution on material phase structure and thermoelectric properties. The following ball milling techniques were used in this research work:

3.4.1 Planetary ball mill

A planetary ball mill can be used for alloying and colloidal grinding due to its good reproducibility, fabricating the sample fast and safe handling features. Planetary ball mills are usually available with 2 or 4 milling stations. In this technique, the grinding bowl containing the powder sample and milling balls is placed on the main disk which rotates around a common central axis. At the same time, the bowl rotates around its own axis but in the opposite direction. Due to the simultaneous effect of the centrifugal forces and the high rotational speed of the bowls /the disk, the mechanical impact develops inside the bowl, which produces repeated cold welding, fracturing and rewelding of powder particles during the process[212, 213].

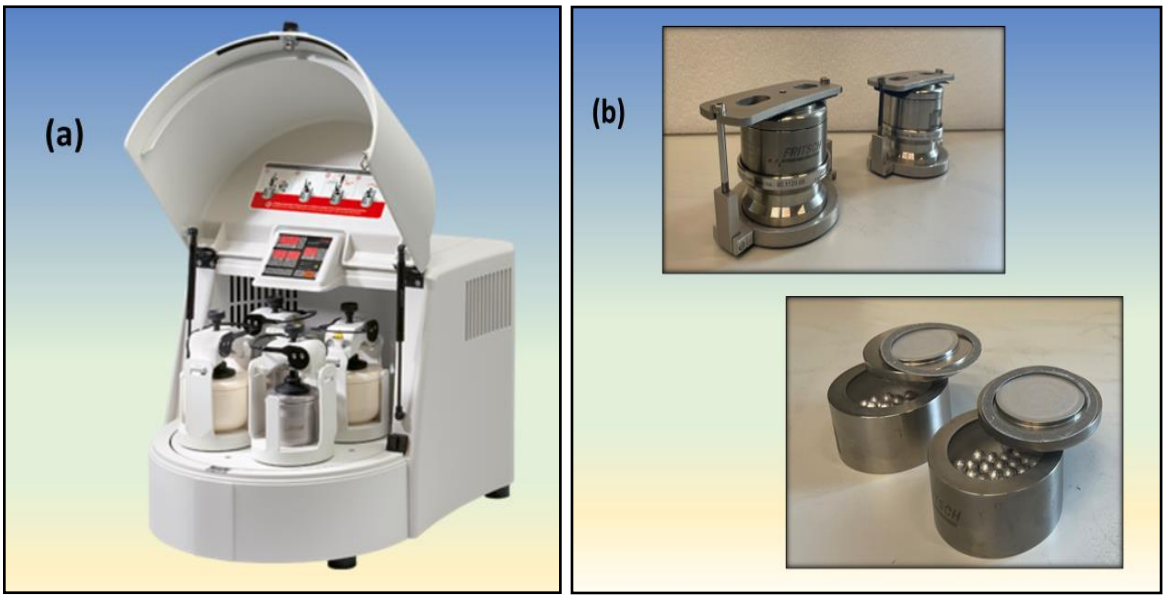

Figure 3. 2 (a) Photograph of Planetary ball mill (Pulverisette 5/4) (b) Grinding bowl (Volume 80ml)

A Fritsch Pulverisette 5/4 planetary ball mill shown in Fig 3.2 (a) was used in this study to perform mechanical alloying (MA) of blended powder samples. This milling equipment has four stations. The mechanical alloying was performed in a stainless-steel grinding bowl with a capacity of 80mL and stainless-steel balls of a diameter of 10mm illustrated in Fig 3.2 (b). The stainless-steel balls are used as grinding media. To perform the milling, the grinding bowl is partially filled with the blended powder sample and grinding balls in an inert atmosphere. After that, the loaded bowl is placed on the rotating disc of PBM, and milling is performed at specific speed parameters. The details of the used parameters for the milling of samples are described in Chapter 4.

3.4.2 SPEX miller

This milling technique is widely used for mechanical alloying, grinding and mixing emulsions[165]. A SPEX 8000M miller allows grinding the dry/wet or brittle sample up to 0.2-10 grams. An image of this miller is shown in Fig 3.3 (a). SPEX miller and their series are also known as high-energy ball mills. This miller is utilised for preliminary studies in this work. It is available with one milling working station and allows the milling of one sample per run. In this method, when the stainless-steel grinding bowl (vial) is loaded with grinding balls and the sample is placed inside the miller, the miller shakes the bowl in a complex motion as represented in Fig 3.3 (b), which combines back-and-forth swings with short lateral movements at each end of the grinding bowl. The movement of the bowl (vial) resulted in the flattening, cold-welding, fracturing, and re-welding of particles at different stages of milling duration [165].

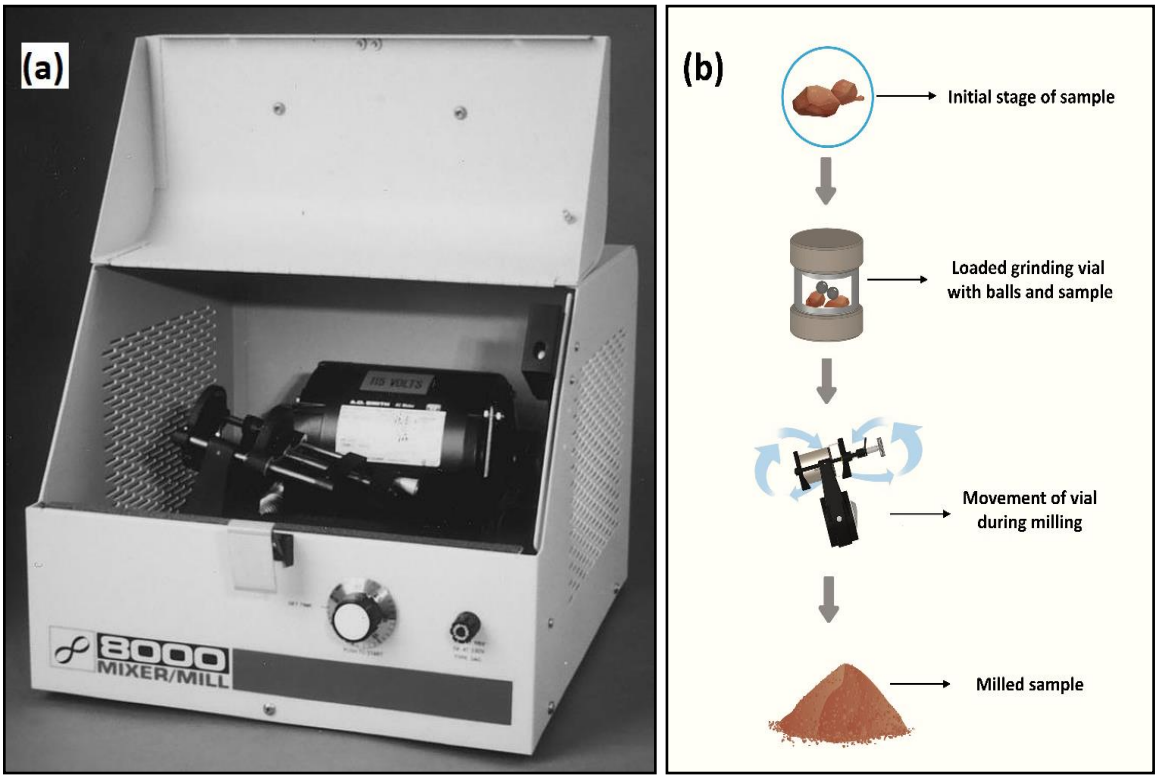

Figure 3. 3 (a) Photograph of SPEX 8000M and (b) Movement of bowl (vial) during milling process

In this work, Planetary ball mill (PBM) was used extensively to conduct various studies. Because it is available with modern operation controlling, energy-saving mode, four milling stations and reversing milling direction features. The programmable control panel of this miller allows us to plan the experiment in the run-pause with four milling stations. However, the SPEX miller has only one milling station which allows the milling of one sample per run. Furthermore, the safety/control operation features, programmable control panel and timer are unavailable for the SPEX. As a result, it is not feasible to plan the experimental activity for an extended milling period based on the run-pause sequences and health-safety concerns. The preliminary results also indicate that the PBM-based bulk samples demonstrate better results in terms of the Seebeck coefficient and PF than the SPEX-based samples (Appendix-A).

- Preliminary results

Fig 3.4 illustrates the SEM micrographs for $Fe_{11}Ti_3Al_6$ powders before milling and milling with PBM and SPEX miller for 5 hrs. The images demonstrate that after 5 hrs of milling, the initial shape of the particles has completely disappeared. Due to the collision of the powder particles with the grinding balls, the larger particles (Fig 3.4 (a)) are broken down into smaller particles (Fig 3.4 (b-c)). In accordance with Fig 3.4 (b-c), the SPEX miller produced finer powder particles than the PBM

miller in the same milling period. The SEM results suggest that both millers can be utilised to perform mechanical alloying.

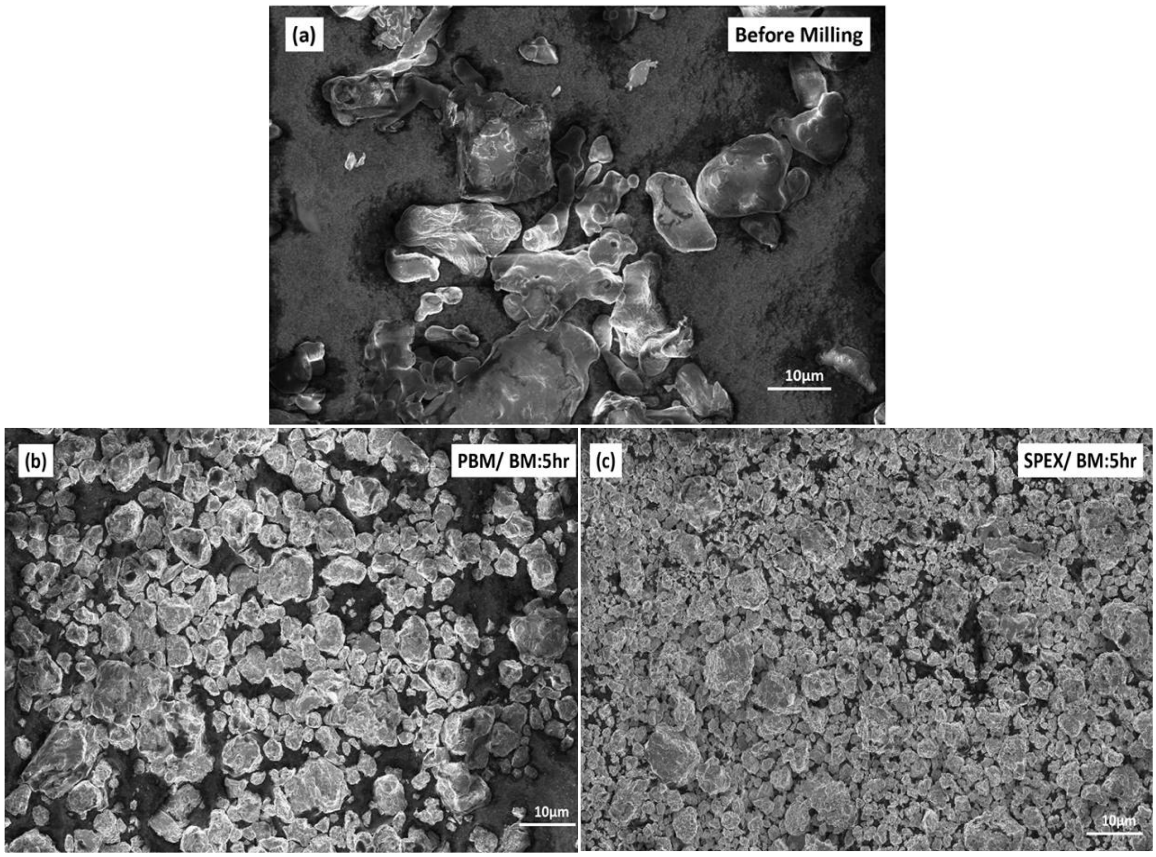

Figure 3. 4 SEM micrographs for Fe-Ti-Al powders (a) Before milling (b) Milling with PBM for 5 hrs and (c) Milling with SPEX for 5 hrs, Magnification =1KX

3.5 Consolidation techniques

In the bottom-up approach, the densification of milled powders is an important step in producing dense bulk samples. The major challenge in densifying powders is obtaining dense compact while maintaining nanostructure/grains[143]. In this work, the following consolidation techniques were used to produce bulk samples:

3.5.1 Cold pressing and annealing

It is a traditional powder consolidation method and has been used to fabricate thermoelectric materials[214-216]. At the beginning of this project, due to the non-availability of the Spark Plasma Sintering technique. This consolidation method was employed to fabricate the bulk sample from milled powders because it is readily available, energy-efficient and low-cost technology[217, 218].

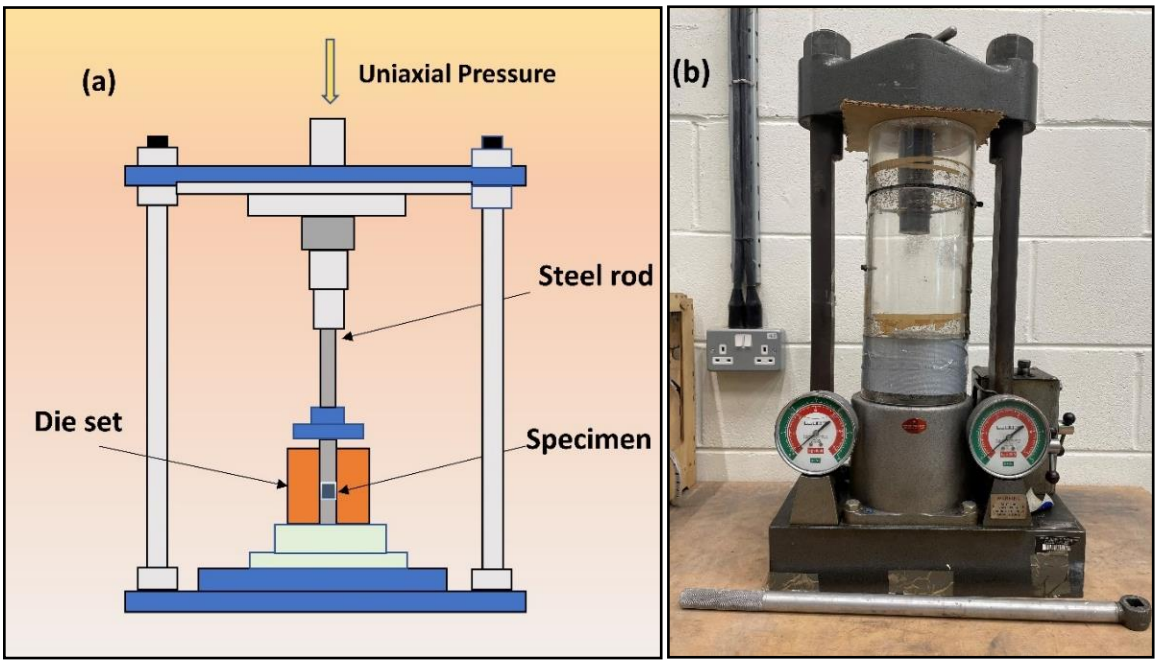

Figure 3. 5 (a) The schematic diagram of the set-up for powder compaction (b) Photograph of cold press station

The standard hydraulic press station is used to perform the cold press of the milled samples i.e., produce the bulk sample. An arrangement of the compaction process method used at room temperature is shown in Fig 3.5. The compaction of the powder sample is carried out inside hardened steel die set having a diameter of 6.35mm by applying uniaxial pressure. Cold pressing followed by an annealing process might be beneficial in improving the inter-connectivity between grains and releasing internal stress. In the literature, it was noted that the annealing process for PbTe[219] and Bi-Te[220] cold-pressed bulk samples is beneficial to improve the thermoelectric properties due to the reduction of charge carrier with residual and recrystallization[220].

The cold-pressed bulk samples were heat-treated using Carbolite MTF 12/38/400 tubular furnace. A schematic diagram of the set-up for the annealing is illustrated in Fig 3.6. A 35mm Quartz tube (multi-lab) was inserted inside the tubular furnace and connected to argon gas (Pureshield 11-W, 11 m^3) using the adapters (KF-40 Swagelok) and cast clamps. The argon gas flow was regulated on the inlet side using a flowmeter (Brooks Instruments).

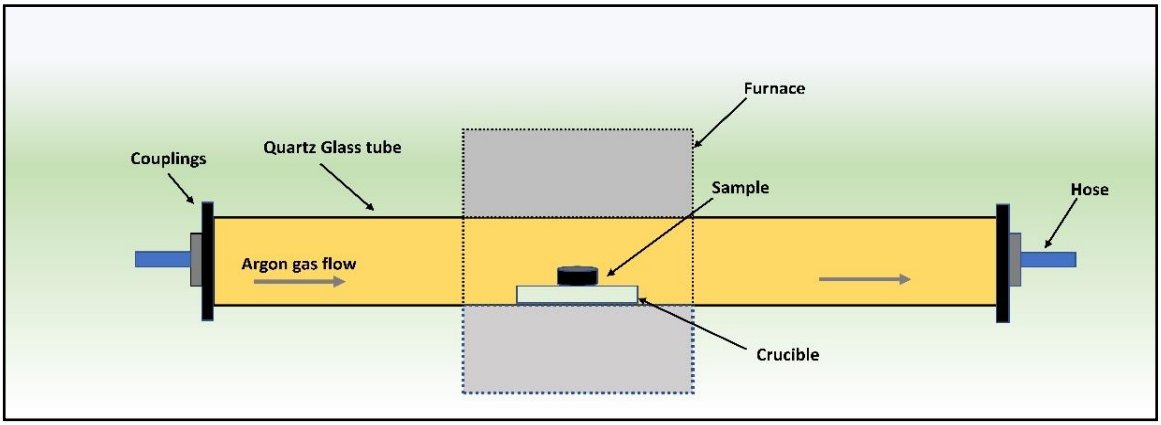

Figure 3. 6 Schematic diagram of the set-up for heat treatment of cold-press samples based on the tubular furnace

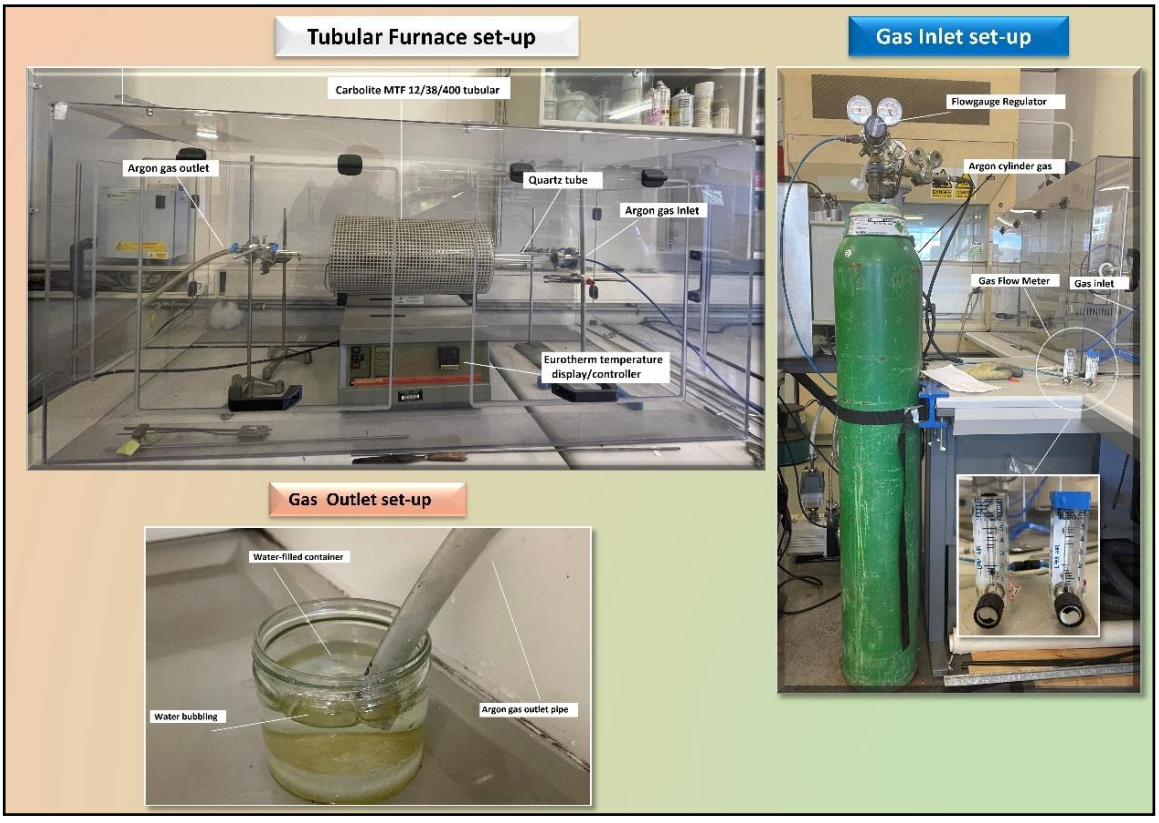

Figure 3. 7 Photograph of Tubular furnace including gas inlet and outlet-setup

Fig 3.7 displays the photograph of the tubular furnace, gas inlet and outlet set-up. The annealing was performed at the centre of the furnace. In order to do that, the bulk samples are first placed on an alumina crucible in the air. Then, from the inlet end of the quartz tube, the loaded crucible was pushed inside the quartz tube to the centre of the furnace using a steel rod. The outlet was connected to the water-filled container to verify the argon gas flow by observing the

water bubbling. The annealing condition for heat treatment, such as pre-conditions, annealing temperature, and period, are described in Section 4.6.

To ensure accurate annealing temperatures, the tubular furnace was calibrated up to 1000^0C using a K-type thermocouple by locating it at the centre of the furnace. The calibration procedure was carried out by comparing the temperatures displayed on the Eurotherm controller of the furnace with the temperatures measured using the thermocouple in contact with the crucible in air and argon flow, respectively. The inbuilt Eurotherm controller of the furnace can set up the temperature of the furnace from 100°C to 1000°C. Fig 3.8 shows the measurement results of the comparison between target temperatures and measured temperatures for different conditions. For each measurement, when the target temperature is selected, and the control panel displays a constant value, it is maintained as an isothermal dwell for 10 min.

An empirical formula y = 1.11x + 33 was derived from this calibration procedure, where x represents the required temperature, and y represents the actual temperature selected by the Eurotherm controller. The data show instability between 0-400°C. To confirm this behaviour, several tests were conducted below 400°C, and the test suggests that the trend of temperature between 0-400°C was repeatable.

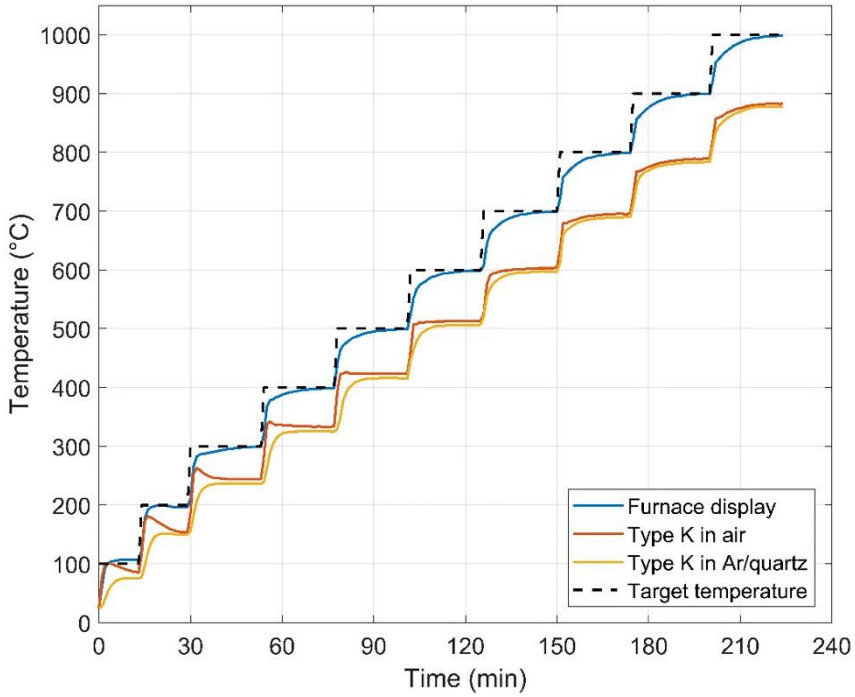

Figure 3. 8 Temperature calibration for tubular furnace in air and argon atmosphere

3.5.2 Spark Plasma Sintering (SPS)

The SPS facility used in this work is HP D 10-SD unit from FCT Systeme GmbH, which has been installed at Cardiff and was used to consolidate Fe-Cr-Ti-Al milled powder samples. An image of

the apparatus is shown in Fig 3.9. The working principle and advantages of this technique over other techniques have been described in Chapter 2.

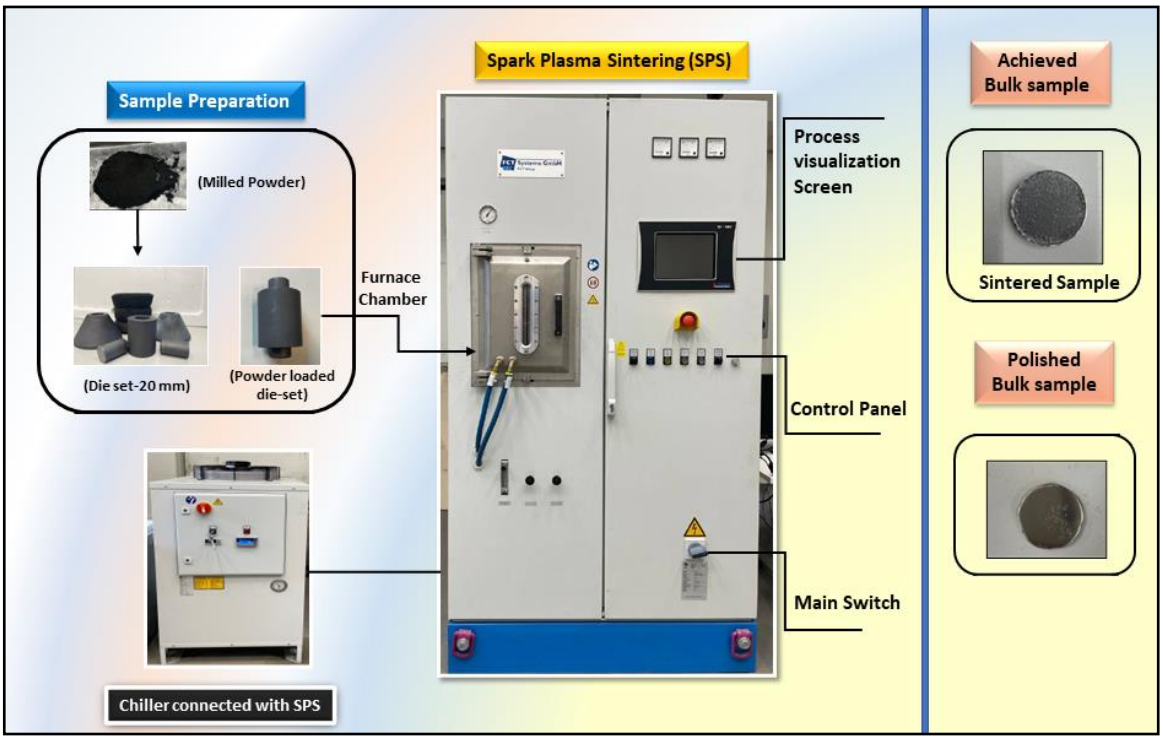

Figure 3. 9 Photograph of Spark Plasma sintering (SPS) facility employed in this work

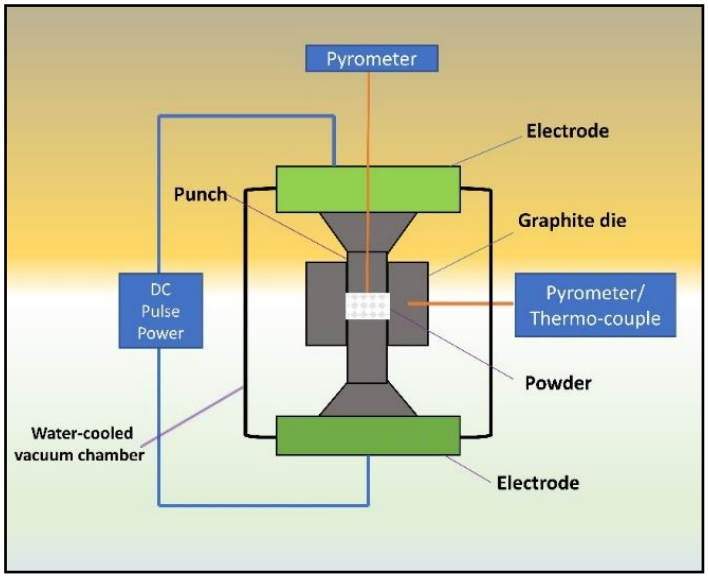

Figure 3. 10 Schematic diagram of Spark Plasma Sintering consolidation process

- Set-up and sample preparation

Firstly, the milled powder sample is loaded into the graphite die with a diameter of 20mm (Duragraph 120, Erodex Ltd.). Before placing it inside the SPS chamber, the cold pre-pressing

technique (described in subsection 3.5.1) is used to assemble the punches appropriately. A carbon felt was used to wrap die-set to provide better thermal insulation during SPS process. After switching on the electrical supply and the air extraction, compressed air and argon gas (pressure of 3 bar) was supplied to the equipment for purging the furnace chamber during operations. The external chiller which was filled with 100 L of type-3 Deionised water having conductivity between 40-100 μS cm^{-1} on was turned on and used as the primary refrigeration system.

Subsequently, the loaded die set is placed into the furnace chamber (Fig 3.10). A 2 KN (displayed on the process visualisation screen) contact force is applied manually by the movement of the bottom piston. To make sure that the alignment between die-set punches and graphite conical holder is straight and placed set-up fitted tightly inside the chamber. The chamber is locked using the control panel, and internal pressure is reduced to 100 mbar to achieve an intermediate vacuum level. The machine is operated by a sintering program, which controls consolidation conditions including pressure, heating rate, dwell time, and cooling rate. During the sintering process, when the electric current passes through the die, punches, and samples, Type-K thermocouples are used to monitor the low temperature inside the chamber (Fig 3.8). The temperatures above 250^0C are measured using the pyrometer located at the top part of the chamber. The SPS process was performed at different sintering temperatures in a vacuum for 30 minutes at a heating rate of 100°C /min[221] and a cooling rate of 50°C/min.

- Sintering cycles

Fe-Cr-Ti-Al powder samples were consolidated at different sintering temperatures from 700^0C to 1000^0C. The sintering program was planned based on previous studies on Fe-Cr alloys[221]. All programs were planned as a sequence of four segments - pressing, heating combined with pressing, dwell time, and cooling. Fig 3.11 displays an example of typical sintering parameters recorded during the consolidation process for the Fe-Cr-Ti-Al sample at a sintering temperature of 1000^0C.

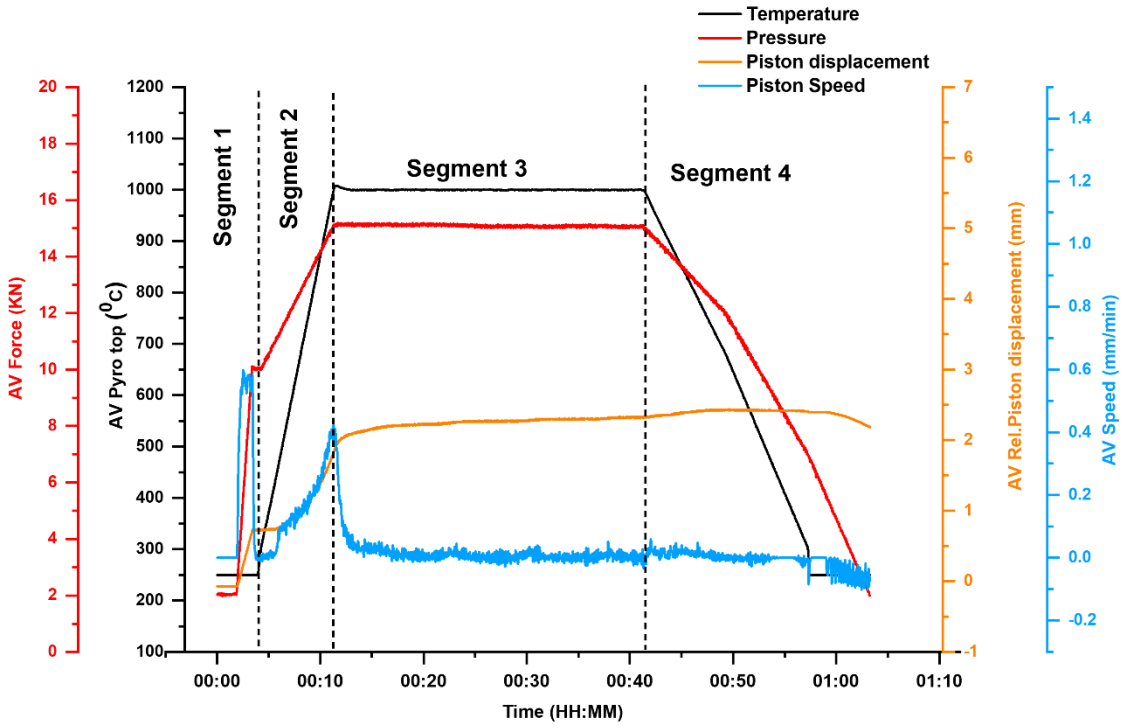

Figure 3. 11 Sintering parameters used for fabricating Fe-Cr-Ti-Al sample at 1000^0C

During segment 1 (pressing), the applied force increases from 2 KN (contact force) to 10 KN (red curve) within 4 minutes. In response to an increase in force, the piston displacement (orange curve) and speed (blue curve) suddenly increased. In segment 2, the pulsating current sequence of 10-5-12-2 (ON time-OFF time-number of pulses -extra pause) was applied, and a temperature of 1000^0C has reached after 11 minutes and 30 seconds. This segment also allows a fast increase in applied force (in uniaxial direction) to 15 KN, resulting in a pressure (P) of 48MPa (P=F/A, where F is applied force and A is the area of surface) across the sample diameter. Upon increasing the temperature, piston displacement increased from 0.7 to 2mm (segment 2), and the piston speed curve demonstrated a significant rise. In segment 3 (dwell stage), the sample was kept at a fixed temperature (1000^0C) and a static pressure of 48MPa for 30 minutes. Within this isothermal segment, a small rise in piston displacement can be seen. The last segment allows the machine to cool down to room temperature with a cooling rate of 50°C/min and drops the applied force (15 KN) to contact force (2 KN). After completion of the sintering cycle, the die set was unloaded, and the consolidated disc was obtained.

3.6 Powder and bulk sample Characterisation

This section presents the details of characterization techniques employed throughout this project to identify phase structure, determine the bulk density and measure the thermoelectric properties of samples.

3.6.1 X-ray diffraction

This technique is employed in this project to analyse the crystalline structure of the blended, milled powder sample and observe the impact of annealing and Spark plasma sintering (SPS) temperatures on the bulk sample.

X-ray diffraction (XRD) is a non-destructive technique based on Bragg's law and a useful method for identifying the crystalline structure and atomic spacing. It does not provide any chemical compositional analysis for scanned samples. In general, to generate X-rays firstly, the filament elements are heated up, which emit electrons through thermionic emission. Then these emitted electrons are accelerated towards a metal target, which is called the anode. The target is usually made up of Copper (Cu). When the accelerated electrons interact with the target which have sufficient energy to eject the inner orbital electrons of Cu. After the ejection of an electron from the inner shell, the atom is left with a vacant energy level. To fill this vacancy the transition of an electron from higher energy state to lower energy state will occur. This electronic transition generates the emission of X-ray photons. Once the X-rays are produced, they are collimated and incident on the sample.

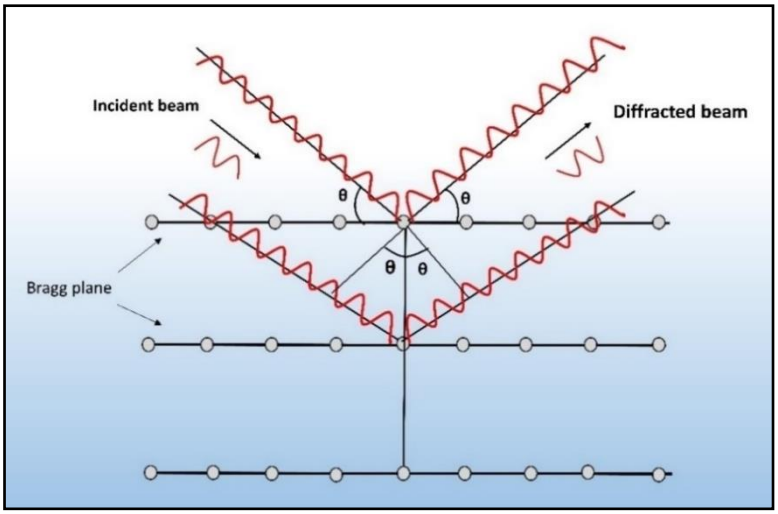

Figure 3. 12 Schematic diagram of the X-ray diffraction on the crystal lattice

According to Laue, when X-rays are incident on the atoms of single crystal sample (consists of a series of parallel crystallographic planes spaced apart by a distance d) then atomic electrons diffract a parallel monochromatic X-ray beam which provides a series of diffracted beams (Fig 3.12). The intensity and direction of the diffracted beams depend on the lattice structure and chemical composition of the sample. Therefore, when a monochromatic X-ray beam having wavelength (λ_b) is incident on the sample at an angle θ, X-rays diffracted in different directions with variable intensities due to reflections from successive planes, differing by a completed number (n) of λ_b. This diffracted pattern follows the Bragg equation, $n\lambda_b = 2d\sin\theta$, where n is an integer number, and d is the interplanar atomic spacing. The intensity of diffracted rays as the function of angular positions is called diffractogram, a unique fingerprint for each crystal or mineral phase.

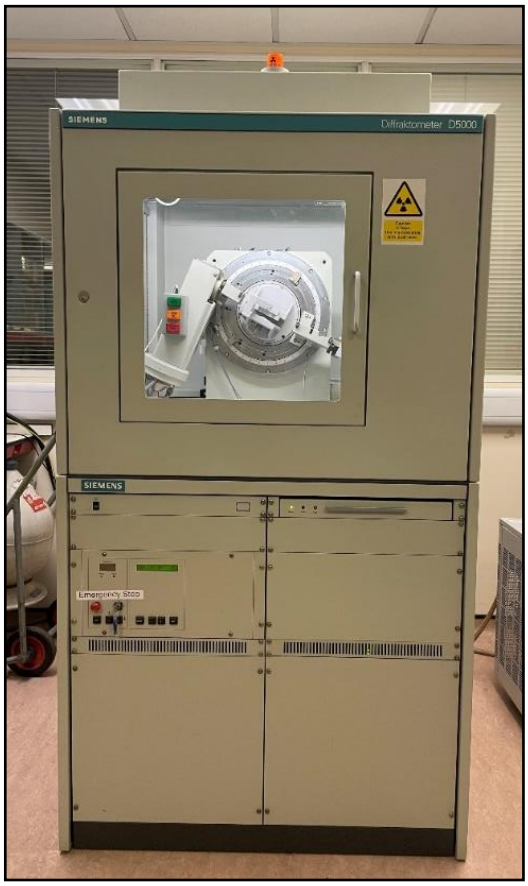

Figure 3. 13 Photograph of Siemens Diffractometer D5000 apparatus

The XRD facility used in this study is a Siemens Diffractometer D5000 (Fig 3.13), employed for determining the crystal structure of the mixed and milled powders, and bulk samples. The X-rays (K_α radiation, the wavelength of 1.54 Å) were generated using Cu (Copper) target by operating the equipment at 20KV and 5mA. The samples are scanned between the 30-90^0 range over the 2θ angle through a 0.02 step increment.

Phase Identification of the tested samples is performed by using High Score Plus software. The crystallographic phases are identified by comparing the obtained XRD spectra with the software data source based on the ICDD (International centre for diffraction data) and COD (Crystallography Open database). After comparison, the software produces a new plot that consists of the original measured XRD spectra with the reference patterns corresponding to the measured spectra. The software was validated by scanning the titanium (Ti) powder sample (purchased from Goodfellow Cambridge Ltd, UK.). Fig 3.14 shows the XRD pattern of the scanned Ti sample with a database file of Ti (JCPDS/ICDD:00-044-1294) produced by the software, indicating the capability of the software for phase analysis of XRD patterns.

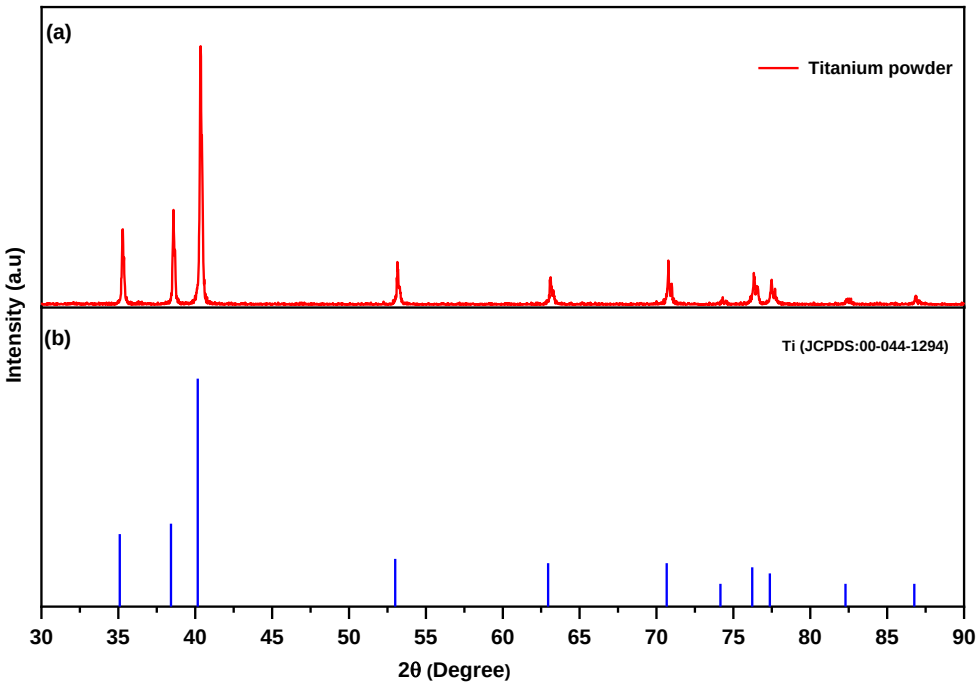

Figure 3. 14 XRD pattern of Ti powder compared with the reference from the database

The crystalline size of a sample can be estimated from its XRD profile by inspecting the line broadening of the XRD peak at half its maximum intensity, referred to as the full width at half maximum (FWHM). The crystalline size can be calculated based on the Scherrer equation[222]:

$$D = \frac{0.94\lambda}{\beta cos\theta} \tag{3.1}$$

Where, D is the mean size of the grain, λ is the X-ray wavelength, β is the line broadening at half of the maximum intensity (FWHM), and θ is the Bragg angle. The FWHM width is a useful parameter to predict crystalline size. The larger FWHM width indicates smaller crystalline sizes, while the smaller FWHM width suggests large grain sizes.

3.6.2 Density measurements

Density is a physical property that represents how tightly a substance's molecules/atoms are packed into space. The apparent density method provides a straightforward way to determine bulk density. It refers to the ratio of the mass and volume of the sample (volume calculated by considering the absence of internal voids and open pores). It can be determined by weighing the mass of the sample and measuring the sample dimensions to calculate the volume. Mathematically, it can be expressed as the mass (M) of a given sample by the outer volume (V_{app} - the external volume of the sample) occupied:

$$\rho_{app} = \frac{M}{V_{app}} \tag{3.2}$$

The weight of BM-CP samples was obtained by using 5-digit Precisa balance 40SM-200A. The volume was calculated by measuring the dimensions of the disc shape sample with the help of RS PRO 0.01mm digital calliper. To minimise the error, for every sample, three measurements of dimensions were taken, and the mean value of thickness and diameter was calculated.

Archimedes density measurement method can provide precise bulk density calculations for irregular/ regular shape samples. It is based on Archimedes Principle, which states that the upward force on the object is equal to the weight of the fluid that the object displaces. Based on equation (3.3), this method allows us to determine the density of the sample in terms of the mass of sample (M) in air, the mass of the sample (M_{app}) in immersed liquid, and the density of the liquid (ρ_{fluid}), without measuring the volume of sample. The following mathematical equation based on the Archimedes Principle was used to calculate the density of the sample:

$$\rho_{Arch} = \frac{M}{M - M_{app}} \rho_{fluid} \tag{3.3}$$

where, ρ_{fluid} is the density of fluid and ρ_{Arch} is the density of the sample. M is the mass of the sample in air and M_{app} is the mass of the sample in liquid respectively.

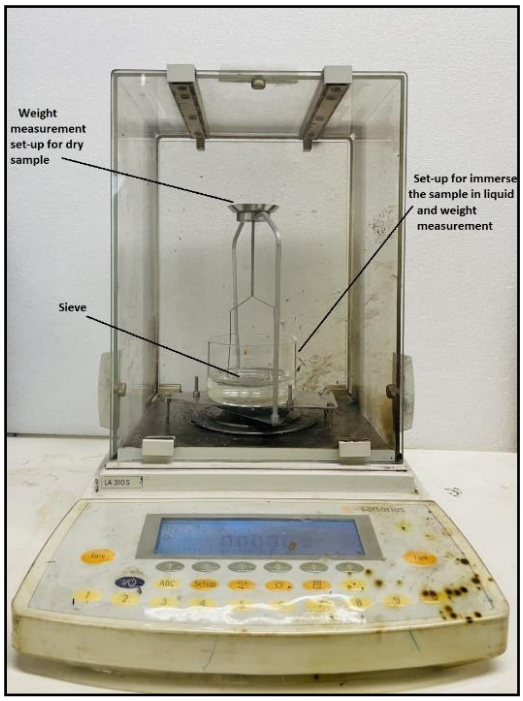

Figure 3. 15 Photograph of an Archimedes density measurement

Fig 3.15 illustrates the photograph of Sartorius YDK 01 kit used for density measurement. This technique involves the immersion of the sample in the liquid container placed on an electronic balance and helps to obtain the material density based on the characteristics of the liquid (water). The volume is determined in terms of change in weight divided by the density of liquid. For each sample, three density measurements were taken, and the mean value was determined. To take each measurement, firstly, the weight of the sample was measured in air. The sample was then immersed in water and weighted. Before performing another measurement, this sample was taken out and allowed to dry for 5-6 hours in the furnace at 80^0C. After that, the second density measurement was taken adopting a similar procedure. This process was repeated for the third measurement as well.

Archimedes method helps to determine the density of dense bulk samples accurately. However, this is not suitable for determining the density of porous samples because when porous samples are placed inside the liquid, their pores can be filled with liquid, and their density will be overestimated. This method was used to measure the density of bulk samples fabricated based on Spark Plasma Sintering. This consolidation technique (SPS) has the potential to produce Fe-Al-based dense bulk samples with the existence of low porosity levels [221, 223]. Considering this, Archimedes principle-based technique could be beneficial to precisely assess the effect of SPS temperatures on the relative density of the sintered sample.

The bulk density measurements using Archimedes method are complicated and time-consuming because it involves steps such as immersion of sample in water and drying the sample for every measurement. However, the Apparent density method is a straightforward and fast method to determine the bulk density. Keeping in consideration these advantages, this method was adopted to assess the density of consolidated bulk samples produced using the cold-press method. Because it can provide a fast assessment of the relation between the sample density and pressing pressure (Section 4.4).

3.6.3 Scanning Electron Microscope (SEM)

SEM technique could be useful to investigate the microstructure of fabricated samples. The SEM images of the annealed samples presented in this work were obtained by Dr Daniel Zabek (Research Fellow at Cardiff University) using a Focused Ion Beam- Zeiss 1540 XB microscope. SEM usually consists of an electron gun which produces electron beams. This generated beam is focused using electromagnetic lenses such as condenser and objective lens (as shown in Fig 3.16[224]). The SEM equipment generally operates under a high vacuum to avoid interference from atmospheric gases/molecules with the electron beam and other disturbances that can affect the scattering of electrons. In this technique, when electrons are accelerated by an electric field and incident on the surface of the sample, then the sample generates different signals such as characteristic X-rays, secondary electrons, back-scattered electrons, and transmitted electrons. All generated multiple signals can be detected and provide information about surface morphology, and chemical composition [225].

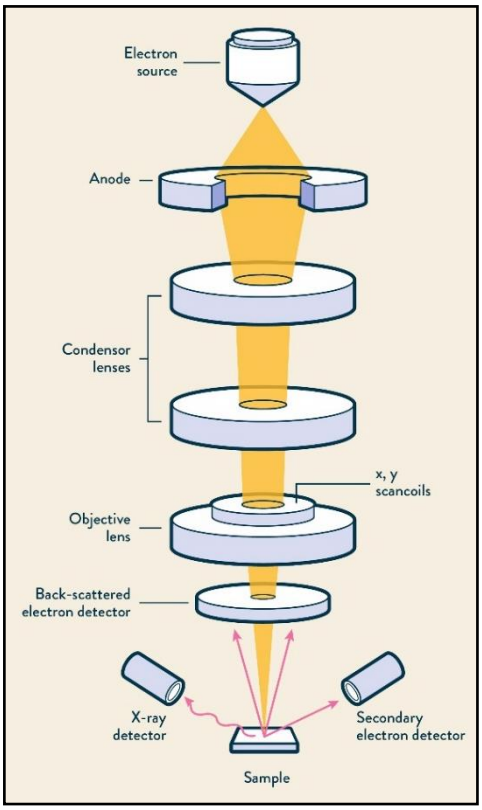

Figure 3. 16 Schematic with main components in SEM unit from electron emission to detection Ref [212]

EDX is a non-destructive analytical technique. It is helpful for the identification of the elemental composition of materials, allows for qualitative and semi-quantitative analysis, and provides information about the spatial distribution of elements. EDX analysis of Fe-Cr-Ti-Al bulk sample sintered sample was performed at the Institute of Carbon Science and Technology (INCAR), Spain, with the support of co-supervisor Dr Victoria García Rocha. Chemical composition analysis was conducted by using Quanta FEG 650 SEM equipped with an energy-dispersive X-ray (EDX) spectrometer.

3.6.4 Hot probe

A hot probe technique provides the easiest and quickest way to measure the Seebeck coefficient at room temperature. The hot-probe apparatus used for this study is homemade equipment shown schematically in Fig 3.17 (a). It consists of the copper block, which acts as a cold side and the copper-hot probe, which act as a hot side. The differential thermocouple is used to measure the temperature gradient. It consists of two Copper (Cu) wires connected by a length of constantan wire. One end of a constantan wire is connected to the hot probe, and the other end is attached to a copper block by drilling holes near their surfaces.

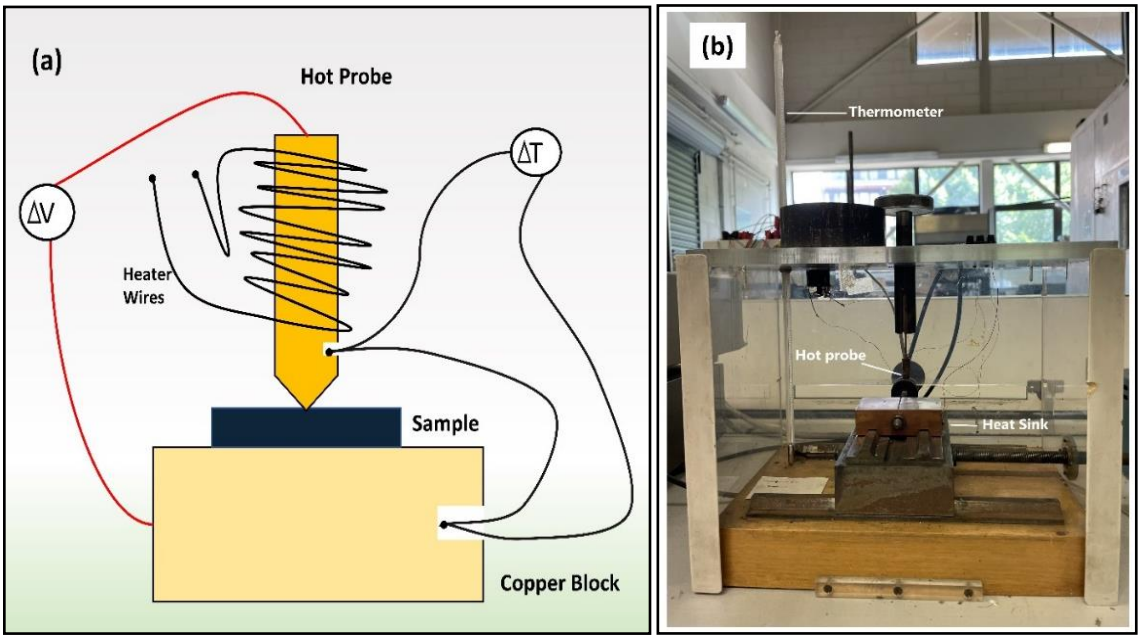

Figure 3. 17 (a) Schematic diagram of the hot probe (b) Photograph of the hot probe apparatus

To perform the measurements, the hot probe is heated above room temperature by turning on the heater coil. After that, the sample is placed between the hot probe (hot side) and the copper block (cold side). The established temperature difference (ΔT) across the sample is measured using a differential thermocouple (i.e., based on copper-constantan thermocouple). A Seebeck voltage (ΔV) is then generated, which was measured by Cu wires connected to the hot probe and the copper block. The value of the Seebeck coefficient (α) can be obtained using the following equation:

$$\alpha = \frac{\Delta V}{\Delta T} \tag{3.4}$$

where the contribution to the Seebeck coefficient from the copper wires is neglected since it is very small (1.8 μV/K).

Table 3. 1 Measured Seebeck coefficient at temperature 290Kand relative error for the reference sample

Sample	Reference value(μV/K)	α (μV/K) ± St.dev.	Relative error (%)
n-type Bi_2Te_3 SRM	-231.36	-217±2.71	6.1

The accuracy of the apparatus is tested using the Bi_2Te_3 standard reference material (SRM) from NIST (Reference 3451)[226]. The measured Seebeck value (α) with standard deviation and relative error for the reference sample is listed in Table 3.1. The standard deviation was obtained from the set of seven measurements (data presented in Appendix-B). These measurements were made at room temperature (290K). However, the data for the reference sample was not available for the corresponding temperature. Due to this, the measured data were compared with the data point closest to 290K in the literature. In order to calculate the relative error, the Seebeck coefficient for the reference sample of -231.36μV/K at 300 K was selected, which is the closest available data point. The measured data display a low standard deviation, and the relative error value indicates that this technique provides good accuracy and repeatability of the measurements for characterising thermoelectric materials, where the Seebeck coefficients are relatively larger.

3.6.5 Multifunctional probe technique

The electrical resistivity of the sample at room temperature is measured using the homemade multifunctional probe apparatus[227]. This equipment allows us to measure the Seebeck coefficient and electrical resistivity at room temperature within 20 seconds [227]. It is designed based on a Van der Pauw set-up where four multifunctional probes contact at the edges of the sample. All multifunctional probes are made up of a Copper tube (30mm long and 1.6mm diameter) welded with a constantan wire at the tip to form a thermocouple. Out of four probes, one probe was designed along with a heater coil inserted inside the Copper tube as shown in Fig 3.18 (a), which can heat up to a few degrees above room temperature for Seebeck coefficient measurements. The copper wires of probes are utilised as electrical contacts. A triple-channel DC power supply (Keithley 2230-30-1) was utilised to provide necessary currents to probes with a single power source. And a Keithley 2000 multimeter was used to measure voltage outputs and resistance. For the quick switching of the current outputs and voltage values, a USB 16-channel relay module (Denkovi DAE-CB/Ro16/Di4-USB) with remote control via USB was used. The equipment and measurements are controlled by LabView.

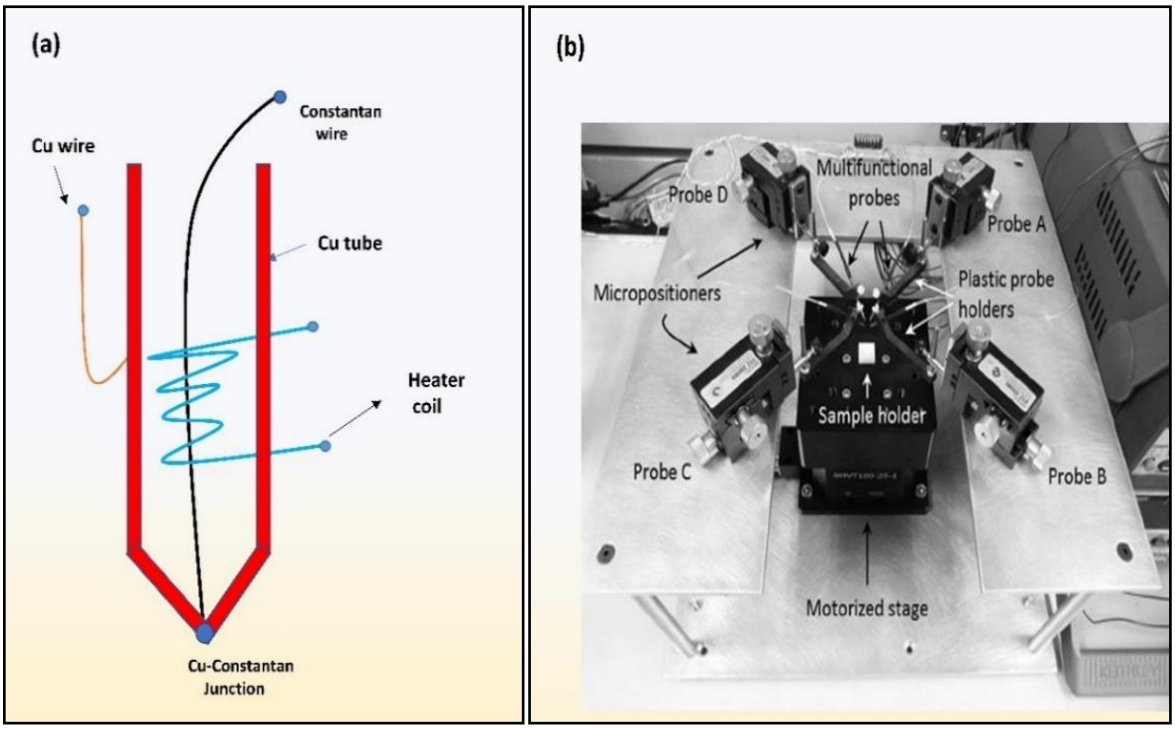

Figure 3. 18 (a) Sketch of a multifunctional probe and (b) Top view of the multifunctional probe equipment

The top view of the multifunctional probe equipment is shown in Fig 3.18(b). Probe A was designed for Seebeck coefficient measurements as described above. The current was passed through the heater coil of probe A to achieve a temperature ~3K higher than probe D. While Probe D is remained at a temperature close to room temperature. When the temperature difference (ΔT) between Probe A and D is established, then the open-circuit voltage (ΔV) between probe B and C was measured using a multimeter[227]. The Seebeck coefficient (α) of the sample was then calculated based on the following equation:

$$\alpha = \frac{\Delta V}{\Delta T} + \alpha_{Cu} \tag{3.5}$$

Where α_{cu} is the absolute Seebeck coefficient of Cu. The determined Seebeck coefficient for Cu was equal to +3.2μV/K[227].

The electrical resistivity is measured using probes A, B, C and D by following the Van der Pau method. Out of four probes, when constant DC current is applied between two probes then remaining two probes were used to measure the induced voltage difference. For example, a current I_{AB} entered the sample from probe A and leave from probe B, producing a voltage ΔV_{CD} between probe C and D. Thus, using the resistance formula, the calculated resistance will be equal to $R_{AB,CD}=\Delta V_{CD}/I_{AB}$. On the other hand, $R_{BA,\ CD}=\Delta V_{DC}/I_{BA}$ can be measured by changing the current direction from probe B to A. The resistance $R_{CD,AB}$ and $R_{DC,BA}$ can be measured by applying a current

across probe C and probe D, and probes A and B can function to measure the voltage difference. These resistances are used to calculated R_A = ($R_{AB,CD}$+ $R_{BA,DC}$ + $R_{CD,AB}$+ $R_{DC,BA}$)/4, R_B = ($R_{BC,AD}$+$R_{CB,DA}$+$R_{AD,BC}$+$R_{DA,CB}$)/4. Both R_A and R_B are required to obtain the sheet resistance R_s by:

$$e^{\left(\frac{-\Pi R_A}{R_S}\right)} + e^{\left(\frac{-\Pi R_B}{R_S}\right)} = 1 \quad (3.6)$$

Equation (3.2) can only be solved analytically when R_A=R_B. Finally, the electrical resistivity (ρ) is given as:

$$\rho = R_S d \quad (3.7)$$

where d is the sample thickness.

This equipment was calibrated using stainless steel sample (NBS, Ref. 1461) for electrical resistivity measurements. Table 3.2 shows the measured resistivity value for the reference sample with the standard deviation and relative error determined from a set of eight measurements (Appendix-C). The low standard deviation and relative error value suggest that this technique provides good accuracy and repeatability for electrical resistivity measurements.

Table 3. 2 Measured resistivity and relative error for the reference sample

Sample	**Reference ρ (10^{-5} x Ωcm)**	**ρ (10^{-5} x Ωcm) ± St.dev.**	**Relative error (%)**
Stainless steel sample	8.1	7.8±0.4	3.4

3.6.6 ZEM-3 and NETZSCH LFA

The temperature-dependent thermoelectric properties of SPS sintered samples were measured using ZEM-3 for the Seebeck coefficient and electrical resistivity and NETZSCH laser flash for thermal conductivity. The measurements were carried out by Dr Matthew Button at Swansea University, Wales.

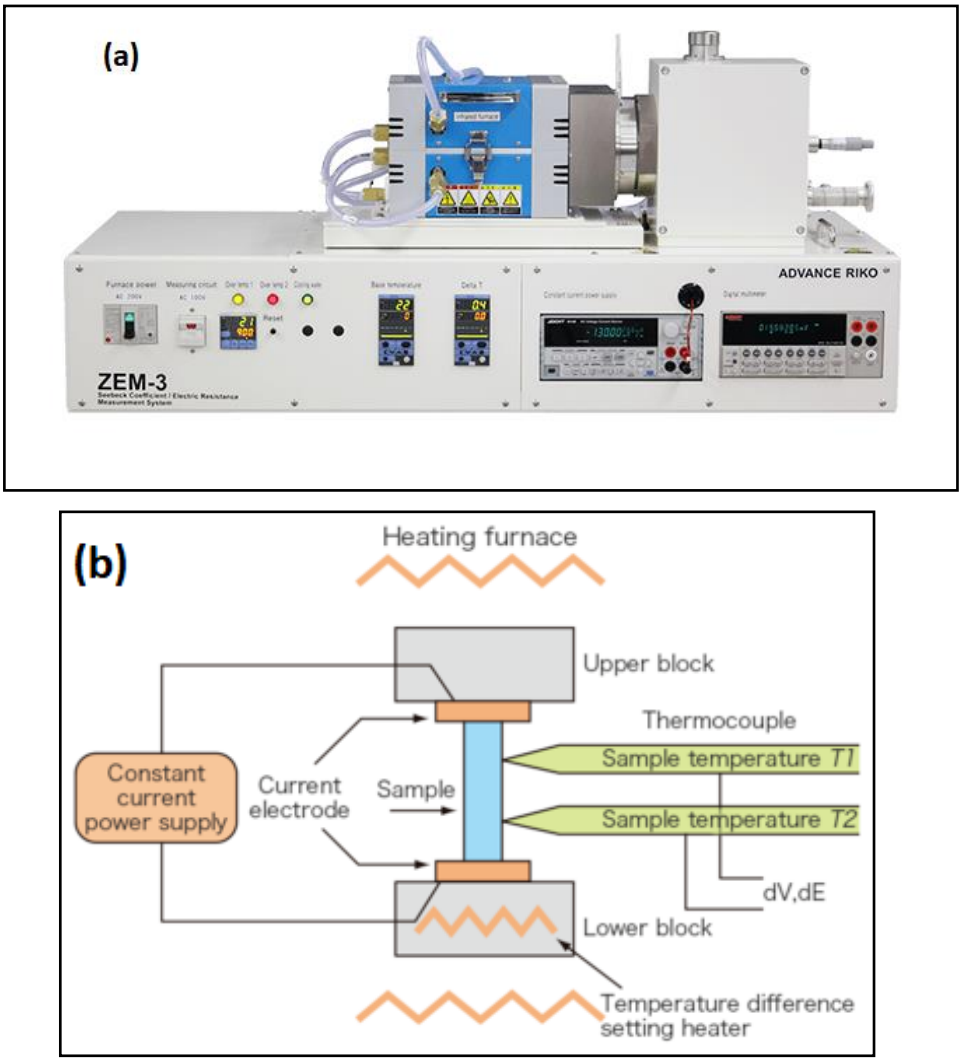

Figure 3. 19 (a) Photograph of ZEM apparatus (b) Schematic of Seebeck coefficient and Electrical resistivity measurements [Ref [216]]

The schematic of ZEM-3-based measurements of Seebeck coefficient and electrical resistivity is depicted in Fig 3.19 (b)[228]. This technique allows to measure of both parameters simultaneously. To perform the measurements, the bar-shaped sample is placed in a vertical position between the upper and lower blocks in the furnace of ZEM. The sample is heated and held at a specified temperature under Helium gas. To measure the Seebeck coefficient, the sample is heated by the heater in the lower block to create a temperature gradient. The upper and lower temperatures (T1 and T2) are measured using thermocouples. And the generated thermal electromotive force (ΔE) between the same wires on one side of the thermocouple (as shown in Fig 3.19 (b)). The Seebeck coefficient is obtained based on the slope of ΔE versus temperature-difference (T2-T1) curve. Electrical resistivity (ρ) was measured using the dc four-terminal method. A constant current (I) is passed through the sample and the voltage difference (V) between same

wires of the thermocouples are measured with subtraction of the thermo-electromotive force between leads. Based on the following equation, the electrical resistivity was calculated:

$$\rho = \frac{V}{I}\frac{A}{S} \tag{3.8}$$

Where A is the cross-section of sample and S is the distance between the thermocouples.

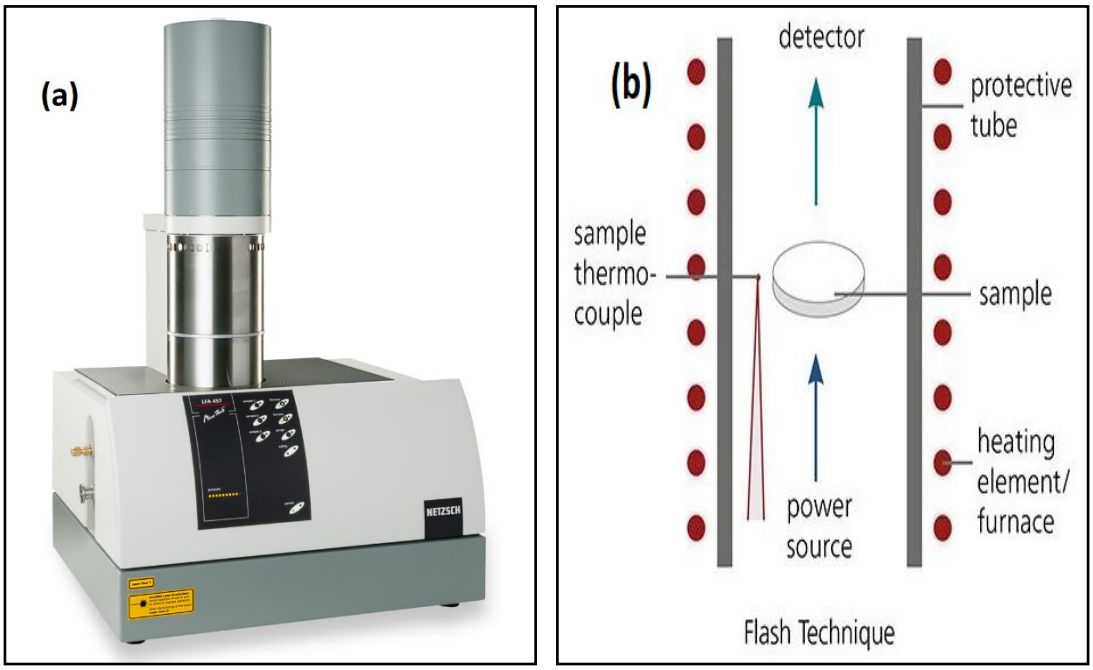

Figure 3. 20 (a) Photograph of NETZSCH laser Flash (b) Principle of Laser Flash Analysis method [Ref [217]]

The thermal conductivity (k) of Fe-Cr-Ti-Al sample is calculated based on the measurement of thermal diffusivity (λ), specific heat capacity (C_p) and density of sample (ρ_{SPS}). The following equation was used to determine it:

$$k = \lambda C_P \rho_{SPS} \tag{3.9}$$

In equation (3.9), to determine the thermal conductivity, the density of the sintered sample was obtained by using Archimedes method.

Fig 3.20 (a) shows the photograph of NETZSCH Laser Flash Apparatus LFA 457 Micro Flash[229]. It allows determining the thermal diffusivity and specific heat. This equipment measures the thermal diffusivity based on the principle that when the bottom side of sample is illuminated by a high-intensity and short-duration laser flash pulse, it causes heat absorption which increases the temperature of the sample. This heat starts diffusing across the cross-plane

of the sample and starts rising the temperature on the top side of the sample. The temperature on the top side is measured continuously with the help of a thermocouple or an infra-red sensor[230]. The observed transient changes in the temperature can be used to calculate the thermal diffusivity based on the Parker expression[179]:

$$\lambda = 0.13\frac{W^2}{t_{50}} \tag{3.10}$$

Where W is the thickness of the sample and t_{50} is the half-rise time (time for the rear face temperature to reach 50 % of its peak value).

Generally, the specific heat of a material is defined as the amount of heat required per unit mass to raise its temperature by 1^0C at a constant pressure. The specific heat of the sample can be determined during diffusivity measurements by comparing the temperature raise of the sample to the reference sample (with a known specific heat value). The measured change in temperature monitored by another IR detector is used to estimate the heat value. When it is required to measure the Specific heat of the sample, then the same estimated heat value for the reference sample is used to calculate it.

3.6.7 Vibrating Sample Magnetometer (VSM)

The magnetic response of BM-CP annealed (at 700^0C) bulk samples was measured by Dr Daniel Zabek using the Vibrating Sample Magnetometer (Model 7410) technique. This equipment measures the magnetic behaviour of the sample based on the Faraday Law of Induction. When the sample is placed in a vibrating perpendicularly uniform magnetic field, the electric voltage induced in the pick-up coils is due to a change in the magnetic field. The magnetic moment of the sample is proportional to the electric voltage induced. A hysteresis curve was obtained for magnetic fields ranging from -2T to 2T at room temperature, and the measurements are presented in Appendix D.

Chapter 4: Preparation and thermoelectric properties of Fe-Ti-Al alloys

4.1 Introduction

In 2016, García-Cañadas et al.[22] discovered that Fe-Ti-Al-based alloys could be considered as promising thermoelectric materials near room temperature. Using the laser melting technique (LMT), they fabricated a series of Fe-Ti-Al alloys and attempted to identify the potential thermoelectric compositions. They concluded that $Fe_{11}Ti_3Al_6$ (molar notation) composition could be considered a potential p-type thermoelectric material, whereas $Fe_3Ti_4Al_1$ (molar notation) composition can be seen as an n-type promising thermoelectric candidate. Currently, a wide variety of methods for the fabrication of thermoelectric materials are available, such as the vacuum-sealed melting method and cold-pressing followed by the annealing route[231], mechanical alloying-hot pressing route[232, 233] and sol-gel method followed by sintering[234]. Mechanical alloying (MA) is a low-cost fabrication technique that provides the easiest way to control the composition and produces fine powders in a short period [167, 235]. This method can also provide a convenient route for investigating the effect of element substitution on the thermoelectric properties of Fe-Ti-Al alloys. The MA technique is a well-established technique and has been adopted in the literature to study the various types of thermoelectric materials such as Co-Sb, Bi-Sb and Fe-V-Al alloys[166, 167, 236].

This chapter aims to prepare and identify the optimal preparation conditions for p-type $Fe_{11}Ti_3Al_6$ and n-type $Fe_3Ti_4Al_1$ samples via the Ball milling (BM)-Cold press (CP) route. BM-CP fabrication routes have never been reported in the literature to prepare Fe-Ti-Al-based bulk alloys. The optimal conditions required to prepare Fe-Ti-Al alloys via BM and CP, followed by an annealing route, are presented in this chapter for the first time.

The experimental procedure for sample preparation is described in the following section. The identification of the optimal milling timing parameter is represented in section 4.3, while section 4.4 describes the procedure adopted to determine the optimal cold-pressing pressure required to consolidate the samples. Subsequent sections examine the thermoelectric properties of both non-annealed and annealed bulk samples.

4.2 Synthesis of $Fe_{11}Ti_3Al_6$ by mechanical alloying-cold press route

The detailed procedure adopted for the fabrication of $Fe_{11}Ti_3Al_6$ bulk samples via mechanical alloying-cold press route, including the method used to identify phase structure and thermoelectric characterisation is presented here.

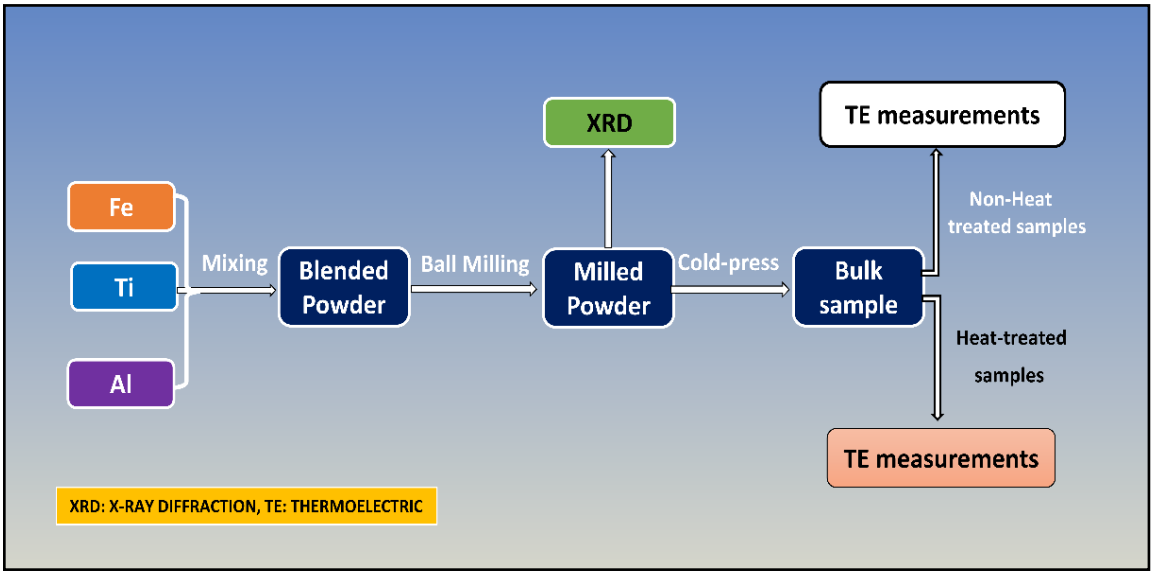

Figure 4. 1 A schematic figure representing the sample preparation procedure

Fig 4.1 illustrates the schematic representation of the procedure adopted to fabricate bulk samples. For the preparation of $Fe_{11}Ti_3Al_6$ composition, the stoichiometric amounts of Iron (Fe-66.78 wt.%), Titanium (Ti-15.62 wt.%) and Aluminium (Al-17.6 wt.%) were mixed in a glove box under a nitrogen environment. 3.42 grams amount of the blended powder was loaded under a nitrogen atmosphere in a glove box into an 80mL stainless-steel bowl with stainless steel balls (10mm) as milling media in a ball-to-powder ratio (BPR) 35:1. Then, the milling media was placed into the Planetary ball mill (Pulverisette 5/4). The mechanical alloying (MA) was carried out at a speed of 300 RPM with a 10-minute rest cycle after every 10 minutes of milling.

After the completion of milling, the milling media was unloaded to obtain the milled powder. A small amount of milled powder was used to perform XRD characterisation and phase structure analysis. Furthermore, around a 2.5-gram amount of the powder was used to produce the disc shape samples with a diameter of 6.35mm via using a cold-press technique. The bulk samples were annealed using a tubular furnace. The detailed annealing procedure is discussed in section 4.6. The thermoelectric characterisation of non-heat-treated and heat-treated bulk samples was performed to assess the thermoelectric potential of Fe-Ti-Al alloys. The details of planetary ball mill, cold-press station, tubular furnace, and thermoelectric properties characterization equipment are described in Chapter 3.

4.3 Optimisation of ball milling for p-type sample

This section discusses the optimisation of BM (ball milling) time to prepare $Fe_{11}Ti_3Al_6$ powder samples. To identify the optimal milling time condition, the mechanical alloying of blended powder was carried out for 4hrs to 20hrs using planetary ball mill. The XRD measurements and phase analysis of blended/milled powders were performed to observe the impact of milling time on the phase structure.

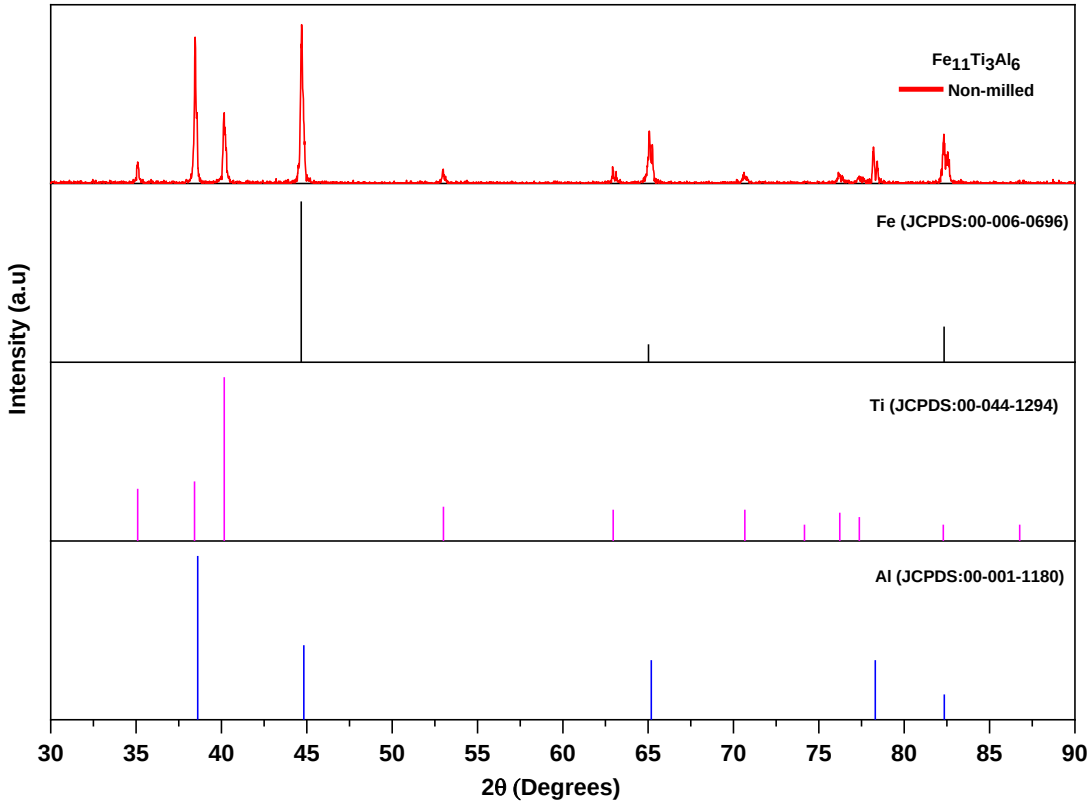

Figure 4. 2 XRD pattern of $Fe_{11}Ti_3Al_6$ sample non-milled powder

Fig 4.2 represents the XRD spectra of the $Fe_{11}Ti_3Al_6$ non-milled (blended) powder sample. The blended powder shows sharp diffraction peaks of Fe, Ti and Al elements. The diffraction peak position and intensities of non-milled powder display good agreement with database files of Fe (JCPDS/ICDD:00-006-0696), Ti (JCPDS/ICDD:00-044-1294) and Al (JCPDS/ICDD:00-001-1180) elements. This analysis confirms that Fe, Ti and Al elements are present in the blended powder sample.

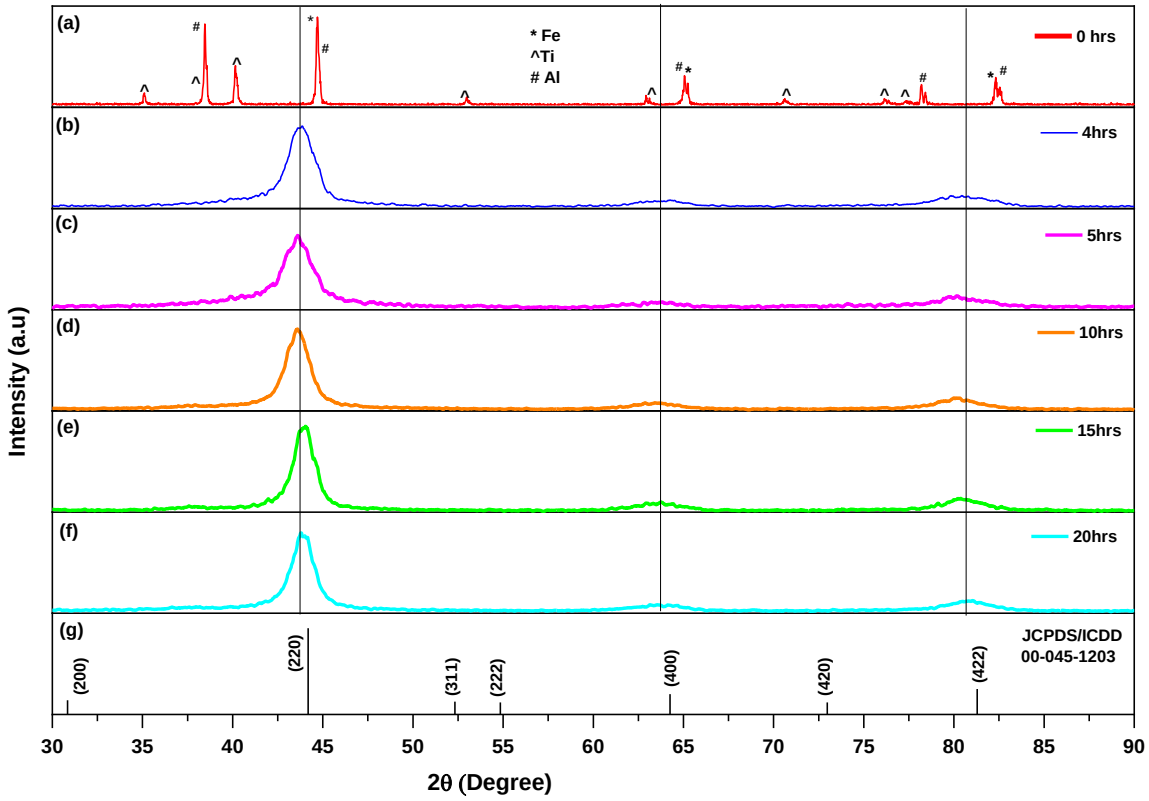

Figure 4. 3 XRD patterns of $Fe_{11}Ti_3Al_6$ milled powder at different milling time (0-20hrs)

Fig 4.3 illustrates the XRD patterns of the $Fe_{11}Ti_3Al_6$ sample milled for different milling periods. The XRD pattern of the 4hrs-BM sample (Fig 4.3. (b)) indicates that the initial powder phase structure has completely transformed into a new phase structure after the milling process. The 4 hrs-BM powder sample shows three diffraction peaks at diffraction angles 43.86^0, 63.7^0 and 80.5^0. The main diffraction peak for the 4 hrs-BM sample is detected around 43.86^0, which is located at lower diffraction angles than Fe and Al peaks (Fig 4.3 a). It occurs due to the dissolution of Al and Ti atoms in the Fe lattice, which results in the formation of Fe(Ti, Al) solid solution with bcc structure[237, 238]. The peak position and intensities of 4hrs-BM powder sample show close agreement with XRD pattern of Fe_3Al intermetallic alloy (JCPDS/ICDD:00-045-1203), which has been described in section 2.5. However, it is unlikely to obtain the $(FeTi)_3Al$ intermetallic phase through mechanical alloying alone[237, 238]. Previous studies have demonstrated that the Fe(Ti,Al) solid solution transforms into the $(FeTi)_3Al$ intermetallic compound upon heating in the temperature range of 350-500°C [237, 238].

To investigate the possibility of the formation of a new phase structure with increasing milling time, mechanical alloying was further conducted for 5hrs to 20hrs. Fig 4.3 (c-f) shows the XRD pattern of the 5hrs-20hrs milled sample. XRD measurements confirm that no new phase is formed, but the pattern slightly shifted towards higher diffraction angles with increasing milling period.

For samples milled for an extended period of 15-20 hours, the peak positions show good agreement with the Fe_3Al alloy ($D0_3$ order). This finding is consistent with previous studies on Fe-Ti-Al [237] and Fe-Al[239]. However, the absence of superlattice diffraction peaks indicates the presence of a disordered crystalline phase [237]. All milled sample exhibits the phase structure close to the well-known Fe_3Al ($Fe_{75}Al_{25}$ (at%)) alloy. The observed XRD pattern suggests that titanium and aluminium have been successfully incorporated into the Fe_3Al alloy structure.

There is no major difference between the XRD pattern of 4hrs and 5hrs milled samples can be observed. Therefore, 4hrs BM duration can be considered the optimal BM timing for the fabrication of $Fe_{11}Ti_3Al_6$ milled powder sample. However, at this stage, it is impossible to predict which milled sample will display the best thermoelectric properties. Because for that, it will be necessary to fabricate bulk samples from all milled powders, and then thermoelectric screening can assist to identify the most promising bulk sample.

4.4 Fabrication of bulk sample and optimisation of the cold pressing condition

This section describes the compaction of milled powders to form bulk (disc-shape) samples. For this purpose, the cold pressing (CP) technique was adopted, and details are described in Chapter 3. Fig 4.4 represents the schematic fabrication process of the bulk samples based on the cold press method. The optimisation of the pressing condition is required to achieve the most suitable compactness. To determine optimal cold pressing conditions, all milled powder samples were consolidated under different pressure. The compactness of BM-CP bulk samples can be determined in terms of density measurements. The Apparent density method was used to estimate the density of bulk, which is described in Section 3.6.2.

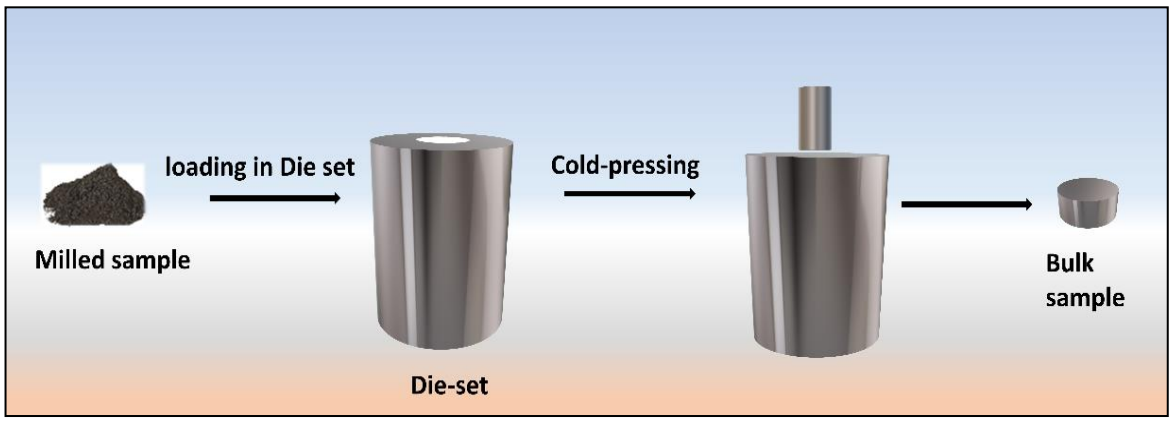

Figure 4. 4 A schematic process of fabrication of bulk samples

In order to compare the apparent density with theoretical density, the theoretical density of the $Fe_{11}Ti_3Al_6$ sample was predicted based on the following equation:

$$\rho_{theory}=\frac{nM}{a^3 N_A} \quad (4.1)$$

where n is the number of atoms per unit cell of the sample, M is the corresponding atomic mass of each element, a is the lattice constant, and N_A is the Avogadro constant (6.023×10^{-23} mol^{-1}). The lattice constant was estimated in terms of d-spacing and miller indices [240]. These parameters were obtained from the XRD data (Fig 4.3). The calculated theoretical density of the $Fe_{11}Ti_3Al_6$ sample is 6.1 g/cm^3. The relative density (ρ_{rel}) was calculated to compare apparent density (ρ_{app}) and theoretical density (ρ_{theory}), which can express as $\rho_{rel}=\left(\frac{\rho_{app}}{\rho_{theory}}\right)*100$. This parameter will help estimate how much compactness has been achieved compared to the theoretical density.

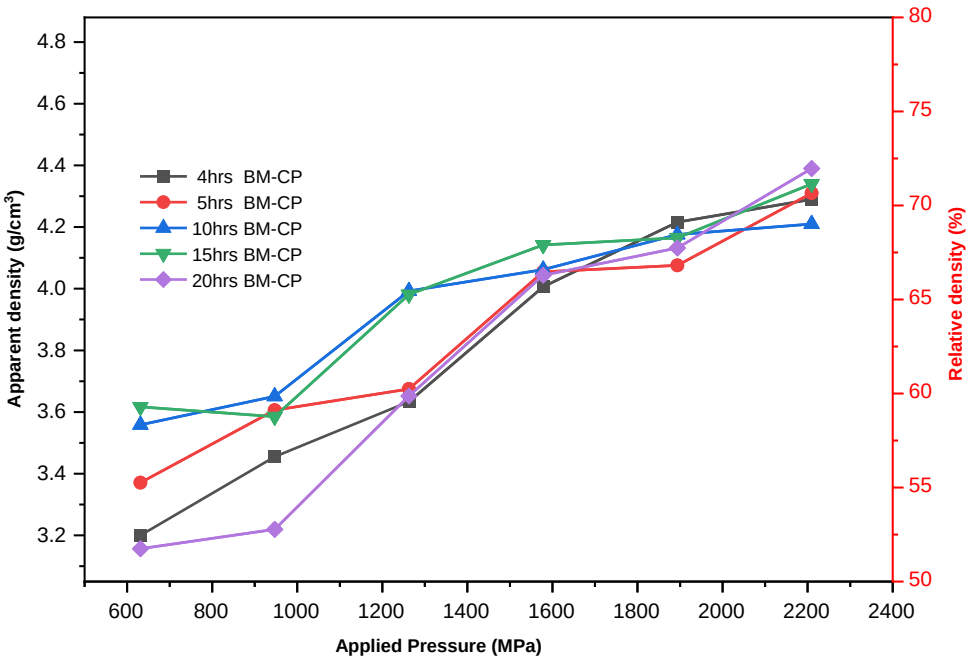

Figure 4. 5 Density of 4hrs, 5hrs, 10hrs, 15hrs and 20hrs BM-CP sample at different applied pressures

Fig 4.5 illustrates the density of 4hrs, 5hrs, 10hrs, 15hrs and 20hrs ball milled-cold press (BM-CP) bulk samples as the function of applied pressure. All bulk samples have a lower density (3-4 g/cm^3) between the 630-1580MPa range. However, the density remained almost constant above 1578Mpa. Between the 1890-2200MPa pressure range, the density of all samples lies in the range of 4.21-4.39 g/cm^3. All BM-CP samples showed the highest relative densities of approximately 71% at 2200MPa. It is evident from this analysis that 2200MPa can be considered the optimal pressure condition for the compaction of all milled powders to form disc shape samples using the cold-press technique.

4.5 Thermoelectric properties of BM-CP samples

The thermoelectric properties of $Fe_{11}Ti_3Al_6$ BM-CP bulk samples at room temperature are presented in this section. The transport characterization was performed to determine whether the BM-CP route is useful for producing a promising $Fe_{11}Ti_3Al_6$ thermoelectric bulk sample or not. The bulk samples (BM-CP) fabricated at the optimal cold-pressing condition of 2200MPa from 4hrs, 5hrs, 10hrs, 15hrs and 20hrs BM powder samples were selected for thermoelectric screening.

Table 4. 1 Measured room temperature Seebeck coefficient (α), Electrical Resistivity (ρ), and Power Factor (PF) of $Fe_{11}Ti_3Al_6$ BM-CP bulk samples

Fabrication route	**BM (hrs)**	**α (μV/K)**	**ρ (μΩm)**	**PF (10^{-7} W/mK^2)**
Ball-milling and Cold-pressing technique	4	-1.43±0.11	20.07±1.32	1.02±0.3
	5	-1.89±0.22	13.76±1.11	2.6±0.82
	10	-3.93±0.16	19.91±1.13	7.77±0.15
	15	-4.83±0.14	25.34±1.39	9.22±1.04
	20	-2.97±0.19	19.5±1.05	4.55±1.25
Laser melting technique (LMT)	-	+27 [22]	1.1 [22]	7000 [22]

Table 4.1 represents the measurements of Seebeck coefficient, electrical resistivity, and power factor (PF) values for 4hrs, 5hrs, 10 hrs, 15 hrs and 20 hrs BM-CP bulk samples.

The Seebeck coefficient of all bulk samples is negative, which suggests that all samples are n-type. The negative sign of the Seebeck coefficient indicates that the conduction is most likely occurring due to electrons. Among all the bulk samples, the 15hrs-bulk sample has attained the lowest Seebeck coefficient of -4.83±0.14μV/K. This value for BM-CP sample is quite low compared to the reported p-type sample[22]. Additionally, all BM-CP samples exhibit an opposite sign of the Seebeck coefficient than the reported p-type sample[22]. This could be attributed to the fact that $(FeTi)_3Al$ intermetallic phase is not formed during mechanical alloying, as discussed in section 4.3 and reported by previous studies on Fe-Al and Fe-Ti-Al [134, 238, 241]. However, this speculation needs further investigation in the future.

The electrical resistivity measurements (Table 4. 1) demonstrate that BM-CP samples have electrical resistivity values ranging from 13.76±1.13μΩm to 25.34±1.4μΩm. 5hrs-bulk sample attained the lowest resistivity value of 13.76±1.13μΩm, which is approximately 13 times higher than previously reported p-type Fe-Ti-Al sample [22]. It occurs due to poor connectivity between grains (Fig 4.11), which affects the mobility of carriers [242].

The power factor (PF) was calculated using the measured data of the Seebeck coefficient and electrical resistivity based on the following equation:

$$PF = \frac{\alpha^2}{\rho} \tag{4.2}$$

where α is the measured Seebeck coefficient, and ρ is the electrical resistivity.

The calculated PF (Table 4. 1) indicates that 15-hr BM-CP sample attained the highest PF value of (0.092±0.01) x10^{-5} W/mK^2. However, this value is relatively lower than the reported p-type sample[22], due to lower Seebeck coefficient and electrical conductivity of BM-CP samples.

The thermoelectric screening suggests that it is difficult to produce $Fe_{11}Ti_3Al_6$ thermoelectric bulk sample via BM-CP route, which can demonstrate the Seebeck coefficient and PF close to the reported p-type sample.

4.6 Influence of annealing temperatures on thermoelectric properties of the bulk sample

The influence of the annealing temperatures on the thermoelectric properties of $Fe_{11}Ti_3Al_6$ BM-CP bulk samples is studied. In order to conduct this investigation, similar to the above section 4.5, the 4hrs, 5hrs, 10hrs, 15hrs and 20hrs BM powders were consolidated at an optimal pressure of 2200Mpa to produce bulk samples. To carry out the annealing of the samples at different temperatures, five bulk samples were prepared from each milled powder sample. The effect of heat-treatment on thermoelectric properties was measured in terms of room temperature Seebeck coefficient, electrical resistivity, and PF.

The literature suggests that heat treatment can improve the thermoelectric properties of cold-pressed samples, as observed in Sn-Se[214] and Bi-Sb-Te[243]. Furthermore, It has been reported that annealing process of Fe-Al and Fe-Ti-Al milled powders leads to transformation of Fe(Al) / Fe(Ti,Al) solid solution into FeAl / $(FeTi)_3Al$ ordered intermetallic compound, as discussed in section 4.3, as well as grain growth [238, 244]. In this study, the heat treatment could affect the phase structure and microstructure of $Fe_{11}Ti_3Al_6$ BM-CP bulk samples and lead to improved thermoelectric properties compared to those observed in the section 4.5.

In this study, the thermal annealing of $Fe_{11}Ti_3Al_6$ bulk samples was performed between 500^0C and 900^0C in an argon environment using the tubular furnace. A schematic procedure adopted for the annealing process is shown in Fig 4.6. The details of the tubular furnace are described in Chapter 3. The 4hrs, 5hrs, 10hrs, 15hrs and 20hrs BM-CP bulk samples were loaded into the tubular furnace (based on the procedure described in Section 3.5.1) to carry annealing at a specific temperature. After that, argon gas was used to purge the existing gases inside the tube. The

purging was carried out for 25-30 minutes. Under an argon gas flow rate of 2l/min, the thermal annealing process was carried out for 6hrs at different annealing temperatures. After completion of 6hrs, the furnace was turned off, and the annealed samples were allowed to cool down under an argon environment. When the furnace temperature reached room temperature then the samples were taken out.

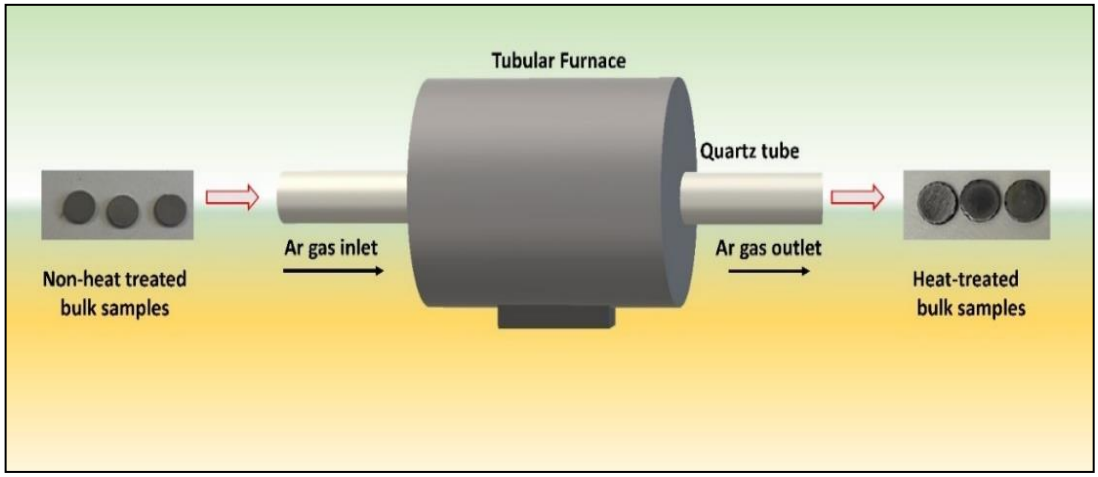

Figure 4. 6 A schematic procedure of the annealing process

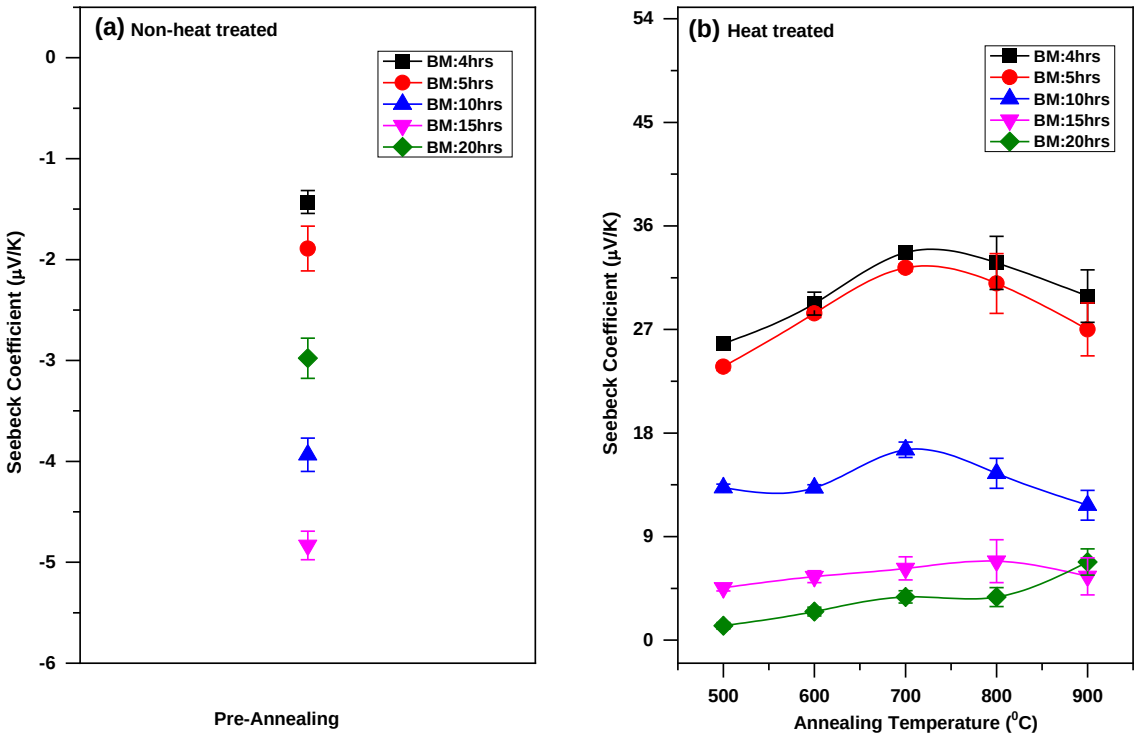

Figure 4. 7 Room temperature Seebeck coefficient of (a) non-heat-treated and (b) heat-treated samples

Fig 4.7 (b) presents the dependence of the room temperature Seebeck coefficient on the annealing temperatures. The Seebeck coefficient for heat-treated samples is positive, which suggests that holes govern conduction. It can also be noted that the Seebeck coefficient for all heat-treated samples is positive, whereas non-heat-treated bulk samples display negative Seebeck coefficient (Fig 4.7 (a)). After heat-treatment, the significant improvement in the Seebeck coefficient and change in its sign is observed. This is attributed to the formation of $(FeTi)_3Al$ intermetallic phase [238] or improvement in grain-grain connectivity (Fig 4.11). However, further studies would be needed to confirm the specific mechanisms underlying this improvement. The 4hr-BM-CP bulk sample followed by annealing at 700^0C achieved the highest Seebeck coefficient of 33.68±0.56μV/K. This peak value is 23% higher than the reported p-type Fe-Ti-Al sample[22]. It can be noted that the Seebeck coefficient of 4hr and 5hr BM-CP heat-treated at 700^0C exhibit quite close values.

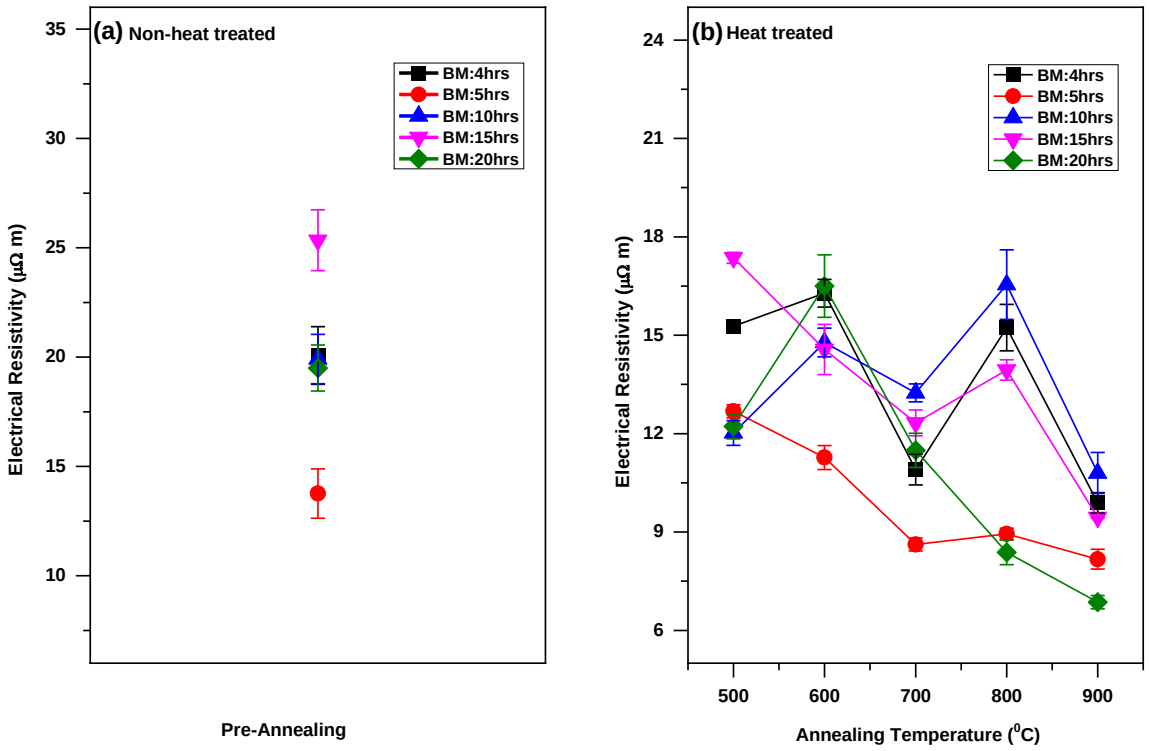

Figure 4. 8 Room temperature electrical resistivity of (a) non-heat-treated and (b) heat-treated samples

Fig 4.8 (b) shows the room temperature electrical resistivity dependence on the annealing temperatures. Among all the samples, 20 hr-BM-CP followed by annealing at 900^0C displayed the lowest electrical resistivity of 6.86±0.2μΩm. It can be seen that heat-treated samples attained lower electrical resistivity values compared to non-heat-treated samples (Fig 4.8 (a)). The reduction in electrical resistivity is observed due to an improvement in connectivity between grains (Fig

4.11)[231]. On the other hand, at 700^{0}C annealing temperature, the 5hr-BM-CP bulk sample attained the lowest resistivity of 8.62±0.19μΩm than other samples annealed at this temperature.

It was noted in Fig 4.7(b)- Fig 4.8 (b) that most annealed samples demonstrated peak Seebeck coefficient and dip in electrical resistivity at 700^{0}C. This dip in electrical resistivity around 700^{0}C is consistent with previous studies on Fe-Al and $Fe_{14}Al_6$ ($Fe_{70}Al_{30}$ (at%)) alloys[245]. In the literature, when $Fe_{14}Al_6$ samples were quenched between 300-1100^{0}C. The room temperature electrical resistivity measurements showed a bit of drop for samples quenched at 700-800^{0}C compared to other quenched samples[245]. This may be attributed to the existence of varying B2 phase order[245]. Additionally, in other studies, $Fe_{14}Al_6$ sample annealed at 700^{0}C showed the DO_3+B2 phase instead of the B2 phase order, despite the Fe-Al phase diagram predicted the presence of only the B2 phase order at 700^{0}C [246]. These investigations suggest that $Fe_{14}Al_6$ sample exhibits a phase order transition around 700-800^{0}C. In this study, $Fe_{11}Ti_3Al_6$ bulk samples annealed at 700^{0}C also show drop in electrical resistivity (Fig 4.8). Therefore, it can be speculated that the dip in electrical resistivity and peak in Seebeck coefficient at 700^{0}C could be associated with the varying degree of $D0_3$ phase order.

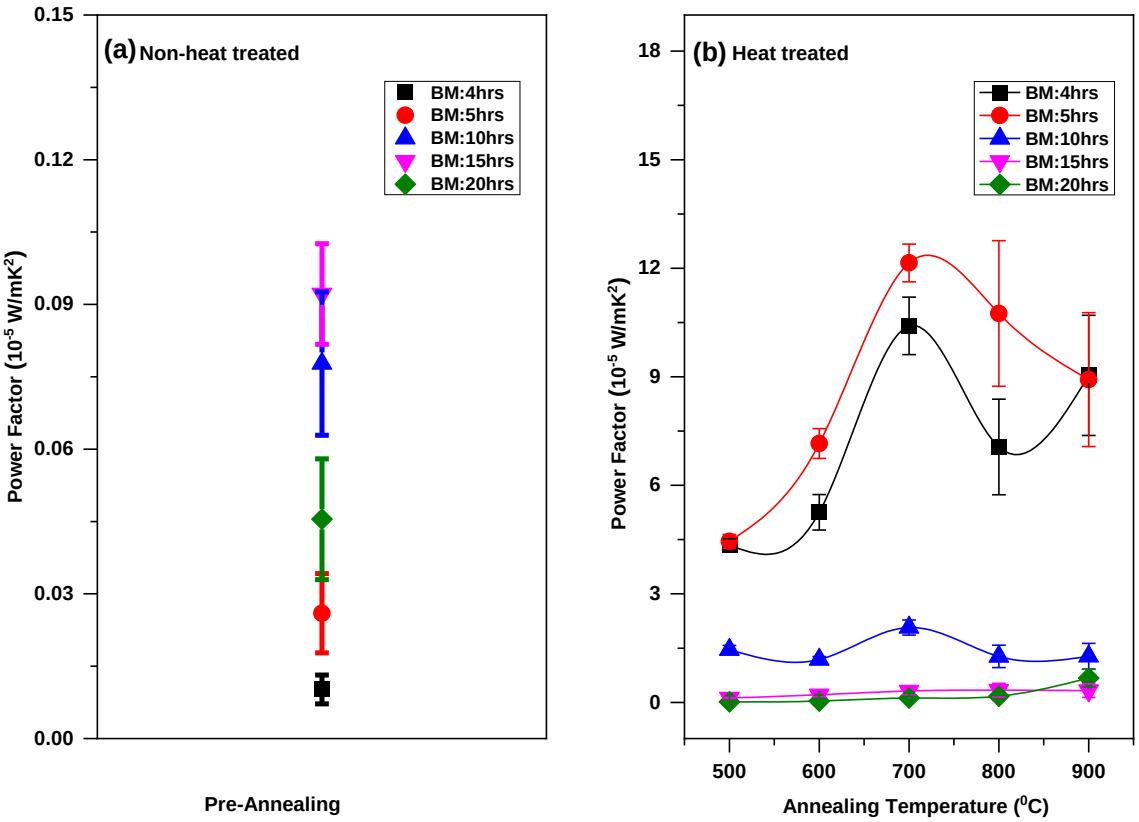

Figure 4. 9 Room temperature Power factor of (a) non-heat-treated and (b) heat-treated samples

Fig 4.9 displays the dependence of the room temperature PF on the annealing temperatures. Among all heat-treated samples, the 5hr-BM-CP sample followed by annealing at 700^0C attained maximum PF equal to (12.14±0.52) x10^{-5} W/mk^2 with the Seebeck coefficient of 32.36±0.32μV/K and electrical resistivity of 8.62±0.19μΩm. This sample displays peak PF due to the high Seebeck coefficient and lower electrical resistivity compared to other annealed bulk samples. However, this peak PF value is 5.76 times lower than the previously reported p-type sample[22], due to the high electrical resistivity of the BM-CP annealed sample.

This investigation demonstrates that the annealing process helps to improve the thermoelectric properties of the $Fe_{11}Ti_3Al_6$ BM-CP bulk sample. Out of all samples, the 5hr-BM-CP bulk sample followed by annealing at 700^0C shows the best thermoelectric properties in terms of PF. Therefore, ball milling for 5 hrs and annealing at 700^0C can be considered the most suitable condition to fabricate promising p-type $Fe_{11}Ti_3Al_6$ thermoelectric sample. These results suggest that p-type $Fe_{11}Ti_3Al_6$ sample with satisfactory thermoelectric properties can be fabricated by employing BM-CP followed by an annealing route.

4.7 Phase structure and microstructure of the annealed sample

The XRD and microstructure for 5hr-BM-CP non-annealed and annealed bulk samples are presented in this section. The effect of annealing temperature on phase structure was examined based on the XRD technique. Furthermore, the surface morphology of annealed samples was investigated using the SEM technique. SEM measurements were performed recently in this study, as it provides an indication of improvement in the thermoelectric properties of bulk samples after heat-treatment.

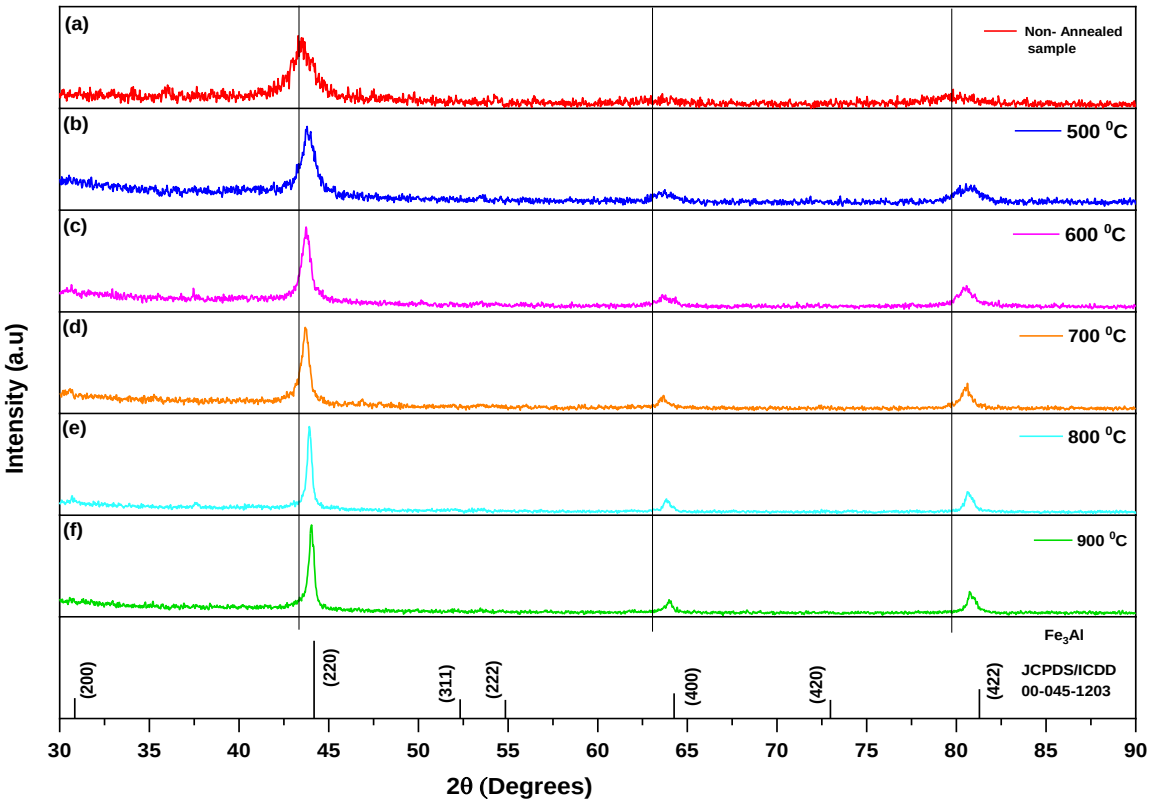

Figure 4. 10 XRD pattern of 5hr BM-CP (a) before heat-treatment (b-f) after heat-treatment between 500-900^{0}C

Fig 4.10 (a-f) illustrates the XRD pattern of 5hr BM-CP bulk samples, both non-heat-treated and heat-treated samples at different temperatures. It is found that no new phases are formed after heat treatment. However, the annealed samples show an absence of superlattice diffraction peaks when compared to Fe_3Al, indicating a disordered structure. This observation is consistent with previous work for Fe-Al heat-treated alloys [239]. Furthermore, the annealed samples exhibit sharp diffraction peaks with narrow full width at half maximum (FWHM) compared to the non-annealed bulk samples. This suggests that during the annealing process, the internal strain was released/ reduced and/or grain growth occurred [238]. The peak position and the intensity of three diffraction peaks suggest that all annealed bulk samples achieved phase structure close to Fe_3Al alloy, similar to the non-annealed bulk sample. It should be noted that as the annealing temperature increased from 500 to 900^{0}C, the XRD peaks show good agreement with position of Fe_3Al, which indicating the formation of intermetallic phase after heat-treatment[238, 247]. However, further investigation is required to confirm the temperature range for formation of intermetallic phase.

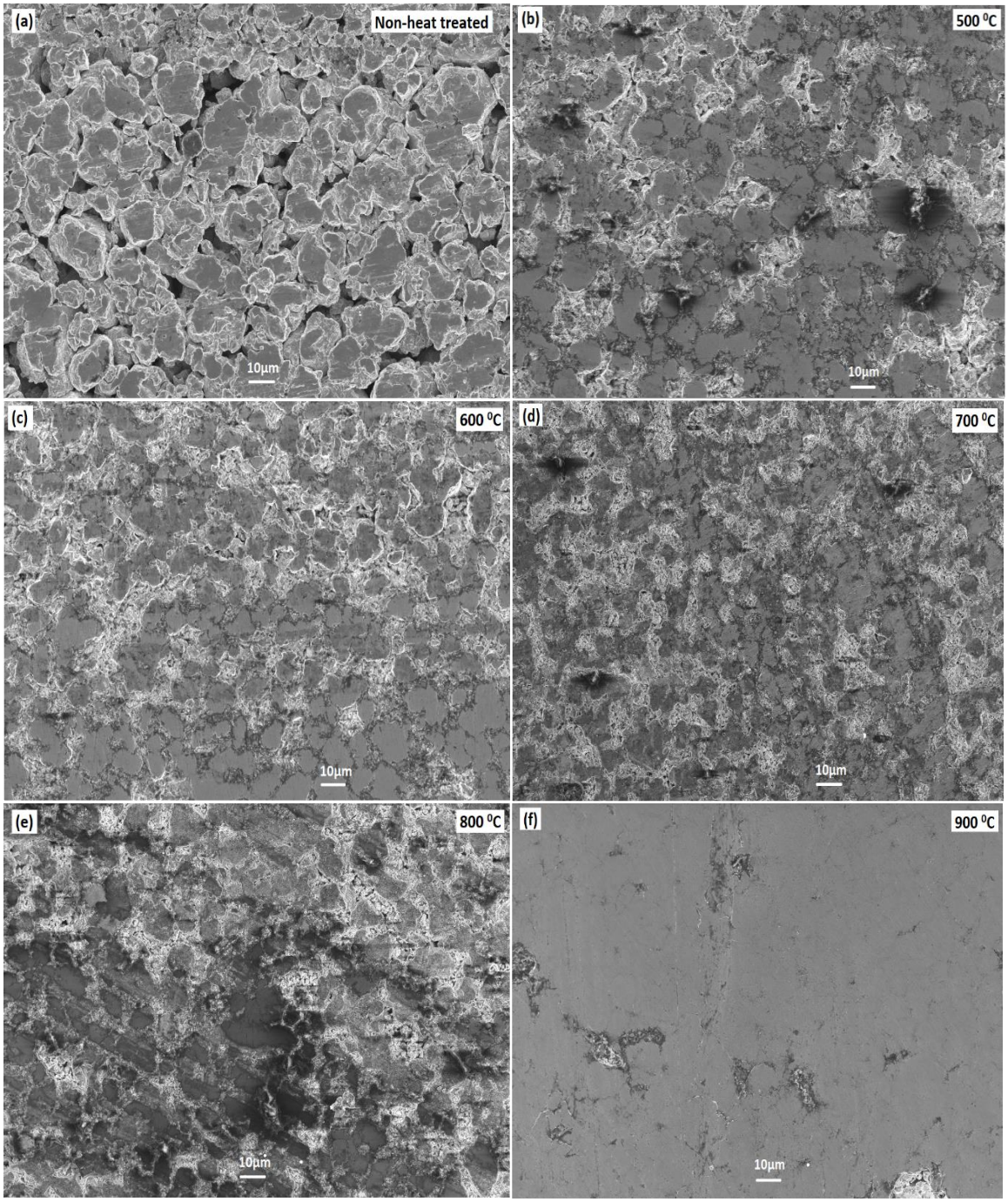

Figure 4. 11 SEM images of 5hr BM-CP sample (a) non-heat treatment (b-f) heat-treatment between 500-900^{0}C, scale bar 10 µm, Magnification =1KX

Fig 4.11 (a) illustrates the SEM image of the 5hr BM-CP non-annealed bulk sample, which shows the existence of pores and poor connectivity between grains. Fig 4.11 (b-f) shows the surface morphology of the annealed bulk sample at different temperatures. The microstructure of annealed bulk sample is entirely different compared to the non-heat-treated sample. After heat-treatment, there is an improvement in grain connectivity occurred, but the pores still existed. Due

to this reason, annealed samples show a significant reduction in electrical resistivity (Fig 4.8) and an improvement in PF. The micrographs display almost similar microstructure features except for the heat-treated sample at 900^0C. The surface morphology of the 900^0C annealed sample is unusual compared to other samples and requires further investigation for it in future. The observed microstructure of annealed samples shows close agreement with the SEM micrograph of Fe-Al annealed bulk sample[248]. The white area corresponds to iron-rich zones, whereas the black ones represent the Al-rich phases[248].

4.8 Attempt for fabrication of an n-type $Fe_3Ti_4Al_1$

In Section 4.1, it was mentioned that García-Cañadas et al.[22] also reported that $Fe_3Ti_4Al_1$ composition could be considered as an n-type promising thermoelectric candidate. It has been successfully demonstrated that p-type $Fe_{11}Ti_3Al_6$ composition can be prepared via BM-CP followed by an annealing route. The present section examines the feasibility of the BM-CP route to fabricating n-type $Fe_3Ti_4Al_1$ bulk sample. The sample preparation details, phase analysis and thermoelectric characterisation are presented here.

4.8.1 Sample preparation

The stoichiometric amount of Fe (43.4 wt. %), Ti (49.6 wt.%) and Al (7 wt.%) powders were added to prepare the $Fe_3Ti_4Al_1$ composition. This sample was mechanically alloyed in a planetary ball milling (Pulverisette 5/4) as described in Section 4.2. The sample was milled from 5hrs to 15hrs. The bulk samples from milled powders were produced by applying uniaxial pressure of 2200MPa followed by annealing at 700^0C for 6hrs using techniques mentioned in Chapter 3.

4.8.2 Phase structure and thermoelectric properties

This sub-section presents the phase structure of mixed powder, milled powder and annealed bulk samples for $Fe_3Ti_4Al_1$. The thermoelectric properties of annealed bulk samples were investigated at room temperature.

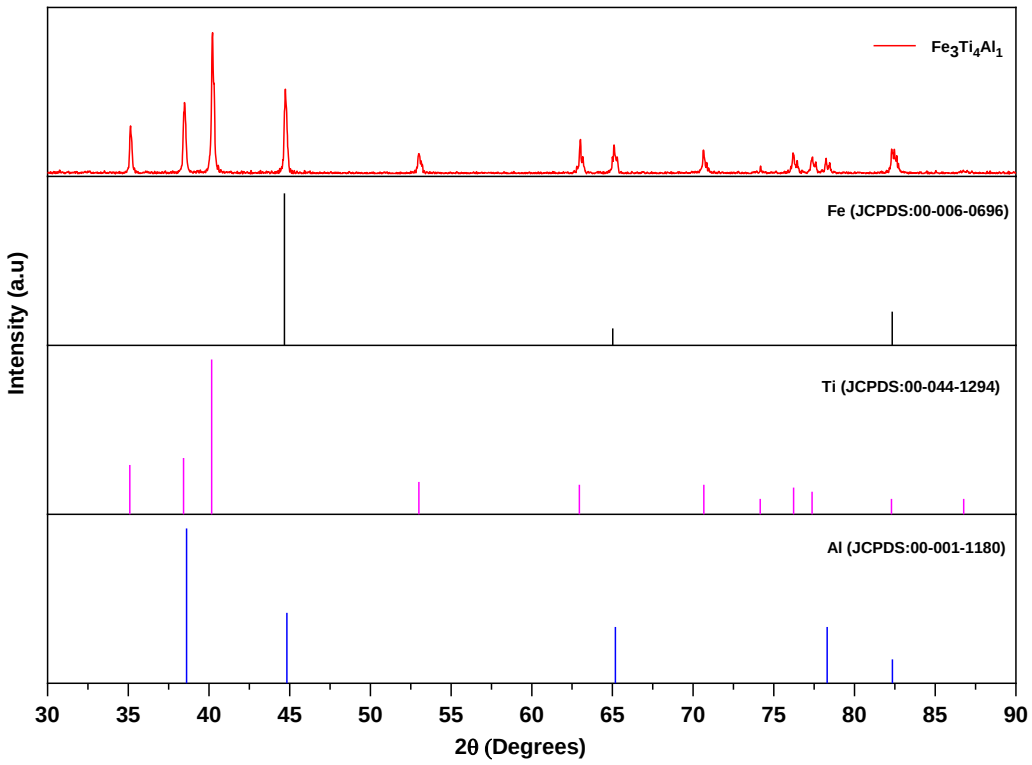

Figure 4. 12 XRD pattern of $Fe_3Ti_4Al_1$ non-milled powder sample

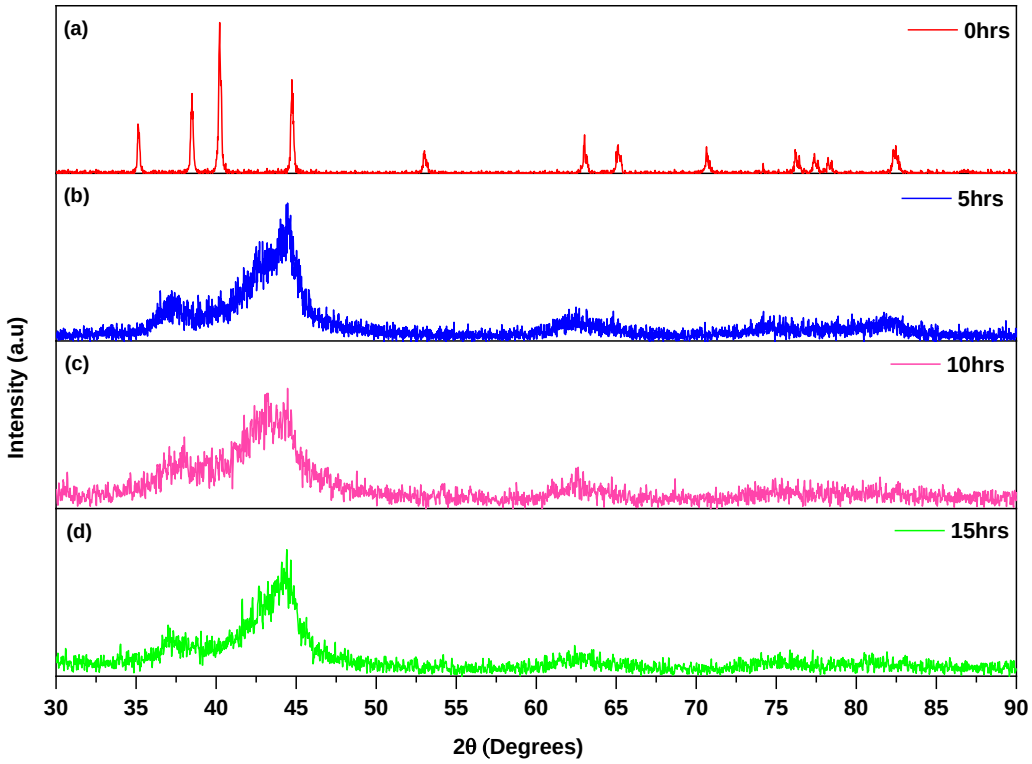

Figure 4. 13 XRD pattern of $Fe_3Ti_4Al_1$ milled powder sample at different milling times (0-15hrs)

Fig 4.12 illustrates the XRD pattern of the $Fe_3Ti_4Al_1$ non-milled (mixed) powder sample. The diffraction pattern of the non-milled powder sample show diffraction peaks corresponding to Fe, Ti and Al elements. The observed diffraction peak positions and intensities show good agreement with the database files for Fe (JCPDS/ICDD:00-006-0696, Ti (JCPDS/ICDD:00-044-1294) and Al (JCPDS/ICDD:00-001-1180) elements. Therefore, this comparison of scanned patterns with database files suggests the presence of Fe, Ti and Al in the blended sample.

Fig 4.13 displays the XRD patterns of $Fe_3Ti_4Al_1$ sample milled at different times. It can be seen that after milling for 5hrs, the width of diffraction peaks increases, and the intensity of peaks decreases compared to non-milled powder. The broad peak pattern suggests the formation of an amorphous phase and the absence of crystalline phase after milling. After continued milling for 10-15hrs, only an amorphous phase was observed i.e., no crystalline phase was formed. This sort of diffraction pattern was observed for Ti-rich compositions such as Ti-Fe[249, 250] and Ti-Fe-Al[251] alloys in the literature. The various reports have concluded that it is challenging to achieve crystalline phase via the mechanical alloying technique for Ti-Fe compositions. Furthermore, many researchers also made efforts to perform the mechanical alloying of Ti-rich samples at the different ball-to-powder ratios and milling period parameters to obtain the crystalline phase. Unfortunately, the amorphous phase was formed[249, 250, 252].

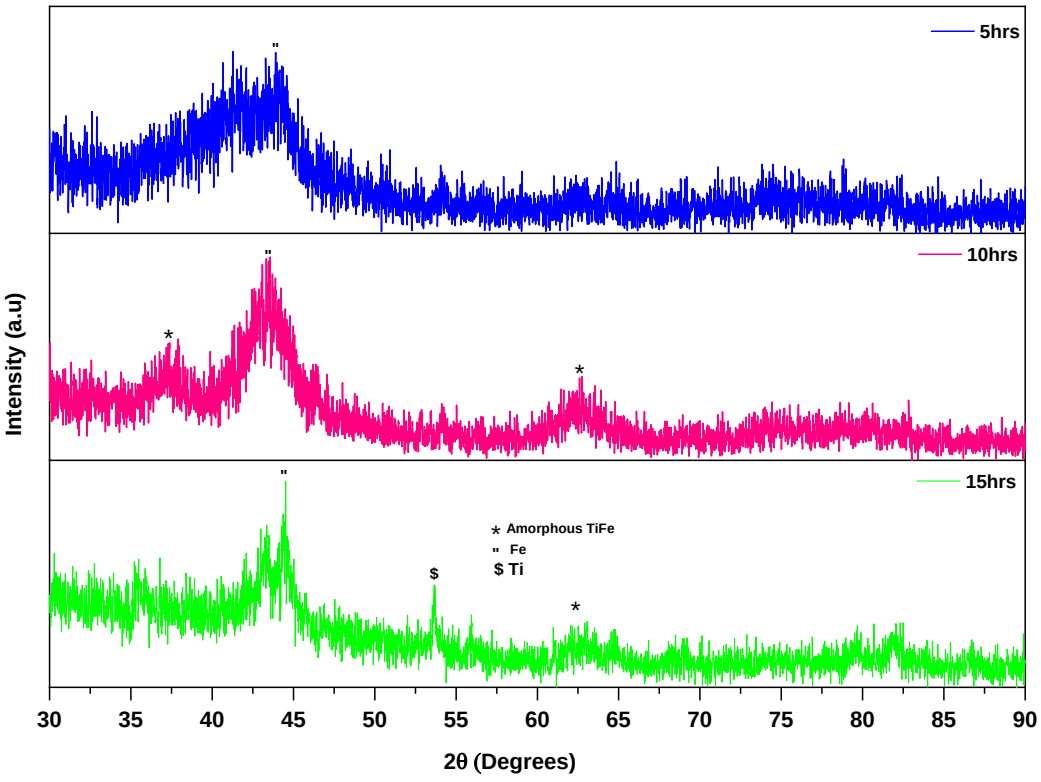

Figure 4. 14 XRD patterns of $Fe_{11}Ti_3Al_6$ annealed bulk samples at 700^0C

Fig 4.14 illustrates the XRD pattern for the $Fe_3Ti_4Al_1$ BM-CP bulk samples annealed at 700^0C. The XRD pattern indicates that only the amorphous phase is observed even after consolidation and heat treatment. It appears that via BM-CP followed by an annealing route, it is difficult to obtain the crystalline phase close to the n-type $Fe_3Ti_4Al_1$ reported sample[22].

Table 4. 2 Measured room temperature Seebeck coefficient (α), Electrical Resistivity (ρ), and Power Factor (PF) of $Fe_3Ti_4Al_1$ BM-CP bulk samples

Fabrication route	**BM (hrs)**	**α (μV/K)**	**ρ (μΩm)**	**PF (10^{-7} W/mK^2)**
Ball-milling and Cold pressing followed by annealing at 700^0 C	5	-2.07±0.15	14.40±0.31	3.0
	10	-5.47±0.90	15.15±0.24	19.75
	15	-0.97±0.27	10.35±0.21	0.91
Laser Melting technique (LMT)	-------	-57[22]	2.45[22]	13255[22]

Table 4.2 illustrates the thermoelectric properties of 5hr, 10hr and 15hr BM-CP followed by annealing at 700^0C. The Seebeck coefficient for all bulk samples is negative, suggesting that all samples are n-type. It can be noted that Seebeck coefficient and PF value of BM-CP annealed samples is quite low compared to the reported n-type $Fe_3Ti_4Al_1$ sample[22]. In section 4.6, it was found that p-type $Fe_{11}Ti_3Al_6$ bulk sample demonstrates promising thermoelectric properties after heat-treatment. In contrast, n-type $Fe_3Ti_4Al_1$ heat-treatment bulk sample display poor thermoelectric properties due to the presence of the non-crystalline/ no intermetallic phase (Fig 4.14). Based on the XRD and thermoelectric screening, it can be concluded that producing a promising n-type $Fe_3Ti_4Al_1$ thermoelectric sample through the BM-CP route is not feasible due to the formation of the amorphous phase during milling and annealing process.

4.9 Conclusion

A systematic investigation was carried out on the preparation and characterisation of p-type $Fe_{11}Ti_3Al_6$ thermoelectric materials via mechanical alloying and cold pressing followed by an annealing route. It is concluded that BM for 5hrs, cold pressing at 2200MPa followed by annealing at 700^0C can be considered as the most suitable conditions to fabricate the p-type $Fe_{11}Ti_3Al_6$ sample in terms of best thermoelectric properties. 5hr BM-CP $Fe_{11}Ti_3Al_6$ bulk sample annealed at 700^0C shows a maximum PF value of (12.14±0.52) x10^{-5} W/mk^2 with the Seebeck coefficient of +32.36±0.32μV/K and electrical resistivity of 8.62±0.19μΩm. The SEM images demonstrate that heat treatment is beneficial to improve grain-grain connectivity, due to which a reduction in

electrical resistivity is observed. The non-annealed and annealed bulk sample of the 5hr BM-CP sample attained a phase structure close to the well-known Fe_3Al intermetallic alloy. Efforts were also made to fabricate the n-type $Fe_3Ti_4Al_1$ sample, but it was found that it is difficult to prepare this sample via the BM-CP route due to the appearance of the amorphous phase.

Chapter 5: Influence of element substitution on thermoelectric properties of $Fe_{11}Ti_3Al_6$

5.1 Introduction

This chapter investigates the effect of element substitution on the thermoelectric properties of $Fe_{11}Ti_3Al_6$. The aim is to identify the promising element for effective substitution that will increase the Seebeck coefficient and PF of the $Fe_{11}Ti_3Al_6$ sample. In the literature, it has been found that the substitution of fourth elements such as W, Ta, Si and Ge for pseudo-gap based Fe_2VAl alloy improves the Seebeck coefficient and PF [123, 124, 253, 254]. Utilising the arc melting technique, Nishino et al. prepared Ge and Si-doped Fe_2VAl samples and concluded that Ge-doped samples show a rapid increase of PF from 10^{-5} W/mK^2 to 5.9x10^{-3} W/mK^2 at 300 K[123]. Mikami et al. synthesised the W and Si-substituted Fe_2VAl samples by employing the MA-PCS route and noticed an improvement in Seebeck value by approximately 3.5 times and 66% reduction in thermal conductivity[253]. Takeuchi et al. fabricated the Ta-doped $Fe_2VAl_{0.9}Si_{0.1}$ samples using a high-frequency induction heating method and reported the highest PF value of 10.3 mW/mK^2, compared to other reports on Fe-V-Al alloys[255].

All bulk samples in this investigation were fabricated using the optimised ball milling (BM), cold pressing (CP), and annealing conditions achieved in chapter 4. The thermoelectric characterisation is performed to investigate the impact of element substitution on the transport properties of $Fe_{11}Ti_3Al_6$. Furthermore, the XRD technique is used to analyse the effect of element substitution on the phase structure and thermoelectric properties of the pristine sample.

The following section describes the procedure adopted for the selection of element substitution. Section 5.3 describes the experimental methods adopted to fabricate bulk samples. The structural and thermoelectric characterisation of different substituted elements samples is discussed in the remaining sections.

5.2 Selection of substitute elements

This section aims to identify possible substitution elements to improve the thermoelectric performance of $Fe_{11}Ti_3Al_6$. The valence electron concentration (VEC) has been reported to associate with the thermoelectric properties of Fe-V-Al[256], Fe-Ti-Sn[257] and Ti-Ni-Co-Sn[258]

samples. As mentioned in section 2.4.9, using the VEC as an indicator is a beneficial strategy to improve the Seebeck coefficient and PF value of Fe_2VAl. For Fe_2VAl alloys, it is concluded that the significant enhancement in the Seebeck coefficient and PF can be obtained due to a slight deviation of VEC from VEC=6 [113]. The improvement in the Seebeck coefficient for Fe-V-Al alloys occurs due to the movement of the Fermi level from the centre of the pseudo gap towards a sharp rising density of states (DOS) without affecting the band structure. This study adopts the VEC concept to identify the promising substitute elements for improving the thermoelectric properties of the $Fe_{11}Ti_3Al_6$ sample.

Table 5. 1 Possible substitute elements on the Fe-site of $Fe_{11}Ti_3Al_6$

Element (Y)	Group no.	Period no.	Atomic radius (nm)	Crystal structure at 25^{0}C	Electronic configuration	Expected Variation in VEC of $Fe_{11-x}Y_xTi_3Al_6$ (x=0 to 4)	
						From	To
V	V	4	0.134	bcc	$[Ar]3d^34s^2$	5.9	5.3
Cr	VI	4	0.128	bcc	$[Ar]3d^54s^1$	5.9	5.5
Mo	VI	5	0.139	bcc	$[Kr]4d^55s^1$	5.9	5.5
W	VI	6	0.139	bcc	$[Xe]\ 4f^{14}5d^46s^2$	5.9	5.5
Mn	VII	4	0.127	bcc	$[Ar]3d^54s^2$	5.9	5.7
Co	IX	4	0.125	hcp	$[Ar]3d^74s^2$	5.9	6.1
Ni	X	4	0.124	fcc	$[Ar]3d^84s^2$	5.9	6.3

The electronic configuration of Fe is [Ar] $3d^6\ 4s^2$, Ti is [Ar] $3d^2\ 4s^2$and Al is [Ne] $3s^2\ 3p^1$. The total number of valence electrons in the $Fe_{11}Ti_3Al_6$ sample is 118. Fe and Ti contribute 72 d-electrons and 28 s-electrons to the net valence electrons, while Al contributes 12 s-electrons and 6 p-electrons. The calculated VEC for the $Fe_{11}Ti_3Al_6$ sample is 5.9. This VEC value can be increased or decreased in a wide range by substituting elements on the Fe-site of $Fe_{11}Ti_3Al_6$. However, VEC can be changed to a limited extent by substituting the elements on the Ti and Al-sample sites of $Fe_{11}Ti_3Al_6$. In this work, the elements listed above in Table 5. 1 were selected to vary the VEC to observe whether the thermoelectric properties of $Fe_{11}Ti_3Al_6$ can be improved by using the VEC concept. The substitution of Group V-VII elements will reduce the VEC (because Group V-VII valence electrons are less than Fe). However, the substitution of Group IX-X elements (having valence electrons greater than Fe) will lead to an increase in VEC. Table 5. 1 provides details on the crystal structure, group and period number, atomic size of selected elements[259, 260], as well as the expected variation range in the VEC of $Fe_{11}Ti_3Al_6$.

5.3 Experimental methods

For the preparation of $Fe_{11-x}Y_xTi_3Al_6$ (x=0 to 4) (Y = V, Cr, Mo, W, Mn, Co and Ni) blended powder samples, the stoichiometric amounts of each element Fe, Y, Ti and Al powders were mixed and milled for 5hrs by using the procedure mentioned in Section 4.2. All milled powder samples were consolidated into the bulk samples (disc shape-diameter of 6.35mm) using a cold-press station under optimal pressure of 2200MPa. After that, the fabricated bulk samples were annealed at the optimal temperature of 700^0 C as determined in section 4.6. The phase structure and room temperature thermoelectric characterization were preformed using techniques described in Chapter 3.

5.4 Effect of element substitution on material structure

This section investigates the possible incorporation of different selected elements into the crystalline structure of $Fe_{11}Ti_3Al_6$ sample. The XRD patterns of Mn, Cr, Mo, W, V, Ni and Co substituted powders after mechanical alloying was obtained experimentally, and the impact of element substitution on the structure of milled powders was analysed using the standard reference database.

5.4.1 Mn substituted powders

The XRD pattern for $Fe_{11-x}Mn_xTi_3Al_6$ (x=0 to 4) milled powders are depicted in Fig 5.1. Fe and Mn elements have atom arrangements in bcc (body-centred cubic) structure, the crystal structure of Ti is hcp (hexagonal close-packed), and Al has fcc (face-centred cubic) crystal structure. However, the XRD pattern of Fe-Mn-Ti-Al milled samples shows three diffraction peaks approximately at 43.7^0, 64^0 and 81^0 diffraction angles, which correspond to the bcc structure. With the increase of Mn content (Fig 5.1(b-e)), no new diffraction peak is observed, indicating no secondary phase was formed during the alloying process. The peak positions and intensities of milled samples show close agreement with the XRD pattern of Fe_3Al intermetallic alloy (JCPDS/ICDD: 00-045-1203). Therefore, it can be considered that all milled powders exhibit a phase structure close to Fe_3Al. The observed three diffraction peaks for samples correspond to (220), (400) and (422) plane positions.

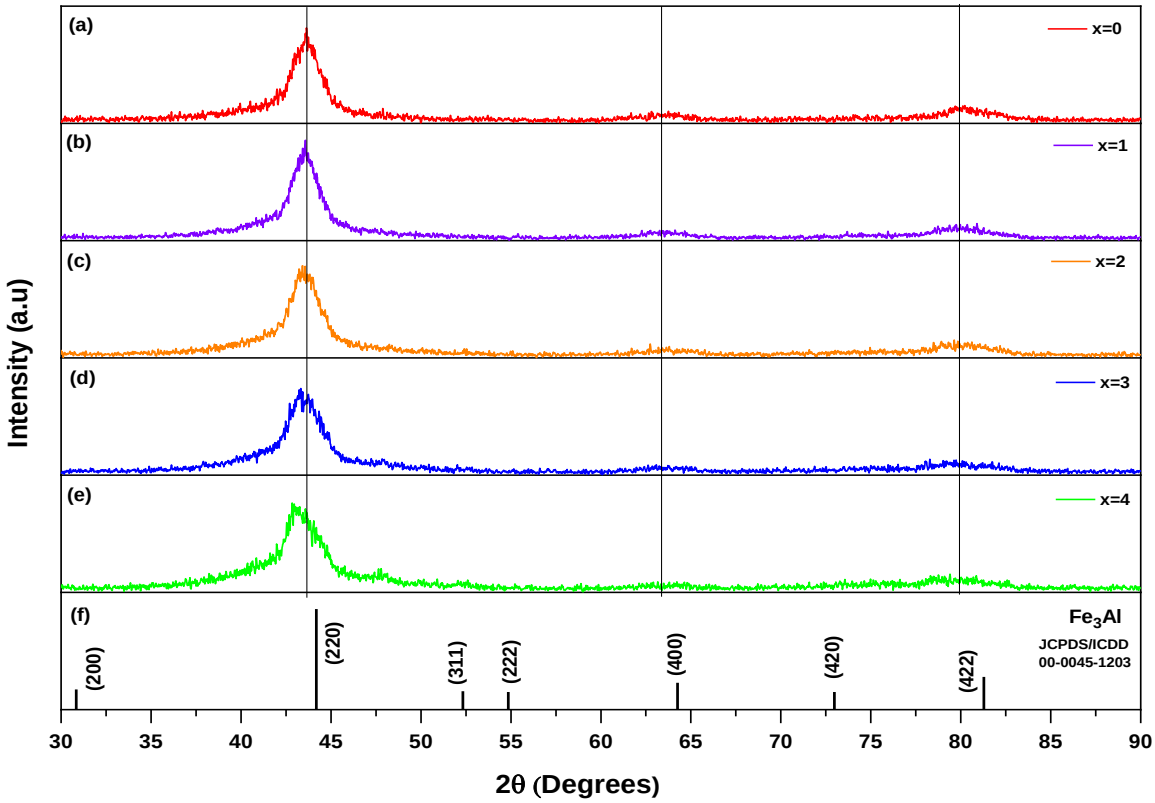

Figure 5. 1 XRD pattern of $Fe_{11-x}Mn_xTi_3Al_6$ (x=0 to 4) milled powder samples (B.M=5hrs)

5.4.2 Cr, Mo and W substituted powders

Cr, Mo, and W belong to the same Group in the periodic table. The impact of their substitution to Fe-site in $Fe_{11}Ti_3Al_6$ was examined based on the experimental XRD patterns shown in Fig 5.2-5.4.

Fig 5.2 illustrates the XRD pattern for $Fe_{11-x}Cr_xTi_3Al_6$ (x=0 to 4) milled powders. As the value of x increases from x =0 to x=4, there is no new secondary phase formed. Although, the diffraction peaks start shifting towards higher diffraction angles, indicating that the lattice contraction occurred. The position and intensities of peaks of milled samples show that all samples exhibit phase structure close to Fe_3Al alloy (JCPDS/ICDD:00-045-1203). Besides, the detected peaks for the x=4 sample are quite closer to Fe_3Al compared to other samples. The observed diffraction patterns show good agreement with the XRD spectra of $Fe_{75-x}Cr_xAl_{25}$ ($19 \leq x \leq 25$) alloys[261]. In our study, the shift of diffraction peaks towards higher diffraction angles likely occurred due to lattice compression in the x-y plane[261, 262].

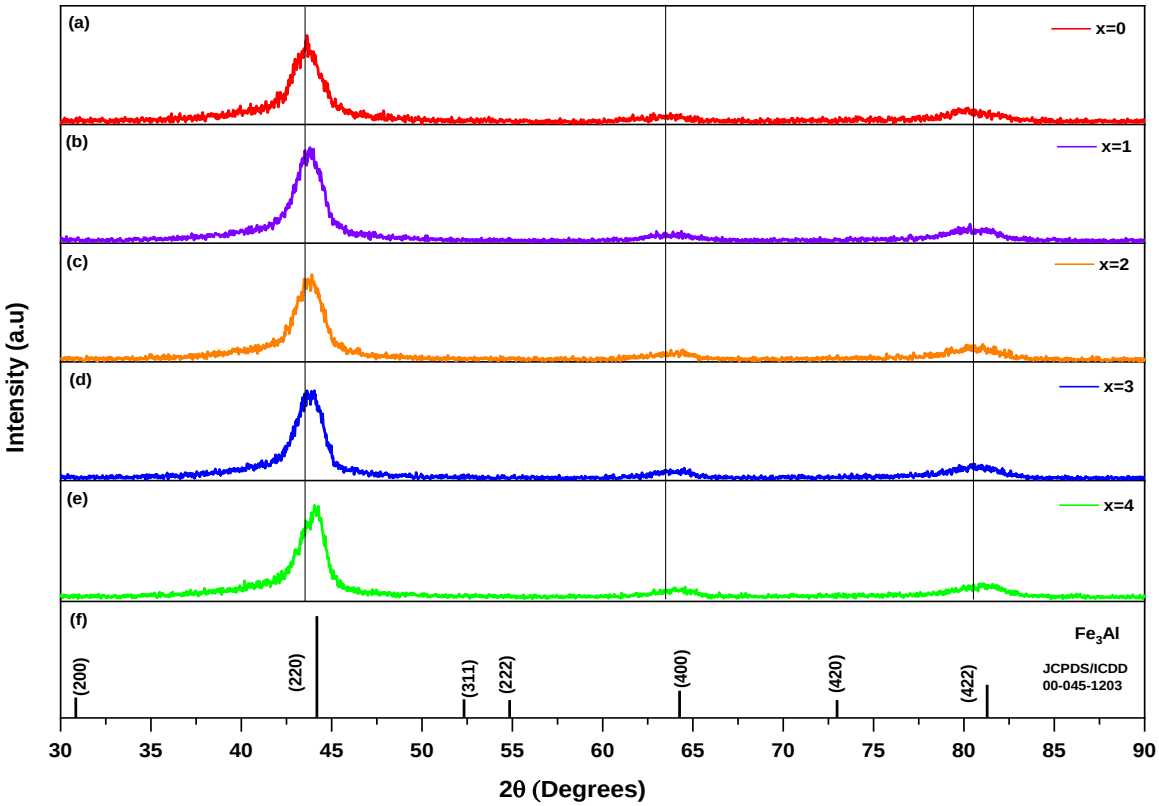

Figure 5. 2 XRD pattern of $Fe_{11-x}Cr_xTi_3Al_6$ (x=0 to 4) milled powder samples (B.M=5hrs)

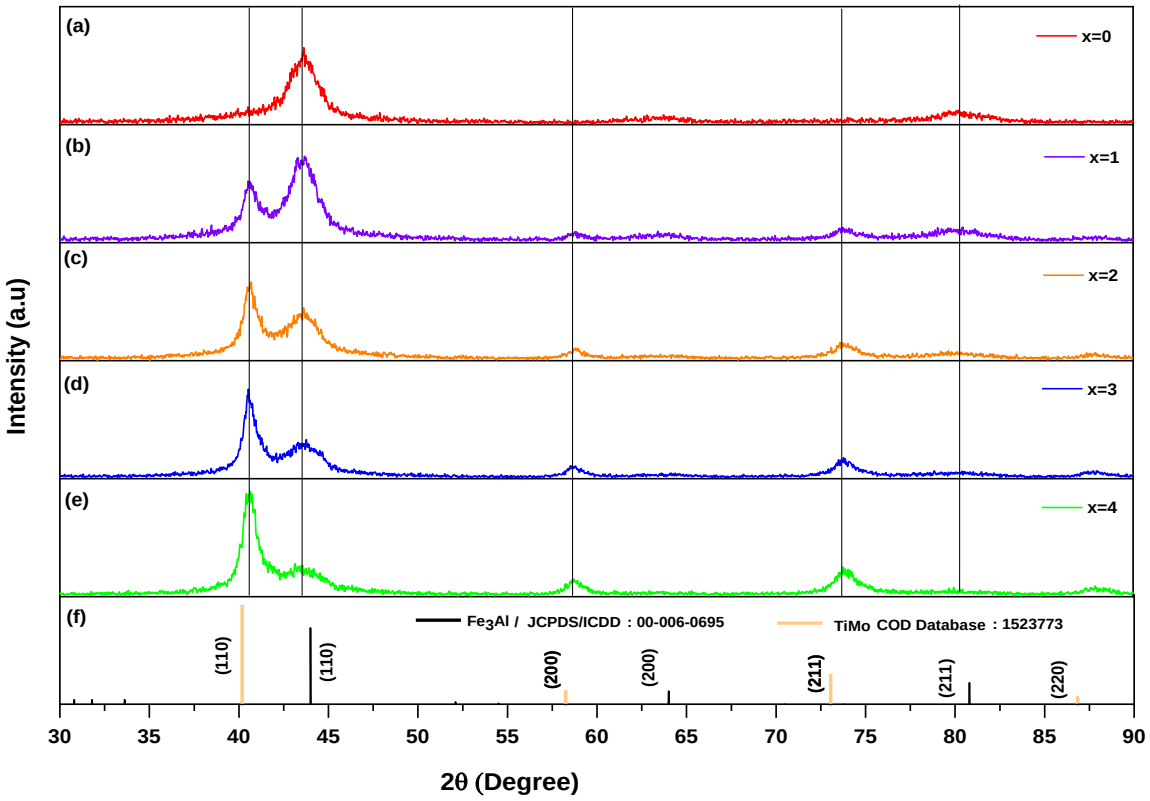

Figure 5. 3 XRD pattern of $Fe_{11-x}Mo_xTi_3Al_6$ (x=0 to 4) milled powder samples (B.M=5hrs)

Fig 5.3 displays the XRD pattern for $Fe_{11-x}Mo_xTi_3Al_6$ (x=0 to 4) milled powders. The XRD pattern of $Fe_{11}Ti_3Al_6$ (x=0) milled powder sample shows three diffraction peaks at 43.6^0, 64^0 and 81^0 diffraction angles. The observed peaks are corresponding to the (220), (400) and (422) crystallographic planes of Fe_3Al alloy (JCPDS/ICDD:00-045-1203). But it can be seen that Mo-substituted milled powder samples (Fig 5.3 (b-e)) exhibit different XRD patterns than the pristine sample (i.e., x=0). The diffraction pattern for the x=1 (Fig 5.3 (b)) shows new peaks at 40.5^0, 58.6^0 and 73.6^0 diffraction angles compared to x=0. This is indicating that the secondary phase was formed with the substitution of the Mo-element. As the value of x increases, the relative intensity of XRD peaks corresponding to the (110), (200), and (211) planes of the TiMo alloy phase increased. The position and intensities of peaks suggest that Mo-substituted milled samples exhibit a mixture phase structure consisting of TiMo alloy (COD Database: 1523773) and Fe_3Al alloy[263]. The solute element Mo has a bcc structure, similar to $Fe_{11}Ti_3Al_6$ which satisfies the Hume Rothery condition for conventional alloys [264]. Additionally, the difference in metallic radius between Mo (0.139nm) and Fe (0.124nm) is larger compared to Ti (0.145nm) and Al (0.143nm). Moreover, Mo belongs to a different period (no.5) and has a larger atomic mass compared to Fe, Ti, and Al, all of which belong to the same period (no.4). These factors could contribute to the formation of a mixed phase Fe-Mo-Ti-Al solid-solution.

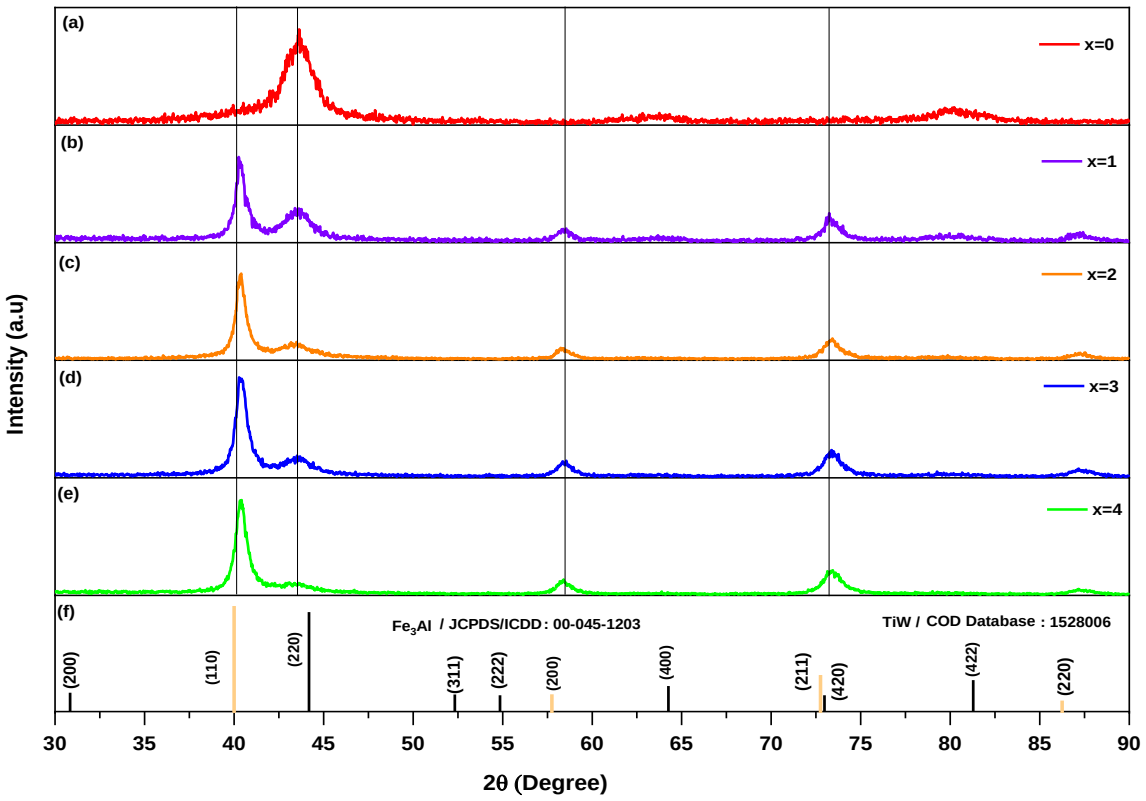

Figure 5. 4 XRD pattern of $Fe_{11-x}W_xTi_3Al_6$ (x=0 to 4) milled powder samples (B.M=5hrs)

Fig 5.4 shows the XRD pattern for $Fe_{11-x}W_xTi_3Al_6$ (x=0 to 4) milled powders. The substitution of the W element demonstrates a similar effect to Mo element substitution on the Fe-site of $Fe_{11}Ti_3Al_6$ sample. W-substitution leads to the formation of mixed-phase structure close to TiW alloy (COD Database: 1528006) and Fe_3Al alloy (JCPDS/ICDD: 00-045-1203), which also shows reasonable agreement with the previous studies[265]. The diffraction pattern of W-substituted samples shows diffraction peaks at 40.25^0, 43.66^0, 58.5^0, 73.5^0 and 87.5^0 diffraction angles. The crystal structure and metallic radius of W are similar to those of Mo (139nm), but it belongs to a higher period (no. 6) and has a higher atomic mass. These factors could contribute to the formation of a mixed solid solution of Fe_3Al and TiW, although further investigation is needed to confirm this hypothesis.

5.4.3 V-Substituted powders

This sub-section explores the impact of V substitution on the phase structure of $Fe_{11}Ti_3Al_6$ powder sample. The V element belongs to Group V and has a bcc crystal structure at a temperature of 25°C.

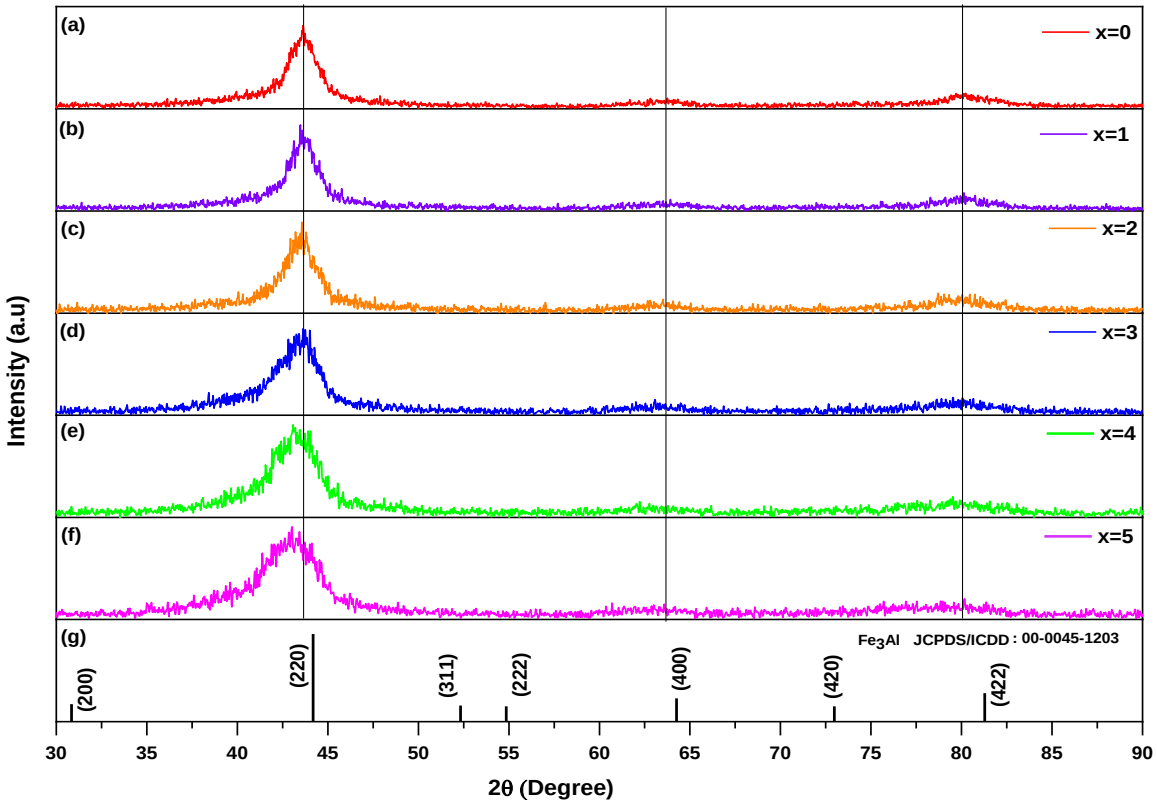

Figure 5. 5 XRD pattern of $Fe_{11-x}V_xTi_3Al_6$ (x=0 to 5) milled powder samples (B.M=5hrs)

Fig 5.5 illustrates the XRD patterns for $Fe_{11-x}V_xTi_3Al_6$ (x=0 to 5) milled powders. Between x=0 to 2, the XRD pattern indicates that the crystalline solid solution formed during the milling process.

The position and intensities of the peaks for milled powder samples (x≤2) show close agreement with the phase structure of Fe_3Al alloy, which has reference code number JCPDS/ICDD:00-045-1203. However, the sample corresponding to x≥3 shows broad haloes in the range of 2θ 40-45^0, suggesting presence of both a crystalline and amorphous solid solution.

5.4.4 Co-Substituted powders

Fig 5.6 show the XRD patterns for Co substituted $Fe_{11}Ti_3Al_6$ powder samples. As the concentration of Co element on the Fe-site of $Fe_{11}Ti_3Al_6$ increases, the diffraction pattern shifts toward higher diffraction angles, and there is no secondary phase was formed. Between x=1 to x=4, the main diffraction peak shifts from 43.7^0 to 44.2^0 which indicates the occurrence of lattice contraction. This shift appeared with the increase of the atomic percentage of Co (hcp), due to the difference in atomic radius of Co (0.125nm) and Fe (0.124nm) [266, 267], and mismatch between their crystal structures. The diffraction patterns for all samples show close agreement with the phase structure of Fe_3Al alloy (JCPDS/ICDD:00-045-1203). Along this, it can be seen that the diffraction peaks for x=2 to 4 are quite close to peaks of Fe_3Al alloy.

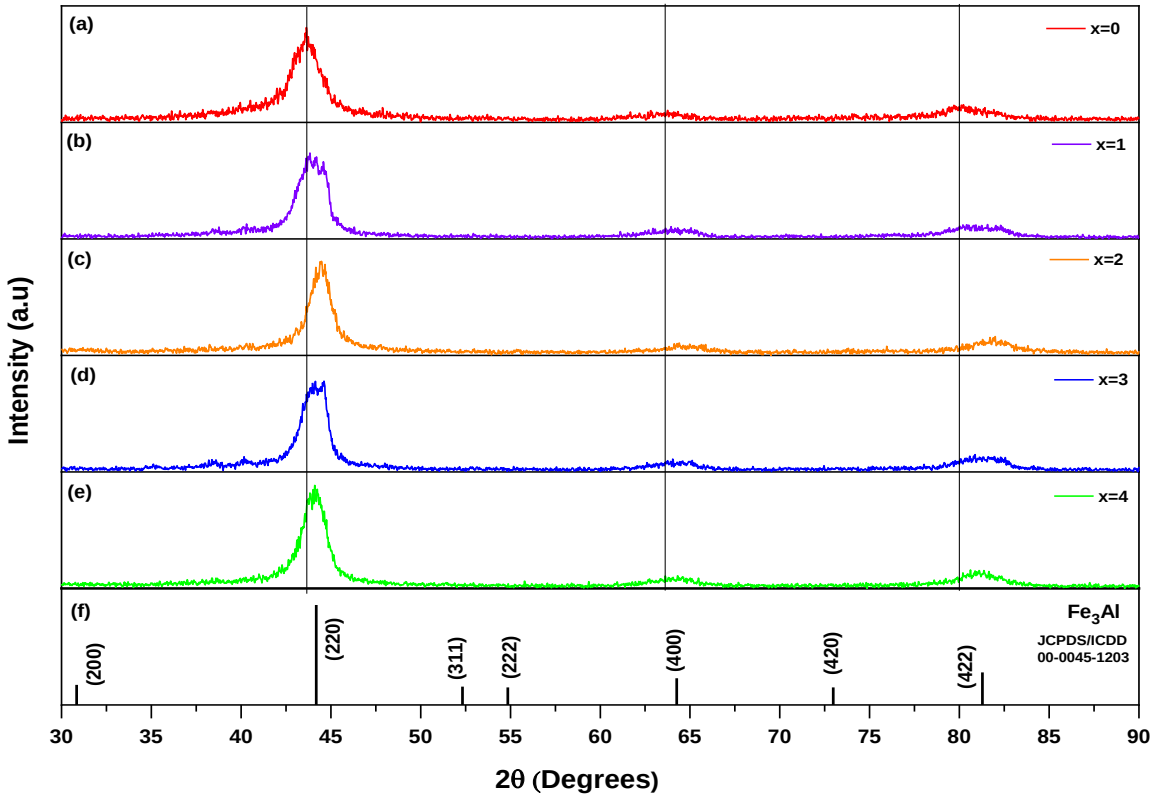

Figure 5. 6 XRD pattern of $Fe_{11-x}Co_xTi_3Al_6$ (x=0 to 4) milled powder samples (B.M=5hrs)

5.4.5 Ni-Substituted powders

The diffraction pattern for $Fe_{11-x}Ni_xTi_3Al_6$ (x=0 to 4) milled powders are depicted in Fig 5.7. The scanned XRD patterns for Ni-substituted samples are similar to $Fe_{11}Ti_3Al_6$ and Mn-substituted samples (Fig 5.1). The prominent diffraction peaks for all samples are detected near the diffraction angles of 43.7^0, 64^0 and 81^0 correspond to the (220), (400) and (422) crystallographic planes of Fe_3Al alloy (JCPDS/ICDD:00-045-1203). The XRD patterns for Ni-substituted milled samples demonstrate good consistency with previous investigations on Fe-Ni-Al alloys[268].

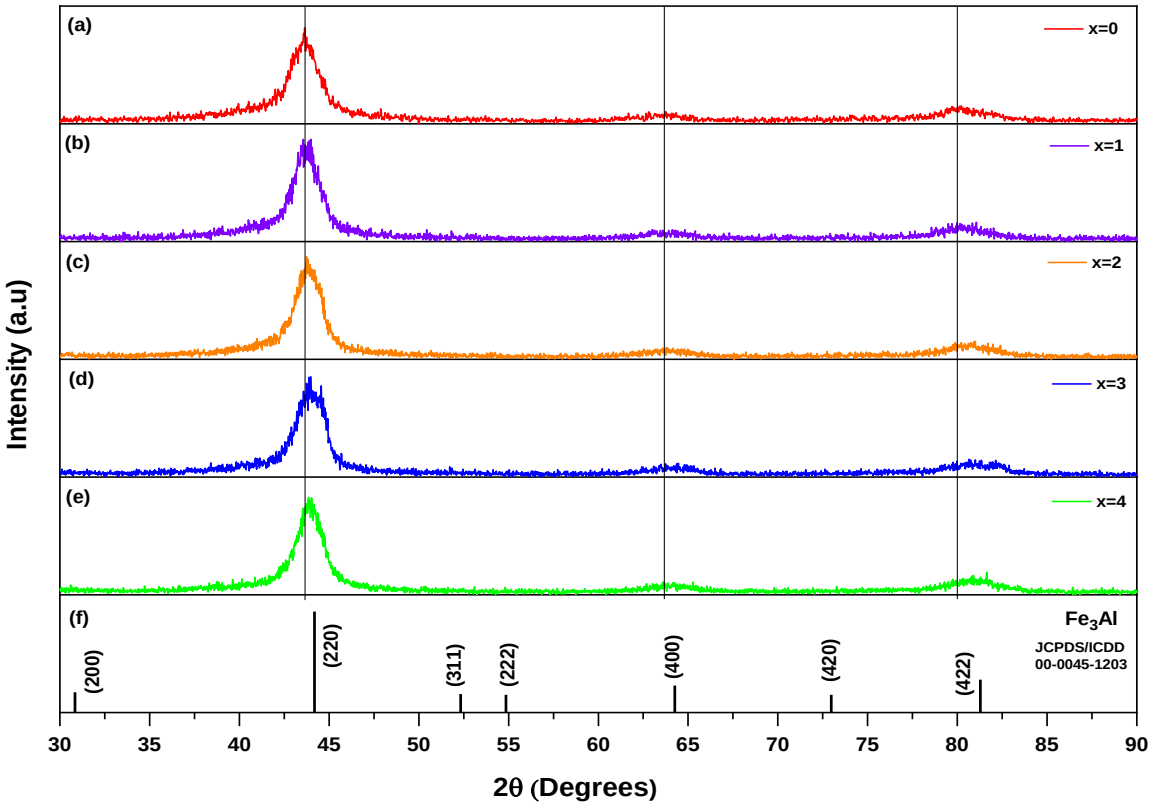

Figure 5. 7 XRD pattern of $Fe_{11-x}Ni_xTi_3Al_6$ (x=0 to 4) milled powder samples (B.M=5hrs)

Overall, in this section, it was observed that Mn, Cr, V, Co and Ni element substitution on the Fe-site of $Fe_{11}Ti_3Al_6$ attained phase structure close to Fe_3Al alloy as similar to pristine ($Fe_{11}Ti_3Al_6$) sample. However, Mo-substituted powder samples exhibit mixed phase structure of TiMo and Fe_3Al alloy. Similarly, a mixed-phase structure of TiW and Fe_3Al alloy was achieved for W-substituted powder samples.

5.5 Influence of the heat treatment on the phase structure

The milled powders examined in the above section were used to fabricate bulk samples for the characterisation of their thermoelectric properties. All milled powder samples (in above section-5.4) were consolidated using the cold pressing method to produce bulk samples and then

heat treatment as detailed in Section 5.3. This section presents the results of XRD analysis on the annealed bulk samples to investigate any possible impact of consolidation and heat treatment on materials structures.

5.5.1 Mn-substituted bulk samples

Fig 5.8 shows the XRD patterns for $Fe_{11-x}Mn_xTi_3Al_6$ (x=0 to 4) annealed bulk samples. It is interesting to note that compared to powder samples (Fig 5.1), the diffraction peaks of annealed samples seem sharp with narrowed full width at half maximum (FWHM), indicating that grain growth occurred during heat treatment or internal stress was released. There is no new diffraction peak is observed for x=0 to x=3 samples, suggesting that there is no secondary phase formed after consolidation followed by the annealing process.

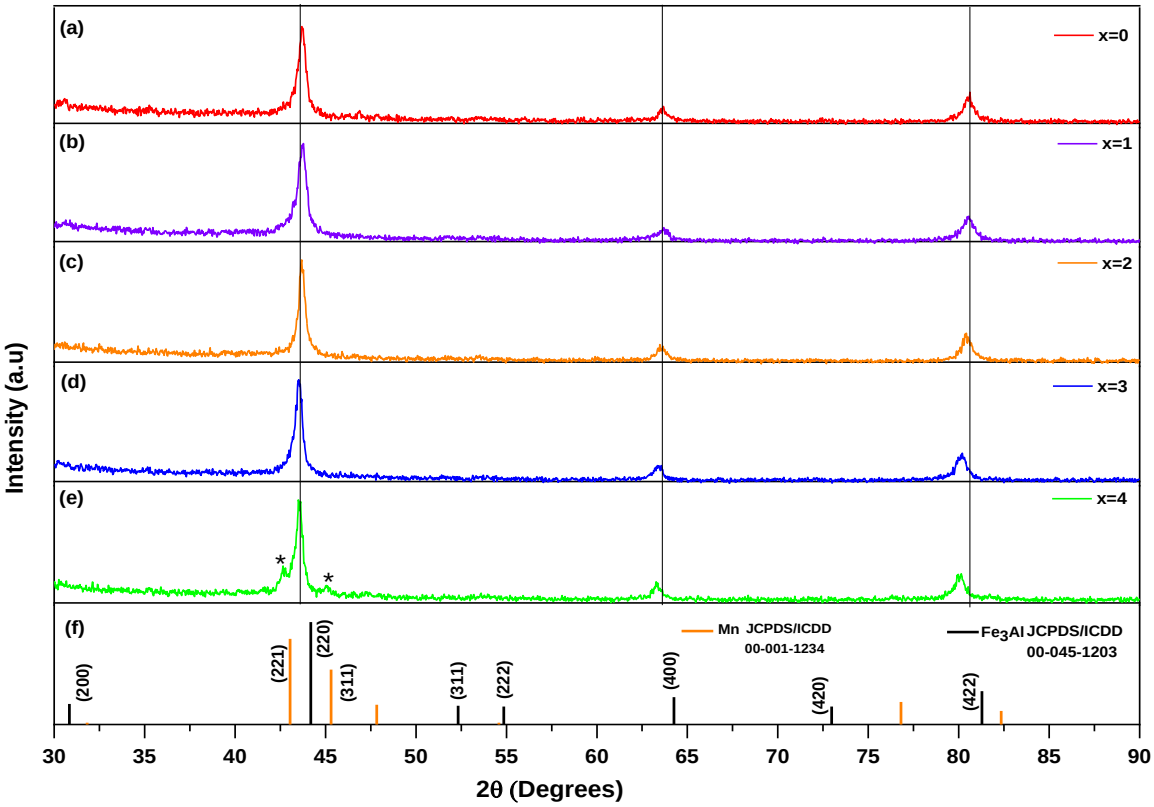

Figure 5. 8 XRD pattern of $Fe_{11-x}Mn_xTi_3Al_6$ (x=0 to 4) annealed bulk samples at 700^0C

XRD pattern corresponding to x=0 to 3 shows close agreement with the phase structure of Fe_3Al alloy (JCPDS/ICDD: 00-045-1203). However, the XRD pattern of the x=4 sample shows new diffraction peaks at 42.7^0 and 45.1^0 diffraction angles compared to their powder sample, indicating the presence of a secondary phase. Therefore, it could be considered that the $Fe_7Mn_4Ti_3Al_6$ annealed sample exhibits a phase structure close to Fe_3Al and an unknown phase (probably Mn

JCPDS/ICDD:00-001-1234). This sort of formation of the secondary phase with the increase of Mn concentration for Fe-Mn-Al alloys has been reported by MM Richo et al. [269].

5.5.2 Cr, Mo and Mo-substituted bulk samples

In this sub-section, we examined the XRD pattern for $Fe_{11-x}Y_xTi_3Al_6$ (x=0 to 4) (Y = Cr, Mo, and W) annealed bulk samples. Fig 5.9 illustrates the XRD patterns for $Fe_{11-x}Cr_xTi_3Al_6$ (x=0 to 4) annealed bulk samples.

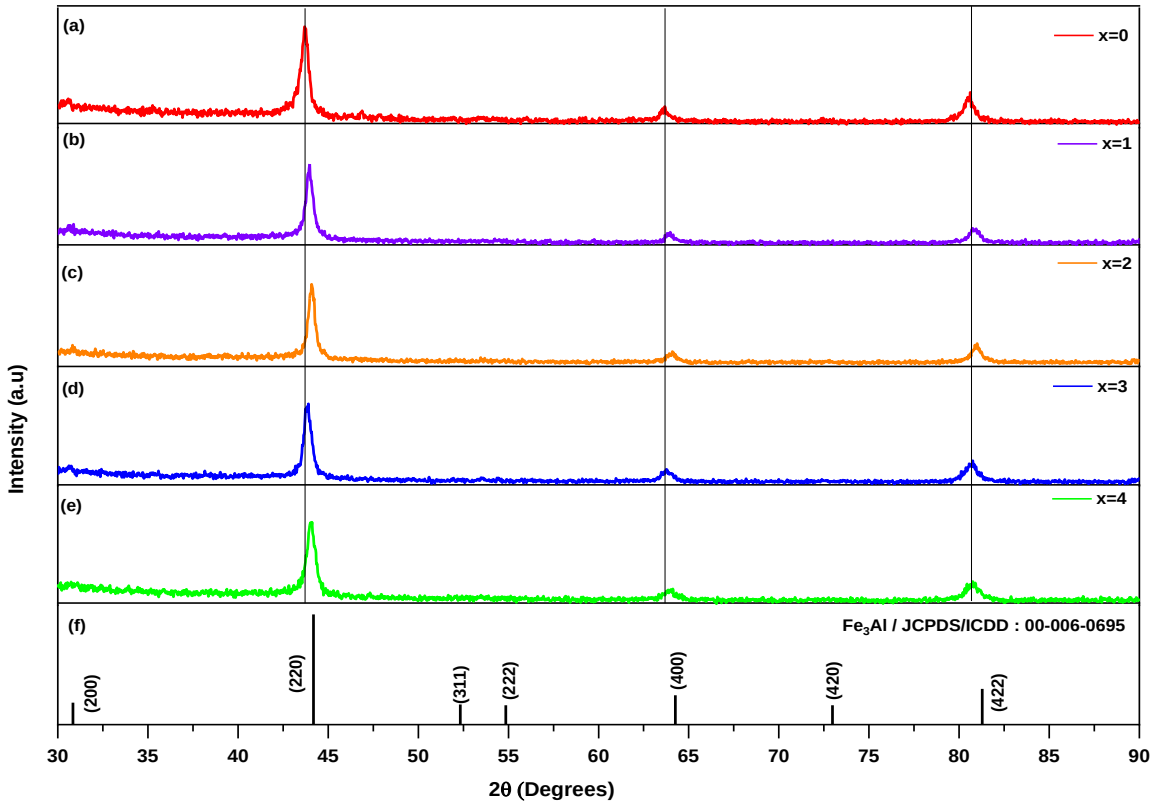

Figure 5. 9 XRD pattern of $Fe_{11-x}Cr_xTi_3Al_6$ (x=0 to 4) annealed bulk samples at 700^0C

The diffraction pattern for annealed bulk samples is similar to Cr-substitution powder milled samples (Fig 5.2). However, the FWHM of the diffraction peaks for the annealed sample is smaller than that of their Cr-substituted milled powder samples, similar to the Mn-substituted annealed sample. The heat-treatment likely assisted to improving the crystallinity and transforming the solid solution to an intermetallic phase[270]. All annealed sample exhibits phase structure close to Fe_3Al alloy (JCPDS/ICDD:00-045-1203), similar to their powder samples. It can be noted that as the value of x increases from x=0 to x=4 diffraction pattern of annealed samples shifts towards a higher 2θ value, indicating that the unit cell shrinks.

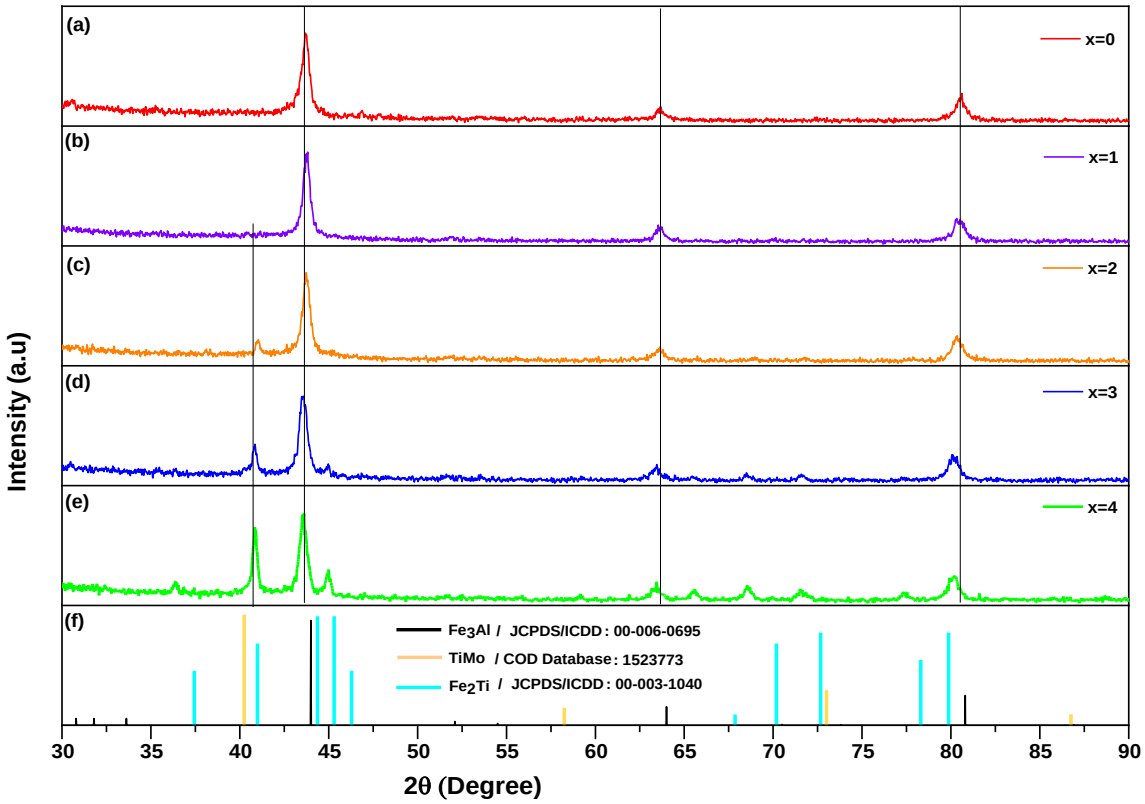

Figure 5. 10 XRD pattern of $Fe_{11-x}Mo_xTi_3Al_6$ (x=0 to 4) annealed bulk samples at 700^0C

Fig 5.10 displays the XRD patterns for $Fe_{11-x}Mo_xTi_3Al_6$ (x=0 to 4) annealed bulk samples. The diffraction pattern of Mo-substituted annealed bulk samples is entirely different compared to their milled powder samples (Fig 5.3). XRD pattern for x=0 and x=1 annealed samples show (Fig 5.10 (a-b)) phase structure close to Fe_3Al alloy (JCPDS/ICDD: 00-045-1203). On the other side, the diffraction pattern for the x=2 annealed bulk sample (Fig 5.10 (c-d)) demonstrates mixed phase structure primarily consisting of the Fe_3Al alloy along with the secondary phase of TiMo alloy (COD database:1523773). The sample corresponds to x≥3 with the increase of Mo content on the Fe-site of the sample attained mixed phase structure. This sort of phase structure changes has been observed for Fe-Ti-Mo alloys (for rich Mo sample) [271].

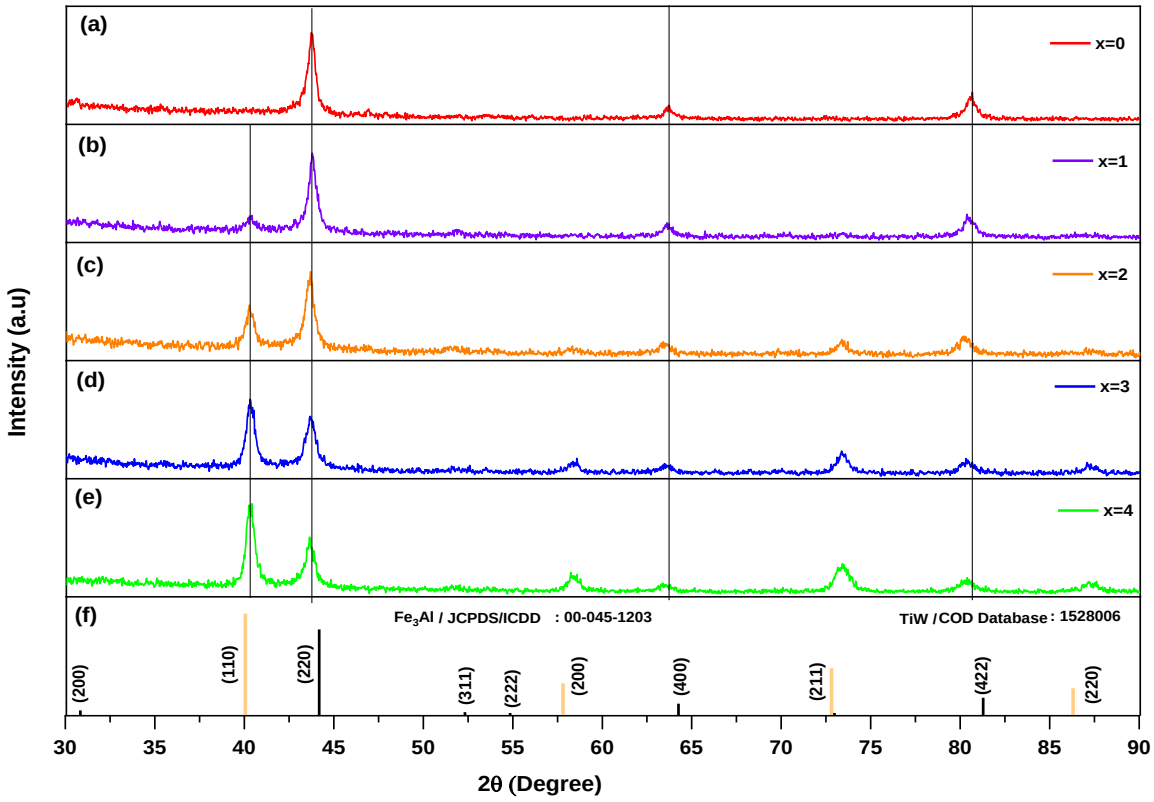

Figure 5. 11 XRD pattern of $Fe_{11-x}W_xTi_3Al_6$ (x=0 to 4) annealed bulk samples at 700^0C

Fig 5.11 illustrates the XRD patterns for W-substituted $Fe_{11}Ti_3Al_6$ annealed bulk samples. The heat treatment affects the crystalline structure of W-substituted bulk samples similarly to Mo-substituted annealed bulk samples. W-substituted bulk samples (Fig 5.11 (b-e)) achieved a mixture phase structure of TiW and Fe_3Al alloy. As the content of W on Fe-site increases, the relative intensity of XRD peaks corresponding to the (110), (200), and (211) planes of the TiW phase increased. This type of phase structure change agrees well with the previous studies[272]. The diffraction peak around 81^0 for x=0 tends to shift towards lower diffraction angles with the increase of the x value. This suggests that the sample containing higher content of W-element attained a large size unit cell.

5.5.3 V-substituted bulk samples

In this sub-section, the XRD pattern of $Fe_{11-x}V_xTi_3Al_6$ (x=0 to 5) annealed bulk samples are presented in Fig 5.12.

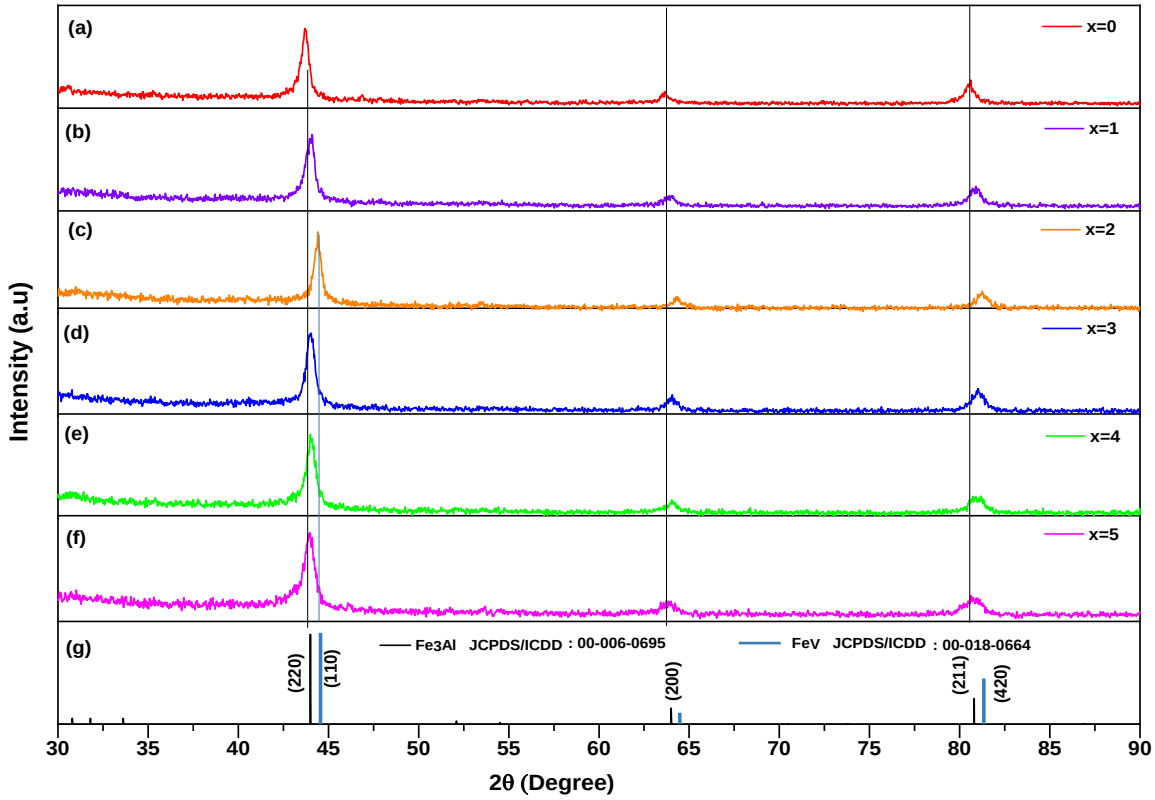

Figure 5. 12 XRD pattern of $Fe_{11-x}V_xTi_3Al_6$ (x=0 to 5) annealed bulk samples at 700^0C

The diffraction peak position and intensities for x=0 and 1 sample display phase structure close to Fe_3Al alloy (JCPDS/ICDD: 00-045-1203). From x=0 to x=2, there is a shift in diffraction peak toward higher diffraction angles occurred which indicates lattice compression[273]. The sample corresponding to x=2 shows phase transformation from Fe_3Al to FeV alloy (JCPDS/ICDD:00-018-0664). For the samples, x≥3, the XRD peak shifted back toward lower diffraction angles and attained the phase structure of Fe_3Al alloy. The shift of pattern towards lower diffraction angles suggests lattice expansion occurred for the sample containing high V-element content [274]. With the increase of V concentration, the size of the unit cell becomes large because the atomic size of the V element (0.134nm) is larger than the Fe element (0.124nm), this unusual structural variation has been reported in the literature[275]. In the case of the V-substitution, the milled samples of x≥3 (Fig 5.5) show a broad peak indicating an amorphous and crystalline phase. However, the samples after consolidation and annealing process show sharp and narrow diffraction peaks, which indicates the formation of the crystalline intermetallic phase after annealing.

5.5.4 Co-substituted bulk samples

Fig 5.13 show the XRD pattern of Co-substituted samples. The diffraction peaks for Co-substituted samples agree well with the peak position of Fe_3Al alloy. The XRD spectra of Co-substituted annealed bulk samples are similar to their powder samples (Fig 5.6), except for the fact that the FHWM of diffraction peaks of annealed samples becomes smaller, which indicates that consolidation and annealing result in grain growth.

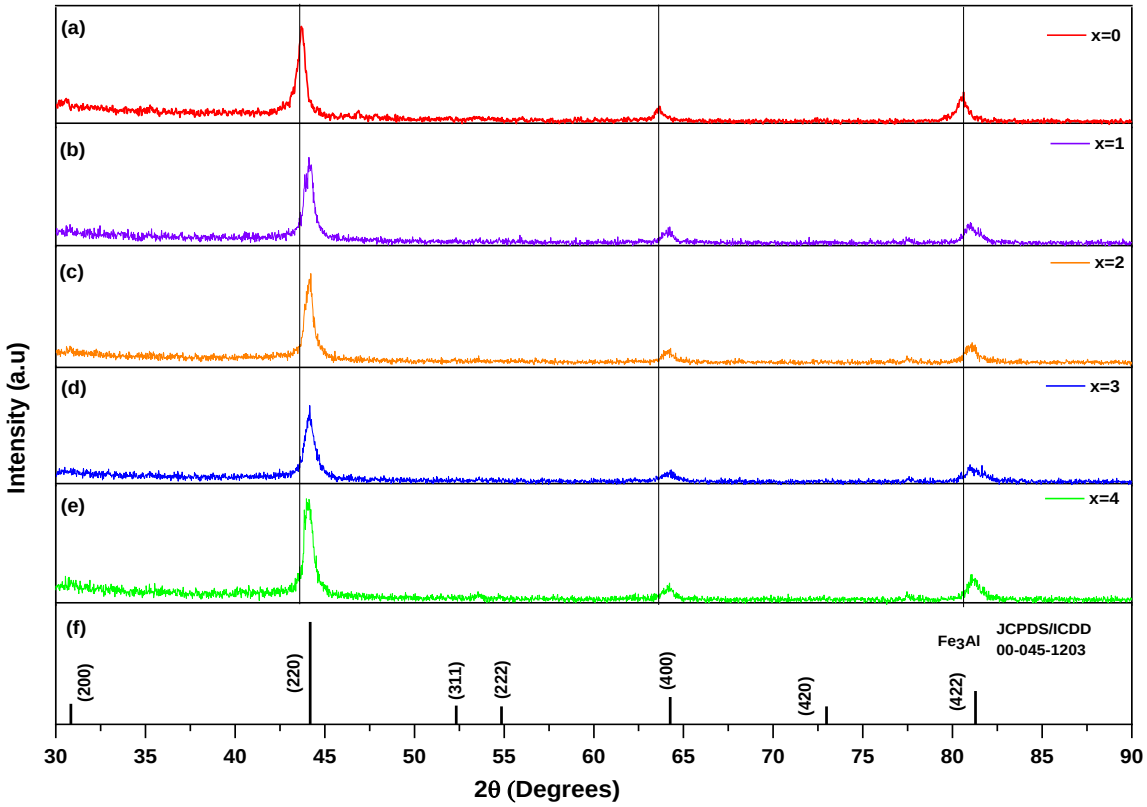

Figure 5. 13 XRD pattern of $Fe_{11-x}Co_xTi_3Al_6$ (x=0 to 4) annealed bulk samples at 700^0C

5.5.5 Ni-substituted bulk samples

Fig 5.14 illustrates the diffraction patterns of $Fe_{11-x}Ni_xTi_3Al_6$ (x=0 to 4) annealed bulk samples. The impact of consolidation and annealing process on the FHWM of diffraction peaks for Ni-substituted samples is similar to Co-substituted annealed samples (Fig 5.13). The peak position of all Ni-substituted annealed bulk samples is close to the pristine bulk sample (x=0). Furthermore, the bulk samples of Ni-substitution attained Fe_3Al alloy (JCPDS/ICDD:00-045-1203) phase structure, similar to their milled powder sample.

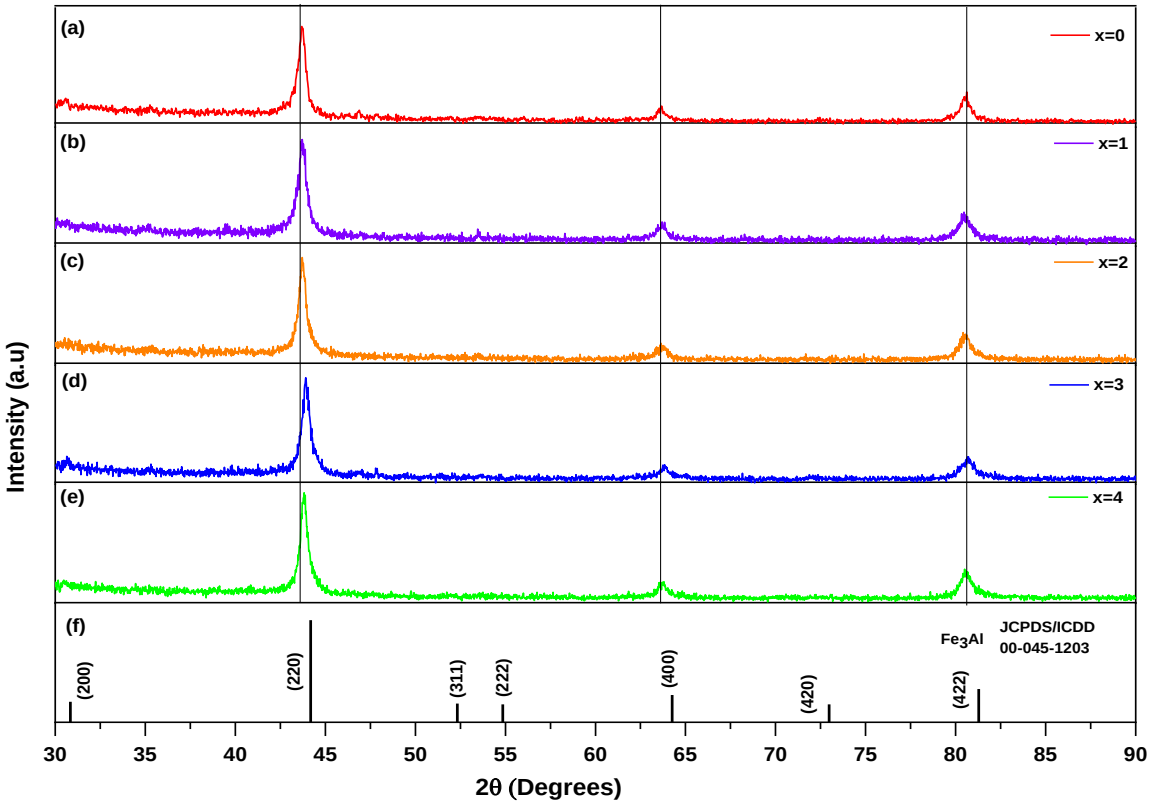

Figure 5. 14 XRD pattern of $Fe_{11-x}Ni_xTi_3Al_6$ (x=0 to 4) annealed bulk samples at 700^0C

In summary, the XRD patterns of Mn, Cr, Co and Ni substituted annealed bulk samples are similar to their powder samples and exhibit a phase structure close to Fe_3Al alloy. However, the annealed bulk samples exhibit sharp peaks with narrow FWHM compared to their powder samples. On the other hand, the cold-pressed and annealed bulk samples of W and Mo-substitution show different XRD patterns compared to their milled samples. Furthermore, V-substituted bulk samples of x≥3 change to crystalline phase after consolidation and annealing, while their milled powder samples show amorphous and crystalline nature.

5.6 Study of the thermoelectric properties of Fe-site substituted samples

The thermoelectric properties, including the Seebeck coefficient, electrical resistivity, and PF of all annealed bulk samples are presented here. The details of measurement techniques used for characterisation are described in Section 5.3. The transport properties were measured to examine the influence of different element substitutions on the Seebeck coefficient, electrical resistivity and PF of the $Fe_{11}Ti_3Al_6$ sample.

5.6.1 Seebeck coefficient and resistivity

Fig 5.15 (a-d) presents the room temperature measurements of the Seebeck coefficient (α) and electrical resistivity (ρ) for Mn, Cr, Mo, W, V, Co and Ni substituted $Fe_{11}Ti_3Al_6$ samples.

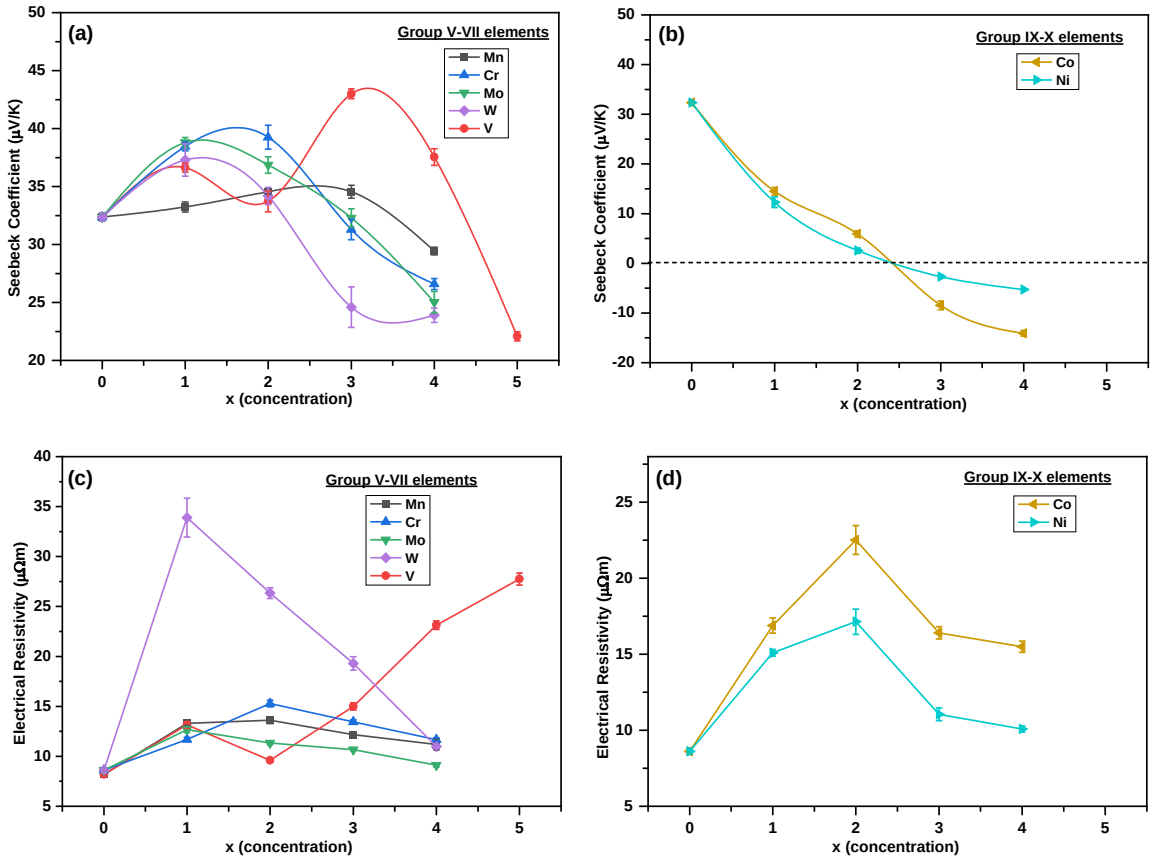

Figure 5. 15 Room temperature (a-b) Seebeck coefficient and (c-d) resistivity of $Fe_{11-x}Y_xTi_3Al_6$ (Y = Cr, Mo, W, Mn, V, Co and Ni) annealed bulk samples

- Group V-VII elements: V, Cr, Mo, W and Mn

V, Cr, Mo, W and Mn elements have less d-electrons than Fe elements. The measured Seebeck coefficient for Group V-VII element substituted samples is positive (Fig 5.15 (a)), indicating that holes primarily dominate the electrical conduction. The Seebeck coefficient and electrical resistivity (Fig 5.15 (c)) increase up to a certain concentration and then decrease for all samples except for V substitution, which shows unique behaviour after x=2. Such a trend is also observed for Fe-Cr-V-Al[122] and Fe-Mn-Cr-Al[276] metallic systems. The fact that both electrical resistivity and Seebeck coefficient change in the same trend for Group V-VII element substitution (expect for V element) show that the increase in both parameters occurs due to a reduction in hole concentration. These results indicate that the effect of Cr, Mo, W and Mn addition is to shift the Fermi level in the direction to reduce the hole concentration. To confirm this speculation, it is necessary to

perform DFT calculations or experimental measurements of the Hall coefficient which is the focus of further studies.

Table 5. 2 The peak Seebeck coefficient with the substitution of Group V-VII elements

Sample	Seebeck coefficient (μV/K)	Electrical resistivity (μΩm)	Improvement in Seebeck coefficient (%)
$Fe_8V_3Ti_3Al_6$	42.9±0.4	14.9±0.35	32.5
$Fe_9Cr_2Ti_3Al_6$	39.2±1	15.2±0.34	21.1
$Fe_{10}Mo_1Ti_3Al_6$	38.8±0.4	12.6±0.28	20.0
$Fe_{10}W_1Ti_3Al_6$	37.3±1.3	33.8±1.95	15.3
$Fe_9Mn_2Ti_3Al_6$	34.6±0.2	13.6±0.33	6.9

Table 5. 2 shows the peak Seebeck coefficient of the substituted samples compared to $Fe_{11}Ti_3Al_6$. Among all-substituted (Group V-VII) samples, $Fe_8V_3Ti_3Al_6$ exhibits a peak Seebeck coefficient of 42.99±0.43 μV/K, which is 32.5% higher than $Fe_{11}Ti_3Al_6$. Furthermore, Group VI elements (i.e., Cr, Mo, and W) show an improvement of the Seebeck coefficient by 15-21 %. In addition, the replacement of Mn gives the smallest improvement in the Seebeck coefficient by 6.9 %. The peak Seebeck coefficient obtained in this study for $Fe_8V_3Ti_3Al_6$ sample is lower than Fe-Ti-V-Al Heusler-based sample (fabricated based on the arc-melting method) [277].

The electrical resistivity of Group V-VII substituted samples (Fig 5.15 (c)) exhibits similar changes with the concentration of the substitution (i.e., x) except for the V-substitution. $Fe_{10}W_1Ti_3Al_6$ (purple curve) attained the highest electrical resistivity of 33.8±1.95μΩm compared to other element substitutions. The trend of electrical resistivity for the V-substitution sample (red curve) is unusual compared to other substitution elements. It can be seen that above x=2, the resistivity for V-element substituted samples increases with increasing V content. A similar trend of the electrical resistivity change with increasing V content on Fe-site had been observed in the case of $(Fe_{1-x}V_x)_3Al$ alloys[278].

- Group IX-X elements: Co and Ni

Group IX-X elements have higher valence electrons than Fe element and Group V-VII elements. The change of the Seebeck coefficient (Fig 5.15 (b)) with substitution using Group IX-X elements is opposite to those using Group V-VII elements. As the value of x increases, the Seebeck coefficient for Co and Ni-substituted sample decreases. Between x=0 and x=2, the Seebeck value is still positive, which indicates that holes govern electrical conduction. For the samples of x≥3, the sign of their Seebeck coefficient changes from positive to negative, indicating that the

electrical conduction is mainly contributed by electrons rather than the holes. This finding is in good agreement with the results of Suzuki et al. [127] It is likely that as a result of Co or Ni substitution, the Fermi level shifts towards the conduction band and electrons become majority charge carriers which alter the sign of the Seebeck coefficient. For Group IX-X substituted samples, the largest negative Seebeck coefficient obtained from this study is -14μV/K obtained from the Co substituted sample of x=4 (i.e., $Fe_7Co_4Ti_3Al_6$). Based on the trend shown in Fig 5.15 (b), a larger negative Seebeck coefficient might be obtained for the Co-substituted samples of x>4. Further investigation is needed.

The change of electrical resistivity with Co and Ni content (Fig 5.15 (d)) is similar to the Mn, Cr, Mo and W-substituted samples (Fig 5.15 (c)). Both Co and Ni substituted samples show a peak resistivity at x=2. $Fe_9Co_2Ti_3Al_6$ exhibits a higher electrical resistivity of 22.52±0.9 μΩm than that of the Ni-substituted samples. It is to be noted that the variation of the Seebeck coefficient with the content of substitution using Group IX-X elements does not show a similar trend to that of their electrical resistivity. It is interesting but challenging to understand. Considering both Co and Ni are ferromagnetic, such interesting trends might be related to the magnetic properties of the materials. Further investigated is needed.

Overall, this investigation suggests that the substitution using Group V-VII elements (i.e., V, Cr, Mo, W and Mn) led to an improvement of the Seebeck coefficient by 6-32 % compared to $Fe_{11}Ti_3Al_6$. While the substitution using Group IX-X elements (i.e., Co and Ni) results in n-type materials.

5.6.2 Power Factor

Fig 5.16 displays the PF for Mn, Cr, Mo, W, V, Ni, and Co substituted samples compared with $Fe_{11}Ti_3Al_6$. The PF was calculated using the Seebeck coefficient and electrical resistivity data. This parameter is helpful in predicting whether the substituted sample demonstrates high PF values (i.e., better thermoelectric performance) than the pristine sample (i.e., $Fe_{11}Ti_3Al_6$).

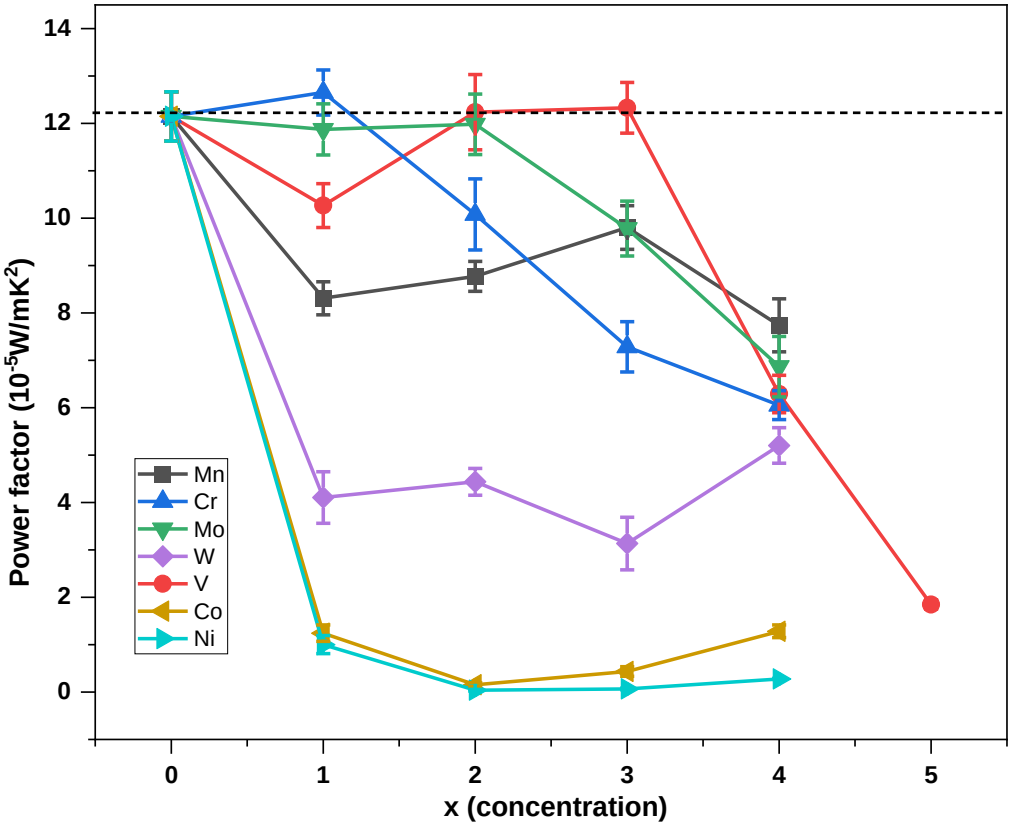

Figure 5. 16 Power factor of $Fe_{11-x}Y_xTi_3Al_6$ (Y = Cr, Mo, W, Mn, V, Co and Ni) annealed bulk samples

It can be seen from Fig 5.16 that there is no significant improvement in the PF by substituting $Fe_{11}Ti_3Al_6$ alloy with a fourth element (i.e., with Mn, Cr, Mo, W, V, Co and Ni, respectively) observed. Due to high electrical resistivity values, W, Co and Ni-substituted samples **(Purple, golden and cyan curve)** exhibit poor thermoelectric performance compared to other substituted samples. For other substitutions, most samples also exhibit a PF value that is lower than that in $Fe_{11}Ti_3Al_6$. However, it is worth noting that the PF of a few samples, including $Fe_{10}Cr_1Ti_3Al_6$ **(on the blue curve)**, $Fe_9Mo_2Ti_3Al_6$ **(on pink curve)**, $Fe_9V_2Ti_3Al_6$ and $Fe_8V_3Ti_3Al_6$ **(on red curve)** is comparable to that of $Fe_{11}Ti_3Al_6$. All these samples exhibit a PF value of approximately 12.7x10^{-5}W/mK^{-2}. Compared to $Fe_{11}Ti_3Al_6$, these samples possess higher electrical resistivity, which will result in a reduced electronic contribution to total thermal conductivity. Consequently, the ZT values of these samples could be increased even though the PF is not increased. Therefore, $Fe_{10}Cr_1Ti_3Al_6$, $Fe_9Mo_2Ti_3Al_6$, $Fe_9V_2Ti_3Al_6$ and $Fe_8V_3Ti_3Al_6$ can be considered potential materials to be investigated for further improvement of ZT. In addition, the results from this investigation also show that it is challenging to increase the PF value of this class of materials by elemental substitution.

5.7 Influence of VEC on Seebeck coefficient

The impact of valence electron concentration (VEC) on Seebeck coefficient of $Fe_{11-x}Y_xTi_3Al_6$ (Y=Mn, Cr, Mo, W, V, Co and Ni) annealed bulk samples, is analysed in this section. The purpose of this analysis was to identify the correlation between the VEC and the Seebeck coefficient.

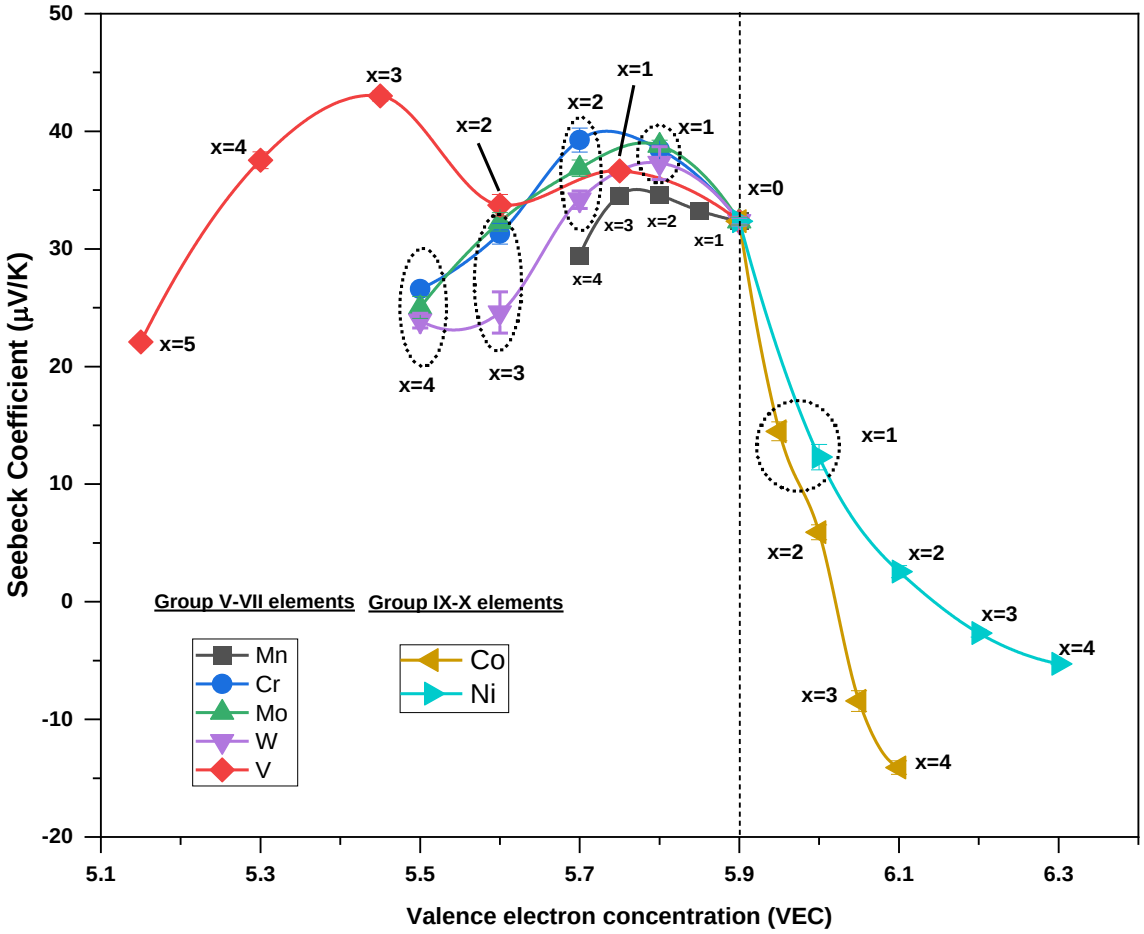

Figure 5. 17 Room temperature Seebeck coefficient as a function of VEC for $Fe_{11-x}Y_xTi_3Al_6$ (Y= Mn, Cr, W Mo V, Co and Ni) samples

Fig 5.17 summarizes the Seebeck coefficient as a function of VEC for all measured samples of $Fe_{11-x}Y_xTi_3Al_6$ (Y=Mn, Cr, Mo, W, V, Co and Ni). The elements used for substitution belong to transition metals in Group V-VII and Group IX-X. The results show that the peak Seebeck coefficient occurs at a VEC value between 5.7 and 5.8, except for V substitution. The Seebeck coefficient is positive for the samples having VEC≤ 6 while it is negative for VEC>6. Since $Fe_{11}Ti_3Al_6$ has a VEC of 5.9, substituting Fe with a Group V-VII element can result in a slight reduction in VEC and consequently an increase in the Seebeck coefficient. A similar observation was also reported in Heusler Fe_2VAl-based alloys [118, 119, 279]. It is believed that the enhancement in the Seebeck coefficient is due to the shift of Fermi level towards valence electron band (VEB) in low DOS origin combined

with its steep slope without modifying the band structure as in the case Fe-V-Al alloys[118, 279]. However, in the case of $Fe_{11}Ti_3Al_6$ alloys, the enhancement in the Seebeck coefficient is not as significant as in Fe_2VAl-based alloys [118, 119, 279].

The substitution using Group IX-X elements led to an increase in VEC and a decrease in the Seebeck coefficient initially and then change from p-type materials for n-type materials when VEC>6.0. The increase of VEC is due to the fact that Co and Ni have more valence electrons than the Fe element. As a result, the Fermi level shifts towards the conduction electron band (CEB).

5.8 Selection of promising candidate for further investigation

In the 5.6.2 sub-section, it was concluded that the $Fe_{10}Cr_1Ti_3Al_6$, $Fe_9Mo_2Ti_3Al_6$, $Fe_9V_2Ti_3Al_6$ and $Fe_8V_3Ti_3Al_6$ samples can be considered as potential thermoelectric candidates for further development. The present section focuses on the selection of promising samples for temperature-dependent thermoelectric properties investigations.

The thermoelectric properties of Fe-V-Ti-Al-based alloys have already been investigated widely in various studies[119, 280]. $Fe_2V_{0.78}Ti_{0.30}Al_{0.92}$ is presently identified as a promising thermoelectric candidate. Y.Nishino et al. fabricated $Fe_2V_{0.78}Ti_{0.30}Al_{0.92}$ samples using arc-melting technique and observed a peak PF of 3.7 $x10^{-3}$ W/mK^2 at 300K with the Seebeck coefficient of +100µV/K and resistivity of 2µΩm[119]. Considering that Fe-Ti-V-Al based alloys have been extensively studied and reported, this work will explore the material compositions with Cr and Mo substitution, which have not been investigated.

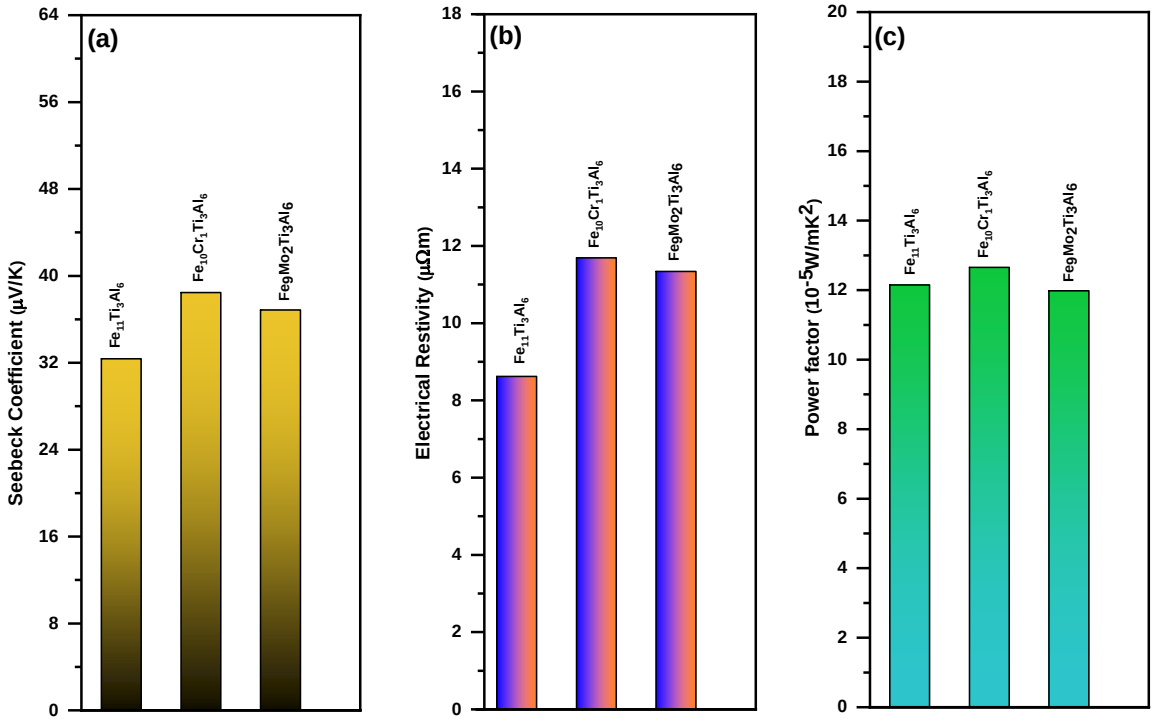

Figure 5. 18 (a) Seebeck coefficient, (b) Electrical Resistivity and (c) Power Factor of $Fe_{11}Ti_3Al_6$, $Fe_{10}Cr_1Ti_3Al_6$ and $Fe_9Mo_2Ti_3Al_6$ samples

Fig 5.18 (a-c) represents the Seebeck coefficient, electrical resistivity, and PF of $Fe_{11}Ti_3Al_6$, $Fe_{10}Cr_1Ti_3Al_6$ and $Fe_9Mo_2Ti_3Al_6$ samples, respectively. It can be seen from Fig 5.18 (c) that these samples have similar PF values of around $12x10^{-5}$ W/mK^2. $Fe_{10}Cr_1Ti_3Al_6$ and $Fe_9Mo_2Ti_3Al_6$ are considered for further investigation because both samples exhibit high Seebeck coefficient and electrical resistivity values compared to the $Fe_{11}Ti_3Al_6$ sample. Since these samples have higher electrical resistivity, they are likely to have a lower electronic thermal conductivity than $Fe_{11}Ti_3Al_6$, which can lead to an improvement in their ZT values if the PF values can be kept unchanged. Furthermore, the fabrication cost of $Fe_{10}Cr_1Ti_3Al_6$ is likely to be significantly lower than that of $Fe_9Mo_2Ti_3Al_6$ because Cr is much cheaper than Mo. Therefore, the investigation in the next stage will concentrate on $Fe_{10}Cr_1Ti_3Al_6$.

5.9 Limitation of BM-CP-Annealing method

This section compares the properties of BM-CP annealed samples ($Fe_{10}Cr_1Ti_3Al_6$) with the reference samples ($Fe_{11}Ti_3Al_6$) prepared previously using the laser melting technique (LMT)[22]. The comparison may help to identify the limitation of the BM-CP-annealing approach and explore appropriate fabrication for further improvement. Table 5.3 displays the thermoelectric properties of $Fe_{11}Ti_3Al_6$ prepared by LMT and $Fe_{10}Cr_1Ti_3Al_6$ prepared by BM-CP-annealing route.

Table 5. 3 Seebeck coefficient (α), electrical resistivity (ρ) and PF values of BM-CP sample and LMT sample

Sample	Fabrication Route	α (μV/K)	ρ(μΩm)	PF (10^{-5} W/mK^2)
$Fe_{10}Cr_1Ti_3Al_6$	BM-CP followed annealing	+38.46	11.69	12.7
$Fe_{11}Ti_3Al_6$ [22]	LMT[22]	+27	1.04	70

It can be seen in Table 5. 3 that $Fe_{10}Cr_1Ti_3Al_6$ BM-CP annealed sample achieved the Seebeck coefficient of +38.46μV/K, which is approximately 1.4 times higher than the $Fe_{11}Ti_3Al_6$ LMT sample. However, the electrical resistivity of the LMT sample is around 11.2 times lower than the BM-CP sample. Clearly, this extremely high electrical resistivity is probably the main reason for such a low PF of $Fe_{10}Cr_1Ti_3Al_6$, which may be related to the low density of the materials prepared using the BM-CP annealed approach.

The theoretical density of the $Fe_{10}Cr_1Ti_3Al_6$ samples can be calculated using equation (4.1). Its actual density can be measured using the Archimedes method. Table 5. 4 shows the comparison between the theoretical density and actual measured density for the $Fe_{10}Cr_1Ti_3Al_6$. It can be seen that the density of the samples prepared using the BM-CP-annealing method is only 76.6%, indicating that the electrical resistivity of the $Fe_{10}Cr_1Ti_3Al_6$ can be reduced by improving the bulk density of the material.

Table 5. 4 Theoretical and measured density of $Fe_{10}Cr_1Ti_3Al_6$ samples

Sample	Form	Method	Density (g/cm^3)	Relative density
$Fe_{10}Cr_1Ti_3Al_6$	Perfect crystal	Theoretical	6.40	100%
	Bulk (annealed)	Archimedes Method	4.9±0.15	76.6%

5.10 Conclusion

A systematic experimental investigation was carried out to study the effect of elemental substitution on the thermoelectric properties of $Fe_{11}Ti_3Al_6$. The study focused on the substitution of Fe using Mn, Cr, Mo, W, V, Co and Ni, respectively. The XRD analysis shows that the substitution using Mn, Cr, V, Co or Ni does not change the structure of the materials significantly for both milled powders and annealed bulks, which exhibit a phase structure similar to Fe_3Al alloys with only slight shifts in the peaks. On the other hand, the substitution using Mo or W resulted in mixed phases

of Fe_3Al with TiMo or TiW, which may be related to the fact Mo and W belong to different periods in the Periodic Table, which have larger atomic size (noted that Mn, Cr, V, Co and Ni are in the same period with Fe).

Although the substitution has little impact on the structure of materials in most cases, it has a significant influence on the thermoelectric properties of the materials. The thermoelectric properties of the substituted materials change significantly with both element and concentration employed for substitution. The substitution using group V-VII elements can lead to an increase in the Seebeck coefficient, while the substitution using group IX-X elements resulted in a fast decrease in the Seebeck coefficient, leading to a transition from p-type to n-type. The electrical resistivity of $Fe_{11-x}Y_xTi_3Al_6$ also increased compared to $Fe_{11}Ti_3Al_6$, with a significant increase occurring at x=1 or 2, except for V substitution.

An analysis was performed to identify the correlation between the thermoelectric properties and valence electron concentration (VEC) of the materials. It is found that the Seebeck coefficient of $Fe_{11-x}Y_xTi_3Al_6$ (Y=Co and Ni, x=0 to 4) approaches zero when their corresponding VEC is around 6.0. When the substitution was performed using group V-VII elements, the VEC value was smaller than 6.0, resulting in p-type materials. On the other hand, if the substitution was performed using group IX-X elements, the VEC value could become larger than 6.0, resulting in n-type materials. This analysis reveals that $Fe_{11-x}Y_xTi_3Al_6$ behaves like a semiconductor with both p and n-type materials being obtainable through appropriate elemental substitution, similar to the “doping” effect in silicon using boron or phosphorous.

The result also shows that the peak Seebeck coefficient occurs at a VEC value between 5.7 and 5.8 for all p-type samples, except for V element substitution. The experimental results of this study show that all samples substituted using group V-VII elements within a certain concentration range exhibit an increase in the Seebeck coefficient compared to the benchmark $Fe_{11}Ti_3Al_6$. However, only $Fe_{10}Cr_1Ti_3Al_6$ demonstrate an improvement in the PF due to a moderate increase in the electrical resistivity. Consequently, $Fe_{10}Cr_1Ti_3Al_6$ has been chosen as a candidate for further investigation in the next stage of research.

Chapter 6: Effect of sintering temperature on thermoelectric properties of $Fe_{10}Cr_1Ti_3Al_6$

6.1 Introduction

In the previous chapter, it was found that the $Fe_{10}Cr_1Ti_3Al_6$ sample, fabricated using the BM-CP annealing route, exhibited a higher Seebeck coefficient than the reported $Fe_{11}Ti_3Al_6$ sample produced through the LMT method[22]. However, this identified composition ($Fe_{10}Cr_1Ti_3Al_6$) had a lower PF value than the reported sample[22]. This was likely due to its high electrical resistivity resulting from the low relative density of the sample, as discussed in section 5.9. The literature suggests that the promising thermoelectric material should have a higher relative density[142], which can be achieved for Fe-Al-based alloys by employing the Spark plasma sintering (SPS) powder consolidation method [281].

Researchers have successfully obtained dense bulk samples of Fe-5Al, Fe-5Al-5Mo, Fe_2VAl, Fe_3Al, and Fe-9Cr using the powder metallurgy-SPS route [221, 282]. J. Wang and his co-workers used the MA-SPS route to fabricate Fe_3Al alloys and found that the SPS technique could produce the Fe-Al sample with a relative density close to the theoretical density[283]. Recently, Tolochyn and his co-workers investigated the influence of Spark plasma sintering temperatures on the phase structure of Fe_3Al powders. They found that this consolidation technique is beneficial to produce dense Fe_3Al bulk samples [223]. Rest et al. also conducted a study to consolidate Fe_2VAl powders by using the SPS method. Their findings showed that the sintering of Fe-V-Al samples at high temperatures (1473K under 40MPa) resulted in a bulk sample with a relative density greater than 99% [284]. Similarly, the densification of Fe-Cr alloys has also been observed at high sintering temperatures [221]. Overall, these studies suggest that the SPS method can effectively consolidate $Fe_{10}Cr_1Ti_3Al_6$ powder samples, leading to dense bulk samples and potentially reduced electrical resistivity and increased power factor.

The primary objective of this chapter is to investigate whether consolidating $Fe_{10}Cr_1Ti_3Al_6$ milled powders using the Spark Plasma sintering technique can lead to an improvement in the densification and thermoelectric properties of the sample. The sample fabrication process is outlined in the following section, followed by a discussion of the effects of sintering temperatures on

the phase structure, relative density, and thermoelectric properties in sections 6.4-6.5. The remaining sections describe the temperature-dependent-thermoelectric properties.

6.2 Preparation and characterisation of $Fe_{10}Cr_1Ti_3Al_6$ bulk sample

The present section describes the preparation of the $Fe_{10}Cr_1Ti_3Al_6$ milled powder samples and consolidation of the milled sample via the Spark plasma sintering (SPS) technique. The phase structure of non-milled, milled, and sintered samples was experimentally investigated using the XRD technique. The details of used XRD equipment are described in Chapter 3. The obtained diffraction pattern was analysed based on the standard reference files from the database.

6.2.1 Initial mixture

The blended powder of $Fe_{10}Cr_1Ti_3Al_6$ composition was prepared by manually mixing 60.9 wt.% of Fe, 5.7 wt.% of Cr,15.7 wt.% of Ti and 17.7 wt.% of Al powders using the set-up described in Section 3.3. The XRD measurements of blended powder were performed from 30^0 to 90^0 to confirm the presence of an individual element.

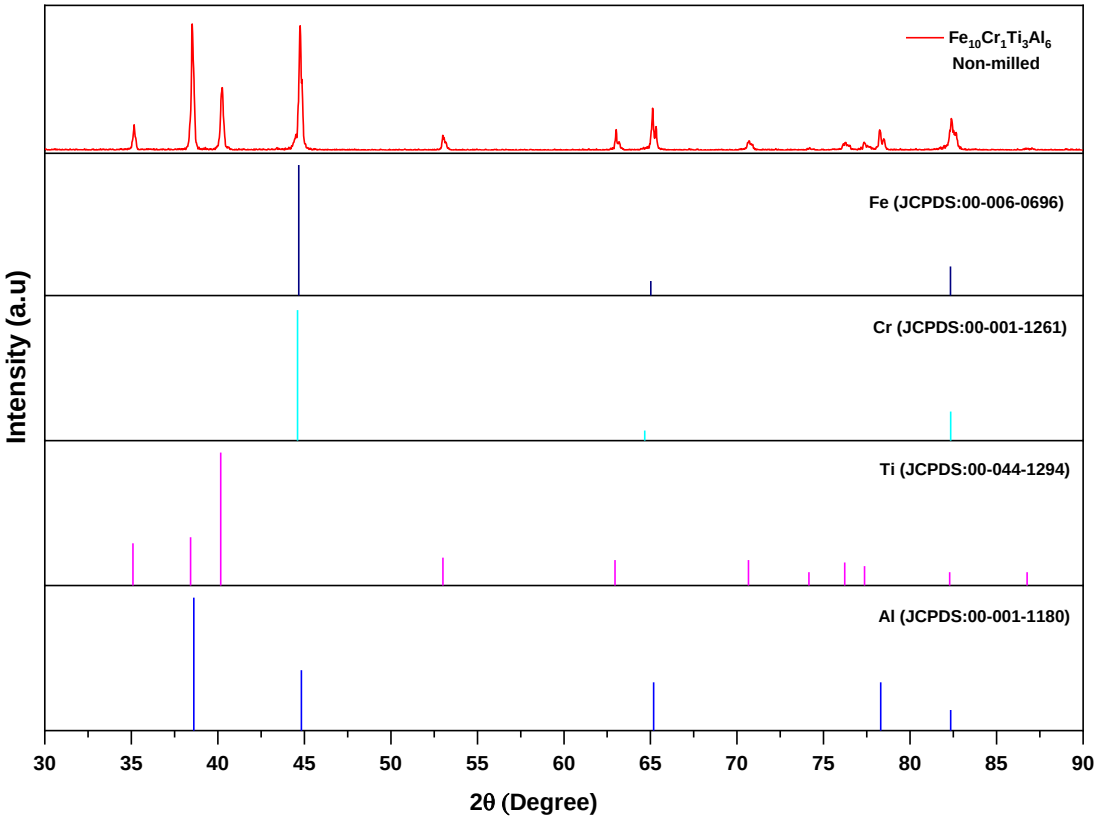

Figure 6. 1 XRD pattern of non-milled $Fe_{10}Cr_1Ti_3Al_6$ powder sample

Fig 6.1 illustrates the XRD pattern of the non-milled powdered sample. The XRD spectra of elemental powders show good agreement with diffraction peak position and intensities of Fe (JCPDS/ICDD:00-006-0696, Cr (JCPDS/ICDD:00-001-1261), Ti (JCPDS/ICDD:00-044-1294) and Al (JCPDS/ICDD:00-001-1180) elements. This analysis confirms the presence of Fe (phase-bcc), Cr (phase-bcc), Ti (phase-hcp) and Al (phase-fcc) elements. It suggests the blended sample demonstrates a mixed phase structure of bcc (body-centred cubic), hcp (hexagonal close-packed) and fcc (face-centred cubic).

6.2.2 Mechanical alloying (MA)

Mechanical alloying (MA) of $Fe_{10}Cr_1Ti_3Al_6$ blended powder was carried out using a planetary ball mill. For that, another blended powder of $Fe_{10}Cr_1Ti_3Al_6$ composition having the amount of 3.42 grams was prepared by adopting a similar procedure as described in the previous sub-section. This blended sample was milled for 5hrs by using the method mentioned in Section 4.2. Around 7-8 blended samples were milled to consolidate the samples at different sintering temperatures.

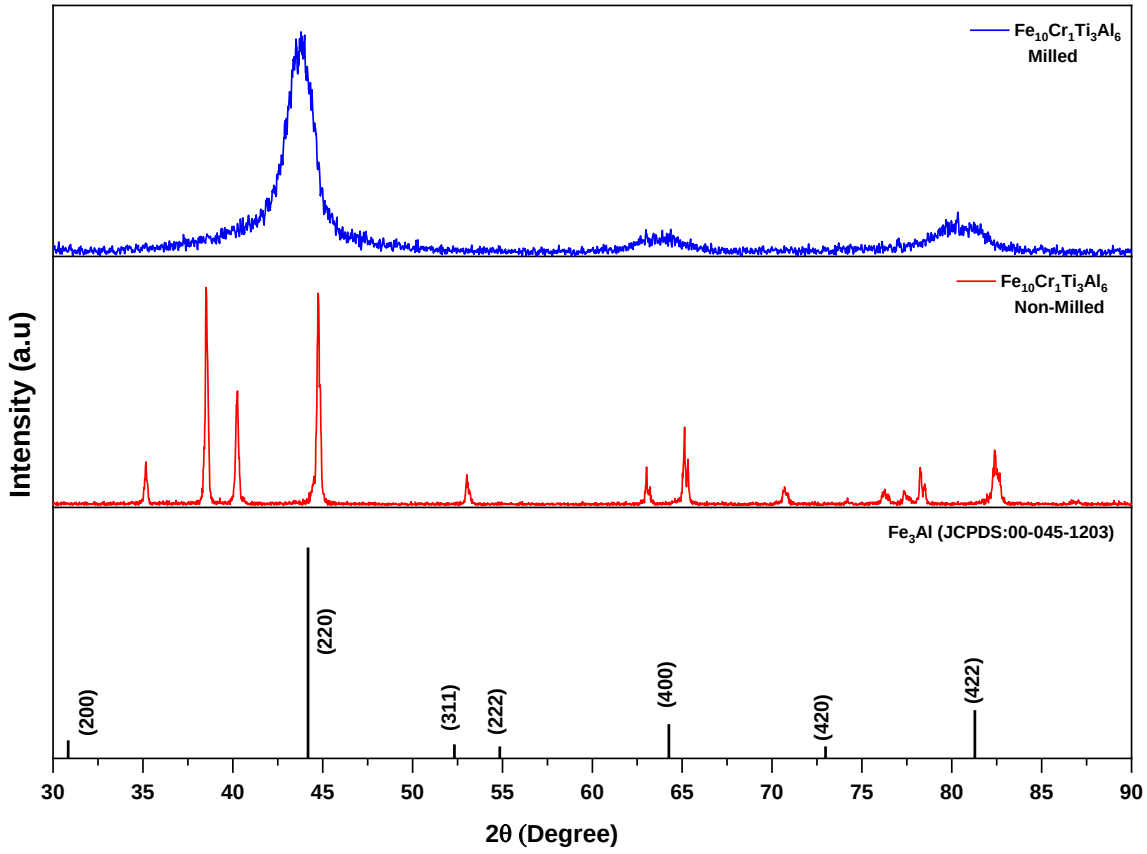

Figure 6. 2 XRD pattern of milled $Fe_{10}Cr_1Ti_3Al_6$ powder sample

Fig 6.2 illustrates the XRD pattern of the milled powder sample. After milling for 5hrs, this composition has achieved a phase structure similar to $Fe_{11}Ti_3Al_6$ milled powder sample and

demonstrated diffraction peaks around 43.80^0, 64^0 and 81^0 diffraction angles. The observed peaks correspond to (220), (400) and (422) plane positions. The position and intensities of peaks of the milled powder indicate that the milled powder sample achieved a phase structure close to Fe_3Al (JCPDS/ICDD:00-045-1203) alloy, and none of the previous peaks from the raw powders was detected.

6.2.3 Influence of sintering temperature on phase structure

In this sub-section, the impact of sintering temperatures on the phase structure of sintered (SPSed) samples was investigated. To do so, $Fe_{10}Cr_1Ti_3Al_6$ milled powders were consolidated into disc-shaped bulk samples (diameter =20mm) using Spark Plasma Sintering (SPS) at sintering temperatures ranging from 700°C to 1100°C for 30 minutes under uniaxial pressure of 48 MPa. The details of SPS equipment, set-up, and procedure for sintering are described in Section 3.5.2.

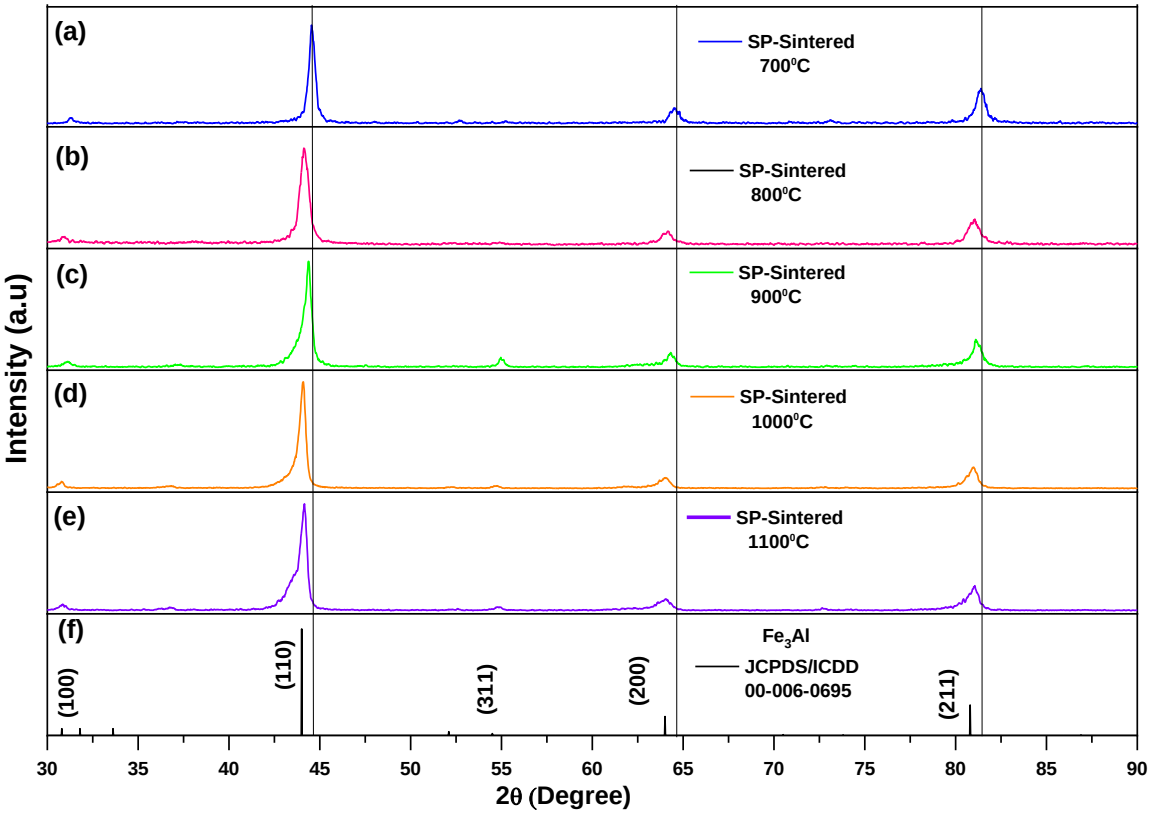

Figure 6. 3 XRD patterns of $Fe_{10}Cr_1Ti_3Al_6$ sintered bulk sample from 700^{0}C to 1100^{0}C

Fig 6.3 represents the XRD patterns for sintered bulk samples at sintering temperatures ranging from 700^{0}C to 1100^{0}C. As the sintering temperature increases, the XRD patterns slightly shift towards the lower angles, suggesting lattice expansion[274]. In addition, above 800^{0}C XRD patterns show a new peak at a diffraction angle of 54.4^{0,} which further confirms that sintered sample

attained phase structure like Fe_3Al alloy[285]. No other phases have been identified, suggesting that titanium and chromium have been successfully incorporated into the Fe_3Al alloy structure. However, it is impossible to pinpoint the exact sites in the crystalline structure where Cr or Ti is located.

6.2.4 EDX analysis and SEM investigation for sample sintered at 1000^0C

This sub-section presents an elemental analysis for the sample sintered at 1000^0C to check the chemical composition. The microstructure of the sample was also examined using the SEM technique. The details of the equipment utilised to perform the EDX (Energy-dispersive X-ray spectroscopy) analysis and SEM investigation are described in Chapter 3. This sample was selected because it displays a high Seebeck coefficient compared to other sintered samples. The thermoelectric measurements for all sintered samples are presented in Section 6.4.

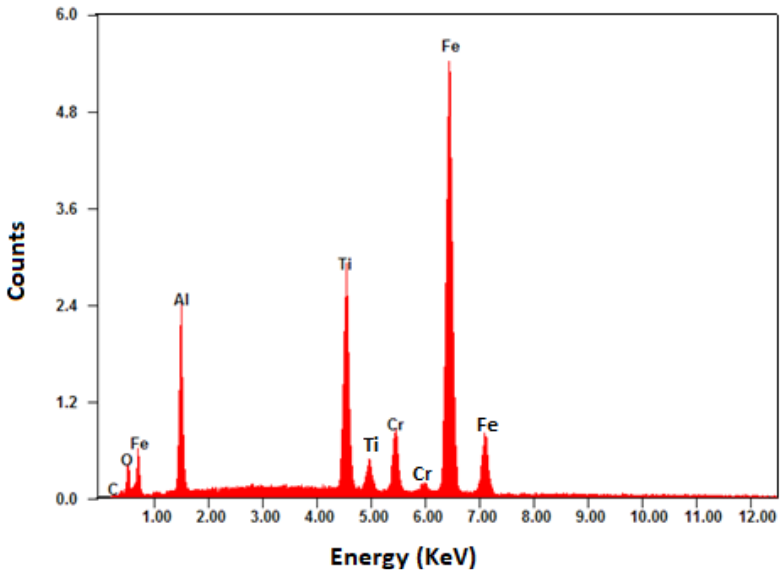

Figure 6. 4 EDX spectrum of sample sintered at 1000^0C

Fig 6.4 displays the EDX spectrum of the sample sintered at 1000^0C. The spectrum shows that the sample contains significant amounts of added elements of Fe, Cr, Ti and Al. The presence of the oxygen and carbon peak is unexpected. The O and C elements are likely to exist at grain boundaries and surfaces of the sample only. The EDX analysis of the sample is presented in Table 6. 1**.** It is seen that all added elements are present after the sintering process with the desired composition. Excluding O and C in Table 6. 1**,** the chemical composition is determined as $Fe_{9.96}Cr_{1.02}Ti_3Al_{4.95,}$ which shows a reasonable agreement with the nominal composition of $Fe_{10}Cr_1Ti_3Al_6$. The results show that the appropriate amount of Cr has been added to the alloy, with the Fe percentage

reduced as expected. The percentage of Al appears to be less than the nominal percentage, indicating that a small amount of Al might be lost during the alloying or sintering process.

Table 6. 1 EDX analysis for sample sintered at 1000^0C

Element	Measured Weight (%)	Measured Atomic (%)	Calculated Weight (%) excluding O and C	Calculated Molar amount from Calculated Weight (%)
Fe	59.47	44.93	62.79	9.96
Cr	5.67	4.60	5.98	1.02
Ti	15.36	13.53	16.20	3
Al	14.23	22.24	15.02	4.95
O	4.36	11.49	----------	----------
C	0.91	3.21	----------	----------

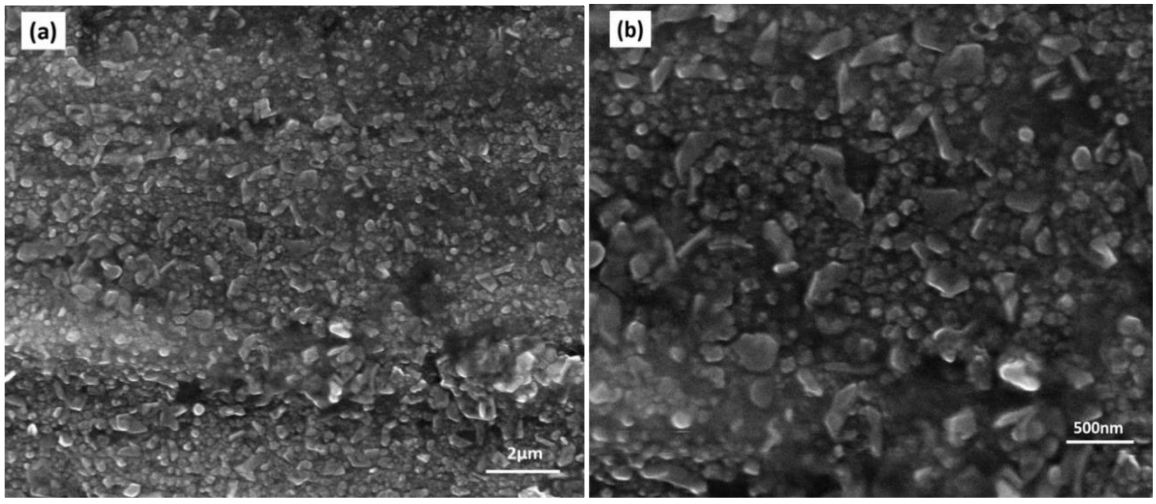

Figure 6. 5 SEM micrographs of $Fe_{10}Cr_1Ti_3Al_6$ sample sintered at 1000^0C (a) Magnification=60K, scale=2µm (b) Magnification=120K, scale=500nm

Fig 6.5 (a-b) shows SEM micrographs of the sample sintered at 1000^0C at different magnifications. These images were captured on the polished surface of the sample at INCAR, Spain. The polishing process was carried out in three steps. Initially, SiC paper (P1200) and water were used to polish the sample. Subsequently, the sample was polished using a cloth pad and water-based alumina suspensions of 3µm. To achieve a highly polished surface, polishing was performed using alumina suspensions of 1µm and a cloth pad.

It can be observed that the sample is composed of large and small size grains, which suggests the presence of bimodal grains. Some grains are quite small, below 500 nm. This finding suggests

grain refinement engineering could be adopted to investigate the thermoelectric properties of the Fe-Cr-Ti-Al sample composed of different-size grains[48, 286, 287].

6.3 Effect of sintering temperatures on relative density

The density measurements for samples sintered between 700-1100^{0}C are presented in this section. The samples were fabricated at different sintering temperatures to achieve the relative bulk density close to the theoretical density based on the BM-SPS fabrication route. The density measurements could assist in concluding whether, through this strategy, the dense bulk samples can be produced. The Archimedes method was used to measure the density of sintered bulk samples.

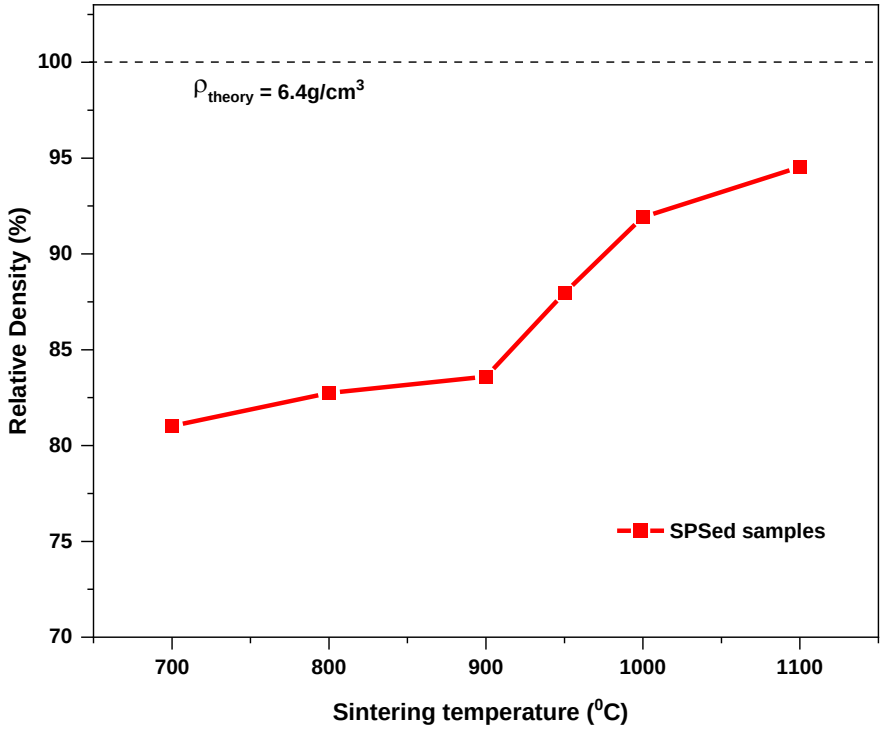

Figure 6. 6 Variation of relative density as the function of sintering temperature

Fig 6.6 represents the variation of relative density as a function of sintering temperatures. The relative density of the sintered sample was calculated using the following equation:

$$\rho_{rel} = \frac{\rho_{SPSed}}{\rho_{theory}} * 100 \quad (6.1)$$

where ρ_{SPSed} is measured density of the sample and ρ_{theory} is the theoretical density of the sample which is equal to 6.4 g/cm^3. The theoretical density was calculated in section 5.9.

Fig 6.6 shows that the relative density increases as the sintering temperature increases. The relative density of the samples sintered at 950^0C is 88%, while those sintered at 1000^0C and 1100^0C possess a relative density of > 91%. Among all the samples, the sample sintered at 1100^0C shows the highest density of 6.05 g/cm^3, which is 1.2 times higher than the BM-CP annealed sample (Density = 4.9 g/cm^3 (section 5.9)). The significant increase in relative density between 900-1000^0C occurred probably due to enhancement in atomic diffusion ability, resulting in increased contact between particles and decreased pores[288]. This sort of variation was also observed in Fe-Al alloys[288-290].

The density measurements indicate that consolidation of $Fe_{10}Cr_1Ti_3Al_6$ powders at higher sintering temperatures >1000^0C via the SPS technique is useful for producing dense-bulk samples with relative density >90%. This increase in densification may also improve connectivity between grains[231], and consequently, the increase in electrical and thermal properties of the materials might be observed.

6.4 Influence of sintering temperatures on the room temperature thermoelectric properties

The present section investigates the effect of spark plasma sintering temperatures on the room-temperature thermoelectric properties of the sample in Fig 6.7-6.8. The transport characterization was performed to evaluate whether the dense samples have the potential to demonstrate better thermoelectric performance than BM-CP annealed samples. At each sintering temperature, one sample was fabricated for these measurements. The standard deviation was calculated from the data set obtained by measuring the parameters on both faces of the disc by making connections at different contact positions.

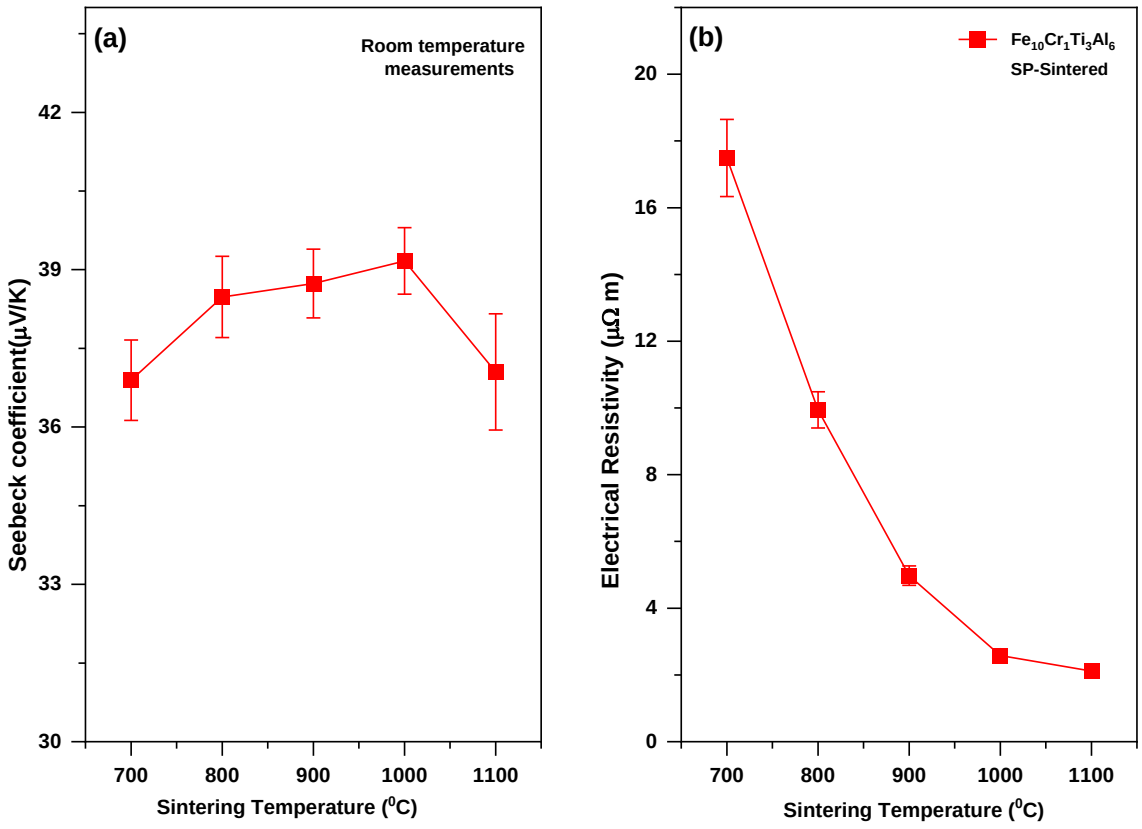

Figure 6. 7 Dependence of (a) Seebeck coefficient and (b) Electrical resistivity on the sintering temperatures

Fig 6.7 (a) illustrates the impact of spark plasma sintering temperatures on the Seebeck coefficient. The sign of the Seebeck coefficient for all sintered samples is positive, implying that all samples are p-type materials. The sample sintered at 1000^0C exhibited the peak value of the Seebeck coefficient of 39.15μV/K. This peak value is 45 % higher than the previously reported p-type Fe-Ti-Al sample[22].

Fig 6.7 (b) displays the dependence of electrical resistivity (ρ) on the sintering temperatures. As the sintering temperature increases, the electrical resistivity decreases. The sample sintered at 1100^0C attained the lowest resistivity value of 2μΩm. The reduction of the electrical resistivity likely occurred due to the increase of the relative density with sintering temperature, which probably improved the connectivity between grains. Consequently, the enhancement in carrier mobility occurred[231, 291, 292]. It can be noted that the SPS sample sintered at temperature ≥ 800^oC displayed lower electrical resistivity than BM-CP annealed samples. The detailed comparison between BM-CP and BM-SPS samples is described in Section 6.5.

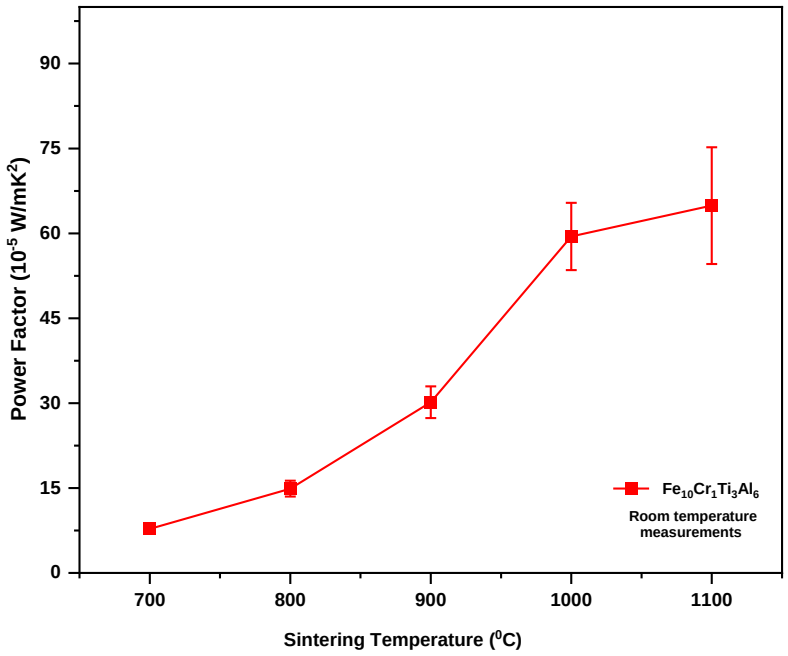

Figure 6. 8 Dependence of Power factor on the sintering temperatures

The PF of the sample was calculated using the Seebeck coefficient and electrical resistivity measurements based on Eq (4.2). Fig 6.8 shows the dependence between the PF and sintering temperatures. As the sintering temperature increases, PF increases as well. The significant increase in PF occurs due to a decrease in electrical resistivity, while the Seebeck coefficient remains relatively unchanged. The sample sintered at 1100^0C exhibits the highest PF value of $64x10^{-5}$ W/mK^2, which is approximately 5 times higher than $Fe_{10}Cr_1Ti_3Al_6$ BM-CP annealed sample, 1.40 times higher than Ti-Ni-Si [129] and comparable to $Al_2Fe_3Si_3$[19]. However, the higher PF achieved for Fe-Cr-Ti-Al at room temperature is approximately three times lower than $Fe_2VAl_{1.6}$[293].

6.5 Comparison of BM-CP and BM-SPS Sample

The thermoelectric properties of $Fe_{10}Cr_1Ti_3Al_6$ bulk samples fabricated via BM-CP and BM-SPS routes are compared in this section. This comparison is performed to identify the most suitable preparation route to produce promising Fe-Cr-Ti-Al thermoelectric bulk materials. Table 6. 2 represents the Seebeck coefficient, electrical resistivity, and PF value $Fe_{10}Cr_1Ti_3Al_6$ sample via different consolidation methods.

Table 6. 2 Comparison of relative density, Seebeck coefficient (α), resistivity (ρ), and PF of $Fe_{10}Cr_1Ti_3Al_6$ BM-CP annealed and BM-SPSed samples

Fabrication route	**Process /Conditions**		**Relative density (%)**	**α (μV/K)**	**ρ (μΩm)**	**PF (10^{-5} W/mK^2)**
BM-CP	Annealing	700^{0}C	76.6	+38.46	11.69	12.7
BM-SPS	Sintering	700^{0}C	81	+36.89	17.49	7.78
		800^{0}C	82.7	+38.48	9.94	14.9
		900^{0}C	83.6	+38.73	4.97	30.2
		1000^{0}C	92	+39.16	2.58	59.4
		1100^{0}C	94.5	+37.05	2.11	64.9

The samples sintered at temperatures ranging from 800^{0}C to 1100^{0}C exhibited higher PF values and lower electrical resistivity compared to the BM-CP annealed sample. Notably, the sample sintered at 1100^{0}C demonstrated the highest value of PF of 64x10^{-5}W/mK^2, which is approximately five times higher than that of the BM-CP annealed sample. It can be clearly seen that BM-SPS samples demonstrate better thermoelectric properties than BM-CP annealed samples due to having high electrical conductivity (i.e low electrical resistivity) and high relative density. Based on this comparison, it can be concluded that the BM-SPS route is beneficial for producing $Fe_{10}Cr_1Ti_3Al_6$ thermoelectric materials rather than the BM-CP route.

6.6 Temperature-dependent thermoelectric properties

The temperature-dependent Seebeck coefficient, electrical resistivity, electronic thermal conductivity, and lattice thermal conductivity for sample sintered at 1000^{0}C are represented in this section. Most thermoelectric material such as Skutterudite, Half-Heusler and Pb-Te demonstrates peak thermoelectric performance at higher temperatures due to the increase of the Seebeck coefficient and electrical conductivity as the function of temperature[294]. The sample sintered at 1000^{0}C exhibits the highest Seebeck coefficient compared to other sintered samples. Based on the previous studies, it is expected that this sintered sample could display the highest thermoelectric performance at higher temperatures. Due to this reason, the sample sintered at 1000^{0}C was selected for temperature-dependent measurement.

6.6.1 Seebeck coefficient and resistivity

The Seebeck coefficient and electrical resistivity of the $Fe_{10}Cr_1Ti_3Al_6$ sintered sample was measured simultaneously in the helium atmosphere using the ULVAC ZEM-3 system (details have been described in Section 3.6.6). The 20mm disc bulk samples were cut into a couple of bars with dimensions of 2x2x10mm for temperature-dependent measurements. Fig 6.9 shows the temperature dependence of the Seebeck coefficient and resistivity of the sample from 51^{0}C to 780^{0}C.

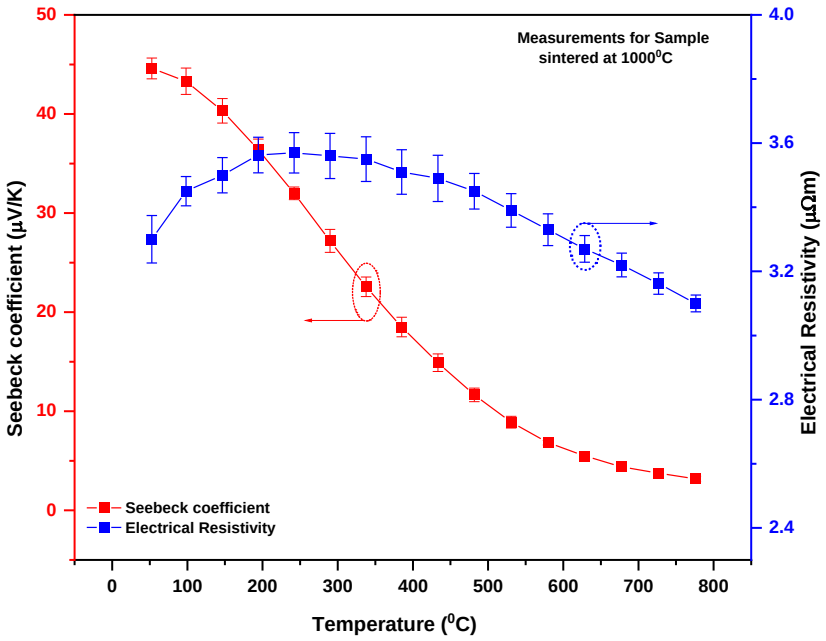

Figure 6. 9 Temperature dependence of Seebeck coefficient and resistivity for $Fe_{10}Cr_1Ti_3Al_6$ sample sintered at 1000^{0}C

The Seebeck coefficient (**red curve**) of the sample decreases with increasing temperature and displays p-type behaviour over the whole temperature range. The decrease in the Seebeck coefficient at high temperatures can be attributed to an increase in thermally excited carriers across the pseudo-gap. The peak Seebeck value of 45μV/K is obtained at 53^{0}C. A similar trend was reported in Fe-Mn-Ti-Sn[128] and Fe_2TiSn[257, 295]. The peak Seebeck coefficient obtained in this work is 1.72 times higher than Fe-Ti-Sn[128, 296, 297] and 1.32 times higher than Fe-Mn-Ti-Sn[128]. However, this peak Seebeck value is approximately three times lower than $Al_2Fe_3Si_3$ [19] and $Fe_2VAl_{1.4}$ [293].

The electrical resistivity of the sample (**blue curve**) increases from 3.3μΩm to 3.58μΩm with increasing temperature from 53^{0}C to 242^{0}C. While beyond 242^{0}C, the electrical resistivity slightly decreases with increasing temperature. The fact that the Seebeck coefficient and electrical resistivity decrease with increasing temperature in the temperature range of 242-776^{0}C indicates that

the sample exhibits hopping conduction over this temperature range. However, there is a significant difference between the temperature for the peak Seebeck coefficient (53^0C) and that for the peak electrical resistivity (242^0C). Such a large difference is unusual and might be associated with the magnetic properties of the material, which needs to be further investigated. At 53^0C, the resistivity value for the $Fe_{10}Cr_1Ti_3Al_6$ sample is approximately similar to the Fe-Mn-Ti-Sn and 0.76 times lower than the Fe-Ti-Sn sample[128].

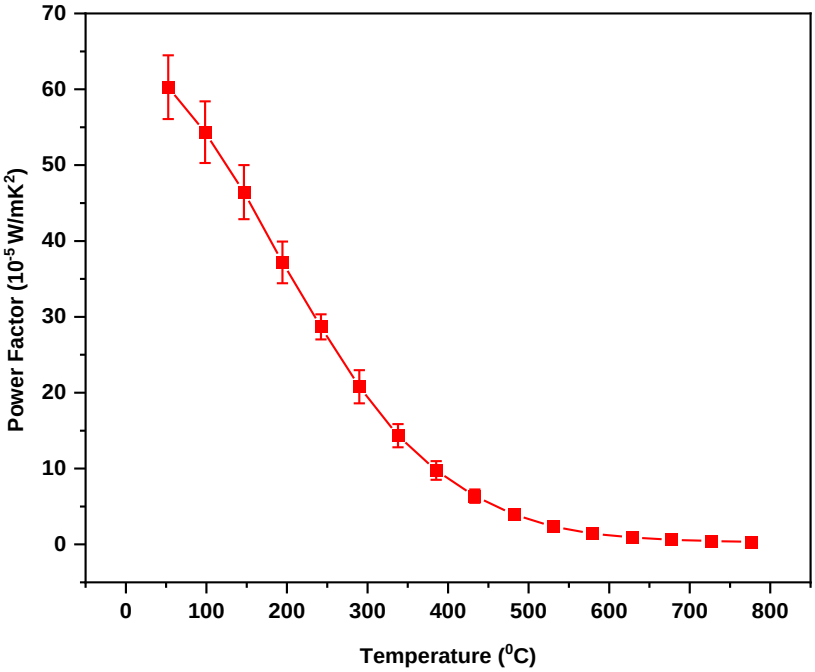

Figure 6. 10 Temperature dependence of power factor for $Fe_{10}Cr_1Ti_3Al_6$ sample sintered at 1000^0C

Fig 6.10 illustrates the temperature dependence of PF. The PF drops from $60x10^{-5}$ W/mK^2 to $0.4x10^{-5}$ W/mK^2 with an increase in temperature from 53^0C to 780^0C. It can be seen that the decrease is mainly due to a significant drop in the Seebeck coefficient. The highest PF value obtained for $Fe_{10}Cr_1Ti_3Al_6$ is $60x10^{-5}$ W/mK^2, which is four times higher than Fe-Ti-Sn[128], 1.72 times higher than Fe-Mn-Ti-Sn[128] and comparable to $Al_2Fe_3Si_3$ alloy[19]. However, this peak value is approximately three times lower than $Fe_2VAl_{1.6}$ sample[293]. The temperature-dependent electronic transport properties measurements demonstrate that the $Fe_{10}Cr_1Ti_3Al_6$ sample exhibits the peak thermoelectric performance in terms of PF value equal to $60x10^{-5}$ W/mK^2 (Fig 6.9) with Seebeck coefficient of 45µV/K (Fig 6.8) around room temperature.

6.6.2 Thermal conductivity

In this sub-section, heat conduction in the $Fe_{10}Cr_1Ti_3Al_6$ sample is described. The thermal conductivity (k) was determined using measured thermal diffusivity (D), density (ρ_{SPS}) and heat capacity (Cp). The details of the laser flash system (NETZSCH-LFA 457 Micro flash, Germany) have been described in Section 3.6.6. For thermal conductivity measurement, the diameter of a 20mm disc shape bulk sample was cut down into a disc-shaped sample with dimensions of 10mm in diameter and 3mm in thickness. The temperature dependence of electronic (k_e), lattice (k_L) and total thermal (k) conductivities are represented in Fig 6.11-6.12.

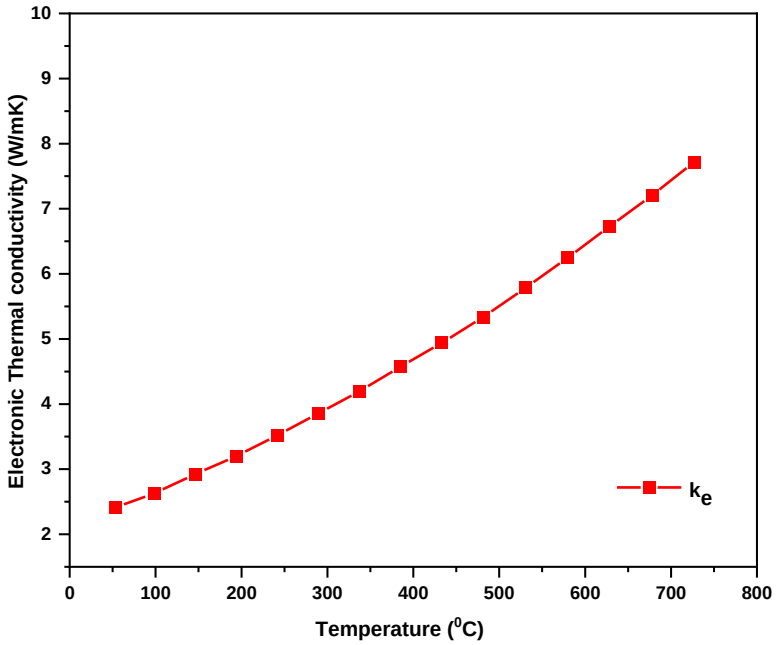

Figure 6. 11 Temperature-dependence of electronic thermal conductivity (K_e) for sample sintered at 1000^{0}C

The electronic thermal conductivity (k_e) is the summation of all heat transferred within the lattice due to the movement of free charge carriers. The k_e of the sample can be calculated by using the Wiedemann-Franz law[47]. This law can be expressed as:

$$K_e = \frac{LT}{\rho} \tag{6.2}$$

Where L is the Lorenz number and ρ is electrical resistivity. Based on the classical free-electron model, the calculated value of L is $2.44 \times 10^{-8} W\Omega K^{-2}$. Fig 6.11 illustrates the temperature-dependent electronic thermal conductivity of the sample. As the temperature increases from 53^{0}C to 727^{0}C, K_e increases from 2.40 to 7.72 W/mK. This increase most likely occurs due to the thermal excitation of charge carriers with increasing temperature.

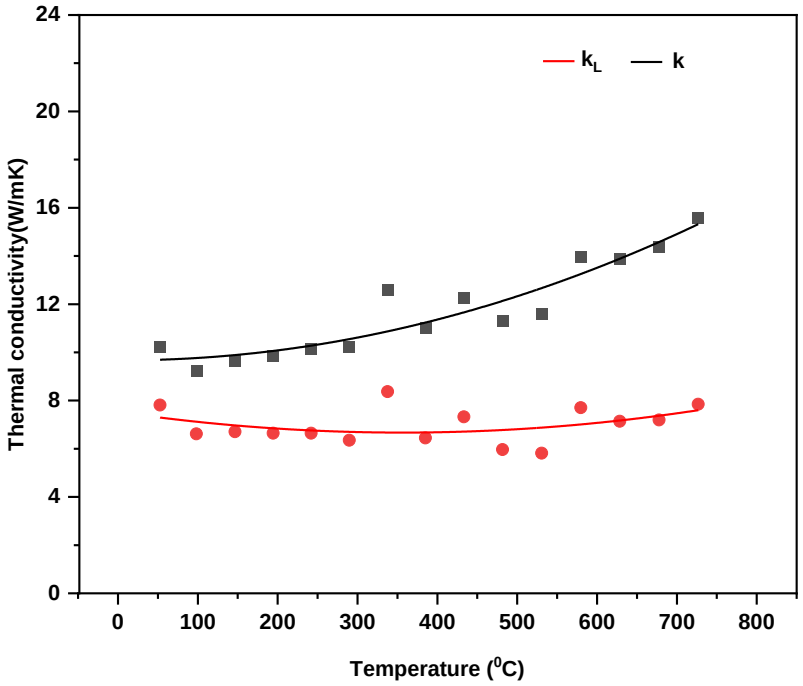

Figure 6. 12 Temperature-dependence of lattice and total thermal conductivity for sample sintered at 1000^0C

Fig 6.12 illustrates the temperature-dependent total (k) and lattice thermal conductivity (k_L) from 53^0C to 727^0C. The total thermal conductivity (k) (**black curve**) increases with increasing temperature, possibly due to the thermal excitation of charge carriers at high temperatures. The thermal conductivity (k) increases from 10.2W/mK at 53^0C to 15.5W/mK at 727^0C. The lattice thermal conductivity (k_L) (**red curve**) is obtained by subtracting the electronic thermal conductivity (k_e) from the measured thermal conductivity (k). The lattice thermal conductivity (K_L) slightly decreases as the temperature increases from 53^0C to 727^0C. The lowest value of k_L is 5.8W/mK, achieved at 526.85^0C. Moreover, it can be observed that lattice thermal conductivity mainly contributes to total thermal conductivity around room temperature. This observation indicates that the thermal conductivity is primarily dominated by phonons rather than charge carriers at room temperature and such observations are consistent with Fe_2VAl-based alloys[123] and $FeAl_2$ alloy[298].

6.6.3 Dimensionless figure of merit (ZT)

In order to assess the thermoelectric conversion efficiency of the $Fe_{10}Cr_1Ti_3Al_6$ sample at absolute temperature (T), the dimensionless figure of merit (ZT) is calculated from the measured Seebeck coefficient (α), resistivity (ρ) and total thermal conductivity (k) based on the following equation:

$$ZT = \left(\frac{\alpha^2}{\rho k}\right) T \tag{6.3}$$

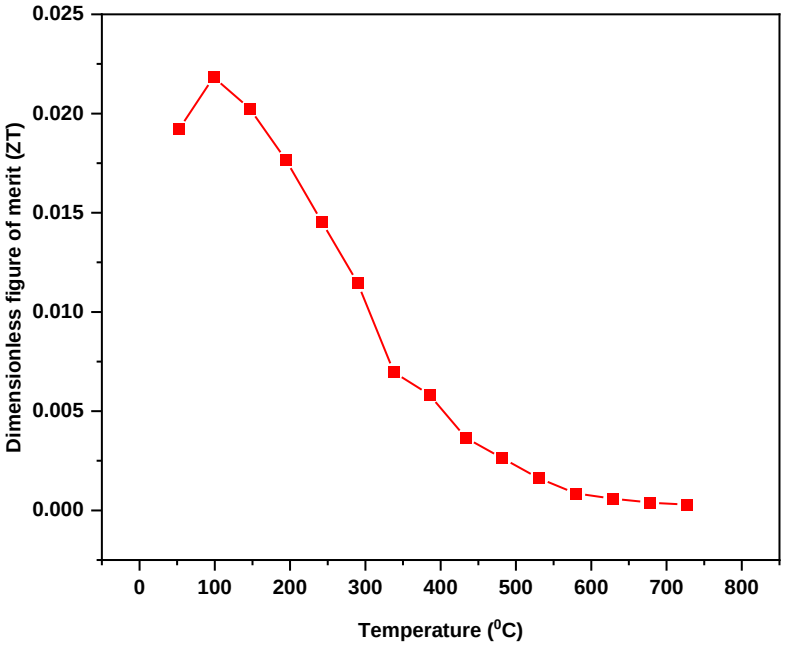

Figure 6. 13 Temperature dependence of dimensionless figure of merit (ZT) for sample sintered at 1000^0C

Fig 6.13 illustrates the ZT as a function of temperature. As the temperature increases, the ZT decreases due to a significant reduction in the PF and an increase in the thermal conductivity. The sample demonstrates an estimated maximum ZT value of 0.02 at 98^0C, which is about 2.5 times higher than the Fe-Ti-Sn[128] and comparable to the Fe-Mn-Ti-Sn[128] samples. However, this maximum ZT value is quite lower than Fe-V-Al[17] and Fe-V-Sb[291]-based alloys.

6.7 Data Analysis of temperature-dependent electronic transport properties

In this section, the data analysis of temperature-dependent electronic transport properties was carried out to understand the conduction mechanism. The data analysis using Small Poloran hopping model could allow us to predict the existence of the hopping conduction mechanism, which has been indicated by temperature-dependent electrical resistivity (Fig 6.9). Various well-established models described in chapter 2 can be used to analyse the charge transport mechanism, such as the Single Parabolic model [299-301], weighted mobility and Small poloran hopping (SPH)[302]. The Single Parabolic model is not suitable for predicting the transport behaviour of the $Fe_{10}Cr_1Ti_3Al_6$ sample because the trend of the temperature dependent Seebeck coefficient should be directly proportional to temperature (T)[299, 301]. However, the measured Seebeck coefficient for this sample shows decreasing trend as the function of temperature, which could be

attempted to understand based on the SPH model. Based on the SPH model, the temperature dependence of the Seebeck coefficient can be expressed as:

$$\alpha = \frac{K_B}{e}\left(\frac{E_a}{K_B T} + A\right) \tag{6.4}$$

where E_a is the activation energy associated with charge carrier generation, and A is a constant related to the kinetic energy of the polarons.

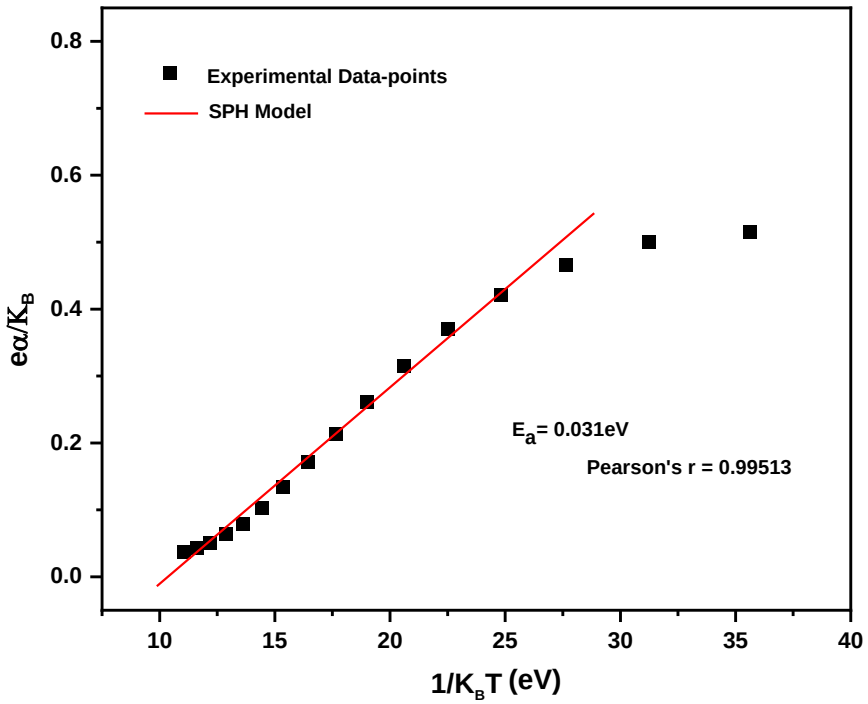

Figure 6. 14 (eα/K_B) vs 1/K_BT plot and linear fitting with SPH model

Fig 6.14 shows the plot of eα/K_B as the function of 1/K_BT. The experimental data points and the fitting line are within good agreement from 11.05K_BT to 24.8 K_BT. On the x-axis, 24.8K_BT is equivalent to 195^{0}C, whereas 11.05 K_BT corresponds to 777^{0}C. The model fitted well between the 195-777^{0}C range, clearly indicating the presence of a hopping mechanism. However, the SPH model fails to explain the behaviour of the Seebeck coefficient below 195^{0}C. The activation energy (E_a) is calculated from the slope of the red line (SPH model), which is equal to 0.031eV.

Similarly, based on the SPH, the temperature dependence of electrical conductivity can be expressed as[302-304]:

$$\sigma=\frac{\sigma_0}{T}\exp\left(-\frac{E_{HOP}}{K_BT}\right) \quad (6.5)$$

where σ is electrical conductivity, σ_0 is a constant, T is the temperature in ^{0}C, K_B is the Boltzmann constant, and E_{HOP} is the energy required for the electron to hop from its original site to an empty localised site.

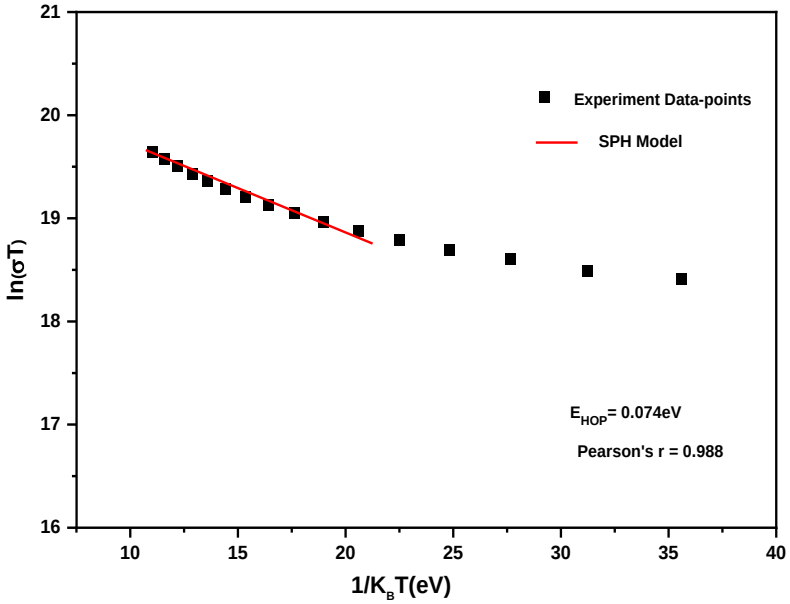

Figure 6. 15 ln σT vs $1/K_BT$ plot and linear fitting with SPH model

Fig 6.15 illustrates the plot of ln σT as the function of the $1/K_BT$. The data points show good agreement with the model line from 11.05K_BT to 22.52 K_BT. On the x-axis, 22.52 K_BT is equivalent to 242^{0}C, whereas 11.05 K_BT corresponds to 777^{0}C. The model fitting indicates the presence of hopping conduction mechanisms at high temperatures. The activation energy (E_{HoP}) is calculated from the slope of the red line (SPH model) is equal to 0.074eV. However, the SPH model fails to explain the conductivity behaviour below 242^{0}C.

6.8 Conclusion

$Fe_{10}Cr_1Ti_3Al_6$ samples were prepared by mechanical alloying and spark plasma sintering route. Compared to BM-CP followed by the annealing route, the BM-SPS route produced $Fe_{10}Cr_1Ti_3Al_6$ dense bulk samples with high relative-density materials (>90 %) at sintering temperature of ≥ 1000^{0}C. It is found that it is beneficial to increase the sintering temperature to improve the densification, electrical conductivity, and PF of the $Fe_{10}Cr_1Ti_3Al_6$ sample. With increasing sintering temperature from 700^{0}C to 1100^{0}C, the room electrical resistivity of the sample decreases from 17.49μΩm to 2.11μΩm. The sample sintered at 1000^{0}C demonstrated the highest temperature-

dependent PF of $60x10^{-5}$ W/mK^2 at 53^{0}C with a Seebeck coefficient of 45µV/K and electrical resistivity of 3.3µΩm. The peak ZT value of 0.022 is observed for the sample at 98^{0}C and demonstrates better thermoelectric performance over the 147-327^{0}C range than the Fe-Mn-Ti-Sn sample. The Small poloran hopping model (SPH) indicates that the hopping mechanism exits between 242^{0}C to 777^{0}C. Overall, this study suggests that the fabrication of $Fe_{10}Cr_1Ti_3Al_6$ thermoelectric material via the BM-SPS route is beneficial compared to the BM-CP route.

Chapter 7: Conclusions and Future work

7.1 Conclusions

The research work was carried out on preparation of low-cost and non-toxic n-type and p-type Fe-Ti-Al alloys based on a bottom-up approach. The phase structure of the prepared samples was analysed using the X-ray diffraction technique. The transport properties including the Seebeck coefficient, electrical resistivity, and power factor of the samples were characterised. The investigations were focused on developing experimental approach for improving the thermoelectric performance of the Fe-Ti-Al alloys based on elemental substitution route. The main attainments of this work are as follows:

- The mechanical alloying of $Fe_{11}Ti_3Al_6$ and $Fe_3Ti_4Al_1$ powder samples was performed by employing a planetary ball mill (5/4) to determine the appropriate ball milling conditions. It was found that with a ball-to-powder ratio of 35:1, the crystalline phase of $Fe_{11}Ti_3Al_6$ alloy can be obtained after 4 hours of milling, which exhibits a phase structure close to the Fe_3Al alloy with only slight shift in intensity peaks, indicating a minor change in lattice constant. However, for $Fe_3Ti_4Al_1$ alloy, the XRD analysis show that only amorphous phase can be obtained using mechanical alloying.
- Employing the cold-press technique, the ball-milled powders of $Fe_{11}Ti_3Al_6$ can be consolidated into disc shaped bulk samples using a hardened steel punch-die set. The relation between the sample density and pressing pressure was investigated. The results show that the density increase with increasing the pressure. The highest density obtained in this study is approximately 80% of the theoretical density for the samples pressed under a pressure of 2200MPa.
- Heat treatments were carried out for all cold-pressed bulk samples at different temperatures ranging from 500 ^{o}C to 900 ^{o}C. The XRD analysis show that no significant changes occurred in the phase structure before and after heat treatment except for slight decrease in the FWHM values, indicating a slight increase in grain size of the alloys. The Seebeck coefficient and electrical resistivity were measured at room temperature and the corresponding power factors were calculated for all $Fe_{11}Ti_3Al_6$ samples before and after heat treatment. It was found that heat-treated samples exhibit better thermoelectric properties compared to those without heat treatment, which can be attributed to an improvement in grain connectivity due to heat treatment. Among all samples investigated, the

samples that were prepared after 5 hours ball milling, followed by cold pressing under 2200MPa and annealing at 700^0C exhibit the highest power factor of $12.1x10^{-5}$ W/mk^2 with a Seebeck coefficient of 32.3μV/K and electrical resistivity of 8.6μΩm. It is concluded that the most suitable conditions for fabricating the $Fe_{11}Ti_3Al_6$ bulk materials based on this processing route are ball milling for 5-hour, cold pressing under 2200MPa and annealing at 700^0C.

- A systematic investigation was carried out to study the effect of elemental substitution on thermoelectric properties of $Fe_{11}Ti_3Al_6$ by replacing the Fe with V,Mn, Cr, Mo, W, Co and Ni. The XRD analysis show that the substitution using the elements from the same period as Fe (e.g., V,Mn, Cr, Co or Ni) does not change the structure of the materials significantly. On the other hand, the substitution using the elements from different period (e.g., Mo or W) resulted in mixed phases, which consist of a Fe_3Al phase and a TiMo or TiW phase. Although the substitution has little impact on the phase structure of the materials in most cases, it has significant impact on the thermoelectric properties. The thermoelectric properties of $Fe_{11-x}Y_xTi_3Al_6$ change with both the substituion element (Y) and concentration (x). The substitution using the elements from group V-VII in Periodic Table can lead to an increase in the Seebeck coefficient (6-32%) while the substitution using the elements from group IX-X resulted in fast decrease in the Seebeck coefficient and can lead to a transition from p-type to n-type.
- The correlation between the thermoelectric properties and valence electron concentration (VEC) of the materials was investigated. It is discovered that the Seebeck coefficient of $Fe_{11-x}Y_xTi_3Al_6$ approaches zero when the corresponding VEC is around 6.0. Furthermore, if the substitution was performed using the elements from group V-VII, the VEC value will be smaller than 6.0 and results in p-type materials. On the other hand, if the substitution was performed using the elements from group IX-X, the VEC value can become larger than 6.0 and results in n-type materials. This discovery reveals that $Fe_{11-x}Y_xTi_3Al_6$ is intermetallic alloy with a pseudo gap, which behaves like a semiconductor with both p-type and n-type materials being obtainable through appropriate elemental substitution, similar to the “doping” effect in silicon using boron or phosphorous. In addition, it is found that the peak Seebeck coefficient occurs at a VEC value between 5.7 to 5.8 for all substitutions investigated (except for V substitution). Since the VEC value of $Fe_{11}Ti_3Al_6$ is 5.9, the substitution using the elements from group V-VII will lead to a reduction in the VEC value and consequently an increase in the Seebeck coefficient.

- The experimental results show that the Seebeck coefficient of +38.4μV/K was obtained in $Fe_{10}Cr_1Ti_3Al_6$ compared to $Fe_{11}Ti_3Al_6$, which has a Seebeck coefficient of +32.3 μV/K. Even though the electrical resistivity of $Fe_{10}Cr_1Ti_3Al_6$ is also increased to 11.7 μΩm from 8.6 μΩm in $Fe_{11}Ti_3Al_6$, this still led to a slight increase in the power factor (from $12.1x10^{-5}$ W/mK^2 to $12.6x10^{-5}$ W/mK^2). Furthermore, a higher electrical resistivity will result in a lower electronic thermal conductivity. Consequently, the ZT value of $Fe_{10}Cr_1Ti_3Al_6$ is anticipated to be higher than that of $Fe_{11}Ti_3Al_6$. This result validates the concept of improving the ZT value through the route of elemental substitution of Fe-Ti-Al alloys.
- Spark Plasma Sintering (SPS) technique was employed to overcome the drawback of the material processing method based on ball-milling followed by cold-pressing and annealing, which produces low density materials (<80%). The effect of SPS processing condition on the density, material structure, the Seebeck coefficient, electrical resistivity and power factor of $Fe_{10}Cr_1Ti_3Al_6$ were investigated. It was found that the sintering temperature has significant impact on the density of the materials and consequently their electrical conductivity and power factor. The $Fe_{10}Cr_1Ti_3Al_6$ alloy with a density of >90% can be achieved using the SPS at a sintering temperature of ≥ 1000 ^{o}C under uniaxial pressure of 48MPa. Due to increase in the sample relative density from 81% to 94%, significant reduction in the electrical resistivity was observed, which changes from 17.5μΩm to 2.1μΩm for the samples sintered at temperature of 700^{0}C and 1100^{0}C, respectively. The sample sintered at 1100^{0}C exhibits the highest power factor of $64x10^{-5}$ W/mK^2, which is approximately 5 times higher than that of the same material prepared using ball-milling, cold-pressing and annealing. It is also 1.40 times higher than Ti-Ni-Si[129] and comparable to $Al_2Fe_3Si_3$[19] and three times lower than $Fe_2VAl_{1.6}$[293].
- The thermoelectric properties of $Fe_{10}Cr_1Ti_3Al_6$ alloy sintered at 1000^{0}C under 48MPa were characterised over a temperature range from 53^{o}C to 780^{o}C. It was observed that the maximum power factor of $60x10^{-5}$ W/mK^2 is achieved at 53^{o}C, with the Seebeck coefficient of 45μV/K and electrical resistivity of 3.3μΩm. The maximum ZT value of 0.02 for this sample is obtained at 98^{0}C. Beyond this temperature, the ZT value decreases quickly with increasing temperature, which is mainly due to a quick drop of the Seebeck coefficient with temperature. The mechanism responsible for this decrease is unknown but might be related to magnetic property of the materials.

7.2 Future Work

The concept of improving thermoelectric properties of Fe-Ti-Al alloys based on the substitution method led to some promising results and preliminary discoveries which needs to be investigated further. Some of the possible research activities for future work are summarised as follows:

- It was discovered that the phase of $Fe_{11-x}Y_xTi_3Al_6$ remains almost the same as the phase of Fe_3Al alloy if substituted using Mn, Cr, V, Co or Ni, while a mixed phase occurs for substitution using Mo or W. It is speculated that this is associated with the fact that Mn, Cr, V, Co and Ni are in the same period as the Fe in Periodic Table, but Mo and W are in the different period to the Fe. It is therefore interesting to confirm if this pattern continues through further experimental study.
- The evidence from this study show that the valence electron concentration (VEC) plays an important role in determining if a $Fe_{11-x}Y_xTi_3Al_6$ alloy is a p-type or n-type. It is interesting to investigate further to find out if this applies to all possible substitutions and, on a wide scale, applies to all intermetallic compounds and alloys.
- The results of Co and Ni substitution show that the Seebeck coefficient (magnitude) of $Fe_{11-x}Y_xTi_3Al_6$ continues to increase with increasing the substitution concentration (x) for all x values investigated in this study. Further study is needed to find out when the Seebeck coefficient will peak corresponding to a x value that is likely to be larger than 4.
- This work reveals that the lattice thermal conductivity of is $Fe_{10}Cr_1Ti_3Al_6$ relatively large compared to the state-of-the-art thermoelectric materials. In order improve its ZT, the possibility and strategies to reduce the lattice thermal conductivity of $Fe_{10}Cr_1Ti_3Al_6$ alloys needs to be accessed.
- It is observed that a fast decrease in the Seebeck coefficient occurs with increasing temperature, which is companied by much less significant change in the electrical resistivity. The mechanisms responsible for this are not understood. It is speculated that this may be associated with the magnetic properties of the $Fe_{10}Cr_1Ti_3Al_6$ alloy. An in-depth understanding of this problem could lead to the possibility of further improvement in its thermoelectric properties.
- DFT calculation of the band structure for $Fe_{11}Ti_3Al_6$ and $Fe_{10}Cr_1Ti_3Al_6$ could help to understand the exact reasons for the improvement in the Seebeck coefficient due to elemental substitution.
- Attempt to understand the reasons for formation of the amorphous phase by ball milling of $Fe_3Ti_4Al_1$ powders could lead to a success in fabricating $Fe_3Ti_4Al_1$ using ball milling

method that will facilitate an easy approach for experimental study of elemental substitution.

References

[1] V. Masson-Delmotte, P. Zhai, H.-O. Pörtner *et al.*, "Global warming of 1.5 C," *An IPCC Special Report on the impacts of global warming of,* vol. 1, no. 5, 2018.

[2] A. Nurhayati, "Utilization of Alternative Renewable Heat Sources to Produce Electrical Energy." pp. 246-249.

[3] F. Martins, C. Felgueiras, M. Smitkova *et al.*, "Analysis of fossil fuel energy consumption and environmental impacts in European countries," *Energies,* vol. 12, no. 6, pp. 964, 2019.

[4] https://www.statista.com/statistics/282774/global-product-demand-outlook-worldwide/.

[5] Z.-G. Chen, G. Han, L. Yang *et al.*, "Nanostructured thermoelectric materials: Current research and future challenge," *Progress in Natural Science: Materials International,* vol. 22, no. 6, pp. 535-549, 2012.

[6] E. Vine, "Breaking down the silos: the integration of energy efficiency, renewable energy, demand response and climate change," *Energy efficiency,* vol. 1, no. 1, pp. 49-63, 2008.

[7] R. Freer, and A. V. Powell, "Realising the potential of thermoelectric technology: A Roadmap," *Journal of Materials Chemistry C,* vol. 8, no. 2, pp. 441-463, 2020.

[8] S. Patidar, "Applications of thermoelectric energy: a review," *International Journal for Research in Applied Science and Engineering Technology,* vol. 6, no. 5, pp. 1992-1996, 2018.

[9] C. B. Vining, "An inconvenient truth about thermoelectrics," *Nature materials,* vol. 8, no. 2, pp. 83-85, 2009.

[10] J. Wei, L. Yang, Z. Ma *et al.*, "Review of current high-ZT thermoelectric materials," *Journal of Materials Science,* vol. 55, no. 27, pp. 12642-12704, 2020.

[11] B. Qin, Y. Zhang, D. Wang *et al.*, "Ultrahigh average ZT realized in p-type SnSe crystalline thermoelectrics through producing extrinsic vacancies," *Journal of the American Chemical Society,* vol. 142, no. 12, pp. 5901-5909, 2020.

[12] Y. Wu, Z. Chen, P. Nan *et al.*, "Lattice strain advances thermoelectrics," *Joule,* vol. 3, no. 5, pp. 1276-1288, 2019.

[13] A. Olvera, N. Moroz, P. Sahoo *et al.*, "Partial indium solubility induces chemical stability and colossal thermoelectric figure of merit in Cu 2 Se," *Energy & Environmental Science,* vol. 10, no. 7, pp. 1668-1676, 2017.

[14] C.-J. Liu, H.-C. Lai, Y.-L. Liu *et al.*, "High thermoelectric figure-of-merit in p-type nanostructured (Bi, Sb) 2 Te 3 fabricated via hydrothermal synthesis and evacuated-and-encapsulated sintering," *Journal of Materials Chemistry,* vol. 22, no. 11, pp. 4825-4831, 2012.

[15] T. R. Wei, C. F. Wu, F. Li *et al.*, "Low-cost and environmentally benign selenides as promising thermoelectric materials," *Journal of Materiomics,* vol. 4, no. 4, pp. 304-320, 2018.

[16] D. M. Rowe, *Modules, systems, and applications in thermoelectrics*: CRC press, 2012.

[17] E. Alleno, "Review of the thermoelectric properties in nanostructured Fe2VAl," *Metals,* vol. 8, no. 11, pp. 864, 2018.

[18] B. C. Sales, "Novel thermoelectric materials," *Current Opinion in Solid State and Materials Science,* vol. 2, no. 3, pp. 284-289, 1997.

[19] A. Srinithi, H. Sepehri-Amin, Y. Takagiwa *et al.*, "Effect of microstructure on the electrical conductivity of p-type Fe–Al–Si thermoelectric materials," *Journal of Alloys and Compounds,* vol. 903, pp. 163835, 2022.

[20] S. Banik, and P. P. Kumar, “Investigation of electronic structure of transition metal silicides MnSi1. 75 and CoSi for enhanced thermoelectric properties,” *Solid State Communications,* vol. 307, pp. 113807, 2020.

[21] Y. Huang, H. Nagai, K. Hayashi *et al.*, “Preparation and thermoelectric properties of pseudogap intermetallic (Ti1-xVx) NiSi solid solutions,” *Journal of Alloys and Compounds,* vol. 771, pp. 111-116, 2019.

[22] J. García-Cañadas, N. J. E. Adkins, S. McCain *et al.*, “Accelerated Discovery of Thermoelectric Materials: Combinatorial Facility and High-Throughput Measurement of Thermoelectric Power Factor,” *ACS Combinatorial Science,* vol. 18, no. 6, pp. 314-319, 2016.

[23] T. J. Seebeck, *Abhandlungen der Deutschen Akademie der Wissenschaften zu Berlin 1822*, p.^pp. 289.

[24] E. Velmre, "Thomas Johann Seebeck and his contribution to the modern science and technology." pp. 17-24.

[25] R. Benedict, *Manual on the Use of Thermocouples Temperature Measurement*: ASTM special technical publications, 1974.

[26] F. A. Peltier, *Notice sur la vie et les travaux scientifiques de J.C.A. Peltier*: Edouard Bautruche, 1847.

[27] E. Lenz, “Einige Versuche im Gebiete des Galvanismus,” *Annalen der Physik,* vol. 120, no. 6, pp. 342-349, 1838.

[28] W. Thomson, *On a Mechanical Theory of Thermo-Electric Currents*, : Proceedings of the Royal Society of Edinburgh

[29] L. Rayleigh, “XLIII. On the thermodynamic efficiency of the thermopile,” *The London, Edinburgh, and Dublin Philosophical Magazine and Journal of Science,* vol. 20, no. 125, pp. 361-363, 1885.

[30] E. Altenkirch, “Elektrothermische Kälteerzeugung und reversible elektrische Heizung,” *Physikalische Zeitschrift,* vol. 12, pp. 920-924, 1911.

[31] A. Ioffe, “The problem of new energy sources,” *The socialist reconstruction and science,* vol. 1, pp. 23, 1932.

[32] D. Beretta, N. Neophytou, J. M. Hodges *et al.*, “Thermoelectrics: From history, a window to the future,” *Materials Science and Engineering: R: Reports,* vol. 138, pp. 100501, 2019.

[33] H. Goldsmid, and R. Douglas, “The use of semiconductors in thermoelectric refrigeration,” *British Journal of Applied Physics,* vol. 5, no. 11, pp. 386, 1954.

[34] M. Vedernikov, and E. Iordanishvili, "AF Ioffe and origin of modern semiconductor thermoelectric energy conversion." pp. 37-42.

[35] R. Chasmar, and R. Stratton, “The thermoelectric figure of merit and its relation to thermoelectric generators,” *International journal of electronics,* vol. 7, no. 1, pp. 52-72, 1959.

[36] B. Blanke, J. Birden, K. Jordan *et al.*, *Nuclear battery-thermocouple type summary report*, Mound Lab., Miamisburg, Ohio, 1960.

[37] V. Parsonnet, A. D. Berstein, and G. Y. Perry, “The nuclear pacemaker: is renewed interest warranted?,” *The American journal of cardiology,* vol. 66, no. 10, pp. 837-842, 1990.

[38] C. Bhandari, and D. Rowe, “Thermal conductivity of highly disordered semiconductor alloys,” *Journal of Physics D: Applied Physics,* vol. 10, no. 5, pp. L59, 1977.

[39] D. Rowe, “Theoretical optimization of the thermoelectric figure of merit of heavily doped hot-pressed germanium-silicon alloys,” *Journal of Physics D: Applied Physics,* vol. 7, no. 13, pp. 1843, 1974.

[40] D. Rowe, V. Shukla, and N. Savvides, “Phonon scattering at grain boundaries in heavily doped fine-grained silicon–germanium alloys,” *Nature,* vol. 290, no. 5809, pp. 765-766, 1981.

[41] G. S. Nolas, J. Sharp, and H. J. Goldsmid, "The phonon—glass electron-crystal approach to thermoelectric materials research," *Thermoelectrics*, pp. 177-207: Springer, 2001.
[42] L. D. Hicks, and M. S. Dresselhaus, "Effect of quantum-well structures on the thermoelectric figure of merit," *Physical Review B,* vol. 47, no. 19, pp. 12727, 1993.
[43] L. Hicks, T. Harman, X. Sun *et al.*, "Experimental study of the effect of quantum-well structures on the thermoelectric figure of merit," *Physical Review B,* vol. 53, no. 16, pp. R10493, 1996.
[44] T. M. Tritt, "Holey and unholey semiconductors," *Science,* vol. 283, no. 5403, pp. 804-805, 1999.
[45] J. Blatt, *Thermoelectric power of metals*: Springer Science & Business Media, 2012.
[46] Y. Apertet, and C. Goupil, "On the fundamental aspect of the first Kelvin's relation in thermoelectricity," *International Journal of Thermal Sciences,* vol. 104, pp. 225-227, 2016.
[47] R. B. Wilson, and D. G. Cahill, "Experimental validation of the interfacial form of the Wiedemann-Franz law," *Physical Review Letters,* vol. 108, no. 25, 2012.
[48] G. J. Snyder, and E. S. Toberer, "Complex thermoelectric materials," *Materials for sustainable energy: a collection of peer-reviewed research and review articles from Nature Publishing Group*, pp. 101-110: World Scientific, 2011.
[49] H. Goldsmid, "Recent studies of bismuth telluride and its alloys," *Journal of Applied Physics,* vol. 32, no. 10, pp. 2198-2202, 1961.
[50] G. Wang, and T. Cagin, "Electronic structure of the thermoelectric materials Bi 2 Te 3 and Sb 2 Te 3 from first-principles calculations," *Physical Review B,* vol. 76, no. 7, pp. 075201, 2007.
[51] D. M. Rowe, *Thermoelectrics handbook: macro to nano*: CRC press, 2018.
[52] H. J. Goldsmid, *Introduction to thermoelectricity*: Springer, 2010.
[53] H. Goldsmid, A. Sheard, and D. Wright, "The performance of bismuth telluride thermojunctions," *British Journal of Applied Physics,* vol. 9, no. 9, pp. 365, 1958.
[54] H.-S. Kim, N. A. Heinz, Z. M. Gibbs *et al.*, "High thermoelectric performance in (Bi0. 25Sb0. 75) 2Te3 due to band convergence and improved by carrier concentration control," *Materials Today,* vol. 20, no. 8, pp. 452-459, 2017.
[55] W. Xie, X. Tang, Y. Yan *et al.*, "Unique nanostructures and enhanced thermoelectric performance of melt-spun BiSbTe alloys," *Applied Physics Letters,* vol. 94, no. 10, pp. 102111, 2009.
[56] B. Poudel, Q. Hao, Y. Ma *et al.*, "High-thermoelectric performance of nanostructured bismuth antimony telluride bulk alloys," *Science,* vol. 320, no. 5876, pp. 634-638, 2008.
[57] S. I. Kim, K. H. Lee, H. A. Mun *et al.*, "Dense dislocation arrays embedded in grain boundaries for high-performance bulk thermoelectrics," *Science,* vol. 348, no. 6230, pp. 109-114, 2015.
[58] J. P. Heremans, V. Jovovic, E. S. Toberer *et al.*, "Enhancement of thermoelectric efficiency in PbTe by distortion of the electronic density of states," *Science,* vol. 321, no. 5888, pp. 554-557, 2008.
[59] P. K. Sharma, T. Senguttuvan, V. K. Sharma *et al.*, "Revisiting the thermoelectric properties of lead telluride," *Materials Today Energy,* vol. 21, pp. 100713, 2021.
[60] X. Chen, X. Hao, X. Zhou *et al.*, "Performance Optimization for PbTe-based Thermoelectric Materials," *Frontiers in Energy Research*, pp. 672.
[61] Y. Pei, A. LaLonde, S. Iwanaga *et al.*, "High thermoelectric figure of merit in heavy hole dominated PbTe," *Energy & Environmental Science,* vol. 4, no. 6, pp. 2085-2089, 2011.
[62] A. D. LaLonde, Y. Pei, and G. J. Snyder, "Reevaluation of PbTe 1− x I x as high performance n-type thermoelectric material," *Energy & Environmental Science,* vol. 4, no. 6, pp. 2090-2096, 2011.

[63] H. Wang, Y. Pei, A. D. LaLonde *et al.*, "Weak electron–phonon coupling contributing to high thermoelectric performance in n-type PbSe," *Proceedings of the National Academy of Sciences,* vol. 109, no. 25, pp. 9705-9709, 2012.

[64] H. Wang, Y. Pei, A. D. LaLonde *et al.*, "Heavily doped p-type PbSe with high thermoelectric performance: an alternative for PbTe," *Advanced Materials,* vol. 23, no. 11, pp. 1366-1370, 2011.

[65] Y. Pei, X. Shi, A. LaLonde *et al.*, "Convergence of electronic bands for high performance bulk thermoelectrics," *Nature,* vol. 473, no. 7345, pp. 66-69, 2011.

[66] K. F. Hsu, S. Loo, F. Guo *et al.*, "Cubic AgPb m SbTe2+ m: bulk thermoelectric materials with high figure of merit," *Science,* vol. 303, no. 5659, pp. 818-821, 2004.

[67] L.-D. Zhao, C. Chang, G. Tan *et al.*, "SnSe: a remarkable new thermoelectric material," *Energy & Environmental Science,* vol. 9, no. 10, pp. 3044-3060, 2016.

[68] Z.-G. Chen, X. Shi, L.-D. Zhao *et al.*, "High-performance SnSe thermoelectric materials: Progress and future challenge," *Progress in Materials Science,* vol. 97, pp. 283-346, 2018.

[69] C. Wang, Y. Xia, Z. Tian *et al.*, "Photoemission study of the electronic structure of valence band convergent SnSe," *Physical Review B,* vol. 96, no. 16, pp. 165118, 2017.

[70] L.-D. Zhao, S.-H. Lo, Y. Zhang *et al.*, "Ultralow thermal conductivity and high thermoelectric figure of merit in SnSe crystals," *Nature,* vol. 508, no. 7496, pp. 373-377, 2014.

[71] A. T. Duong, V. Q. Nguyen, G. Duvjir *et al.*, "Achieving ZT= 2.2 with Bi-doped n-type SnSe single crystals," *Nature communications,* vol. 7, no. 1, pp. 1-6, 2016.

[72] S. Li, Y. Wang, C. Chen *et al.*, "Heavy Doping by Bromine to Improve the Thermoelectric Properties of n-type Polycrystalline SnSe," *Advanced Science,* vol. 5, no. 9, pp. 1800598, 2018.

[73] C. Zhou, Y. K. Lee, Y. Yu *et al.*, "Polycrystalline SnSe with a thermoelectric figure of merit greater than the single crystal," *Nature materials,* vol. 20, no. 10, pp. 1378-1384, 2021.

[74] Y. He, T. Day, T. Zhang *et al.*, "High thermoelectric performance in non-toxic earth-abundant copper sulfide," *Advanced Materials,* vol. 26, no. 23, pp. 3974-3978, 2014.

[75] H. Liu, X. Shi, F. Xu *et al.*, "Copper ion liquid-like thermoelectrics," *Nature materials,* vol. 11, no. 5, pp. 422-425, 2012.

[76] D. Yang, X. Su, J. Li *et al.*, "Blocking ion migration stabilizes the high thermoelectric performance in Cu2Se composites," *Advanced Materials,* vol. 32, no. 40, pp. 2003730, 2020.

[77] T. Geballe, and G. Hull, "Seebeck effect in silicon," *Physical Review,* vol. 98, no. 4, pp. 940, 1955.

[78] R. He, W. Heyn, F. Thiel *et al.*, "Thermoelectric properties of silicon and recycled silicon sawing waste," *Journal of Materiomics,* vol. 5, no. 1, pp. 15-33, 2019.

[79] J. Dismukes, L. Ekstrom, E. Steigmeier *et al.*, "Thermal and electrical properties of heavily doped Ge-Si alloys up to 1300 K," *Journal of Applied Physics,* vol. 35, no. 10, pp. 2899-2907, 1964.

[80] A. I. Boukai, Y. Bunimovich, J. Tahir-Kheli *et al.*, "Silicon nanowires as efficient thermoelectric materials," *nature,* vol. 451, no. 7175, pp. 168-171, 2008.

[81] A. I. Hochbaum, R. Chen, R. D. Delgado *et al.*, "Enhanced thermoelectric performance of rough silicon nanowires," *Nature,* vol. 451, no. 7175, pp. 163-167, 2008.

[82] J. A. Martinez, P. P. Provencio, S. Picraux *et al.*, "Enhanced thermoelectric figure of merit in SiGe alloy nanowires by boundary and hole-phonon scattering," *Journal of Applied Physics,* vol. 110, no. 7, pp. 074317, 2011.

[83] H. Udono, H. Tajima, M. Uchikoshi *et al.*, "Crystal growth and characterization of Mg2Si for IR-detectors and thermoelectric applications," *Japanese Journal of Applied Physics,* vol. 54, no. 7S2, pp. 07JB06, 2015.

[84] E. Nikitin, "Study of temperature dependence of electrical conductivity and thermal EMF of silicides," *SOVIET PHYSICS-TECHNICAL PHYSICS,* vol. 3, no. 1, pp. 20-22, 1958.

[85] M. I. Fedorov, V. K. Zaitsev, and G. N. Isachenko, "High effective thermoelectrics based on the Mg2Si-Mg2Sn solid solution." pp. 286-292.

[86] M. Rull-Bravo, A. Moure, J. Fernández *et al.*, "Skutterudites as thermoelectric materials: revisited," *Rsc Advances,* vol. 5, no. 52, pp. 41653-41667, 2015.

[87] D. J. Singh, and W. E. Pickett, "Skutterudite antimonides: Quasilinear bands and unusual transport," *Physical Review B,* vol. 50, no. 15, pp. 11235, 1994.

[88] G. Nolas, M. Kaeser, R. Littleton IV *et al.*, "High figure of merit in partially filled ytterbium skutterudite materials," *Applied Physics Letters,* vol. 77, no. 12, pp. 1855-1857, 2000.

[89] J. R. Sootsman, D. Y. Chung, and M. G. Kanatzidis, "New and old concepts in thermoelectric materials," *Angewandte Chemie International Edition,* vol. 48, no. 46, pp. 8616-8639, 2009.

[90] H. Tashiro, Y. Notohara, T. Sakakibara *et al.*, "Effects of doping Pd/Pt in CoSb3 crystals on electrical and thermoelectric properties." pp. 326-329.

[91] Q. Lu, J. Zhang, X. Zhang *et al.*, "Effects of double filling of La and Ce on thermoelectric properties of Ce m La n Fe 1.0 Co 3.0 Sb 12 compounds by spark plasma sintering," American Institute of Physics, 2005.

[92] X. Shi, J. Yang, J. R. Salvador *et al.*, "Multiple-filled skutterudites: high thermoelectric figure of merit through separately optimizing electrical and thermal transports," *Journal of the American Chemical Society,* vol. 133, no. 20, pp. 7837-7846, 2011.

[93] G. Rogl, A. Grytsiv, P. Heinrich *et al.*, "New bulk p-type skutterudites DD0. 7Fe2. 7Co1. 3Sb12− xXx (X= Ge, Sn) reaching ZT> 1.3," *Acta Materialia,* vol. 91, pp. 227-238, 2015.

[94] R. Funahashi, and S. Urata, "Fabrication and application of an oxide thermoelectric system," *International journal of applied ceramic technology,* vol. 4, no. 4, pp. 297-307, 2007.

[95] I. Terasaki, Y. Sasago, and K. Uchinokura, "Large thermoelectric power in NaCo 2 O 4 single crystals," *Physical Review B,* vol. 56, no. 20, pp. R12685, 1997.

[96] R. Funahashi, I. Matsubara, H. Ikuta *et al.*, "An oxide single crystal with high thermoelectric performance in air," *Japanese Journal of Applied Physics,* vol. 39, no. 11B, pp. L1127, 2000.

[97] T. Itoh, and I. Terasaki, "Thermoelectric properties of Bi2. 3-xPbxSr2. 6Co2Oy single crystals," *Japanese Journal of Applied Physics,* vol. 39, no. 12R, pp. 6658, 2000.

[98] S. Hébert, S. Lambert, D. Pelloquin *et al.*, "Large thermopower in a metallic cobaltite: the layered Tl-Sr-Co-O misfit," *Physical Review B,* vol. 64, no. 17, pp. 172101, 2001.

[99] D. Pelloquin, A. Maignan, S. Hébert *et al.*, "New misfit cobaltites [Pb0. 7A0. 4Sr1. 9O3][CoO2] 1.8 (A= Hg, Co) with large thermopower," *Chemistry of materials,* vol. 14, no. 7, pp. 3100-3105, 2002.

[100] Y. Gu, X.-L. Shi, L. Pan *et al.*, "Rational electronic and structural designs advance BiCuSeO thermoelectrics," *Advanced Functional Materials,* vol. 31, no. 25, pp. 2101289, 2021.

[101] S. Ohta, T. Nomura, H. Ohta *et al.*, "Large thermoelectric performance of heavily Nb-doped SrTiO 3 epitaxial film at high temperature," *Applied physics letters,* vol. 87, no. 9, pp. 092108, 2005.

[102] K. Koumoto, I. Terasaki, and R. Funahashi, "Complex oxide materials for potential thermoelectric applications," *MRS bulletin,* vol. 31, no. 3, pp. 206-210, 2006.

[103] F. Heusler, "Verh. Deutsche Physikalische Gesellschaft. 5, S," *Verh. Deutsche PhysikalischeGesellschaft5*, 1903.

[104] T. Graf, C. Felser, and S. S. Parkin, "Simple rules for the understanding of Heusler compounds," *Progress in solid state chemistry,* vol. 39, no. 1, pp. 1-50, 2011.

[105] R. Asahi, T. Morikawa, H. Hazama *et al.*, "Materials design and development of functional materials for industry," *Journal of Physics: Condensed Matter,* vol. 20, no. 6, pp. 064227, 2008.

[106] Y. Kimura, H. Ueno, and Y. Mishima, “Thermoelectric Properties of Directionally Solidified Half-Heusler (M 0.5 a, M 0.5 b) NiSn (Ma, Mb= Hf, Zr, Ti) Alloys,” *Journal of electronic materials,* vol. 38, no. 7, pp. 934-939, 2009.

[107] M. Zhou, L. Chen, C. Feng *et al.*, “Moderate-temperature thermoelectric properties of TiCoSb-based half-Heusler compounds Ti 1− x Ta x Co Sb,” *Journal of Applied Physics,* vol. 101, no. 11, pp. 113714, 2007.

[108] H. Hohl, A. P. Ramirez, C. Goldmann *et al.*, “Efficient dopants for ZrNiSn-based thermoelectric materials,” *Journal of Physics: Condensed Matter,* vol. 11, no. 7, pp. 1697, 1999.

[109] Y. Kimura, T. Kuji, A. Zama *et al.*, “High-Performance of Half-Heusler MNiSn (M= Hf, Zr) Single-Phase Thermoelectric Alloys Fabricated using Optical Floating Zone Melting,” *MRS Online Proceedings Library (OPL),* vol. 886, 2005.

[110] S. Sakurada, and N. Shutoh, *Appl. Phys. Lett.,* vol. 86, pp. 2105, 2005.

[111] H. Zhu, J. Mao, Y. Li *et al.*, “Discovery of TaFeSb-based half-Heuslers with high thermoelectric performance,” *Nature communications,* vol. 10, no. 1, pp. 1-8, 2019.

[112] G. Mahan, and J. Sofo, “The best thermoelectric,” *Proceedings of the National Academy of Sciences,* vol. 93, no. 15, pp. 7436-7439, 1996.

[113] Y. Nishino, "Pseudogap engineering of Fe2VAl-based thermoelectric Heusler compounds," *Thermoelectric Energy Conversion*, pp. 143-156: Elsevier, 2021.

[114] H. Okamura, J. Kawahara, T. Nanba *et al.*, “Pseudogap formation in the intermetallic compounds (Fe 1− x V x) 3 Al,” *Physical review letters,* vol. 84, no. 16, pp. 3674, 2000.

[115] C.-S. Lue, and J. H. Ross, “Semimetallic behavior in Fe 2 VAl: NMR evidence,” *Physical Review B,* vol. 58, no. 15, pp. 9763, 1998.

[116] M. Kato, Y. Nishino, S. Asano *et al.*, “Electrical resistance anomaly and Hall effect in (Fe1-xVx) 3Al alloys,” *Nippon Kinzoku Gakkaishi (1952),* vol. 62, no. 7, pp. 669-674, 1998.

[117] G. Guo, G. Botton, and Y. Nishino, “Electronic structure of possible 3dheavy-fermion'compound,” *Journal of Physics: Condensed Matter,* vol. 10, no. 8, pp. L119, 1998.

[118] Y. Nishino, "Development of thermoelectric materials based on Fe2VAl Heusler compound for energy harvesting applications." p. 142001.

[119] Y. Nishino, S. Kamizono, H. Miyazaki *et al.*, “Effects of off-stoichiometry and Ti doping on thermoelectric performance of Fe2VAl Heusler compound,” *AIP Advances,* vol. 9, no. 12, pp. 125003, 2019.

[120] Y. Nishino, "Thermoelectric properties of the pseudogap Fe2VAl system." pp. 909-912.

[121] Y. Nishino, H. Kato, M. Kato *et al.*, “Effect of off-stoichiometry on the transport properties of the Heusler-type Fe 2 VAl compound,” *Physical Review B,* vol. 63, no. 23, pp. 233303, 2001.

[122] P. D.-I. A. Riss, P. D.-I. F. Garmroudi, P. D.-I. M. Parzer *et al.*, “Physical properties of Fe2-xCrxVAl-type full Heusler compounds,” 2021.

[123] Y. Nishino, S. Deguchi, and U. Mizutani, “Thermal and transport properties of the Heusler-type Fe 2 VAl 1− x Ge x (0≤ x≤ 0.20) alloys: Effect of doping on lattice thermal conductivity, electrical resistivity, and Seebeck coefficient,” *Physical Review B,* vol. 74, no. 11, pp. 115115, 2006.

[124] T. Takeuchi, Y. Terazawa, Y. Furuta *et al.*, “Effect of heavy element substitution and off-stoichiometric composition on thermoelectric properties of Fe2VAl-based Heusler phase,” *Journal of electronic materials,* vol. 42, no. 7, pp. 2084-2090, 2013.

[125] K. Fukuta, K. Tsuchiya, H. Miyazaki *et al.*, “Improving thermoelectric performance of Fe2VAl-based Heusler compounds via high-pressure torsion,” *Applied Physics A,* vol. 128, no. 3, pp. 1-8, 2022.

[126] Y. Takagiwa, Y. Isoda, M. Goto *et al.*, “Conduction type control and power factor enhancement of the thermoelectric material Al2Fe3Si3,” *Journal of Physics and Chemistry of Solids,* vol. 118, pp. 95-98, 2018.

[127] R. O. Suzuki, and T. Kyono, “Thermoelectric properties of Fe2TiAl Heusler alloys,” *Journal of alloys and compounds,* vol. 377, no. 1-2, pp. 38-42, 2004.
[128] T. Zou, T. Jia, W. Xie *et al.*, “Band structure modification of the thermoelectric Heusler-phase TiFe2Sn via Mn substitution,” *Physical Chemistry Chemical Physics,* vol. 19, no. 28, pp. 18273-18278, 2017.
[129] Y. Huang, H. Nagai, K. Hayashi *et al.*, “Preparation and thermoelectric properties of pseudogap intermetallic (Ti1-xVx)NiSi solid solutions,” *Journal of Alloys and Compounds,* vol. 771, pp. 111-116, 2019.
[130] S. Sk, N. Shahi, and S. K. Pandey, “Experimental and computational approaches to study the high temperature thermoelectric properties of novel topological semimetal CoSi,” *Journal of Physics: Condensed Matter,* vol. 34, no. 26, pp. 265901, 2022.
[131] X. Li, “Al-rich Fe–Al based alloys: Phase equilibria, microstructures, coarsening kinetics and mechanical behavior,” Fakultät für Maschinenbau, Ruhr-Universität Bochum Bochum, Germany, 2016.
[132] E. Airiskallio, E. Nurmi, M. Heinonen *et al.*, “High temperature oxidation of Fe–Al and Fe–Cr–Al alloys: The role of Cr as a chemically active element,” *Corrosion Science,* vol. 52, no. 10, pp. 3394-3404, 2010.
[133] M. Palm, F. Stein, and G. Dehm, “Iron aluminides,” *Annual Review of Materials Research,* vol. 49, pp. 297-326, 2019.
[134] F. Hadef, “Solid-state reactions during mechanical alloying of ternary Fe–Al–X (X= Ni, Mn, Cu, Ti, Cr, B, Si) systems: A review,” *Journal of Magnetism and Magnetic Materials,* vol. 419, pp. 105-118, 2016.
[135] O. Kristanovski, R. Richter, I. Krivenko *et al.*, “Quantum many-body intermetallics: Phase stability of Fe 3 Al and small-gap formation in Fe 2 VAl,” *Physical Review B,* vol. 95, no. 4, pp. 045114, 2017.
[136] Y. Nishino, C. Kumada, and S. Asano, “Phase stability of Fe3Al with addition of 3d transition elements,” *Scripta materialia,* vol. 36, no. 4, pp. 461-466, 1997.
[137] G. Frommeyer, Z.-G. Liu, J. Wesemann *et al.*, “Investigations on field-ion image formation and field evaporation sequences of DO3-ordered Fe3Al,” *Ultramicroscopy,* vol. 92, no. 2, pp. 57-66, 2002.
[138] P. Paufler, "JH Westbrook, RL Fleischer (eds.). Intermetallic Compounds. Principles and Practice. John Wiley & Sons, Chichester 1995. Vol. 1. Principles. 1126 S. ISBN 0–471–94219–7. Vol. 2: Practice. 752 S. ISBN 0–471–93454–2. Set: ISBN 0–471–93453–4. Preis:£ 385.–," Wiley Online Library, 1995.
[139] F. Stein, A. Schneider, and G. Frommeyer, “Flow stress anomaly and order–disorder transitions in Fe3Al-based Fe–Al–Ti–X alloys with X= V, Cr, Nb, or Mo,” *Intermetallics,* vol. 11, no. 1, pp. 71-82, 2003.
[140] I. Ohnuma, C. Schön, R. Kainuma *et al.*, “Ordering and phase separation in the bcc phase of the Fe–Al–Ti system,” *Acta materialia,* vol. 46, no. 6, pp. 2083-2094, 1998.
[141] K. Brzakalik, “Nearest-neighbor configurations of Fe atoms in Fe3− xTixAl ordered alloys,” *Intermetallics,* vol. 16, no. 9, pp. 1053-1060, 2008.
[142] G. S. Nolas, J. Sharp, and J. Goldsmid, *Thermoelectrics: basic principles and new materials developments*: Springer Science & Business Media, 2001.
[143] D. M. Rowe, *Materials, preparation, and characterization in thermoelectrics*: CRC press, 2017.
[144] G. J. Snyder, A. H. Snyder, M. Wood *et al.*, “Weighted mobility,” *Advanced Materials,* vol. 32, no. 25, pp. 2001537, 2020.
[145] D. M. Rowe, *CRC handbook of thermoelectrics*: CRC press, 2018.
[146] E. M. Conwell, “Impurity band conduction in germanium and silicon,” *Physical Review,* vol. 103, no. 1, pp. 51, 1956.
[147] N. Mott, “Canad,” *J: Phys,* vol. 34, pp. 1356, 1956.

[148] E. Tetsi, *AB_2O_6 oxides: potential thermoelectric and magnetic materials*: The University of Liverpool (United Kingdom), 2017.
[149] V. H. Crespi, L. L. Y. Jia, K. Khazeni *et al.*, "Thermopower of single-crystal Nd 1− x (S r, P b) x Mn O 3− δ," *Physical Review B,* vol. 53, no. 21, pp. 14303, 1996.
[150] M. Jaime, M. Salamon, M. Rubinstein *et al.*, "High-temperature thermopower in La 2/3 Ca 1/3 MnO 3 films: Evidence for polaronic transport," *Physical Review B,* vol. 54, no. 17, pp. 11914, 1996.
[151] W. Khan, A. H. Naqvi, M. Gupta *et al.*, "Small polaron hopping conduction mechanism in Fe doped LaMnO3," *The Journal of chemical physics,* vol. 135, no. 5, pp. 054501, 2011.
[152] J. He, M. G. Kanatzidis, and V. P. Dravid, "High performance bulk thermoelectrics via a panoscopic approach," *Materials Today,* vol. 16, no. 5, pp. 166-176, 2013.
[153] J. He, S. N. Girard, M. G. Kanatzidis *et al.*, "Microstructure-lattice thermal conductivity correlation in nanostructured PbTe0. 7S0. 3 thermoelectric materials," *Advanced Functional Materials,* vol. 20, no. 5, pp. 764-772, 2010.
[154] J. P. Heremans, B. Wiendlocha, and A. M. Chamoire, "Resonant levels in bulk thermoelectric semiconductors," *Energy & Environmental Science,* vol. 5, no. 2, pp. 5510-5530, 2012.
[155] K. Biswas, J. He, I. D. Blum *et al.*, "High-performance bulk thermoelectrics with all-scale hierarchical architectures," *Nature,* vol. 489, no. 7416, pp. 414-418, 2012.
[156] K. Nielsen, "Another Kind of Light: The Work of TJ Seebeck and His Collaboration with Goethe, Part 2," *Historical studies in the physical and biological sciences,* vol. 21, no. 2, pp. 317-397, 1991.
[157] C. M. Jaworski, B. Wiendlocha, V. Jovovic *et al.*, "Combining alloy scattering of phonons and resonant electronic levels to reach a high thermoelectric figure of merit in PbTeSe and PbTeS alloys," *Energy & Environmental Science,* vol. 4, no. 10, pp. 4155-4162, 2011.
[158] S.-C. Ur, P. Nash, and I.-H. Kim, "Solid-state syntheses and properties of Zn4Sb3 thermoelectric materials," *Journal of alloys and compounds,* vol. 361, no. 1-2, pp. 84-91, 2003.
[159] Q. Shen, L. Zhang, L. Chen *et al.*, "Thermoelectric properties of ZrNiSn-based half-Heusler compounds by solid state reaction method," *Journal of materials science letters,* vol. 20, no. 24, pp. 2197-2199, 2001.
[160] J. Y. Yang, Y. Chen, J. Peng *et al.*, "Phase transformation and synthesis of Ni substituted CoSb3 skutterudite synthesis during solid state reaction." pp. 857-860.
[161] A. Tyagi, and R. S. Ningthoujam, *Handbook on Synthesis Strategies for Advanced Materials*: Springer, 2021.
[162] Y. Kawaharada, K. Kurosaki, M. Uno *et al.*, "Thermoelectric properties of CoSb3," *Journal of alloys and compounds,* vol. 315, no. 1-2, pp. 193-197, 2001.
[163] L. Huang, R. He, S. Chen *et al.*, "A new n-type half-Heusler thermoelectric material NbCoSb," *Materials Research Bulletin,* vol. 70, pp. 773-778, 2015.
[164] J. Yu, C. Fu, Y. Liu *et al.*, "Unique role of refractory Ta alloying in enhancing the figure of merit of NbFeSb thermoelectric materials," *Advanced Energy Materials,* vol. 8, no. 1, pp. 1701313, 2018.
[165] C. Suryanarayana, "Mechanical alloying and milling," *Progress in materials science,* vol. 46, no. 1-2, pp. 1-184, 2001.
[166] C. Chen, D.-W. Liu, B.-P. Zhang *et al.*, "Enhanced thermoelectric properties obtained by compositional optimization in p-Type Bi x Sb2− x Te3 fabricated by mechanical alloying and spark plasma sintering," *Journal of electronic materials,* vol. 40, no. 5, pp. 942-947, 2011.
[167] W.-S. Liu, B.-P. Zhang, J.-F. Li *et al.*, "Enhanced thermoelectric properties in CoSb 3-x Te x alloys prepared by mechanical alloying and spark plasma sintering," *Journal of Applied Physics,* vol. 102, no. 10, pp. 103717, 2007.

[168] Q. Tan, and J.-F. Li, “Thermoelectric properties of Sn-S bulk materials prepared by mechanical alloying and spark plasma sintering,” *Journal of electronic materials,* vol. 43, no. 6, pp. 2435-2439, 2014.

[169] C.-H. Lee, S.-H. Lee, S.-Y. Chun *et al.*, “Fabrication of Mg2Si thermoelectric materials by mechanical alloying and spark-plasma sintering process,” *Journal of nanoscience and nanotechnology,* vol. 6, no. 11, pp. 3429-3432, 2006.

[170] Q. He, Q. Hao, X. Wang *et al.*, “Nanostructured Thermoelectric Skutterudite Co1− x Ni x Sb3 Alloys,” *Journal of Nanoscience and Nanotechnology,* vol. 8, no. 8, pp. 4003-4006, 2008.

[171] J. Yang, R. Chen, S. Bao *et al.*, “Thermoelectric properties of silver-doped n-type Bi2Te3-based material prepared by mechanical alloying and subsequent hot pressing,” *Journal of alloys and compounds,* vol. 407, no. 1-2, pp. 330-333, 2006.

[172] G.-E. Lee, and I.-H. Kim, “Thermoelectric and Transport Properties of Permingeatite Cu3SbSe4 Prepared Using Mechanical Alloying and Hot Pressing,” *Materials,* vol. 14, no. 5, pp. 1116, 2021.

[173] A. D. LaLonde, and P. D. Moran, “Synthesis and characterization of p-Type Pb0. 5Sn0. 5Te thermoelectric power generation elements by mechanical alloying,” *Journal of electronic materials,* vol. 39, no. 1, pp. 8-14, 2010.

[174] M. Zhou, Z. M. Gibbs, H. Wang *et al.*, “Optimization of thermoelectric efficiency in SnTe: the case for the light band,” *Physical Chemistry Chemical Physics,* vol. 16, no. 38, pp. 20741-20748, 2014.

[175] S. S. Kistler, “Coherent expanded-aerogels,” *The Journal of Physical Chemistry,* vol. 36, no. 1, pp. 52-64, 2002.

[176] M. Kruszewski, and R. Zybała, “Review of rapid fabrication methods of skutterudite materials,” *Materials Today: Proceedings,* vol. 44, pp. 3475-3482, 2021.

[177] M. D'Arienzo, R. Scotti, B. Di Credico *et al.*, “Synthesis and characterization of morphology-controlled TiO2 nanocrystals: Opportunities and challenges for their application in photocatalytic materials,” *Studies in Surface Science and Catalysis,* vol. 177, pp. 477-540, 2017.

[178] J. J. Ritter, and P. Maruthamuthu, “Synthesis of polycrystalline bismuth telluride by a metal-organo complex method,” *Inorganic Chemistry,* vol. 34, no. 16, pp. 4278-4280, 1995.

[179] L. Marques-Garcia, “Preparation and characterisation of nanostructured bulk Bi2Te3 thermoelectric materials using ultrasound milling,” Cardiff University, 2016.

[180] J. Creighton, and P. Ho, “Introduction to chemical vapor deposition (CVD),” *Chemical vapor deposition,* vol. 2, pp. 1-22, 2001.

[181] A. D. LaLonde, T. Ikeda, and G. J. Snyder, “Rapid consolidation of powdered materials by induction hot pressing,” *Review of Scientific Instruments,* vol. 82, no. 2, pp. 025104, 2011.

[182] H. Kuhn, “Forging and hot pressing,” *ASM Handbook,* vol. 7, pp. 632-637, 1998.

[183] O. Guillon, J. Gonzalez-Julian, B. Dargatz *et al.*, “Field-assisted sintering technology/spark plasma sintering: mechanisms, materials, and technology developments,” *Advanced Engineering Materials,* vol. 16, no. 7, pp. 830-849, 2014.

[184] K. C. Cho, R. H. Woodman, B. R. Klotz *et al.*, “Plasma pressure compaction of tungsten powders,” *Materials and Manufacturing Processes,* vol. 19, no. 4, pp. 619-630, 2004.

[185] P. Cavaliere, B. Sadeghi, and A. Shabani, "Spark plasma sintering: process fundamentals," *Spark plasma sintering of materials*, pp. 3-20: Springer, 2019.

[186] M. Suárez, A. Fernández, J. Menéndez *et al.*, “Challenges and opportunities for spark plasma sintering: a key technology for a new generation of materials,” *Sintering applications,* vol. 13, pp. 319-342, 2013.

[187] R. Davis, B. McDermott, and C. Koch, “Mechanical alloying of brittle materials,” *Metallurgical Transactions A,* vol. 19, no. 12, pp. 2867-2874, 1988.

[188] B. Cook, B. Beaudry, J. Harringa *et al.*, "The preparation of SiGe thermoelectric materials by mechanical alloying." pp. 693-700.

[189] H. Okamura, M. Niino, Y. Park *et al.*, "Preparation and thermoelectric properties of p-type Si-Ge thermoelectric materials by mechanical alloying," *Materials Science and Engineering Serving Society*, pp. 251-254: Elsevier, 1998.

[190] A. Usenko, D. Moskovskikh, M. Gorshenkov *et al.*, "Optimization of ball-milling process for preparation of Si–Ge nanostructured thermoelectric materials with a high figure of merit," *Scripta Materialia,* vol. 96, pp. 9-12, 2015.

[191] N. Bouad, R. Marin-Ayral, and J. Tedenac, "Mechanical alloying and sintering of lead telluride," *Journal of alloys and compounds,* vol. 297, no. 1-2, pp. 312-318, 2000.

[192] N. Bouad, R. Marin-Ayral, G. Nabias *et al.*, "Phase transformation study of Pb–Te powders during mechanical alloying," *Journal of alloys and compounds,* vol. 353, no. 1-2, pp. 184-188, 2003.

[193] C. Papageorgiou, E. Hatzikraniotis, C. B. Lioutas *et al.*, "Thermoelectric properties of nanocrystalline PbTe synthesized by mechanical alloying," *Journal of electronic materials,* vol. 39, no. 9, pp. 1665-1668, 2010.

[194] Q. Zhang, S. Yang, Q. Zhang *et al.*, "Effect of aluminum on the thermoelectric properties of nanostructured PbTe," *Nanotechnology,* vol. 24, no. 34, pp. 345705, 2013.

[195] P. Pierrat, A. Dauscher, B. Lenoir *et al.*, "Preparation of the Bi8Sb32Te60 solid solution by mechanical alloying," *Journal of materials science,* vol. 32, no. 14, pp. 3653-3657, 1997.

[196] M. Miyajima, K. Takagi, H. Okamura *et al.*, "Thermoelectric properties of Bi-Sb composite prepared by mechanical alloying method." pp. 18-21.

[197] L. Xue-Dong, and Y.-H. Park, "Structure and transport properties of (Bi1-xSbx) 2Te3 thermoelectric materials prepared by mechanical alloying and pulse discharge sintering," *Materials Transactions,* vol. 43, no. 4, pp. 681-687, 2002.

[198] G.-E. Lee, I.-H. Kim, S.-M. Choi *et al.*, "Process controls for Bi2Te3-Sb2Te3 prepared by mechanical alloying and hot pressing," *Journal of the Korean Physical Society,* vol. 65, no. 12, pp. 2066-2070, 2014.

[199] H. Mansouri, S. A. Sajjadi, A. Babakhani *et al.*, "Microstructure and thermoelectric performance evaluation of p-type (Bi, Sb) 2Te3 materials synthesized using mechanical alloying and spark plasma sintering process," *Journal of Materials Science: Materials in Electronics,* vol. 32, no. 8, pp. 9858-9871, 2021.

[200] M. Umemoto, "Preparation of thermoelectric β-FeSi2 doped with Al and Mn by mechanical alloying (Overview)," *Materials Transactions, JIM,* vol. 36, no. 2, pp. 373-383, 1995.

[201] H. Nagai, K.-i. Nagai, T. Katsura *et al.*, "Thermoelectric properties of β-FeSi2 mechanically alloyed with Si and C," *Materials Transactions, JIM,* vol. 39, no. 11, pp. 1140-1145, 1998.

[202] M. Ito, T. Tada, and S. Hara, "Thermoelectric properties of hot-pressed β-FeSi2 with yttria dispersion by mechanical alloying," *Journal of alloys and compounds,* vol. 408, pp. 363-367, 2006.

[203] J. Yang, Y. Chen, J. Peng *et al.*, "Synthesis of CoSb3 skutterudite by mechanical alloying," *Journal of alloys and compounds,* vol. 375, no. 1-2, pp. 229-232, 2004.

[204] T. Itoh, T. Yamashita, and K. Kitagawa, "Synthesis of CoSb3 Compound by MA-SPS Method and Its Thermoelectric Properties," *Journal of the Japan Society of Powder and Powder Metallurgy,* vol. 51, no. 6, pp. 441-446, 2004.

[205] S.-C. Ur, J.-C. Kwon, and I.-H. Kim, "Thermoelectric properties of Fe-doped CoSb3 prepared by mechanical alloying and vacuum hot pressing," *Journal of alloys and compounds,* vol. 442, no. 1-2, pp. 358-361, 2007.

[206] V. Trivedi, M. Battabyal, P. Balasubramanian *et al.*, "Microstructure and doping effect on the enhancement of the thermoelectric properties of Ni doped Dy filled CoSb 3 skutterudites," *Sustainable Energy & Fuels,* vol. 2, no. 12, pp. 2687-2697, 2018.

[207] M. Mikami, A. Matsumoto, and K. Kobayashi, “Synthesis and thermoelectric properties of microstructural Heusler Fe2VAl alloy,” *Journal of alloys and compounds,* vol. 461, no. 1-2, pp. 423-426, 2008.

[208] L. Lu, M. Lai, and M. Hoe, “Formaton of nanocrystalline Mg2Si and Mg2Si dispersion strengthened Mg-Al alloy by mechanical alloying,” *Nanostructured materials,* vol. 10, no. 4, pp. 551-563, 1998.

[209] K. Sridhar, and K. Chattopadhyay, “Synthesis by mechanical alloying and thermoelectric properties of Cu2Te,” *Journal of alloys and compounds,* vol. 264, no. 1-2, pp. 293-298, 1998.

[210] T. Aizawa, R. Song, and A. Yamamoto, “Solid-state synthesis of thermoelectric materials in Mg–Si–Ge system,” *Materials transactions,* vol. 46, no. 7, pp. 1490-1496, 2005.

[211] C. Suryanarayana, and E. Ivanov, “Mechanical alloying for advanced materials,” *Powder Materials: Current Research and Industrial Practices III*, pp. 169-178, 2010.

[212] M. Ramezani, and T. Neitzert, “Mechanical milling of aluminum powder using planetary ball milling process,” *Journal of Achievements in Materials and Manufacturing Engineering,* vol. 55, no. 2, pp. 790-798, 2012.

[213] C. F. Burmeister, and A. Kwade, “Process engineering with planetary ball mills,” *Chemical Society Reviews,* vol. 42, no. 18, pp. 7660-7667, 2013.

[214] J. M. Ferreiro, D. Diaz-Droguett, D. Celentano *et al.*, “Effect of the annealing on the power factor of un-doped cold-pressed SnSe,” *Applied Thermal Engineering,* vol. 111, pp. 1426-1432, 2017.

[215] W. Wang, Y. Sun, Y. Feng *et al.*, “High thermoelectric performance bismuth telluride prepared by cold pressing and annealing facilitating large scale application,” *Materials Today Physics,* vol. 21, pp. 100522, 2021.

[216] B. A. Kuropatwa, and H. Kleinke, “Thermoelectric properties of stoichiometric compounds in the (SnTe) x (Bi2Te3) y system,” *Zeitschrift für anorganische und allgemeine Chemie,* vol. 638, no. 15, pp. 2640-2647, 2012.

[217] E. Gutmanas, and A. Lawley, *Cold Sintering-A New Powder Consolidation Process*, DREXEL UNIV PHILADELPHIA PA DEPT OF MATERIALS ENGINEERING, 1983.

[218] R. Madhuri, S. Narayana Iyer, and S. Ganesanpotti, “Insights into the microstructure and dielectric properties of cold sintered NaCa2Mg2V3O12 based composites,” *Frontiers in Materials,* vol. 8, pp. 665033, 2021.

[219] O. Falkenbach, D. Hartung, P. J. Klar *et al.*, “Thermoelectric properties of nanostructured bismuth-doped lead telluride Bi x (PbTe) 1− x prepared by co-ball-milling,” *Journal of electronic materials,* vol. 43, no. 6, pp. 1674-1680, 2014.

[220] J. Sung-Jin, S. K. Kim, P. Hyung-Ho *et al.*, “Effect of Mechanical Deformation on Thermoelectric Properties of p-Type (Bi 0. 225 Sb 0. 775) 2 Te 3 Alloys,” *Journal of Nanomaterials,* vol. 2013, 2013.

[221] A. Kundu, A. Sittiho, I. Charit *et al.*, “Development of Fe-9Cr alloy via high-energy ball milling and spark plasma sintering,” *JOM,* vol. 71, no. 8, pp. 2846-2855, 2019.

[222] A. Valério, and S. L. Morelhao, “Usage of Scherrer's formula in X-ray diffraction analysis of size distribution in systems of monocrystalline nanoparticles,” *arXiv preprint arXiv:1911.00701*, 2019.

[223] O. Tolochyn, O. Tolochyna, H. Bagliuk *et al.*, “Influence of sintering temperature on the structure and properties of powder iron aluminide Fe3Al,” *Powder Metallurgy and Metal Ceramics,* vol. 59, no. 3, pp. 150-159, 2020.

[224] "SEM," https://www.technologynetworks.com/analysis/articles/sem-vs-tem-331262.

[225] B. Hafner, “Scanning electron microscopy primer,” *Characterization Facility, University of Minnesota-Twin Cities*, pp. 1-29, 2007.

[226] N. D. Lowhorn, W. Wong-Ng, Z.-Q. Lu *et al.*, "Development of a Seebeck coefficient Standard Reference Material™," *Journal of materials research,* vol. 26, no. 15, pp. 1983-1992, 2011.

[227] J. García-Cañadas, and G. Min, "Multifunctional probes for high-throughput measurement of Seebeck coefficient and electrical conductivity at room temperature," *Review of Scientific Instruments,* vol. 85, no. 4, 2014.

[228] "ZEM,"https://ulvac.eu/products/components/thermal-analysis/zem 3/#Downloadsd84c-df65.

[229] NETZSCH. https://analyzing-testing.netzsch.com/en/products/thermal-diffusivity-and-conductivity/lfa-457-micro-flash.

[230] H. Johra, "Description of the laser flash analysis method for thermal diffusivity measurement with the LFA 447," 2019.

[231] X. Chen, A. Weathers, A. Moore *et al.*, "Thermoelectric properties of cold-pressed higher manganese silicides for waste heat recovery," *Journal of Electronic Materials,* vol. 41, no. 6, pp. 1564-1572, 2012.

[232] B. Feng, G. Li, Y. Hou *et al.*, "Enhanced thermoelectric properties of Sb-doped BiCuSeO due to decreased band gap," *Journal of Alloys and Compounds,* vol. 712, pp. 386-393, 2017.

[233] F. Yang, Z. Rong, X. Cai *et al.*, "Characterization and thermoelectric properties of Bi0. 4Sb1. 6Te3 nanostructured bulk prepared by mechanical alloying and microwave activated hot pressing," *Ceramics international,* vol. 41, no. 5, pp. 6817-6823, 2015.

[234] P.-P. Shang, B.-P. Zhang, J.-F. Li *et al.*, "Effect of sintering temperature on thermoelectric properties of La-doped SrTiO3 ceramics prepared by sol–gel process and spark plasma sintering," *Solid State Sciences,* vol. 12, no. 8, pp. 1341-1346, 2010.

[235] T.-R. Wei, Z. Li, F.-H. Sun *et al.*, "Thermoelectric SnS and SnS-SnSe solid solutions prepared by mechanical alloying and spark plasma sintering: Anisotropic thermoelectric properties," *Scientific reports,* vol. 7, no. 1, pp. 1-7, 2017.

[236] M. Mikami, S. Tanaka, and K. Kobayashi, "Thermoelectric properties of Sb-doped Heusler Fe2VAl alloy," *Journal of Alloys and Compounds,* vol. 484, no. 1-2, pp. 444-448, 2009.

[237] M. Rafiei, M. Enayati, and F. Karimzadeh, "Characterization and formation mechanism of nanocrystalline (Fe, Ti) 3Al intermetallic compound prepared by mechanical alloying," *Journal of alloys and compounds,* vol. 480, no. 2, pp. 392-396, 2009.

[238] S.-M. Zhu, and K. Iwasaki, "Characterization of mechanically alloyed ternary Fe–Ti–Al powders," *Materials Science and Engineering: A,* vol. 270, no. 2, pp. 170-177, 1999.

[239] M. Enayati, and M. Salehi, "Formation mechanism of Fe 3 Al and FeAl intermetallic compounds during mechanical alloying," *Journal of materials science,* vol. 40, pp. 3933-3938, 2005.

[240] J. Shou-Yong, L. Li-Bin, H. Ning-Kang *et al.*, "Investigation on lattice constants of Mg-Al spinels," *Journal of materials science letters,* vol. 19, pp. 225-227, 2000.

[241] S. M. Zhu, and K. Iwasaki, "Characterization of mechanically alloyed ternary Fe-Ti-Al powders," *Materials Science and Engineering A,* vol. 270, no. 2, pp. 170-177, 1999.

[242] J. Montes, F. Cuevas, and J. Cintas, "Porosity effect on the electrical conductivity of sintered powder compacts," *Applied Physics A,* vol. 92, no. 2, pp. 375-380, 2008.

[243] W. Wang, Y. Sun, Y. Feng *et al.*, "High thermoelectric performance bismuth telluride prepared by cold pressing and annealing facilitating large scale application," *Materials Today Physics,* vol. 21, 2021.

[244] S. E. Haghighi, K. Janghorban, and S. Izadi, "Structural evolution of Fe-50 at.% Al powders during mechanical alloying and subsequent annealing processes," *Journal of Alloys and Compounds,* vol. 495, no. 1, pp. 260-264, 2010.

[245] M. Marcinkowski, and R. Smoluchowski, “Electrical resistivity of iron-aluminum superlattices near Fe3Al,” *Journal of Physics and Chemistry of Solids,* vol. 26, no. 1, pp. 185-189, 1965.

[246] E. Elsukov, E. Voronina, A. Shuravin *et al.*, “Structure of the Fe100− x Alx alloys (25< x< 35 at.%) annealed in a temperature range of 400–800° C and the effect of the ordering type on the magnetic properties,” *The Physics of Metals and Metallography,* vol. 102, no. 1, pp. 55-60, 2006.

[247] D. Panda, P. Bhuyan, L. Kumar *et al.*, “Synthesis of Fe _ 3 Fe 3 Al Intermetallic Compound by Mechanical Alloying,” *Arabian Journal for Science and Engineering,* vol. 42, pp. 4427-4437, 2017.

[248] M. Masmoudi, M. Mhadhbi, L. Escoda *et al.*, “Microstructural evolution and corrosion behavior of nanocrystalline FeAl synthesized by mechanical alloying,” *Journal of Alloys and Compounds,* vol. 657, pp. 330-335, 2016.

[249] Y. Xu, S. Zhou, B. Liao *et al.*, “Effect of milling time on the microstructure and magnetic properties of amorphous Ti50Fe50 alloys prepared by mechanical alloying,” *Journal of Materials Research and Technology,* vol. 8, no. 5, pp. 3929-3935, 2019.

[250] V. Livramento, C. Rangel, J. B. Correia *et al.*, "Synthesis of FeTi hydrogen storage material via ball milling: effect of milling energy and atmosphere."

[251] M. Krasnowski, and T. Kulik, “Amorphisation process during mechanical alloying of Al-Fe-Ti powders and crystallisation of the milling products,” *Rev. Adv. Mater. Sci,* vol. 18, pp. 393-397, 2008.

[252] S. Zhou, Y. Xu, B. Liao *et al.*, “In-situ synthesis of Ti-Fe-based alloys prepared by the combination of mechanical alloying and laser melting deposition: microstructure and corrosion resistance,” *Journal of Alloys and Compounds,* vol. 768, pp. 697-706, 2018.

[253] M. Mikami, Y. Kinemuchi, K. Ozaki *et al.*, “Thermoelectric properties of tungsten-substituted Heusler Fe2VAl alloy,” *Journal of Applied Physics,* vol. 111, no. 9, pp. 093710, 2012.

[254] C. S. Lue, C. Chen, J. Lin *et al.*, “Thermoelectric properties of quaternary Heusler alloys Fe 2 VAl 1− x Si x,” *Physical Review B,* vol. 75, no. 6, pp. 064204, 2007.

[255] F. Garmroudi, A. Riss, M. Parzer *et al.*, “Boosting the thermoelectric performance of Fe 2 VAl− type Heusler compounds by band engineering,” *Physical Review B,* vol. 103, no. 8, pp. 085202, 2021.

[256] H. Miyazaki, S. Tanaka, N. Ide *et al.*, “Thermoelectric properties of Heusler-type off-stoichiometric Fe2V1+xAl1-x alloys,” *Materials Research Express,* vol. 1, no. 1, 2014.

[257] T. Saito, “Thermoelectric and Magnetic Properties of (Fe,Co)2tisn Heusler Compounds,” *https://ssrn.com/abstract=4023276*, 2022.

[258] A. Karati, V. S. Hariharan, S. Ghosh *et al.*, “Thermoelectric properties of half-Heusler high-entropy Ti2NiCoSn1-xSb1+x (x = 0.5, 1) alloys with VEC>18,” *Scripta Materialia,* vol. 186, pp. 375-380, 2020.

[259] B. Chanda, and J. Das, “Composition dependence on the evolution of nanoeutectic in CoCrFeNiNbx (0.45≤ x≤ 0.65) high entropy alloys,” *Advanced Engineering Materials,* vol. 20, no. 4, pp. 1700908, 2018.

[260] M. Mantina, R. Valero, C. J. Cramer *et al.*, “Atomic radii of the elements,” *CRC handbook of Chemistry and Physics,* vol. 94, 2013.

[261] C. Paduani, W. Pöttker, J. Ardisson *et al.*, “Mössbauer effect and magnetization studies of the Fe2+ xCr1− xAl system in the L 21 (X2YZ) structure,” *Journal of Physics: Condensed Matter,* vol. 19, no. 15, pp. 156204, 2007.

[262] V. Sharma, S. Pattanaik, H. Parmar *et al.*, “Magnetocaloric properties and magnetic cooling performance of low-cost Fe75− xCrxAl25 alloys,” *MRS Communications,* vol. 8, no. 3, pp. 988-994, 2018.

[263] A. J. Knowles, N. G. Jones, O. M. D. M. Messé *et al.*, "Phase equilibria in the Fe-Mo-Ti ternary system at 1000 °C," *International Journal of Refractory Metals and Hard Materials,* vol. 60, pp. 160-168, 2016.

[264] U. Mizutani, "The Hume-Rothery rules for structurally complex alloy phases," *Surface Properties and Engineering of Complex Intermetallics*, pp. 323-399: World Scientific, 2010.

[265] W. Dai, S. Liang, Y. Luo *et al.*, "Effect of W powders characteristics on the Ti-rich phase and properties of W-10 wt.% Ti alloy," *International Journal of Refractory Metals and Hard Materials,* vol. 50, pp. 240-246, 2015.

[266] Z. Yu, N. Zhang, Z. Yao *et al.*, "Synthesis of hierarchical dendritic micro-nano structure Co x Fe 1− x alloy with tunable electromagnetic absorption performance," *Journal of Materials Chemistry A,* vol. 1, no. 40, pp. 12462-12470, 2013.

[267] S. Yan, L. Zhen, C. Xu *et al.*, "Synthesis, characterization and electromagnetic properties of Fe1− xCox alloy flower-like microparticles," *Journal of magnetism and magnetic materials,* vol. 323, no. 5, pp. 515-520, 2011.

[268] A. Abuchenari, F. Sharifianjazi, A. Pakseresht *et al.*, "Effect of aluminum on microstructural and magnetic properties of nanostructured (Fe85Ni15) 97Al3 alloy produced via mechanical alloying," *Advanced Powder Technology,* vol. 32, no. 2, pp. 337-345, 2021.

[269] M. M. Rico, L. E. Zamora, G. A. Pérez Alcázar *et al.*, "Magnetic and structural study of mechanically alloyed Fe0.7-xMnxAl0.3," *Physica Status Solidi (B) Basic Research,* vol. 220, no. 1, pp. 445-448, 2000.

[270] W. Maziarz, J. Dutkiewicz, and J. Senderski, "Processing of nanocrystalline FeAl X (X= Ni, Mn) intermetallics using a mechanical alloying and hot pressing techniques," *Journal of materials science,* vol. 39, pp. 5425-5429, 2004.

[271] A. Knowles, N. Jones, C. Jones *et al.*, "Phase Equilibria in the Fe-Mo-Ti Ternary System at 1173 K (900° C) and 1023 K (750° C)," *Metallurgical and Materials Transactions A,* vol. 48, no. 9, pp. 4334-4341, 2017.

[272] A. J. Knowles, D. Dye, R. J. Dodds *et al.*, "Tungsten-based bcc-superalloys," *Applied Materials Today,* vol. 23, 2021.

[273] M. Mikami, and K. Kobayashi, "Effect of Bi addition on microstructure and thermoelectric properties of Heusler Fe2VAl-sintered alloy," *Journal of Alloys and Compounds,* vol. 466, no. 1-2, pp. 530-534, 2008.

[274] R. Hasan, and S. C. Ur, "Thermoelectric and Transport Properties of FeV1−xTixSb Half-Heusler System Synthesized by Controlled Mechanical Alloying Process," *Electronic Materials Letters,* vol. 14, no. 6, pp. 725-732, 2018.

[275] Y. Nishino, "Electrical resistance anomaly in Fe3Al-based alloys," *Materials Science and Engineering A,* vol. 258, no. 1-2, pp. 50-58, 1998.

[276] K. Yadav, S. Singh, O. Muthuswamy *et al.*, "Anomalous dependence of thermoelectric parameters on carrier concentration and electronic structure in Mn-substituted Fe2CrAl Heusler alloy," *Philosophical Magazine,* vol. 102, no. 4, pp. 357-374, 2022.

[277] Y. Nishino, S. Kamizono, H. Miyazaki *et al.*, "Effects of off-stoichiometry and Ti doping on thermoelectric performance of Fe2VAl Heusler compound," *AIP Advances,* vol. 9, no. 12, 2019.

[278] M. Kato, Y. Nishino, U. Mizutani *et al.*, "Temperature dependence of electrical resistivity in (Fe1-xTix)3Al alloys," *Journal of Physics Condensed Matter,* vol. 12, no. 43, pp. 9153-9162, 2000.

[279] Y. Nishino, and Y. Tamada, "Doping effects on thermoelectric properties of the off-stoichiometric Heusler compounds Fe2− x V1+ x Al," *Journal of Applied Physics,* vol. 115, no. 12, pp. 123707, 2014.

[280] M. Mikami, K. Ozaki, H. Takazawa *et al.*, "Effect of Ti substitution on thermoelectric properties of W-doped Heusler Fe2VAl alloy," *Journal of electronic materials,* vol. 42, no. 7, pp. 1801-1806, 2013.

[281] R. Orrù, R. Licheri, A. M. Locci *et al.*, "Consolidation/synthesis of materials by electric current activated/assisted sintering," *Materials Science and Engineering R: Reports,* vol. 63, no. 4-6, pp. 127-287, 2009.

[282] E. Ghasali, Y. Palizdar, A. Jam *et al.*, "Effect of Al and Mo addition on phase formation, mechanical and microstructure properties of spark plasma sintered iron alloy," *Materials Today Communications,* vol. 13, pp. 221-231, 2017.

[283] J. Wang, J. Xing, Z. Qiu *et al.*, "Effect of fabrication methods on microstructure and mechanical properties of Fe3Al-based alloys," *Journal of Alloys and Compounds,* vol. 488, no. 1, pp. 117-122, 2009.

[284] C. van der Rest, V. Dupont, J.-P. Erauw *et al.*, "On the reactive sintering of Heusler Fe2VAl-based thermoelectric compounds," *Intermetallics,* vol. 125, pp. 106890, 2020.

[285] M. H. Enayati, and M. Salehi, "Formation mechanism of Fe3Al and FeAl intermetallic compounds during mechanical alloying," *Journal of Materials Science,* vol. 40, no. 15, pp. 3933-3938, 2005.

[286] F. Yan, T. Zhu, X. Zhao *et al.*, "Microstructures and thermoelectric properties of GeSbTe based layered compounds," *Applied Physics A,* vol. 88, no. 2, pp. 425-428, 2007.

[287] C. Nagarjuna, P. Dharmaiah, K. B. Kim *et al.*, "Grain refinement to improve thermoelectric and mechanical performance in n-type Bi2Te2. 7Se0. 3 alloys," *Materials Chemistry and Physics,* vol. 256, pp. 123699, 2020.

[288] A. Sun, Y. Liu, D. Wang *et al.*, "Sintering behavior and properties of Mo-Cu composites," *Advances in Materials Science and Engineering,* vol. 2018, 2018.

[289] S. Paris, E. Gaffet, and F. Bernard, "Control of FeAl composition produced by SPS reactive sintering from mechanically activated powder mixture," *Journal of Nanomaterials,* vol. 2013, 2013.

[290] T. Skiba, P. Haušild, M. Karlík *et al.*, "Mechanical properties of spark plasma sintered FeAl intermetallics," *Intermetallics,* vol. 18, no. 7, pp. 1410-1414, 2010.

[291] M. Zou, J.-F. Li, and T. Kita, "Thermoelectric properties of fine-grained FeVSb half-Heusler alloys tuned to p-type by substituting vanadium with titanium," *Journal of Solid State Chemistry,* vol. 198, pp. 125-130, 2013.

[292] T.-H. An, S.-M. Choi, W.-S. Seo *et al.*, "Effects of spark plasma sintering temperature on thermoelectric properties of higher manganese silicide," *Journal of electronic materials,* vol. 42, no. 7, pp. 2269-2273, 2013.

[293] M. Parzer, F. Garmroudi, A. Riss *et al.*, "High solubility of Al and enhanced thermoelectric performance due to resonant states in Fe2VAlx," *Applied Physics Letters,* vol. 120, no. 7, pp. 071901, 2022.

[294] S. Chen, and Z. Ren, "Recent progress of half-Heusler for moderate temperature thermoelectric applications," *Materials today,* vol. 16, no. 10, pp. 387-395, 2013.

[295] T. Saito, S. Kamishima, and D. Nishio-Hamane, "Thermoelectric and magnetic properties of (Fe, Co) 2TiSn Heusler compounds," *Physica B: Condensed Matter*, pp. 413984, 2022.

[296] T. Saito, "Thermoelectric and Magnetic Properties of (Fe,Co)2tisn Heusler Compounds.," 2022.

[297] A. Novitskii, I. Serhiienko, A. Nepapushev *et al.*, "Mechanochemical synthesis and thermoelectric properties of TiFe2Sn Heusler alloy," *Intermetallics,* vol. 133, 2021.

[298] C.-S. Lue, and Y. Kuo, "Thermal and electrical transport properties of ordered FeAl2," *Journal of Physics: Condensed Matter,* vol. 15, no. 6, pp. 877, 2003.

[299] A. F. May, and G. J. Snyder, "Introduction to modeling thermoelectric transport at high temperatures," *Materials, Preparation, and Characterization in Thermoelectrics*, pp. 11-1-11-18, 2017.

[300] H. Naithani, and T. Dasgupta, "Critical Analysis of Single Band Modeling of Thermoelectric Materials," *ACS Applied Energy Materials,* vol. 3, no. 3, pp. 2200-2213, 2020.

[301] M. Tang, Z. Chen, X. Guo *et al.*, “Reducing Effective Mass for Advancing Thermoelectrics in Sb/Bi-Doped AgCrSe2Compounds,” *ACS Applied Materials and Interfaces,* vol. 12, no. 32, pp. 36347-36354, 2020.

[302] K. Tanwar, D. S. Gyan, S. Bhattacharya *et al.*, “Enhancement of thermoelectric power factor by inducing octahedral ordering in La2-xSrxCoFe O6 double perovskites,” *Physical Review B,* vol. 99, no. 17, 2019.

[303] H. Matsuura, A. Takeshita, T. Imamura *et al.*, “Transition of conduction mechanism from band to variable-range hopping conduction due to Al doping in heavily Al-doped 4H-SiC epilayers,” *Japanese Journal of Applied Physics,* vol. 58, no. 9, 2019.

[304] T. Maiti, M. Saxena, and P. Roy, “Double perovskite (Sr2B'B''O6) oxides for high-temperature thermoelectric power generation - A review,” *Journal of Materials Research,* vol. 34, no. 1, pp. 107-125, 2019.

Appendix

Appendix A- Thermoelectric properties of $Fe_{11-x}Cr_xTi_3Al_6$ (x=0 to 4) samples based on SPEX-CP (BM=5hrs) and PBM-CP (BM=5hrs) followed by annealing at 700^0C

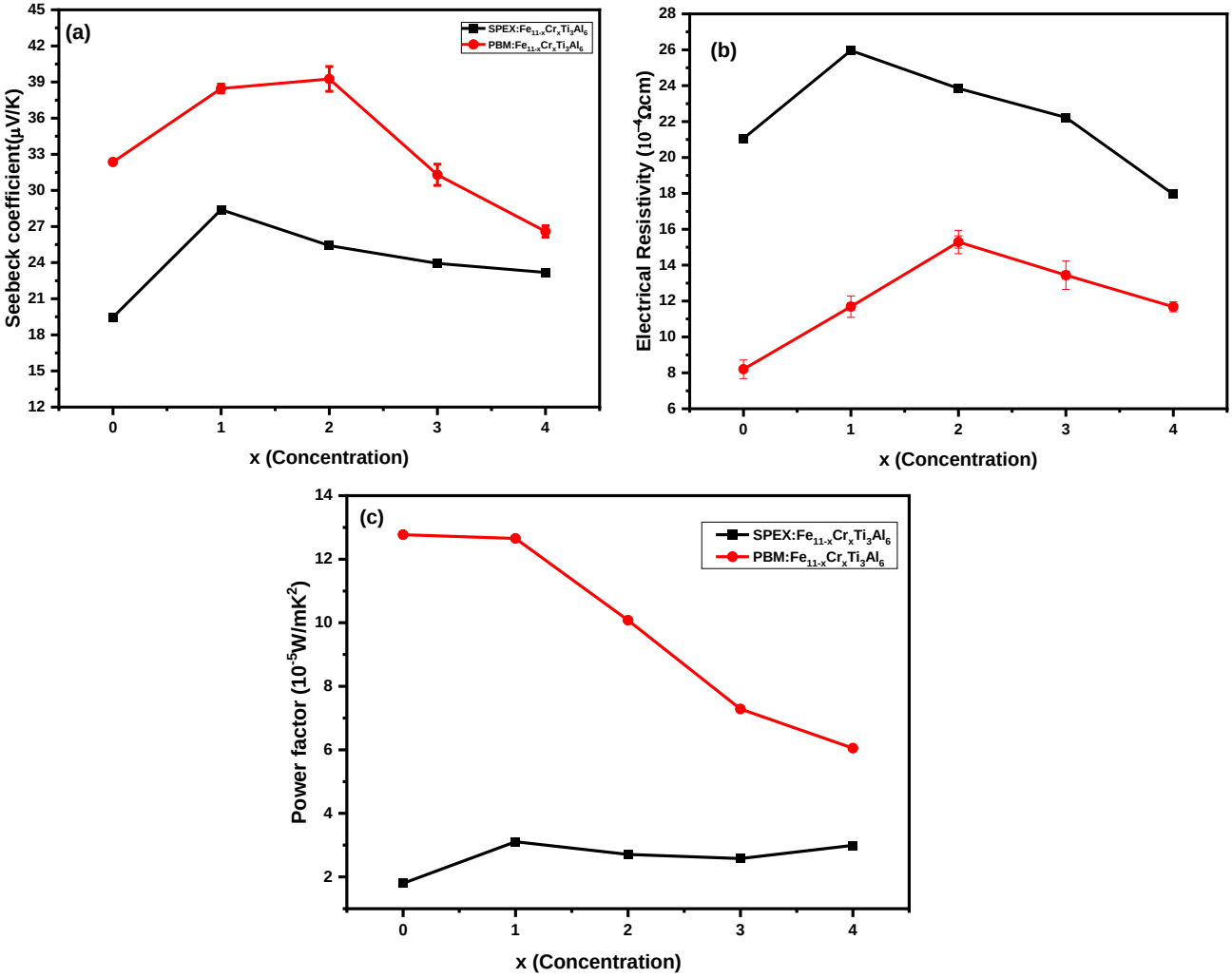

Figure A. 1 Measured (a) Seebeck coefficient (b) Electrical resistivity and (c) Power factor

Appendix B- Measured data of Seebeck coefficient for Bi_2Te_3 (NIST Ref.3451) based on Hot-probe

V_S (mV)	V_T (mV)	Seebeck Coefficient (µV/K)
-1.32	0.243	-217.28
-1.35	0.248	-217.74
-1.35	0.242	-223.14
-1.32	0.245	-215.51
-1.32	0.244	-216.39
-1.32	0.247	-213.76
-1.32	0.244	-216.39

Average value of Seebeck coefficient = -217.17±2.71 µV/K

All measurements were performed at room temperature=290K .Please note that in equation (3.4), the temperature was determined in terms of voltage measured by Cu-constantan thermocouple based on following equation:

$$\Delta T = \frac{\Delta V_T}{\alpha_{Cu-constantan}}$$

Where $\alpha_{Cu-constantan}$ is Seebeck coefficient, which is equal to +40µV/K near room temperature.

Appendix C: Measured data of Electrical resistivity for Stainless steel (SRM) using Multifunctional probes

Sr.No	ρ(10^{-5} Ωcm)
1	7.98
2	7.93
3	8.47
4	7.33
5	8.50
6	7.84
7	7.56
8	7.45

Average electrical resistivity (ρ)= (7.8±0.4) x10^{-5} Ωcm

Appendix D: Magnetic Hysteresis of Fe-Ti-Al-based alloys

(Hysteresis curve was measured for sample fabricated via BM-CP route only)

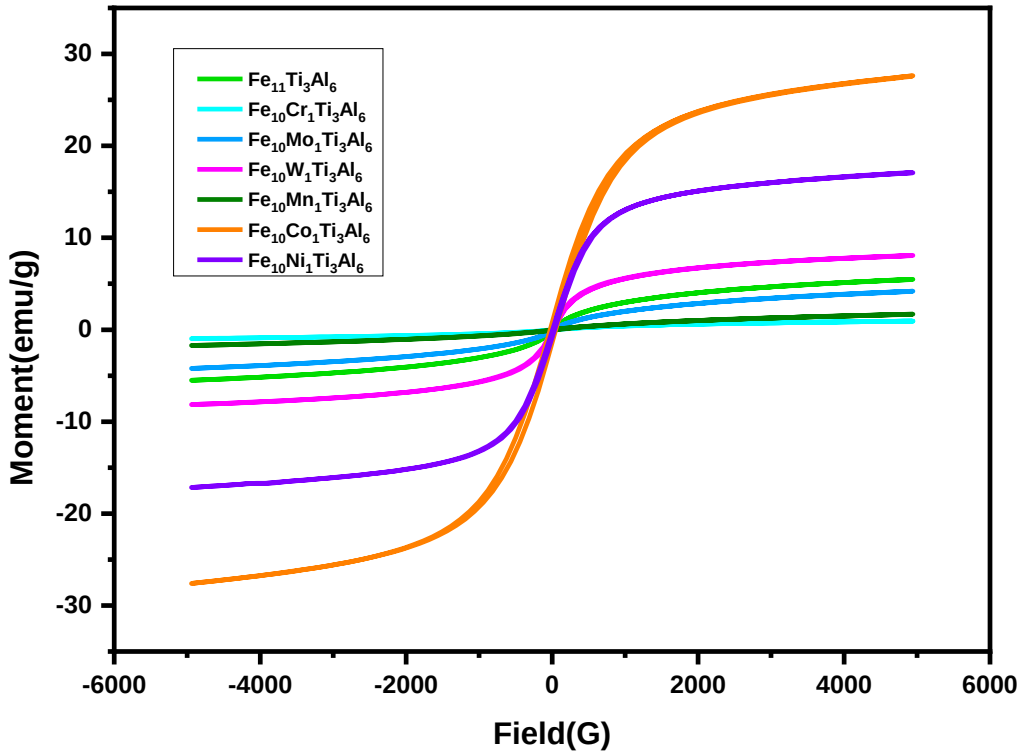

Figure A. 2 Hysteresis curves of Fe-Ti-Al-based alloys